Carnegie Mellon University

CARNEGIE INSTITUTE OF TECHNOLOGY

THESIS

SUBMITTED IN PARTIAL FULFILLMENT OF THE REQUIREMENTS

FOR THE DEGREE OF Doctor of Philosophy

TITLE **CMOS-MEMS Probe Arrays for Tip-Based Nanofabrication**

PRESENTED BY **Yang Zhang**

ACCEPTED BY THE DEPARTMENT OF

Electrical and Computer Engineering

ADVISOR, MAJOR PROFESSOR — AUG. 11, 2014 DATE

DEPARTMENT HEAD — 8/13/2014 DATE

APPROVED BY THE COLLEGE COUNCIL

DEAN DATE

CMOS-MEMS Probe Arrays for Tip-Based Nanofabrication

Submitted in partial fulfillment of the requirements for

the degree of

Doctor of Philosophy

In

ELECTRICAL AND COMPUTER ENGINEERING

Yang Zhang

B.S., Materials Science and Engineering, Zhejiang University
M.S., AMASE, European Erasmus Mundus Programme

Carnegie Mellon University
Pittsburgh, PA

August, 2014

Acknowledgments

My first and foremost thanks go to ECE@CMU, who provides me this valuable chance to join one of the most prestigious and diverse engineering communities to learn from, communicate with and contribute to, if ever, a group of most talented people.

What I have been learning from Prof. Gary Fedder, my academic advisor, is countless. I still remembered the first official individual meeting when he taught me what was spreadsheet and how he derived the beam equation from the very first step, which I had learned eight years before and not a single piece was left by then. Prof. Fedder embodies all the essential qualities, innovative, hard-working, collaborative, and etc., that constitute a leading figure in the field of engineering. Above all, His enthusiasm and love of MEMS is from the innermost part of his heart, which makes him available any time for the discussion on MEMS issues. I realize that passion and love is the motivation for establishing a meaningful career and life.

Suresh Santhanam is my mentor in my career of nanofabrication. He built my full skill-set from scratches, guiding me step by step from photoresist spin to various etching to process flow design and integration. His over 30 years' experience, unique sensitivity and meticulousness to any subtle phenomenon helped get me out of various tricky problems with ease in cleanroom life.

The first CMU member I talked with is Dr. Jingwei Liu, who is always patient and give me numerous help and guidance throughout my PHD time. And it was him who encouraged me to target on my current academic advisor, Prof. Gary Fedder, one of the alphas in MEMS community.

Numerous intelligent sparks flew in our TFAN weekly brainstorm meetings that greatly broadened my horizon and enriched my creativity. Great thanks go to TFAN group members:

Prof. David Ricketts, Prof. James Bain, Prof. L. Richard Carley, Prof. Robert Davis, Prof. Metin Sitti, Dr. Joshua Smith, Dr. Shingo Taramu, Dr. Yingyi Dang and Dr. Weihua Hu. Special thanks to Yingying Tang with whom we spent numberless time on the realization of dual-probe STM construction and imaging.

Great help and support, both in academics and life, is from MEMS lab and CMU community. I thank all the friends and colleagues that shared their valuable time with me: Prof. Tamal Mukherjee, Prof. Yi Luo, Prof. Mark Kryder, Prof. Jimmy Zhu, Prof. Peter Gilgunn, Dr. Matthew Moneck, Dr. Yunchuan Kong, Dr. Andrew Gamble, Dr. Amy Tsao, Dr. Nathan Lazarus, Dr. Yu-Jen Fang, Dr. Congzhong Guo, Dr. John Reinke, Dr. Leon Wang, Erdinc Tatar, Chenyang Wu, Jie Wang, Ashwati Krishnan, Sean Yen, Lionel Wong, Louis Draghi, Philip Bergeron, Albert Patterson, Mary Beth Galanko, Rozana Hussin.

I would also like to express my sincere thanks to CMU staff: Dir. Chris Bowman, Carsen Kline, Tim Fisher, Mike Sakaluk, Christina Cowan, Amanda Formato, Becca Gray, Patricia Grieco, Matt Koeske, Jacqueline Chraska, Tom Nurfer and Jason Wolf.

I will never forget the time with my officemate, Weihua Hu, Jason Gao and Dongzhi Guo. We spent four years together dealing with various challenges both in research and life. It is so lucky to meet such nice and pure souls at a place over 20 hours' flight away from family.

I would like to extend my great gratitude to my dissertation committee members, Prof. Maarten P. de Boer, Prof. James A. Bain and Prof. L. Richard Carley, for their valuable suggestions, critiques, advice and feedback on my research and thesis.

The financial support for the work contained in this PHD dissertation was provided by DARPA Tip Based Nanofabrication Program (Grant #N66001-08-1-2039) and in part by the

N/MEMS S&T Fundamentals (Grant N66001-10-1-4009) issued by the Space and Naval Warfare Systems Center Pacific.

My thesis committee:

Prof. Gary K. Fedder, Advisor

Prof. Maarten P. de Boer

Prof. James A. Bain

Prof. L. Richard Carley

Abstract

Scanning probe microscopy (SPM) tip-based nanofabrication (TBN) is a technique that directly creates a variety of nanostructures on a substrate using the nanoscale probe tips. SPM TBN possesses superior resolution and flexibility: nanostructures with feature size under 5 nm have been achieved via SPM TBN, which is beyond what the state-of-the art optical-based lithography technique can provide. However, the inherent serial nature of SPM TBN makes it a low throughput process. Multi-probe SPM systems have therefore been developed to increase the nanofabrication efficiency. Atomic force microscopy (AFM) and scanning tunneling microscopy (STM) are two most commonly used SPM TBN techniques. Most of prior work has focused on contact-mode AFM-based TBN. This work, using CMOS MEMS technology as the design and fabrication platform, develops an active conductive probe array that aims to perform parallel surface imaging and nanofabrication in non-contact STM mode. The CMOS-MEMS process provides a monolithic integration of MEMS devices with CMOS electronics that can facilitate future automation and parallel probe operation.

The CMOS-MEMS probe adopts a micro-cantilever structure and applies bimorph electrothermal actuation to control the vertical displacement of the probe tips. The cantilever is designed to be stiff, with a spring constant of 36 N/m that is larger than the force gradient of the cantilever tip-sample interaction forces in the working distance regime of STM in order to avoid the tip-to-sample "snap-in" and ensure the stability of the STM feedback system.

A modified Spindt tip process, compatible with post-CMOS MEMS processing, is developed to batch fabricate Ni/Pt composite tips on CMOS-MEMS probe arrays that are used as STM end-effectors. The integrated Ni/Pt tips on the MEMS probes have a tip radius down to 50

nm. The Spindt tip demonstrates the capability of both imaging and nanowire fabrication in STM mode.

A hierarchical dual-servo STM system is constructed for the parallel STM imaging using two CMOS-MEMS probes. The system consists of a piezoelectric actuator-driven servo and an electrothermal actuator-driven servo to control the vertical displacement of two probe tips and maintain a constant current between the tips and the sample. Both servos use a proportional-integral controller. The dual-servo STM system is capable of parallel STM image acquisition using CMOS MEMS probe arrays.

An on-chip electrothermal proximity sensor pair and probes with embedded micro-goniometers are designed to assist the alignment between the CMOS-MEMS probe array and the examined sample surface. The electrothermal proximity sensor pair is used to measure the separation and the non-parallelism between the probe chip and the sample. The electrothermal proximity sensor has a positioning accuracy of around 1 μm. An electrothermal micro-goniometer platform is developed to hold a one-dimensional array of active CMOS-MEMS probes and serves to provide the *in situ* fine adjustment of relative height among these probes. The micro-goniometer has a maximum tilt of 1.2°, which is sufficient to compensate the probe chip-sample misalignment and the possible height difference among array probes introduced by process variations.

Table of Contents

List of Figures

List of Tables

Chapter 1. Introduction

This chapter introduces the thesis subject of active CMOS-MEMS probe arrays for STM-based nanofabrication. Section 1.1 presents the background of SPM techniques and proposes the motivation for developing STM-oriented active MEMS probe arrays. The prior work on SPM probe arrays is then reviewed and compared with STM probe arrays in section 1.2. Section 1.3 offers CMOS-MEMS background that is used in the design and fabrication of STM-oriented MEMS probe arrays. Section 1.4 gives the thesis statement and the contribution of this work is described in section 1.5.

1.1 Motivation

Motivation of maskless lithography

Modern nanofabrication in industry is mainly based on mask-based photolithography techniques, and typical technologies involved are thin film deposition, patterning and film modification via etching. The minimum circuit feature size has reached 22 nm in production, and 14 nm processes are already in development. With ever decreasing critical dimensions and escalating mask-set cost, other alternative nanofabrication techniques, mainly maskless lithography and direct writing techniques, have been extensively investigated. These are perceived as promising technologies because of their superior resolution and flexibility of surface modification at specified locations.

SPM TBN feature size

Scanning probe microscopy (SPM) is a well-known representative of direct tip-based nanofabrication (TBN), in which a microscopic stylus is moved across the surface, and the nano-patterns are formed by spatially confined reactions, physical or chemical, between the probe and the substrate. Using atomic force spectroscopy (AFM), nanowires with width down to 20 nm were written on various sample surfaces [1]; using a scanning tunneling microscopy (STM) tip-directed deposition, sub-5 nm feature size was achieved in fabricating metallic nanowires [2, 3]. Hence, TBN is regarded as a promising technology in fabricating nanoelectronics and quantum devices.

SPM TBN writing efficiency

One major drawback of SPM-based TBN is its low throughput limited by the serial nature of the process, *i.e.*, only a singular probe cantilever works at a time. A typical line scan rate is of the order of 1 – 10 µm /s, which suggests tens of hours' scanning to cover a 4" diameter wafer. This rate is even lower if images of high resolution are required. In scanning tunneling microscopy (STM), atomic resolution is obtained at a scan rate of 10 – 100 nm/s, and the scan area is often limited to 50 nm by 50 nm. A similar tip-moving rate is required for nanostructure patterning.

Way 1to enhance TBN writing efficiency

To address this issue of low efficiency of TBN, effort is made in two directions. One is to increase the scanning and writing speed of the tip. This can be realized by building scan head with high resonance frequency, developing high bandwidth electronics, implementing advanced control topologies, or the combination of all [4] .

Way 2 to enhance TBN writing efficiency

The second approach is to build a multiple SPM probe array system. A probe array comprises several probes placed in parallel that observe, examine, modify or fabricate patterns over multiple µm-sized areas on the substrate simultaneously, so the throughput is multiplied. Nanostructures can be batch fabricated accordingly. Fig. 1.1 shows the probe array concept.

AFM TBN advantage

While similar amount of research has been devoted to STM-based and AFM-based TBN techniques, when expanded to multi-tip array for parallel TBN, most of the current work focuses on contact-mode AFM-based techniques. Compared to STM-based TBN techniques, AFM-based ones have two advantages. First, AFM is a more versatile technique, where a variety of interactions between the tip and the sample can be made use of for nanofabrication: the tip, when coated with conductive materials, can be used to provide localized electron source for resist exposure or local anodic oxidation (LAO); the tip, when heated, can locally modify and pattern heat-sensitive materials; the tip can also be used as medium for molecular transport like in dip pen lithography (DPN); finally, the tip, if coated with hard materials like diamond, can be directly used to scratch nanowires on soft materials. In STM, tunneling current is the only interaction between the tip and the sample that is relied on for TBN. Secondly, AFM has a less constraint over sample: AFM can work on most samples while STM needs the samples to be conducting.

STM TBN advantage

Nevertheless, non-contact STM has the advantage that it is able to achieve atomic resolution and single atom manipulation. This is based on the fact that STM relies on the short range tip-sample interaction that is comparable to the size of the atoms [5]. Tunneling current is the interaction signal between the tip and the sample and only flows within a region of diameter ~5Å, which is of the same order of magnitude as the size of the atom. AFM relies on various kinds of forces between the tip and the sample that take place in a region of few nanometers and above, which is also the typical resolution of AFM. To achieve atomic resolution, though workable, is much harder, because these tip-sample interactions, like van der Waals force and water meniscus force when in the air, decay much more slowly than the quantum tunneling current which limits the ultimate resolution of AFM [6]. This indicates that the non-contact mode SPM may be able to produce an even smaller feature size than the contact mode SPM.

Why STM probe array needed

To have major improvement in SPM-based techniques, making it a mainstream nanofabrication tool in the future generations of logic and memory devices, a multi-scale multi-resolution hybrid system should be developed to provide different accuracy or tolerance requirements in nanostructure fabrication [7]. Therefore, STM-based multiple-tip system, which can provide a resolution an order of magnitude smaller than AFM-based one, is also needed to be developed and combine with AFM-based multiple-tip system to realize the ultimate multi-scale system.

Why CMOS-MEMS

In the development of multiple-tip based multi-scale fabrication system, a high degree of control in sensing and actuation is required. One respect towards this goal is the chip-level integration of mechanical tip arrays with SPM control electronics. CMOS MEMS techniques, among others, are one approach to providing a path of integrating mechanical probes and electronics onto a single CMOS chip. This work is a step toward an active MEMS probe array for non-contact STM mode nanofabrication via CMOS MEMS techniques that will achieve a highly compact multi-functional STM system with nm-resolution.

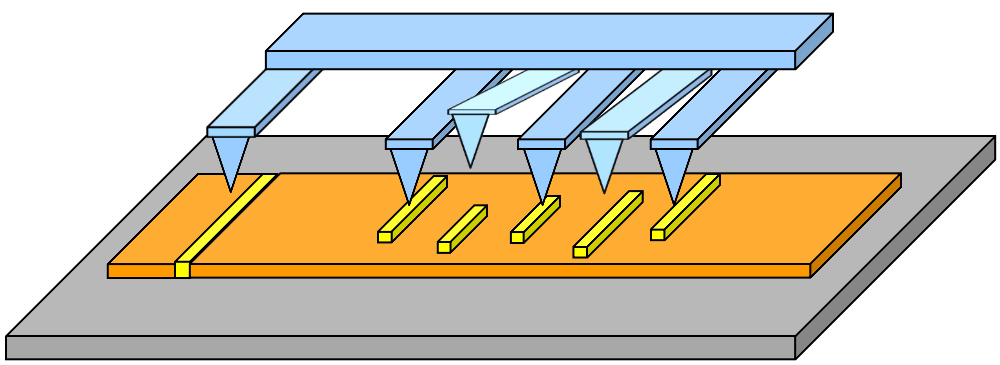

Fig. 1.1 The concept of SPM probe array based nanofabrication: array probes operate in parallel to examine and modify the surface. Probes can be lifted up and down independently of others so different patterns can be created under different probes.

1.2 Prior work on TBN with SPM probe arrays

Passive vs. active probe arrays

SPM probe arrays may be categorized into two types: passive and active. Passive arrays have all tips in the array move in unison, sharing only one z-axis actuator and feedback loop. Active arrays include probes that contain one or more actuators that allow it to be lifted in x-, y-, and/or z-directions independently of the other probes. In SPM scanning, this allows the scanning process for each probe to be turned on and off at will and permits adjacent probes to create different surface structures while following the same general scan.

Work of other groups on SPM array

Several research groups are developing various kinds of probe array systems. These systems are used for high speed AFM imaging, Dip Pen Nanolithography (DPN) and bio-sensing. Quate's group [8] created a 1×50 active probe array system for parallel AFM, shown in Fig. 1.2, where each probe contains a dedicated integrated polysilicon piezoresistive sensor and an integrated ZnO piezoelectric actuator. A computer system was developed for automated control. The system scanned with a bandwidth of 20 kHz and a noise level of less than 50 Å, achieving a scan rate of 4 mm/s on typical samples. They also developed a hybrid AFM/STM system for field-emission assisted nanopatterning, but in contact mode [9].

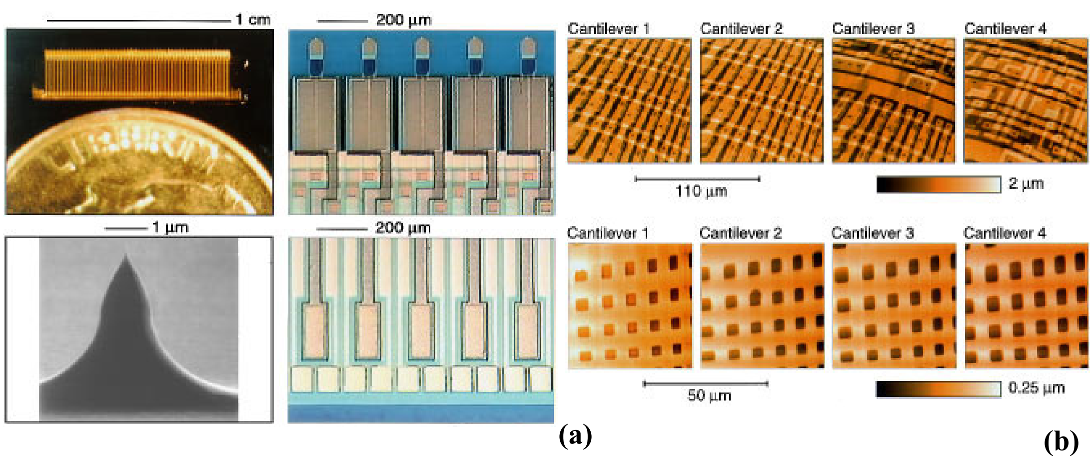

Fig. 1.2 Parallel AFM in Quate's group [8]: (a) A 1×50 AFM probe array; (b) 4×1 AFM images of a memory cell of an IC circuit (upper) and 2D grating (lower) obtained in parallel with the cantilevers shown in (a).

Chang Liu's group [10] exploited the use of an electrothermally actuated active AFM probe array in DPN, and developed a multifunctional 1D probe array that combined imaging and writing in one array, shown in Fig. 1.3. In these two array implementations, however, SPM electronics are separate from the probe array, which ultimately limits its scalability.

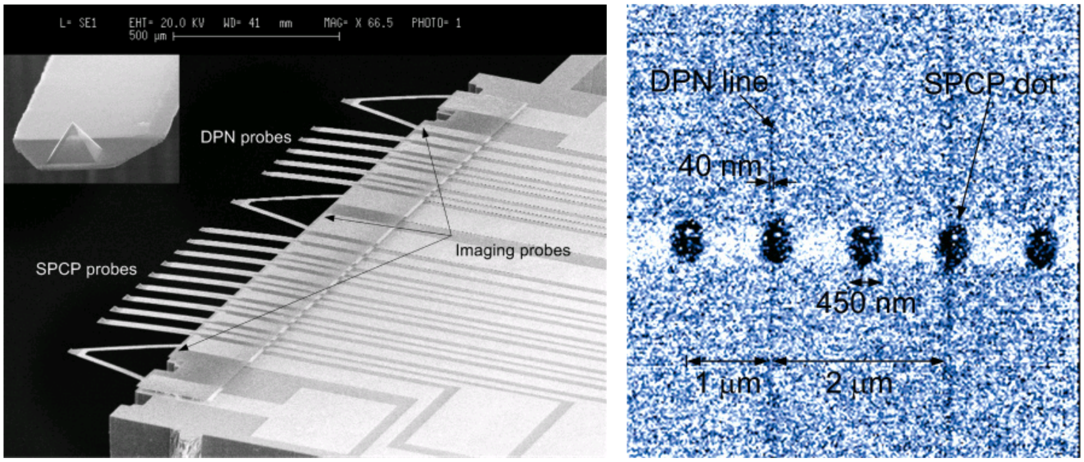

(a) (b)

Fig. 1.3 Parallel AFM in Liu's group [10]: (a) A multi-functional probe array; (b) The nano features created by the writing probes and imaged by the reading probe.

King's group at the University of Illinois at Urbana-Champaign explored the application of AFM cantilevers with integrated heaters in nanoscale materials characterization and manufacturing. The cantilevers are made of doped single-crystal silicon where the tip heater region at the end of the cantilever is less doped than other cantilever parts so that most joule heat is generated in the tip [11] .They used a heated nano-tip for polymer nanowire deposition and nano-mechanical resonator fabrication [12]. Working in tapping mode, the AFM cantilever can perform thermal topography imaging with a resolution of 7 nm at a scan speed of 1.46 mm/s [13]. A scalable 1D array of heated microcantilevers is also developed for parallel thermomechanical lithography and thermal topographic imaging, as shown in Fig. 1.4 [14].

Based on CMOS foundry processes, Hierlemann's group at ETHZ used CMOS-MEMS techniques to make 1D probe arrays for AFM imaging [15], shown in Fig. 1.5. This technique achieves high integration, *i.e.*, integrating the MEMS probe structure and control electronics on a single monolithic chip of 7 mm by 10 mm area. A vertical resolution of <1 nm is evidenced by the monolithic AFM system. The sharp silicon nitride SPM tips essential to AFM were separately fabricated and then transferred on CMOS cantilevers with translation stages under a stereo microscope.

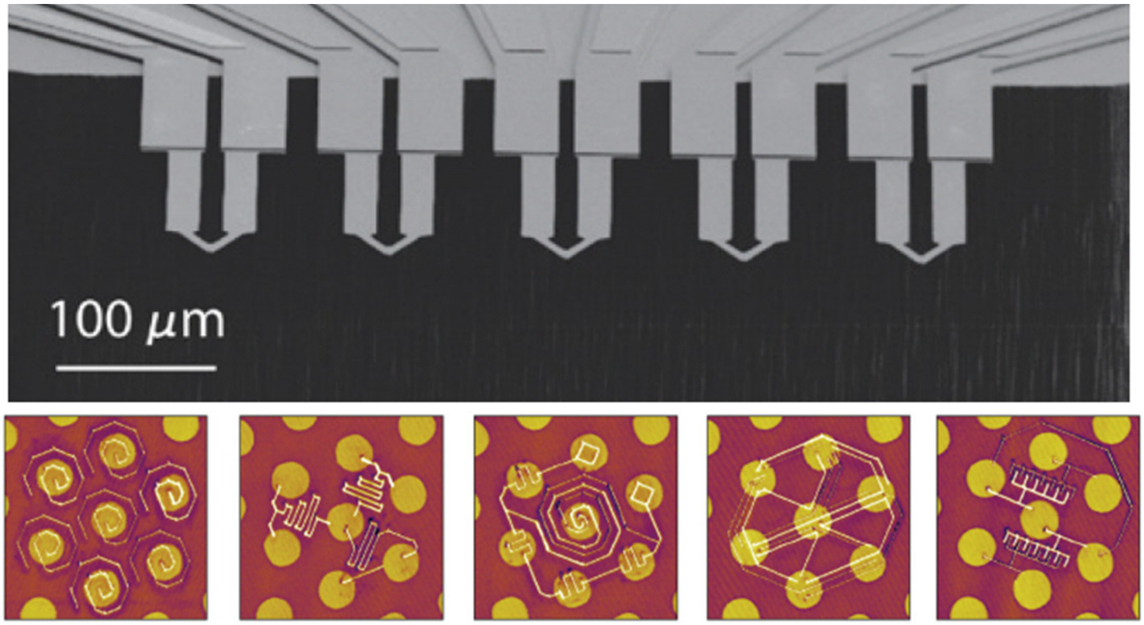

Fig. 1.4 Heated microcantilever array in King's group [14]: (a) 1×5 cantilever array. (b) Parallel patterning and imaging on fluorocarbon thin film.

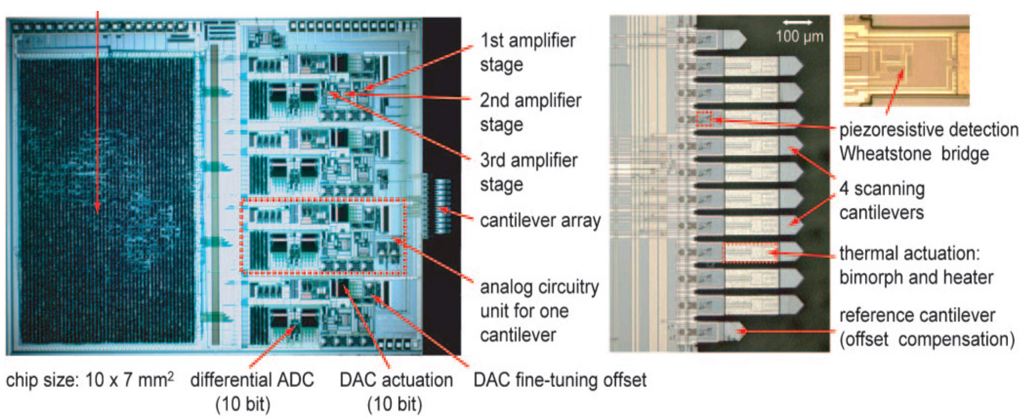

Fig. 1.5 Parallel AFM [15]: An array of AFM cantilever structures fabricated out of a standard CMOS chip so it naturally integrates with the actuation, detection and control circuitry on a single chip

Two-dimensional (2D) probe SPM arrays have also been studied. IBM Zurich research developed large 2D arrays of MEMS cantilevers for ultrahigh-density storage starting in 2000 [16]. In the project known as the "Millipede", 4,096 (64 × 64) cantilevers with integrated tips and sensors were fabricated using silicon micromachining techniques, shown in Fig. 1.6 (a). A CMOS back-end-of-line (BEOL) compatible, wafer-scale device transfer, and interconnect method was developed and used to integrate the cantilever array with the CMOS analog front-end chip where the driving and sensing electronics resided [17]. Storage densities beyond 1 Tb/in^2 were achieved using this probe-based data-storage system.

Microcantilever array applications are also extended to bio-science and bio-engineering. In sensing applications, cantilevers are functionalized with receptor molecules, and are used to detect specific species: when the analyte binds onto a functionalized cantilever with the receptor, it adds to its mass and changes its resonance frequency. If the cantilever is oscillating, the resonance shift can be used to identify the analyte. By using an array structure, simultaneous detection of multiple analytes is possible [18,19].

2D passive cantilever arrays are fabricated to investigate the stiffness and adhesion characteristics of cancerous cells [20,21]. An interferometric system was developed to determine the cantilever deflections. The force resolution on the order of 10 pN was achieved.

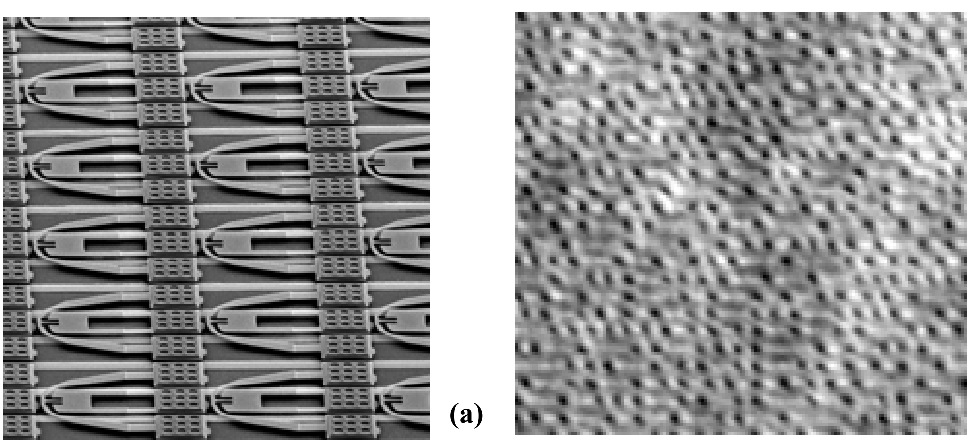

(a) (b)

Fig. 1.6 IBM "Millipede" array [17]: (a) A 2D cantilever array; (b) A high density of patterned nano-dots created for data storage.

Probe array@CMU

CMOS-MEMS probe arrays have also been developed in the Carnegie Mellon MEMS lab in prior years. These probes were intended to mechanically address and pass current to reconfigure phase change via "switches" that are used in radio frequency integrated circuits [22]. The probes were designed to be used in contact mode, with a low spring constant of between 1 N/m to 5 N/m. The probe tips were coated with gold, and achieved contact resistance of few ohms when in contact with commercial tungsten test probes.

Summary: STM TBN resolution

Up to date, most efforts in parallel scanning probe array applications are based on AFM-mode imaging and contact-mode nanostructure formation. The tip-substrate interactions made use of are mainly force, electromagnetics, thermal and mass transfer. A non-contact multi-probe system for STM, in contrast, has not been reported. The nano-scale resolution of STM-based nanofabrication points to the feature size needed for future generations of logic and memory devices, and is beyond what optical-based lithography can provide. This leads to the motivation of developing a STM-based multi-probe system.

1.3 CMOS-MEMS background

CMOS technology introductio n

The CMOS-MEMS process, used to fabricate the active MEMS probe array in this work, is a process where the MEMS devices are directly fabricated out of a standard CMOS chip, which leads to a natural on-chip integration of MEMS with electronics. The processing of MEMS can be performed either before, in the middle of, or after standard CMOS processing. Post-CMOS MEMS technology, where all the MEMS processing steps take place after standard CMOS chip processing, avoids any customization of the CMOS process, and so it is generally adaptable to CMOS from different foundries and from different technology generations. The CMOS-MEMS probes fabricated in this work use three foundry CMOS processes: TSMC 0.35 μm CMOS, TowerJazz 0.35 μm BiCMOS and TowerJazz 0.18 μm CMOS.

CMOS MEMS process flow

In CMOS-MEMS, MEMS structures are created out of the metal-dielectric stacks in the standard CMOS process. The various metal layers in the CMOS act as the masks to define the structure geometry. Fig. 1.7 shows a general post-CMOS process flow to make the MEMS structure. Fig. 1.7 (a) shows the CMOS chip from the foundry. First, the exposed oxide on the chip is subjected to an anisotropic $CHF_3/CF_4/O_2$ reactive ion etch (RIE). During this oxide etch, the top-most metal layers act as masks that define the MEMS structure and protect the transistors underneath from being attacked by the etchant. Areas not covered by metal layers are completely removed of SiO_2 and the Si substrate is exposed. In the second step, a Si deep anisotropic RIE (DRIE) using SF_6/O_2 is performed to create deep trenches in the Si substrate. Last, the Si isotropic RIE via SF_6 is carried out to undercut the silicon substrate and release the defined microstructures from the substrate.

Structures created in CMOS-MEMS

Beams of different geometry can be created via the CMOS-MEMS process. Fig. 1.8 shows an example of beam structures with different metal layers as top layers, resulting in beams of different thicknesses. In general, MEMS structural beams can be made of stacks of different number of layers, depending on the specific needs and processing constraint. For example, MEMS lateral and vertical actuators can be realized by using a designed combination of oxide layers and metal layers. The vertical actuator is a bimorph structure composed of two layers: the metal-1 aluminum layer and the dielectric oxide layer directly underneath the aluminum, as shown in Fig. 1.8 (a). The lateral actuator is a multi-morph structure composed of a metal-321 beam with metal-2 and metal-1 offset to one side of the beam [23], as shown in Fig. 1.8 (f). Polysilicon resistors can be embedded directly in the lower dielectric oxide part of the beam, like the one shown in Fig. 1.8 (b), or in neighboring structures to provide Joule heating for thermal actuation. In this work, MEMS vertical bimorph actuator beams and probe cantilevers were created. The probe stiffness constraint requires a cantilever of maximum possible thickness.

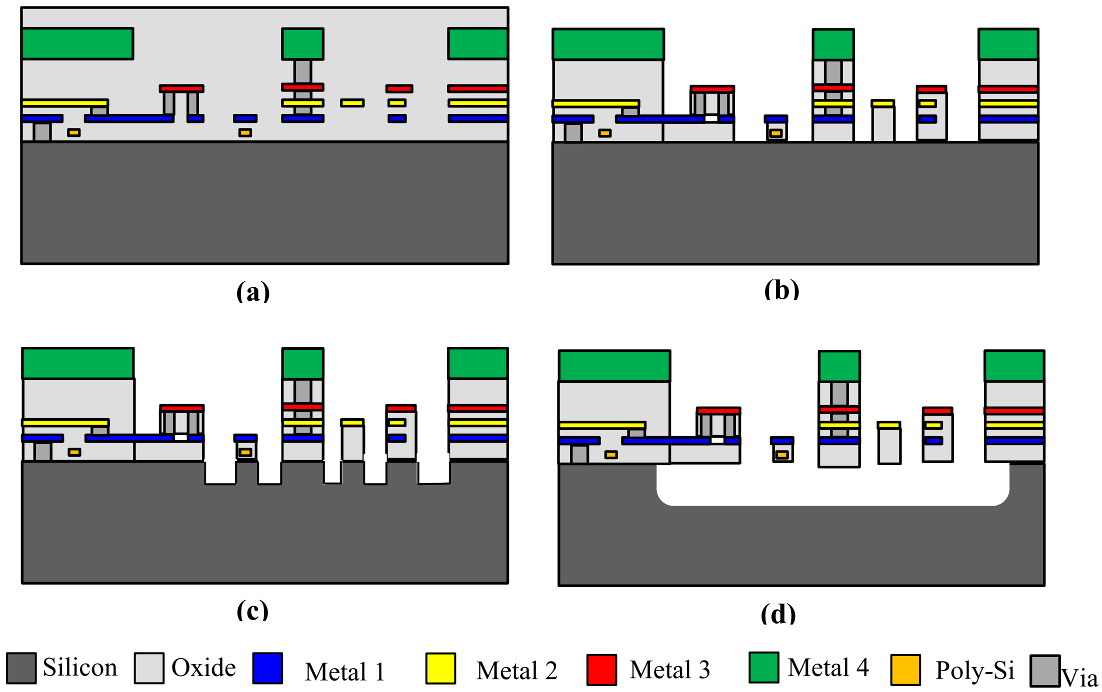

Fig. 1.7 CMOS-MEMS process flow@CMU: (a) Fresh CMOS chip from foundry; (b) Anisotropic SiO_2 RIE etch; (c) Anisotropic RIE Si etch; (d) Isotropic RIE Si etch release the full MEMS structure.

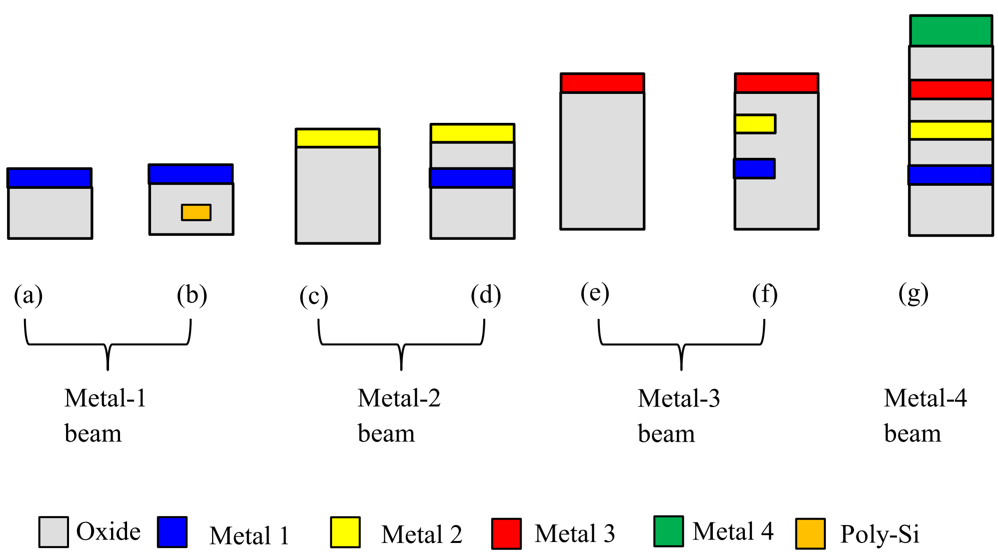

Fig. 1.8 Examples of cross-section schematics of beams of different thickness created by using different metal layers in CMOS process to define the structure.

1.4 Thesis statement

Thesis content

In this thesis, the feasibility of a multi-functional CMOS-MEMS active probe array system suitable for STM-based surface imaging and surface modification (*i.e.*, writing) with parallel tip operation is explored. Towards this objective, a prototype dual probe is designed, fabricated and tested.

CMOS techniques adopted for building compact STM probe array

In a general SPM system, the mechanical components and the electronic components are built separately and then assembled together. The system is designed for single probe manipulation. To develop a SPM probe array equipped with multiple scanning drives and servos, the commercial SPM configuration would not be sufficient. New types of drives need to be adopted; more electronics need to be added. Above all, a high level of integration is desirable, where a higher-density of functional electronics and mechanics can be fabricated as a single package, rather than package-on-package, to minimize the external feedthrough and disturbances, and without increasing the overall SPM system size. Two main approaches can address this integration. One approach is to assemble a CMOS IC and a MEMS chip with through silicon vias (TSVs) that are used to route the electrical signals between the chips [24]. The other approach, adopted in this thesis, is directly building the sensing and control electronics and mechanical components as probes and actuators on a single CMOS IC, taking advantage of the post-CMOS MEMS processing technique.

Task 1: probe array design

CMOS-MEMS electrothermally (ET) actuated probes qualified for STM operation were designed and fabricated. The dynamics of the active probes used as the plant in the STM servo loop were characterized. In-situ probe ET actuation sensitivity during STM scanning was measured, as the basis for STM image construction using ET actuator-based STM.

Task 2: batch tip process on CMOS

In the various SPM tip processes used today, tips and cantilevers are fabricated from a same wafer, or the tips are fabricated separately and then transferred to the probe cantilever manually. No batch SPM tip fabrication techniques on CMOS chips have ever been reported. Thus, the process of fabricating conductive STM Pt tips was investigated and developed. The functionality of STM tips were examined in both imaging and nanofabrication.

Task 3:dual-probe system demo.

To demonstrate the parallel STM working of CMOS-MEMS probe array, a dual-probe array system was built. Two STM servos were used for the control of each array probe. A custom calibration sample was made. Experimental STM dual scanned images were compared with AFM of the calibration sample.

Task 4: ET position sensor and goniometer

To facilitate the STM operation of CMOS MEMS probe arrays, particularly in an ultra-high-vacuum (UHV) system where a macro-goniometer for tip-substrate parallelization is not easily implementable, on-chip micro ET proximity sensors and micro-goniometers were designed. These ancillary devices were characterized to evaluate their performance as probe chip-sample alignment assistance tools.

1.5 Thesis contributions

The first contribution of this work, presented in chapter 2, is the design of an active CMOS-MEMS conductive probe platform suitable for incorporation of sharp tips for STM operation. The MEMS probes have stiffness and ET actuation-based travel range designed to be suitable for STM operation. The probe has a spring constant of 36 N/m, drive sensitivity of ~131 nm/mW, and a maximum stroke of around 2 μm.

A second contribution, presented in Chapter 3, is a modified Spindt tip process compatible with post-CMOS MEMS processing. This process flow establishes feasibility to batch fabricate STM tips on a multiple probe array. Sharp platinum tips with tip radius down to

10 nm are obtained. These Spindt Pt tips on MEMS probes are capable of STM imaging. A parallel approach of fabricating Pt tips on CMOS MEMS probes via electro bean induced deposition (EBID) was also investigated. EBID tips were used for the test of the prototype dual probe array system.

Chapter 4 documents the demonstration of parallel STM using the prototype dual probe array system, which is the third major thesis contribution. A hierarchical dual servo system was created. A master servo controls position of the probe chip and its master tip relative to the STM substrate and uses the piezoelectric actuator embedded in a conventional STM system. The second, slave servo controls the second, slave tip relative to the STM substrate and uses the ET actuator embedded in the slave probe. The dual probe scanning is performed on a custom calibration sample with gratings of known period and pitch height. Two STM images were obtained simultaneously via the dual CMOS-MEMS probe array system. The features on both images agree with the designed pattern characteristics, thereby establishing system feasibility.

In chapter 5, on-chip ET probe proximity sensors and a micro-goniometer design are presented, constituting the fourth contribution of the thesis. The ET proximity sensors make use of the thermal perturbation when the heated probe approaches the substrate as a proximity signal. A positioning accuracy of 1µm was measured. Two ET proximity sensors placed on the corners of the CMOS-MEMS probe chip with a spacing of around 2.4 mm are able to reduce the misalignment between the chip and the sample to 0.024°. The micro-goniometer has a maximum tilt of around 1°, which is sufficient to cover the misalignment of probe chip-sample and the possible height difference among array probes introduced by process variations.

Chapter 2. Widely-spaced Active CMOS-MEMS Probe Arrays

Features of CMOS MEMS probes for STM

In this work, an active conductive probe array is constructed that is designed for STM application. It is different from most previous work on SPM probe arrays in two respects. First, most prior probe array work has been focused on AFM, while this work exploits the tunneling effect between the tip and the sample for material characterization and imaging. When cantilever probes are used as STM end-effectors, the tip-sample interaction force, which is of attractive nature in the working distance regime of STM, could make probes jump into contact if they are not stiff enough. Probes with sufficient spring constant are thus required to avoid snap-in. Second, most SPM probes are made with silicon-based MEMS cantilevers, while the present STM probe array is fabricated using a CMOS-MEMS technology, which is well established at Carnegie Mellon University (CMU).

Chapter content

In this chapter, the design of an active CMOS-MEMS probe array qualified for STM application is presented, and the fabricated array probes are characterized. Section 2.1 reviews the previous design features of active CMOS-MEMS probes developed at CMU, based on which a topology of active CMOS-MEMS probes for STM is presented. Section 2.2 reviews the different actuators used in MEMS probes, and provides detail of the mechanism of bimorph electrothermal (ET) actuation that is adopted to drive the CMOS-MEMS probes. Section 2.3 describes the various interaction forces between an STM tip and the sample surface that puts a mechanical constraint on probe stiffness. Section 2.4 defines the geometry of the CMOS-MEMS probes based on the selected ET actuation mechanism and the probe stiffness requirements. Section 2.5 presents the characterization results of the fabricated design.

2.1 Overview of CMOS-MEMS probe design

2.1.1 Review of CMOS-MEMS probes

Application of CMOS-MEMS probes

CMOS-MEMS probes have been previously developed for MEMS Instrumented Self-Configuring Integrated Circuits (MISCIC) at CMU [25]. The MEMS conductive probes are used to mechanically address and pass current to reconfigure vias on an RF integrated circuit chip that is made of phase change materials. More specifically, the MEMS probe with the conductive tip is expected to make a reliable contact with the vias, having low contact resistance of a few ohms. It is envisioned that MEMS probe switches will perform superior to transistor switch for RF IC reconfiguration.

Design Specs of probes

To meet the MISCIC vision, active CMOS-MEMS probes were designed. Fig. 2.1 shows a version of such probes. The probes have a spring constant of 1~ 5 N/m and a travel range of ~10 μm, establishing a maximum contact force up to 50 μN needed for good probe-sample contact.

Design elements on the probe

Electrothermal actuation is chosen as the actuation mechanism for the active CMOS-MEMS probe mainly because of the low drive voltage needed and the large stroke provided. The main challenges with ET actuation in the MEMS probe are the uneven temperature distribution among an array of actuators and the low ET drive sensitivity. Dummy heater beams (DHB) were placed along each side of the metal-1 bimorph flexure beams as "outer beams" to improve the temperature uniformity along ET array actuators. Probes without DHBs were reported to have severe thermal bucking at high drives. Thermal isolation structures (TIS) were added between the metal-1 bimorph and the main chip body to reduce the heat loss through the chip so that the ET drive sensitivity is maximized. The probe was also equipped with on-cantilever piezoresistive sensors to detect the probe bending. The force resolution of the piezoresistive sensor is set by the noise level in the resistance measurement, which is a function of the piezoresistive coefficient, the sheet resistivity and the geometry of the piezoresistors, among other things. In [25], it reported that the designed piezoresistive sensor had a force resolution of μN-scale. It also pointed out that the force resolution could be improved by more than 100 times by using a piezoresistor with a larger sheet resistivity and by optimizing the geometry of the piezoresistor. Further improvement could be realized by subjecting the piezoresistors to annealing with proper conditions to increase the piezoresistive coefficient.

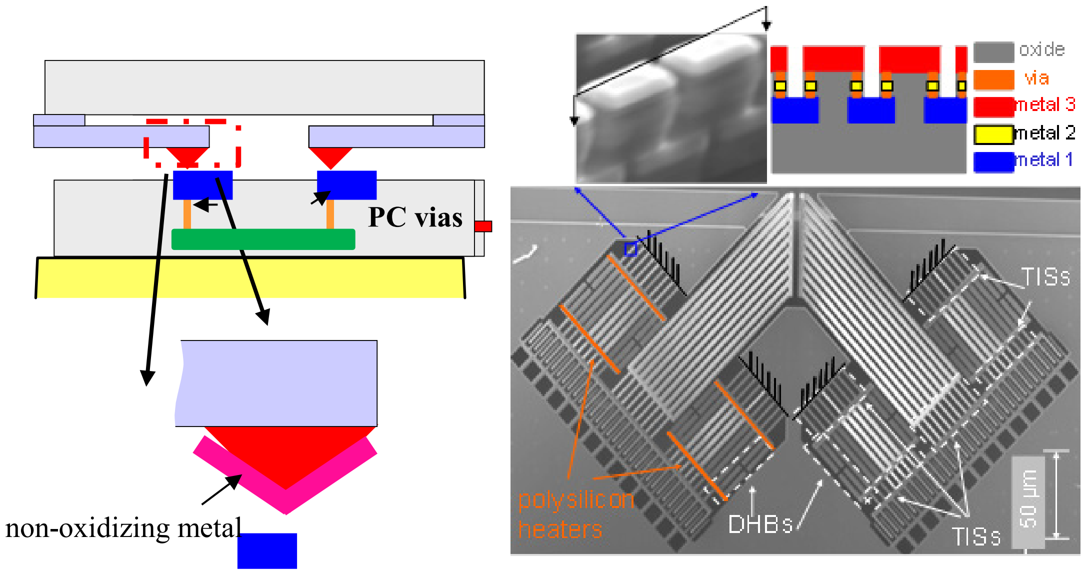

(a) MISCIC concept (b) A typical MISCIC CMOS-MEMS probe

Fig. 2.1 CMOS-MEMS probes for MISCIC. The probes are electrothermally actuated, with TISs to increase drive sensitivity and DHBs to make an even temperature distribution among heat area [25].

The MISCIC CMOS-MEMS probe provides a base for the development of active conductive STM probe and probe arrays, as is introduced in the next section.

2.1.2 Active CMOS-MEMS probe for STM

Adoption of some previous features

CMOS-MEMS probes and arrays are constructed to perform parallel STM imaging and localized tip based nanofabrication, where each probe is individually addressable. The schematic in Fig. 2.2 illustrates a conceptual cantilever STM probe design including the key components. Several basic features in a MISCIC probe are inherited in the design of TBN probes: bimorph ET actuators to realize probe vertical displacement, DHBs included to improve the temperature uniformity of ET array actuators and TISs included to enhance thermal drive sensitivity. They are tailored to meet STM probe requirement.

Features on STM CMOS MEMS probe

In addition, several extra elements on an active probe need to be involved for STM task. A mechanically stiff cantilever structure is required to perform STM operation. A sharp STM metal tip is needed to be integrated on the top metal tip platform at the cantilever end for tunneling current generation and sensing. Each probe needs to be equipped with a STM feedback loop comprising the sensing and control electronics. In the following sections, the design elements will be separately introduced.

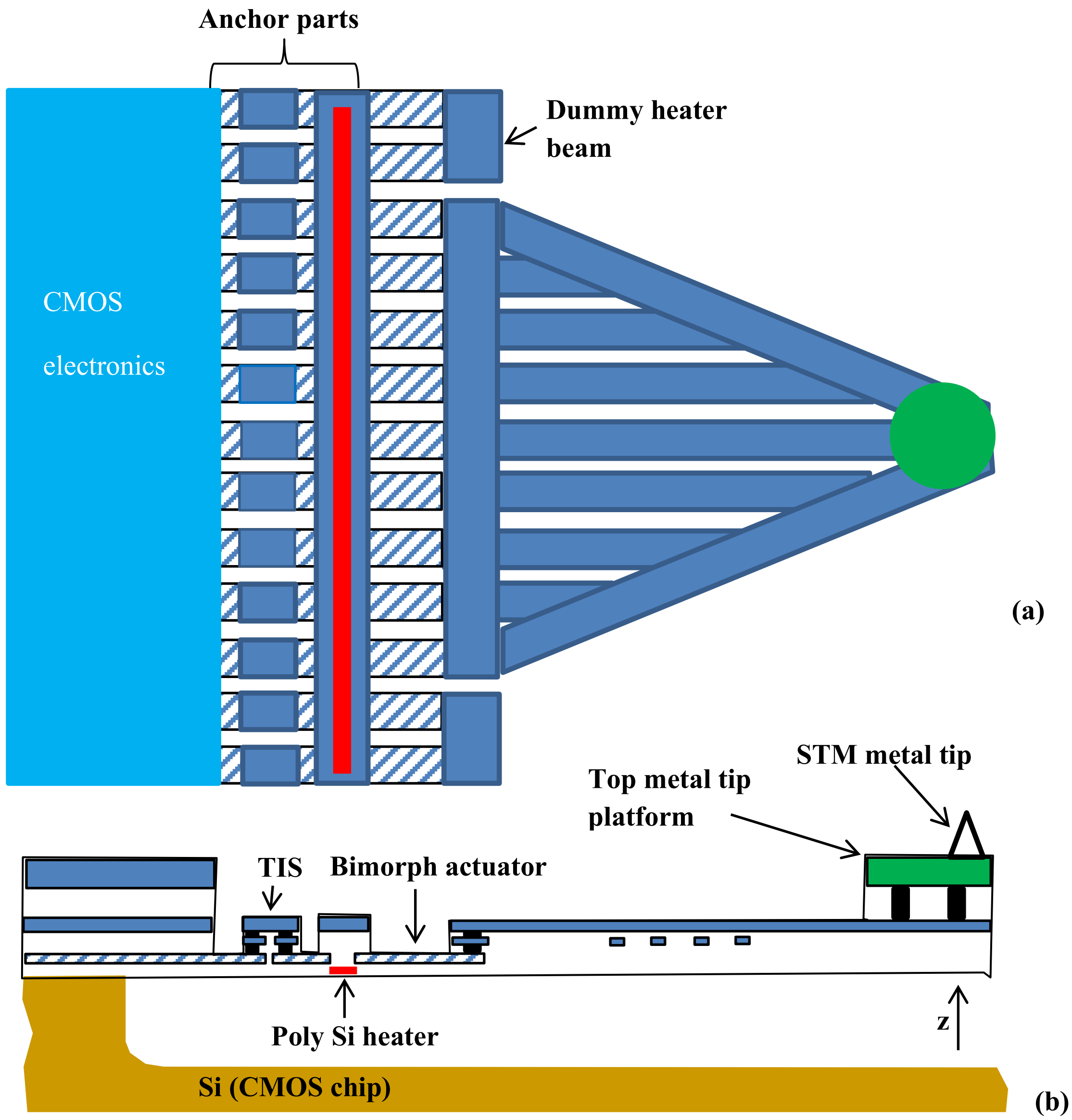

Fig. 2.2 Schematic design of a MEMS probe for STM: (a) top view; (b) side view. TIS stands for thermal isolation structure.

2.2 Probe actuation

Four types of actuators

The actuation mechanism is an essential active element in the probe design. For a scalable probe array system where each probe is individually addressable, integrated micro-actuators are required. Four micro-actuation approaches are cited in prior work: piezoelectric ZnO, electrostatic (ES), electrothermal (ET) and electromagnetic (EM). EM actuators have several fabrication challenges and material selection limitations, so they are not as popular as the other three types.

ZnO actuators

Piezoelectric actuation is the most important and commonly used approach in nano-scale positioning, such as in SPM instruments, because it has a linear displacement-voltage relationship with nm-scale precision. In commercial SPM, piezoelectric ceramic materials based on modified lead zirconate titanate (PZT) and barium titanate are the most common actuator materials, and these ceramics are machined to tube or stack for use. Zinc oxide, ZnO, is the piezoelectric material adopted for a prior micro-scale SPM probe array system in Calvin Quate's research group [26, 27]. The ZnO MEMS actuator took the form of a thin film layer of 3.5 µm thick, with a drive sensitivity of 577 Å/V and a deflection of 4 µm for a drive voltage of ±35 V. Using the ZnO actuated cantilever in the constant force mode, they achieved an scan speed of 3 mm/s and a vertical resolution of 60 Å in a 10 Hz – 7 kHz bandwidth. ZnO material can be easily incorporated in the process flow of a probe cantilever fabrication and is also CMOS compatible, unlike many other piezoelectric materials that are sources of contaminant for the CMOS transistors.

ES actuators

Electrostatic actuation approaches operate by applying a voltage difference between two electrodes. An attractive ES force is produced between the two electrodes that causes their relative displacement.

The parallel-plate actuator and interdigitated comb drive are two basic geometries in implementation of ES actuation. The parallel-plate style ES actuator was used as a vertical drive in MEMS high speed SPM [28], as shown in Fig. 2.3 (a). Fig. 2.3 (b) shows a parallel plate configuration, where the ES drive force is given by

$$F_{es} = -\frac{\varepsilon_0 A}{2(g_0+z)^2} V_{act}^2 \tag{2.1}$$

where V_{act} is the actuation voltage, g_0 is the gap between the two parallel plates at zero voltage difference, z is the displacement of the movable plate from the initial position, A is the surface overlap of two plates, and ε_0 is the dielectric permittivity of the vacuum or air, where SPM operation takes place. The vertical scan range is limited by the gap, g_0. With open-loop control, the actuator scan range is limited by electrostatic pull-in to one-third of the gap [29].

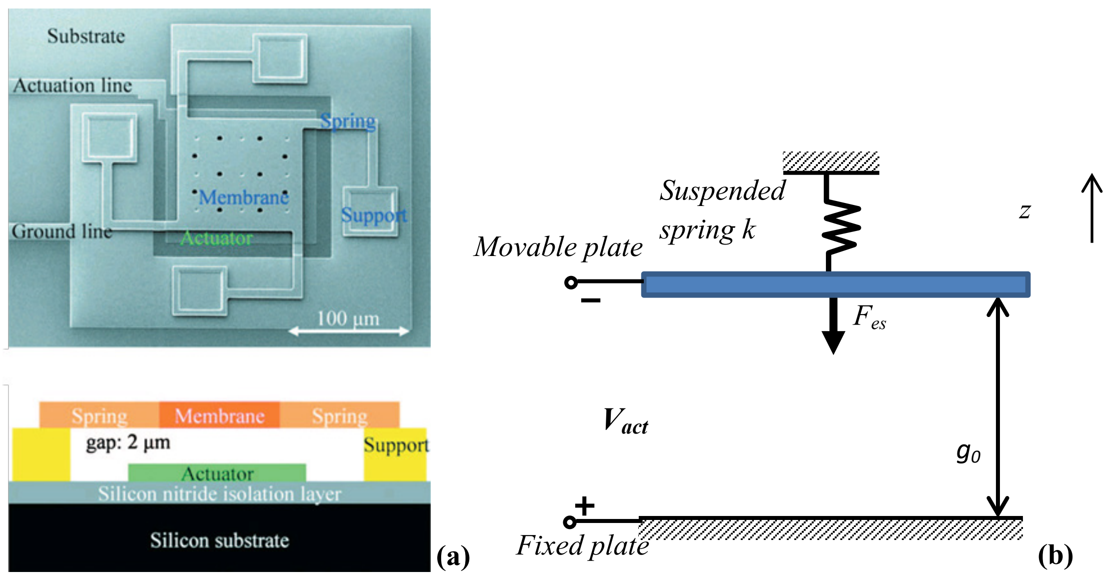

Fig. 2.3 (a) Parallel-plate ES actuator used as a z-scanner in SPM [28]. (b) Schematic of a parallel-plate ES actuator. The movable plate is subjected to an ES force and a spring force.

ES actuators have the virtues of low power operation, fast speed and simple fabrication. Yet a high drive voltage is often needed for a relatively large stroke. In the case of a MEMS probe, 16 μN is required to provide a stroke of 400 nm for a cantilever with spring constant of 40 N/m. If the cantilever and the substrate, with a face-to-face area of 50 × 50 μm^2 and separation distance of 2 μm, a 76 V drive voltage is required. This high drive voltage and/or area needed for a required large stroke is a main drawback.

ET actuators

Electrothermal actuators make use of the thermal expansion of materials to drive the movement of MEMS devices. A variety of structures have been used to realize thermal actuation: thermal bimorph and multi-morph [30], 'chevron' shaped thermal actuator [31] and hot/cold arm actuators [32]. Chang Liu's research group [33] used an Au/Si_3N_4 composite layer as the thermal actuator for independent manipulation of individual probes in their multifunctional SPM probe array for nano-patterning, where the ET actuators provide a vertical stroke up to 30 µm and are able to establish and break probe-sample mechanical contact as required.

ET actuators have advantages of low drive voltage, high force, large stroke and simple fabrication. A main constraint is their low speed. For an ET actuator, the variation of the temperature of the actuator lags behind that of heating power due to the thermal capacitance of the mechanical structure. This relation can be approximated as a first order system, and expressed as

$$\frac{\text{Temperature(s)}}{\text{heating power(s)}} = T_p * \frac{\omega_{cf}}{s + \omega_{cf}} \tag{2.2-a}$$

where T_p is the static power sensitivity (*i.e.*, the temperature change per unit change of power, in mks units of K/W), ω_{cf} is the 3-dB thermal cut-off frequency determined by the thermal conductance, R_{th}, and thermal capacitance, C_{th}, of the actuator structure, and expressed by

$$\omega_{cf} = \frac{1}{R_{th} * C_{th}} \tag{2.2-b}$$

ET micro-scale actuators generally have thermal cut-off frequency of hundreds of Hz. This low frequency, however, can be compensated in the servo-loop design.

ES and ET actuators are comparatively easy to be designed in CMOS-MEMS. In our work, ET actuator is chosen as it has an easier implementation as a vertical direction drive and a much larger displacement range than ES actuators for the cantilever stiffness value required for STM operation of around 36 N/m (see Section 2.3).

2.2.1 Electrothermal actuation via bimorph: working principle

Bimorph

Electrothermal actuation in this work is realized by a bimorph composite beam. A bimorph is a cantilever consisting of two active layers with different thermal coefficients of expansion (TCE). Upon heating, generally electrical Joule heating in MEMS, the temperature change will cause two layers to expand by different amounts, resulting in the bending of the cantilever.

Bimorph deflection-T relations

A bimorph beam can be configured as a cantilevered, guided-end or fixed-fixed beam. Timoshenko [34] gave a detailed modeling and analysis to calculate the temperature dependent deflection of a thermal bimorph. For a cantilevered bimorph geometry shown in Fig. 2.4, upon a temperature change of ΔT, the curvature, κ, the radius of curvature, ρ, and the angle, θ, and the vertical displacement at the free end of the cantilever, z_L, are given, respectively, by:

$$\kappa = \frac{1}{\rho} = \frac{6E_m E_o t_m t_o (t_m + t_o)(\alpha_m - \alpha_o)\Delta T}{(E_m {t_m}^2)^2 + (E_o {t_o}^2)^2 + 2E_m E_o t_m t_o (2{t_m}^2 + 3t_m t_o + 2{t_o}^2)} \tag{2.3}$$

$$\theta_L = \frac{L}{\rho} \tag{2.4}$$

$$z_L = \frac{L^2}{2\rho} \tag{2.5}$$

where α_o and α_m are the temperature coefficients of expansion (TCE) and E_o and E_m are the Young's moduli of the oxide and metal, respectively. Combining (2.5) and (2.3), the probe vertical displacement, z_L, is shown to be linearly dependent on the temperature change.

Bimorph Component in CMOS MEMS

In the CMOS-MEMS, the sandwiched metal layers and the dielectric oxide layers are used to make bimorph or multimorph beams. To realize a vertical actuation, the CMOS metal-1 aluminum layer and the SiO_2 layer directly underneath form a bimorph. Due to the tensile stress in Al and the compressive stress in SiO_2 introduced in 0.35 μm CMOS fabrication process used in this work, the Al-SiO_2 composite beam will have an upward deflection at room temperature upon MEMS structure release after post CMOS processing. Upon ET actuation, the beam will bend downwards, as shown in Fig. 2.4.

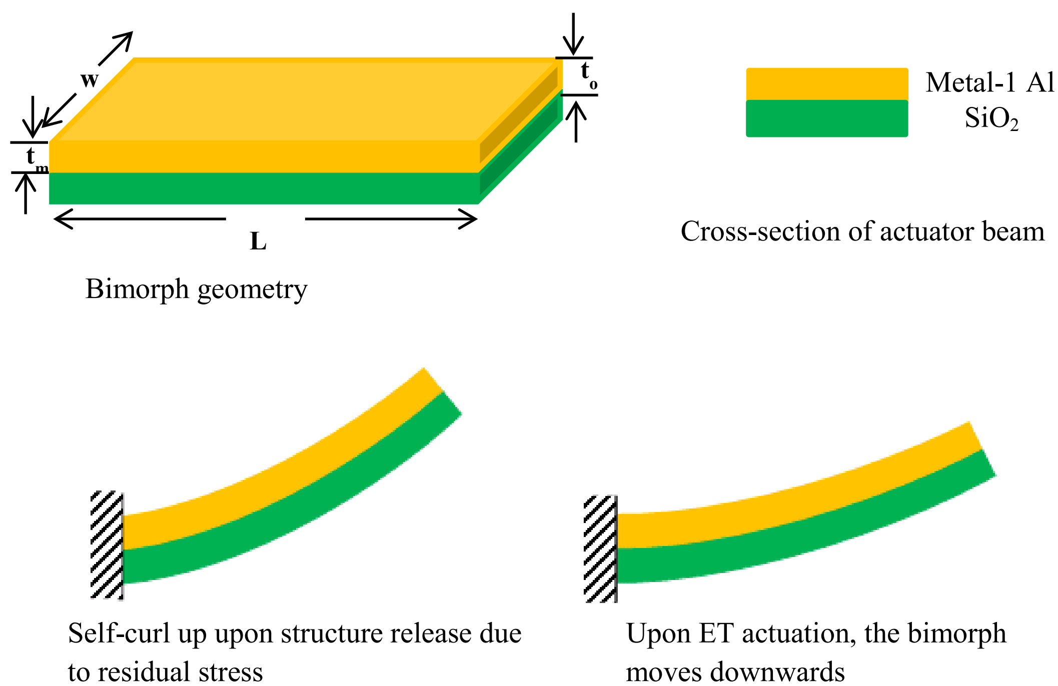

Fig. 2.4 Bimorph beam structure in CMOS-MEMS for vertical electrothermal actuation.

Bimorph sizing through length only

Since the thicknesses of the metal and dielectric layers are fixed in the CMOS process, the length and the width of the bimorph is determined by the required displacement and choice of beam mechanical constraints.

In the STM application, the probe needs to be able to move up and down to cover the surface topography. Although the movement of a bimorph ET actuator is unidirectional, its position can be centered in its travel range by a pre-actuation bias voltage so that the probe will have room for voltage control of both upward and downward displacement.

2.3 Probe tip–sample interactions

Why adopt soft cantilever geometry

A traditional fixed STM tip is mounted on and moves with the piezo-scanner, with a spring constant of ~10^7 N/m and so is considered “infinitely” stiff. Building an array of “infinitely” stiff STM tips with an array of piezo-scanners, which has a dimension of 1 mm by 1 mm by 5 mm for a 200 nm range of movement, on commercial STM equipment, however, is impractical due to the system’s volume constraint. It is also of little significance to build such a system because it is a mere addition of multiple SPMs.

In contrast to most STM probes, a compliant probe, like in a conventional AFM, is easy to actuate with on-cantilever embedded actuators and thus possible to be scaled to an array of probes. This approach is taken with implementation in a CMOS-MEMS process to create an AFM-like probe that works in non-contact STM mode.

Snap-in issue with cantilever

However, accompanied with the AFM-like compliant probe design is the issue, when working in STM mode that the cantilever with limited stiffness may snap down onto the surface because of the attraction force between the tip and the surface. This problem does not arise when using “infinitely stiff” STM probes. Snap-in occurs when a soft AFM cantilever approaches the sample surface to the extent that the tip-sample attractive force gradient becomes larger than the spring constant of the free cantilever. This effect is referred as the jump-to-contact discontinuity [35,36].

Various tip-sample force

Generally, the tip-sample separation range is several angstroms in the STM operating modes, where the ES force, Van Der Waals (VDW) force, and meniscus force dominate in this distance range.

ES force

When a bias is applied on the sample, the ES force acting on the tip is estimated to be [37]:

$$F_{es-tip} = \frac{\pi \varepsilon_0 \varepsilon_r V_b^2 r^2}{z(z+r)} \tag{2.6}$$

where r is the tip radius, z is the tip-to-sample distance, V_b is the tip-to-sample potential difference, and ε_r is the dielectric permittivity of the medium between the tip and the surface. In an ultra-high vacuum (UHV) system, ε_r = 1, while in air the relative permittivity of water should be applied because of the existence of a water contamination layer on the surface. At 20°C, the relative permittivity of water is ε_r = 80.4.

The STM metal tip is fabricated on a circular tip platform made of the top metal layer in the CMOS process, which is at the same electrical potential as the tip. Therefore an ES force is also acting on the metal tip platform and is evaluated assuming it is in parallel with the sample surface:

$$F_{es-plate} = \frac{\pi h^2 \varepsilon_0 V_b^2}{2 l_t^2} \tag{2.7}$$

where h is the radius of tip platform and πh^2 is the area of tip platform, l_t is the height of the tip.

VDW force

The VDW force between an STM tip and a substrate, modeled as an infinitely large plane, is derived based on Lennard-Jones potential [38]:

$$F_{vdw} = \frac{A_H r}{6\sigma^2}\left[\frac{\sigma^2}{z^2} - \frac{1}{30}\frac{\sigma^8}{z^8}\right] \tag{2.8}$$

where A_H is the Hamaker constant, whose value is determined by the material property of two interacting bodies, and σ is the inter-atomic distance given by the equilibrium separation of the two atomic planes modeling the tip and substrate.

Meniscus force

The meniscus force exists when performing the ambient-condition STM scanning. In air, water will spontaneously condense from vapor into cracks and pores on surfaces, forming a contamination layer, as shown in Fig. 2.5. A localized water meniscus will form between the

SPM tip and the sample surface when they are very close. The curvature of the meniscus, r_{men}, is related to the relative humidity, and is given by [39]:

$$r_{men} = \frac{\gamma_L V}{RT\ln(p/p_{sat})} \tag{2.9}$$

where γ_L is the surface tension of water, R is gas constant, V is the mole volume of water, and p/p_{sat} is the relative humidity. For water at 20˚C, $\gamma_L V/RT$ = 0.54 nm.

The meniscus force between the tip and the sample surface is expressed as:

$$F_{mes} = 4\pi\gamma_L r\cos\theta\left(1-\frac{z}{2r_{men}\cos\theta}\right) = 4\pi\gamma_L r\cos\theta\frac{1}{1+\frac{z}{d}} \tag{2.10}$$

where θ is the contact angle between the water meniscus and the substrate surface, and $d = 2r_{men}\cos\theta - z$ is the distance the tip extends to the meniscus. In an UHV system, the meniscus force is zero.

Total force gradient

Adding (2.6), (2.7), (2.8) and (2.10) and differentiating with respect to z, the interaction force gradient is

$$k_{int} = \frac{\delta F_{int}}{\delta z} = \frac{\delta F_{es-tip}}{\delta z} + \frac{\delta F_{es-plate}}{\delta z} + \frac{\delta F_{vdw}}{\delta z} + \frac{\delta F_{mes}}{\delta z} \tag{2.11}$$

Table 2-1 lists the related parameters used in the interaction force calculation. Fig. 2.6 shows the tip-sample force-distance curve. The ES force between the tip platform and sample surface is very small compared to other forces.

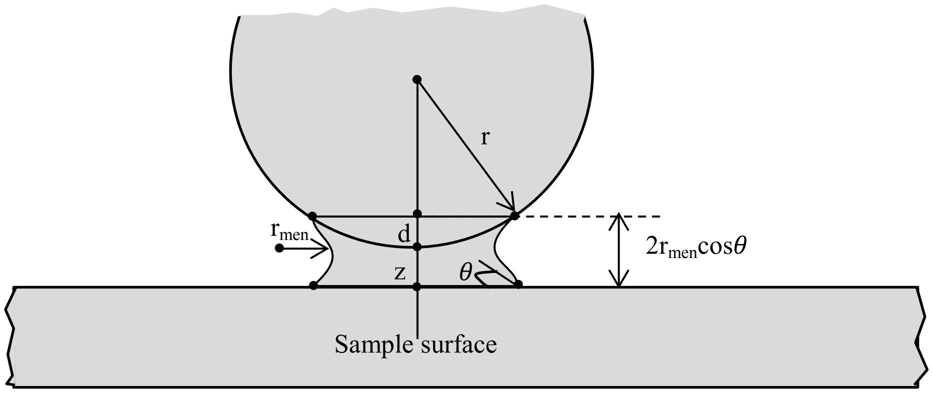

Fig. 2.5 Geometry of capillary bridge between a sphere and a flat surface. *d* is the depth the tip is immersed into the water layer, with $d + z \approx 2r \cos\theta$. [39]

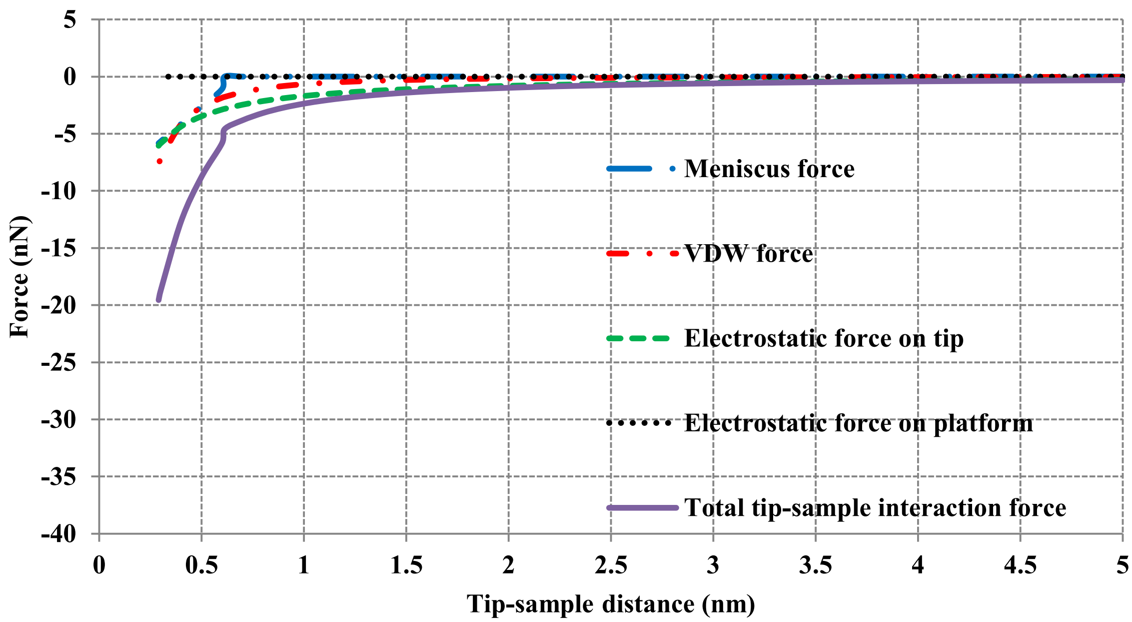

Fig. 2.6 (a) Tip-sample interaction forces *vs.* tip-sample separation.

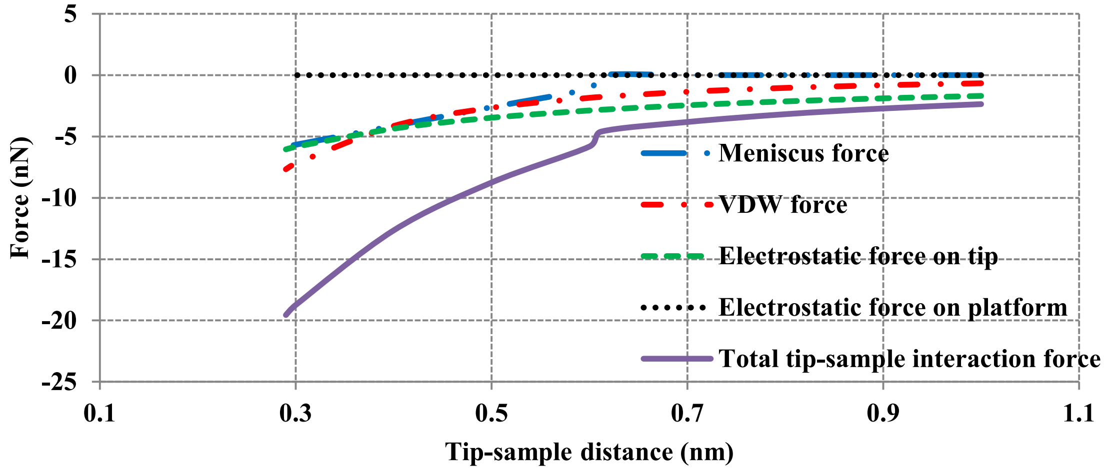

Fig. 2.6 (b) Tip-sample interaction forces *vs.* tip-sample separation in the range between 0.3 nm and 1nm

Table 2-1 *Parameters in calculation of tip-sample interaction force*

Parameters	Value	Description
Sample bias, V_b	200 mV	20 ~ 200 mV for conductive sample
Tip radius, r	20 nm	
Hamaker constant, A_H	200 zJ	$A_H \approx (A_{Pt} A_{Au})^{1/2}$
Vacuum permittivity, ε_0	8.85×10^{-12} F/m	
relative permittivity, ε_r	80.4	relative permittivity of H_2O
Interatomic distance of Au	0.288 nm	A mean of 0.282 nm is used in the calculation
Interatomic distance of Pt	0.276 nm	
Gas constant, R	8.314 J/mol/K	
Surface tension of water, γ_L	0.073 N/m	
Room Temperature, T	293.15 K	
Contact angle, θ, of Au	59.3°	surface condition dependent
Relative humidity, p/p_{sat}	40%	

As a conservative estimation with a tip-sample separation of $z = 6$ Å at 40% relative humidity, the force gradient is 26 N/m. Therefore, the mechanical spring constant of the designed probe should be at least 26 N/m to counteract the pull-in interaction force gradient for one probe tip. Higher stiffness will give a more robust system performance.

The model for the calculation of the total force between the probe tip and the sample is built based on the addition of various force models collected from literature. The suitability of these force models for estimating STM tip-sample interaction needs to be experimentally examined. *In situ* force measurement techniques can be introduced to characterize the interaction between the STM tip and the sample in operation [40], such as an optical interference to detect the deflection of the cantilever bending [41]. For CMOS MEMS probes, polysilicon piezoresistive sensors can be embedded into the STM cantilever beams to serve the purpose of *in situ* bending and force measurement. The electrostatic force acting on the tip can be investigated by examining the relationship between the bending of the probe cantilever and the tip-to-sample potential difference. By operating the STM scanning in environment at different humidity levels and ultra-high-vacuum conditions and measuring the cantilever bending, the effect of meniscus force can be quantified.

2.4 Probe cantilever design methodology

Based on the stiffness requirement of the probe and the actuation mechanism adopted, the probe cantilever structure is determined, with its schematic shown in Fig. 2.2. An array of TISs is added between the bimorph actuator and the CMOS chip body for thermal loss reduction.

2.4.1 Thermal isolation structures

TIS concept and structure

During the manipulation of electrothermally actuated devices, electric energy is dissipated throughout the actuation to maintain a device position other than at rest. To reduce the power consumption, thermal isolation structures are introduced between the ET actuator and its neighboring structures to increase the drive efficiency. Fig. 2.7 shows the schematic of thermal isolation solutions adopted in the CMOS-MEMS ET actuator structures [1,42,43]. Because aluminum has a much larger thermal conductivity (~250 W/m/K) than silicon oxide (~1 W/m/K), the thermal resistance of a CMOS-MEMS structure is determined by the length and width of the metal. The philosophy behind the TIS design is to use a slotted structure that lengthens the metal path – a fast heat conduction channel – to maximize the thermal resistance. Fig. 2.7 (b) shows a TIS unit of a 3-metal slotting structure [25]. Compared to a simple metal-1 beam structure shown in Fig. 2.7 (a) that has an effective thermal conductivity of 71 W/m/K, the effective thermal conductivity of the 3-metal slotting is reduced by more than three times. In this work, the 3-metal slotting structure is adopted as the thermal isolation solution.

TIS sizing

As can be seen in the MISCIC probes shown in Fig. 2.1, more than three TIS units connected in series are placed at actuator anchor points. The resulted probe stiffness is less than 5 N/m. Due to the stiffness constraint imposed on STM probe cantilevers, the total length of TISs should be made as small as possible. Fig. 2.7 (b) shows the size of a TIS unit implemented in the design of STM probe geometry. l_{m1} is determined by MEMS release design rules on the minimum gap width between two structures and is 0.5 µm. l_{via} and l_{m3} are determined by the CMOS design rules and are 0.9 µm and 0.5 µm, respectively. The minimum length of a TIS unit is 3.3 µm. To maximize probe stiffness, only one array of TISs is placed at the probe anchor point, as shown Fig. 2.7 (c) and (d).

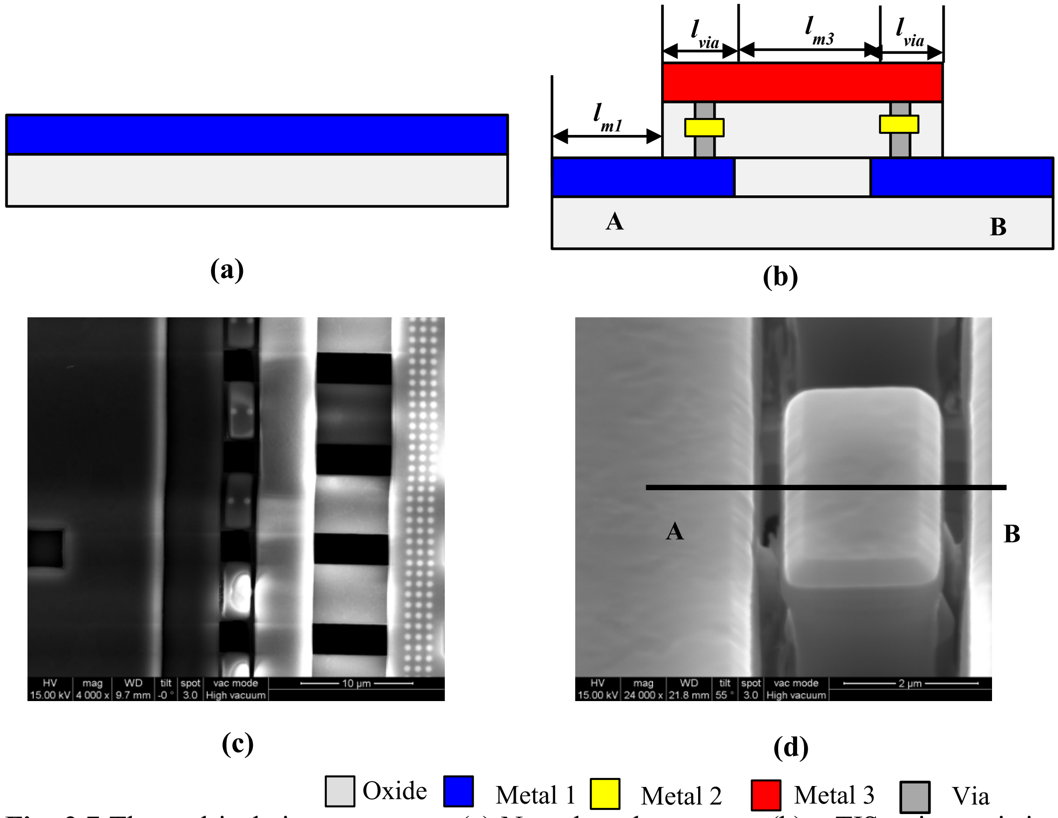

Fig. 2.7 Thermal isolation structures: (a) Non-slotted structure; (b) a TIS unit consisting of a 3-metal slotting structure; (c) & (d) SEM images of TISs.

2.4.2 Cantilever geometry

Geometry simplification of sizing

To facilitate the sizing of the probe cantilever, simplified probe geometry is used for analytical estimation of the probe stiffness, as shown in Fig. 2.8. The simplified cantilever consists of a metal-1 beam, labeled 'beam *a*', and a metal-3 beam, labeled 'beam *b*'. The two beams are in series. The metal-1 beam represents the bimorph ET actuator plus the anchor parts that connects the actuator and the CMOS chip body, as shown in Fig. 2.2. Although TIS is a slotted structure of metal-1 and metal-3 beam, they are treated as metal-1 beam as a conservative estimation. The extension of a thicker metal-3 beam in series acts as a lever arm providing the required probe stiffness and stroke. This structure should satisfy two conditions: a spring constant no less than 26 N/m and a sufficient vertical stroke of around 1 μm.

Estimate probe spring constant

Euler-Bernoulli beam theory [44] is used to calculate the deflection characteristics of beams because of the small deflection variation of beams during STM operation. The spring constant of two beams in series can be calculated as follows. Assume a force F is applied in the vertical direction at the free end of the probe. The probe will have a vertical displacement, z, which can be divided to three components: z_a, resulting from the vertical displacement of beam a; z_θ, the vertical displacement of beam b caused by the slope at the conjunction point P between beam a and beam b; and z_b, the vertical displacement of beam b caused by the applied force at the beam end.

For beam a, it is subjected to a vertical force of F and torque of FL_b at its end, so the shape function of beam a, is:

$$z_a(x) = -\frac{Fx^3}{6(EI)_a} + \frac{F(L_a + L_b)x^2}{2(EI)_a} \tag{2. 12-a}$$

And the vertical displacement of beam a at P is

$$z_a(L_a) = \frac{FL_a^2(2L_a + 3L_b)}{6(EI)_a} \tag{2. 12-b}$$

where $(EI)_{i\ (i=a,b)}$ is the composite beam's effective flexural rigidity, and is a function of the widths and thicknesses of layers comprising the beam.

The slope of beam a at the conjunction point, P, $\tan\theta$, is:

$$\tan\theta\,(x) = \frac{dz_a}{dx} = -\frac{Fx^2}{2(EI)_a} + \frac{F(L_a + L_b)x}{(EI)_a} \tag{2.13-a}$$

$$\tan\theta\,(L_a) = \frac{FL_a(L_a + 2L_b)}{2(EI)_a} \tag{2.13-b}$$

and the displacement at the cantilever end caused by this slope is

$$z_\theta \approx L_b \tan\theta\,(L_a) = \frac{F L_a L_b (L_a + 2L_b)}{2(EI)_a} \tag{2.13-c}$$

The shape function of beam b, in the reference coordinate system x', is

$$z_b(\tilde{x}) = -\frac{F\tilde{x}^3}{6(EI)_b} + \frac{F L_b \tilde{x}^2}{2(EI)_b} \tag{2.14-a}$$

$$z_b(L_b) = \frac{F L_b^3}{3(EI)_b} \tag{2.14-b}$$

The total displacement at the end of the cantilever, z, is then expressed as

$$z = z_a(L_a) + z_\theta + z_b(L_b) \tag{2.15}$$

and the spring constant, k_{sc}, is given by:

$$k_{sc} = \frac{F}{z} = \frac{F}{z_a(L_a) + z_\theta + z_b(L_b)} = \frac{1}{\frac{z_a}{F} + \frac{z_\theta}{F} + \frac{z_b}{F}} \tag{2.16-a}$$

A more elegant expression for k is

$$\frac{1}{k_{sc}} = \frac{z_a(L_a)}{F} + \frac{z_\theta}{F} + \frac{z_b(L_b)}{F} \triangleq \frac{1}{k_a} + \frac{1}{k_\theta} + \frac{1}{k_b} \tag{2.16-b}$$

Design parameters in probe geometry

The parameter values to evaluate the spring constant of the probe are given in Table 2-2. An initial value of 70 GPa is assumed for Young's modulus of both Al and SiO_2. In the post-CMOS micromachining process, the available thicknesses of each beam are fixed, specified by the defined top metal layer that acts as the etch mask for the structural dielectric etch. The actual beam thickness after the structural dielectric etch will be smaller than that provided by the foundry, because the top metal layers are subjected to ion milling and get thinner during the MEMS structure release. Beam thicknesses used in Table 2-2 are from the measurement of a structure released probe structure. The probe stiffness is inversely proportional to the cube of the probe length, so short cantilever length is desired. The probe width is limited by the size of the chip and the number of probes expected to be placed along the edge of the chip. In the design, a 'net' probe width of 190 µm is chosen. The actual full width of the probe, as shown in Fig. 2.2, consists of two parts: the sum of width of the finger cantilever beams that constitute the probe solid structure and the gaps between these beams. These gaps are necessary as required by the stress constraint and structure release constraint in the CMOS MEMS. The full width of a probe is estimated to be 340 µm. Up to six probes can fit along one side of a 2.4 mm by 2.4 mm chip. Therefore, the ratio of the length of beam *a* to the length of beam *b* in the beam geometry can be designed to determine the desired probe spring constant.

Probe sizing using max. stroke constraint

The maximum vertical stroke of the probe obtained by the metal-1 bimorph ET actuator is calculated from thermal bimorph expansion. Generally the working temperature of an ET bimorph actuator on a CMOS chip does not go beyond 150°C to 200°C, therefore a temperature difference of 150°C is assumed for maximum vertical stroke of the bimorph. The vertical displacement of the beam *a* at the maximum temperature difference, using (2.5), is:

$$z_{amax} = \frac{(L_a - L_{TIS})^2}{2\rho} \tag{2.17}$$

where L_a is the total length of the bimorph actuator plus the TISs. Because TISs are a slotted structure of metal-1 beam and metal-3 beam, and because they are near the fixed end of the probe structure, their bending is small and so is subtracted from L_a in the estimation of the deflection of the bimorph actuator.

The displacement at the probe cantilever end contributed by the slope of beam *a* at the conjunction point, *P*, is given by:

$$z_{\theta max} = L_b tan\theta(L_a) = \frac{(L_a - L_{TIS})L_b}{\rho} \tag{2.18}$$

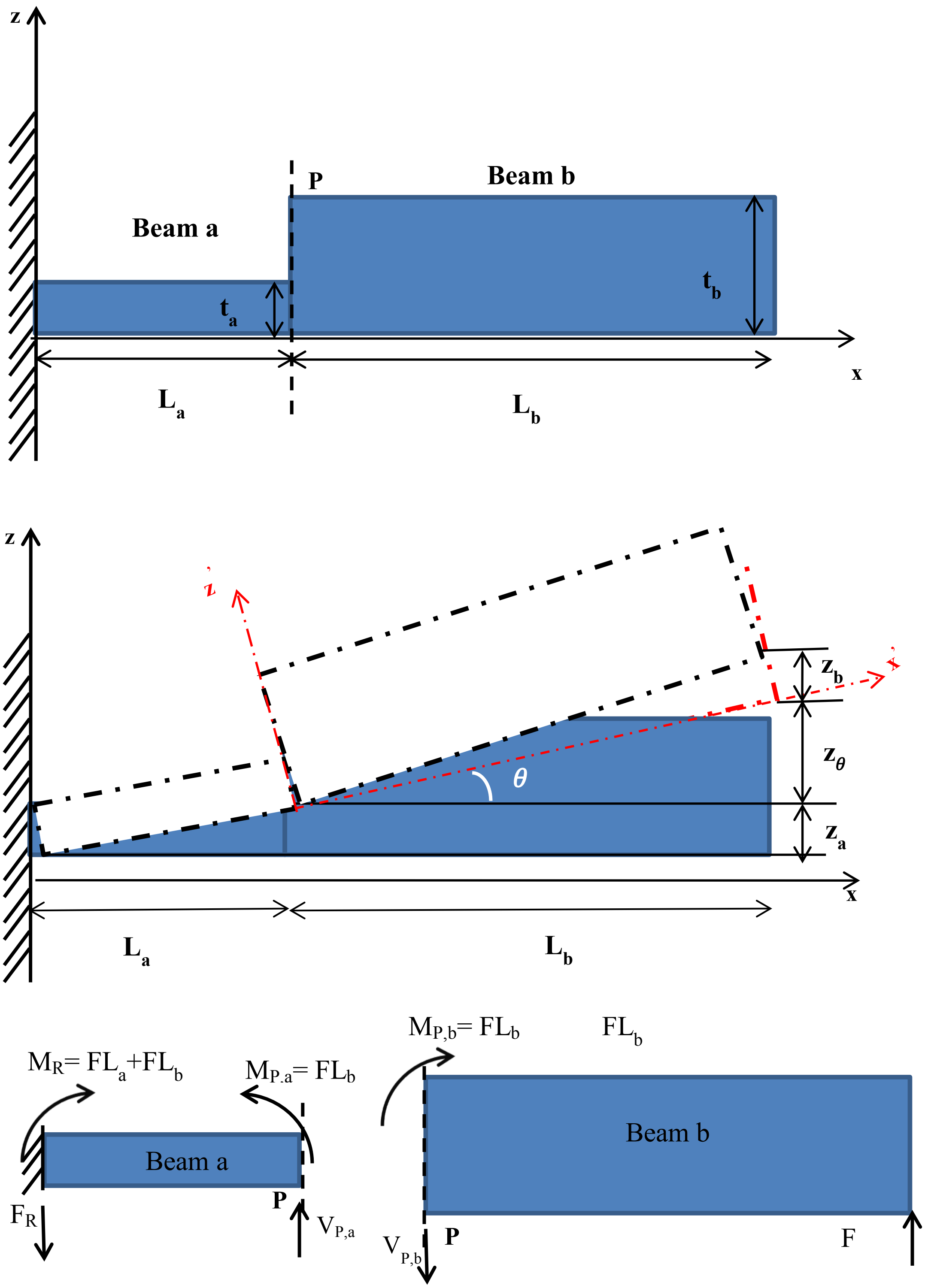

Fig. 2.8 Simplified probe geometry for analysis of beam deflection: (a) Probe consisting of two beams in series; (b) Vertical displacement of the probe; (c) Force diagrams of two beams showing the reaction forces, shear forces and moments that each beam is subjected to.

The maximum total displacement produced by the electrothermal actuation is

$$z_{max} = z_{amax} + z_{\theta max} \tag{2.19}$$

so z_{max} is a function of L_a and L_b.

In the actual design, a total probe cantilever length of 100 μm is adopted comparable to the length of a commercial AFM cantilever. A shorter cantilever length might be possible, but it will be harder to observe under the optical microscope which helps the probe chip-sample alignment. Nevertheless, probe with shorter cantilever length can be designed and its actual maneuverability should be examined because a shorter cantilever length gives a much greater probe stiffness that is the critical design specification to guarantee a stable STM operation.

Geometry dependence of probe stiffness

Fig. 2.9 shows the dependence of the probe spring constant and the maximum vertical stroke on the length of beam a, L_a. The total cantilever length, $(L_a + L_b)$, is 100 μm. The parameters used are listed in Table 2-2. The shaded area indicates the range of L_a that meets the probe stiffness and stroke requirement lies between 13.5 μm and 31 μm.

COMSOL simulation

The probe is modeled and simulated in COMSOL, using the geometry sizing of the probe via the analytical estimation as the starting points as a design verification. In the final probe geometry determination, L_a is set to 15.3 μm, and L_b is set to 84.5 μm. The bimorph length is 7μm. This structure gives a probe stiffness of 45.8 N/m and a vertical stroke of 1.15 μm at 150 K temperature difference, as shown in Fig. 2.10, which is close to the analytical calculation of 42.1N/m and stroke of 1.39 μm, respectively.

Table 2-2 *Parameters in the geometry sizing of the CMOS-MEMS probe*

Parameters	Value	Description
E_a & E_b	70 GPa	Effective beam Young's modulus
$(L_a + L_b)$	100 μm	Total probe length
w_a	190 μm	Effective beam width of a
w_b	190 μm	Effective beam width of b
t_a	1.75 μm	Metal-1 beam thickness
t_b	4.75 μm	Metal-3 beam thickness
α_m	23.1μK^{-1}	TCE of Al
α_o	0.5μK^{-1}	TCE of SiO_2
L_{TIS}	8.3 μm	Length of TISs plus the connection between TISs and ET actuator

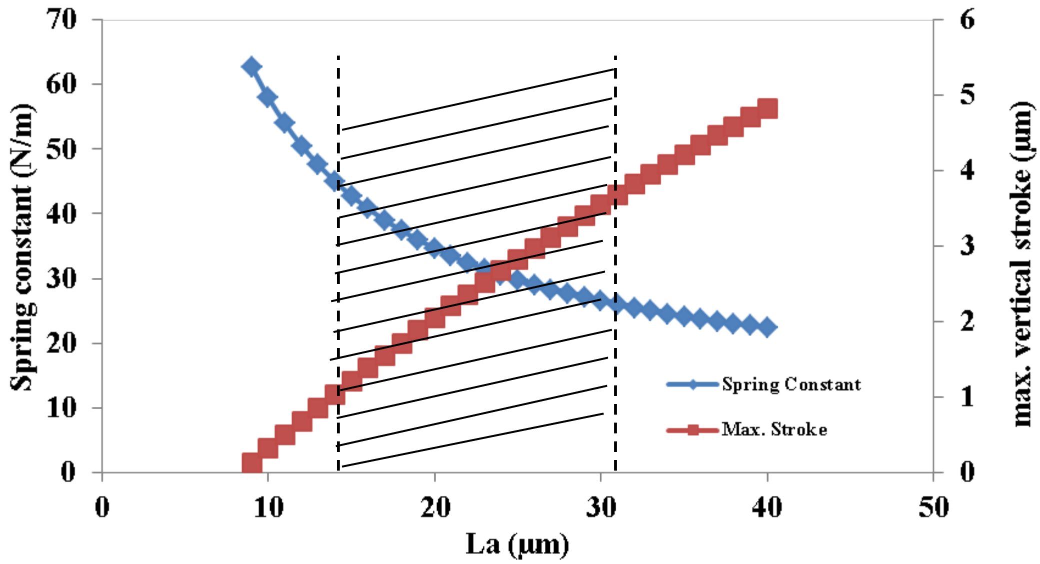

Fig. 2.9 The probe spring constant and maximum vertical stroke *vs.* the length of beam *a*.

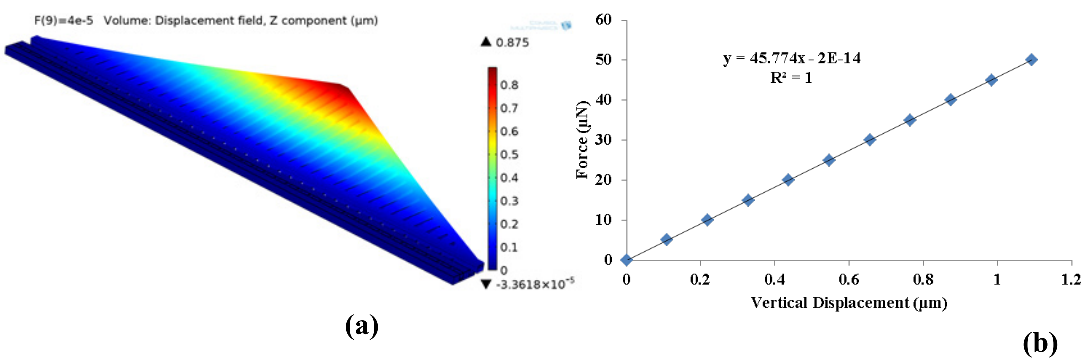

Fig. 2.10 Simulated force-displacement relationship of the designed probe: (a) Vertical displacement of 0.88 µm at $F = 40$ µN. (b) An extracted spring constant of 45.8 N/m is extracted from the force-displacement relationship.

2.5 Probe characterization

Probe design implementation in TSMC

The widely-spaced active CMOS-MEMS probe array design is implemented via TSMC 0.35 μm CMOS technology. The designed CMOS chip is processed with an anisotropic oxide etch, and then a directional silicon etch followed by an isotropic silicon etch to undercut the structure for the release. The probe array is called “widely-spaced” because the spacing between two neighboring array probes is 340 μm, around 22 times larger than the spacing in “narrowly-spaced” probe array that is to be introduced in chapter 5.

SEM characterization

Fig. 2.11 shows the SEM images of the freshly released CMOS-MEMS probes. An array of five probes is placed along one edge of the chip, while all the bond pads are placed along the opposite edge of the chip to facilitate external wire-connections. All the freshly released array probes purposefully curl up away from the silicon substrate due to the residual stress gradient in the CMOS layers. The 7 μm-long metal-1 “hinges” act as a stress bimorph and curl up most because it is the thinnest section along the cantilever.

Fig. 2.12 shows the SEM images of the cross section of the released CMOS-MEMS probes. The metal-1 beam thickness is 1.75 μm, and the metal-3 beam thickness is 4.75 μm. The thickness is smaller than that provided by the foundry, because the top metal layers are subjected to ion milling and get thinner during the MEMS structure release.

Stiffness measurement

The mechanical stiffness, actuation sensitivity and probe frequency response are measured, respectively. The stiffness of the probe is examined by Hysitron TI 900 TriboIndenter. The probe displacement is obtained by sweeping the forcer exerted on the end of the cantilever by the diamond tip in the nanoindenter. Fig. 2.13 (a) shows the measured force-displacement relationship. The spring constant of the probe is around 36.3 N/m, which exceeds the design target of 26 N/m and is stiff enough for STM operation. Using the measured spring constant and structure geometry, the effective Young's modulus of the CMOS MEMS probe is determined to be 56 GPa. Fig. 2.13 (b) and (c) shows the simulated probe force-displacement relationship in COMSOL using the effective Young's modulus, with the derived spring constant equal to 36.3 N/m as expected.

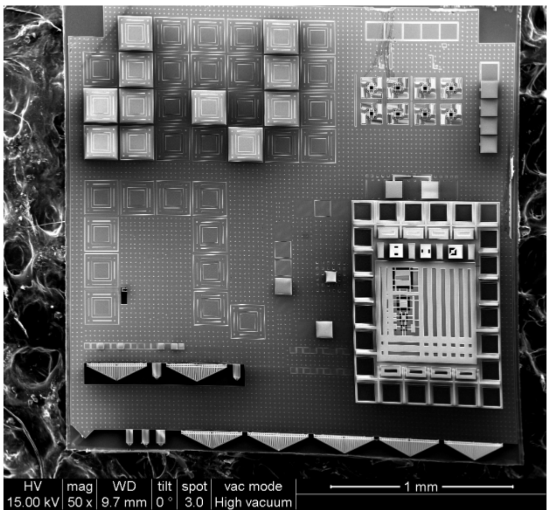

(a): Full probe chip after structure release

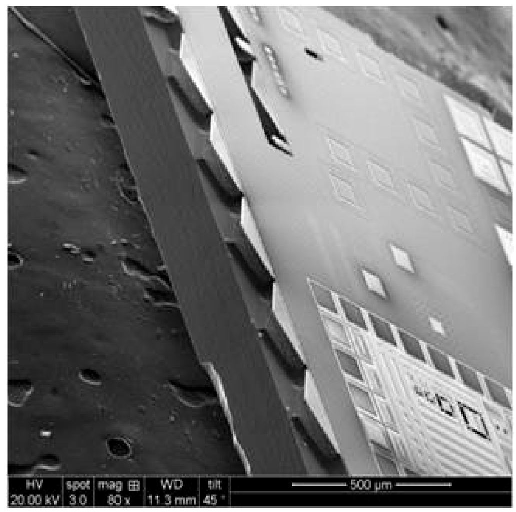

(b): A 1×5 probe array

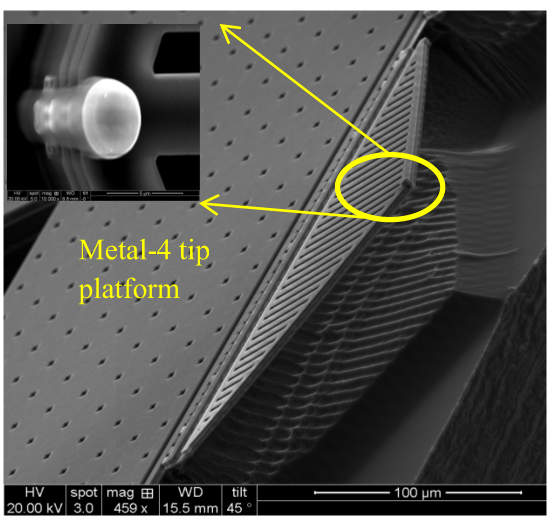

(c): Tilted view of the probe. Inset: top metal-5 tip platform

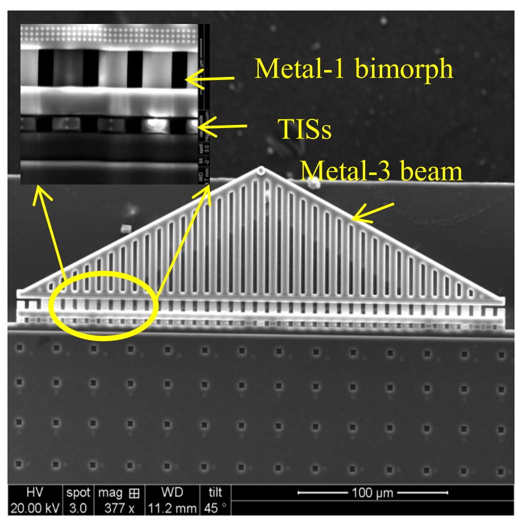

(d): Top view of the probe. Inset: metal-1 tip platform and TIS structure

Fig. 2.11 SEM images of an active CMOS MEMS probe array.

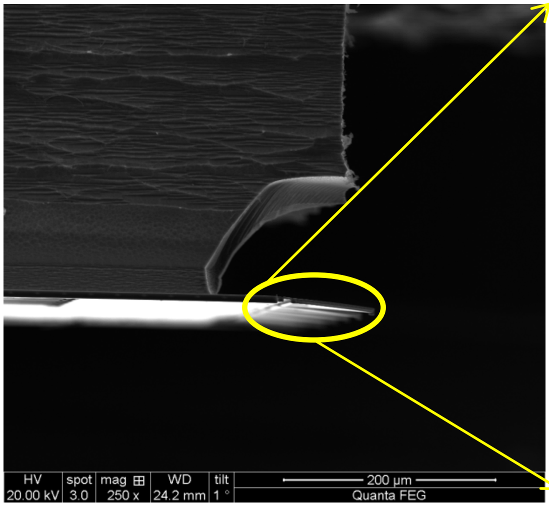

(a): Side view of the CMOS chip

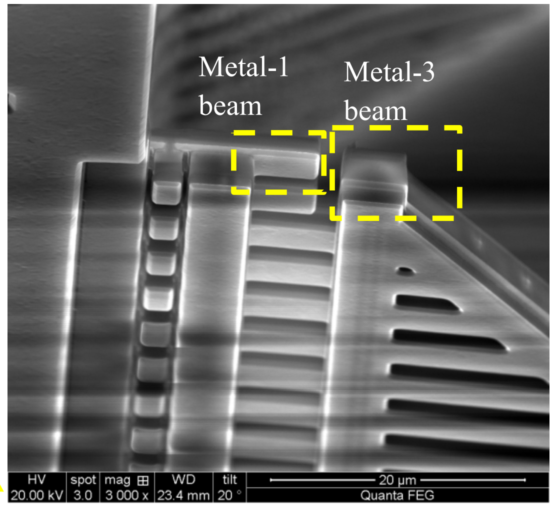

(b): Side view of the MEMS beam

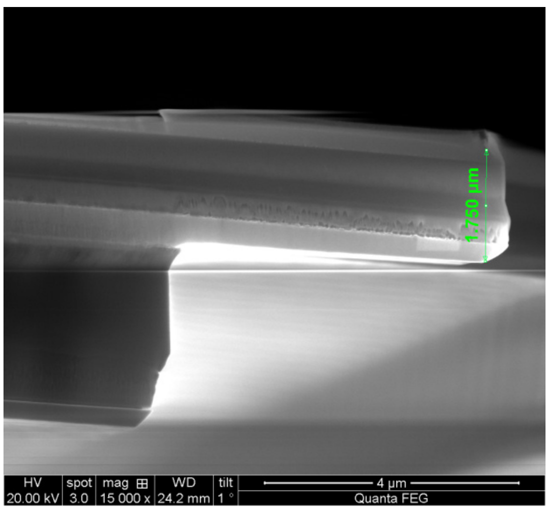

(c): Zoom-in of metal-1 beam

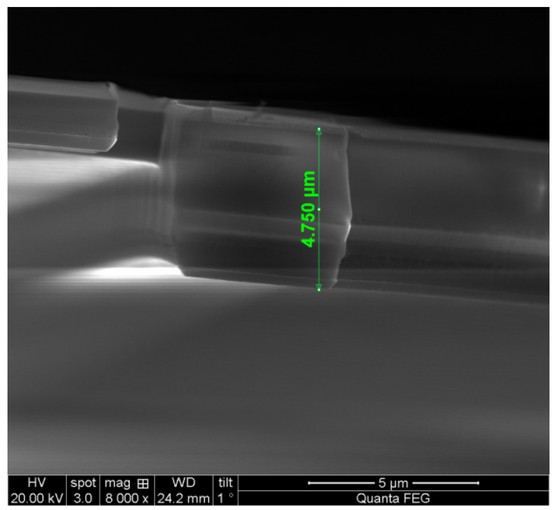

(d): Zoom-in of metal-3 beam

Fig. 2.12 SEM images of the side view of the released CMOS MEMS probe, showing the thicknesses of metal-1 beam and metal-3 beam after MEMS structure release

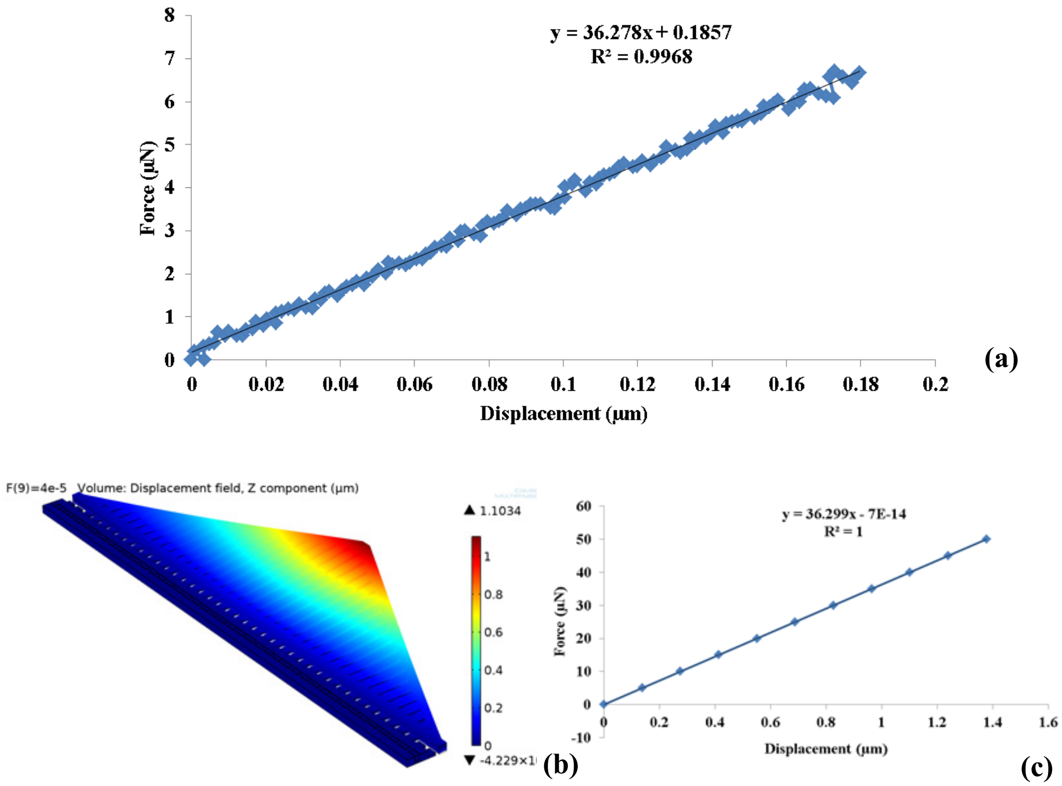

Fig. 2.13: (a) Measured force-displacement relationship of the CMOS-MEMS probe via nanoindenter, indicating a spring constant of 36.3 N/m. (b) & (c) Simulated force-displacement relationship using the effective Young's modulus of the materials of 56 GPa. The simulated spring constant is 36.3 N/m, in accordance with the measured

Interferometer characterization

A Veeco WYKO NT3000 white-light interferometer is used to measure the probe topography. The beam curling results in a 7.6 µm upward tip deflection (Fig. 2.14 (b)). The deflection difference among array probes is smaller than 0.2 µm. Fig. 2.14 shows the curl up of one of the probe.

Upon actuation, the probe is displaced downwards (*i.e.*, toward the probe substrate) because the upper Al layer in the bimorph expands more than the lower SiO_2 layer. The probe can bend downwards up to 2 µm, which is sufficient to cover the general topography of a STM sample plus the variation of self-curl up among array probes. Each probe may be actuated separately to different height using different actuation voltages, as demonstrated in the interferometer image of Fig. 2.14 (c) and (d), where two of them are not actuated while the left one is actuated, so it is lower than other two probes.

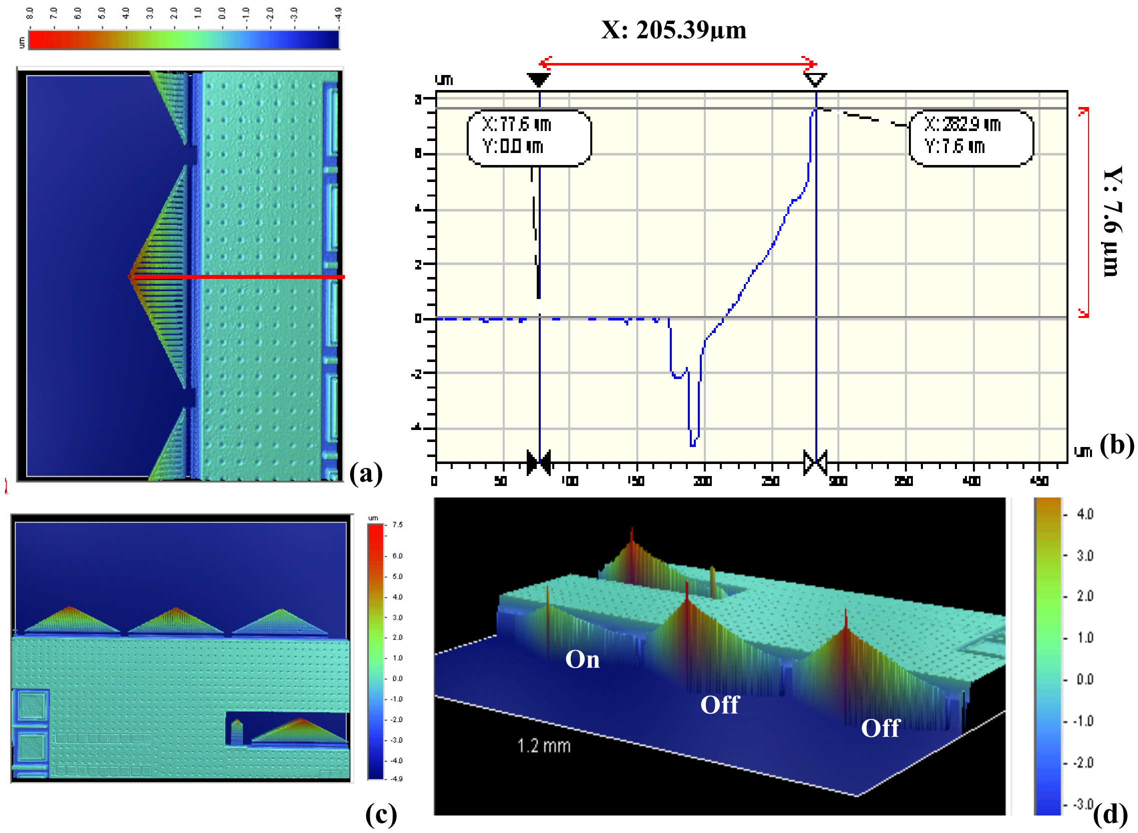

Fig. 2.14 Interferometer images of CMOS MEMS probes: (a) & (b) ~7.6 µm self curl-up upon release; (c) & (d) Independent actuation of array probes. The actuated probe bends downwards and so is lower than the un-actuated ones.

Probe drive sensitivity measurement

The probe ET drive sensitivity is *in situ* characterized during the STM scanning. The probe chip is mounted on the piezo-actuator of a commercial Veeco Dim3000 SPM system. One of the CMOS-MEMS array probes is used as a regular STM end-effector, relying on the piezo-actuator-driven feedback loop to perform the constant current mode STM scanning while the *x*- and *y*- direction movement is disabled. When operating in STM constant current mode, the separation between the tip and the sample surface is fixed by the current set point. When using the on-cantilever ET actuator to drive the probe, it moves vertically and the tip-sample distance changes. To compensate for this distance change so as to maintain the constant current between the tip and the sample, the piezo actuator has to respond accordingly, *i.e.* the piezo actuator has to drive the probe in the direction opposite to ET actuator's movement. The measurement method is described in Fig. 2.15. Fig. 2.16 shows the relationship between the ET drive power and the piezo drive voltage, indicating that the travel distance caused by change of 1 V drive voltage on piezo scanner is equivalent to that caused by 0.129 mW drive power on ET actuator. The ET drive sensitivity is 131 nm/mW using the measured piezoelectric drive sensitivity of 17 nm/V. The characterization of piezoelectric drive sensitivity is documented in Appendix E.

In the dual-probe STM system as will be introduced in chapter 4, the ET-driven probe and its STM feedback loop responds not only to sample topography variation but also to the vertical movement of the piezo actuator. This relationship between the ET drive sensitivity and the piezo drive sensitivity will be used to construct the STM image scanned by the ET driven probe.

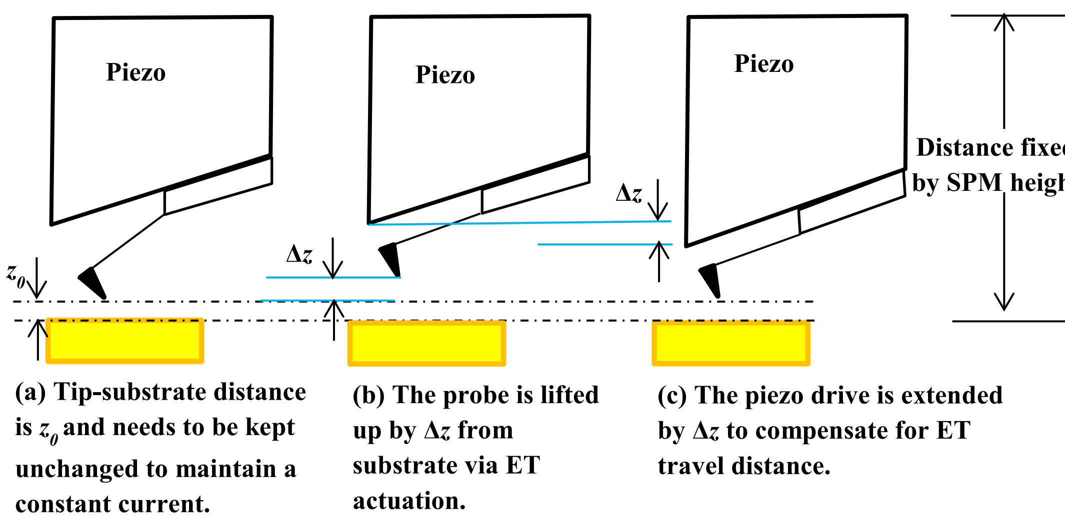

Fig. 2.15 Schematic of the measurement of ET drive sensitivity via *in situ* STM scanning in constant current mode.

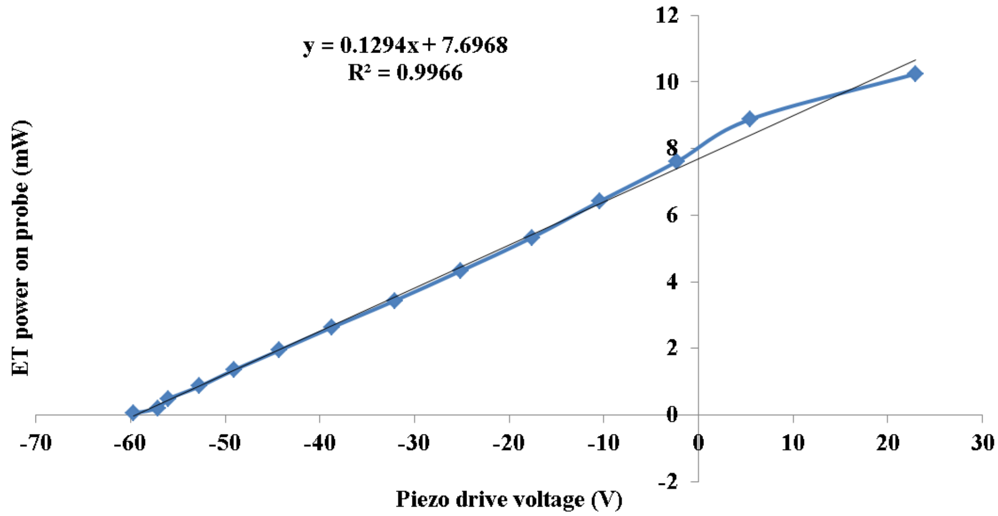

Fig. 2.16 *In situ* measurement of the relationship of ET drive power *vs* piezoelectric drive voltage.

Frequency response

Frequency test via microvision

The MIT microvision system was used to measure the frequency response of the probe ET actuator. A DC bias of 7 V and a sinusoidal actuation voltage of 2 V were applied to the heating polysilicon resistors embedded in the bimorph actuator. The frequency was swept from 10 Hz to 300 kHz.

Fig. 2.17 shows the measured frequency response. Fig. 2.17 (a) shows the frequency sweep from 10 Hz to 250 kHz. Because the probe is very stiff, the probe thermal cut-off frequency and resonance frequency are orders of magnitude apart. The frequency sweep measurement is then divided into several parts to increase the accuracy. Fig. 2.17 (b) shows the frequency sweep from 10 Hz to 1 kHz, where the thermal 3 dB cut-off frequency, ω_{ET}, is identified as 280 Hz. Fig. 2.17 (c) shows the frequency sweep from 4 kHz to 50 kHz. For comparison, also shown in Fig. 2.17 (c) is the vertical displacement of the probe when only a DC bias is applied and no sinusoidal actuation voltage is applied. The amplitude of the probe decreases to below 20 nm when the drive frequency is over 10 kHz, comparable to the noise level of around 10 nm when no AC drive voltage is applied. No obvious resonant peaks are identified during this frequency range. Fig. 2.17 (d) shows the frequency sweep from 201 kHz to 211 kHz, where the probe mechanical resonance frequency, ω_r, occurs at 206 kHz, with a fitted quality factor of 180. Therefore, the transfer function of the ET-driven CMOS-MEMS probe can be expressed as:

$$\frac{\text{Displacement}}{\text{ET power}} = C * \frac{\omega_{ET}}{s + \omega_{ET}} * \frac{{\omega_r}^2}{s^2 + \frac{\omega_r}{Q}s + {\omega_r}^2} \tag{2.20}$$

The parameters and their values are summarized in Table 2-3. The frequency characteristics of the ET drive are used in the design of the STM feedback loop, which will be reported in chapter 4.

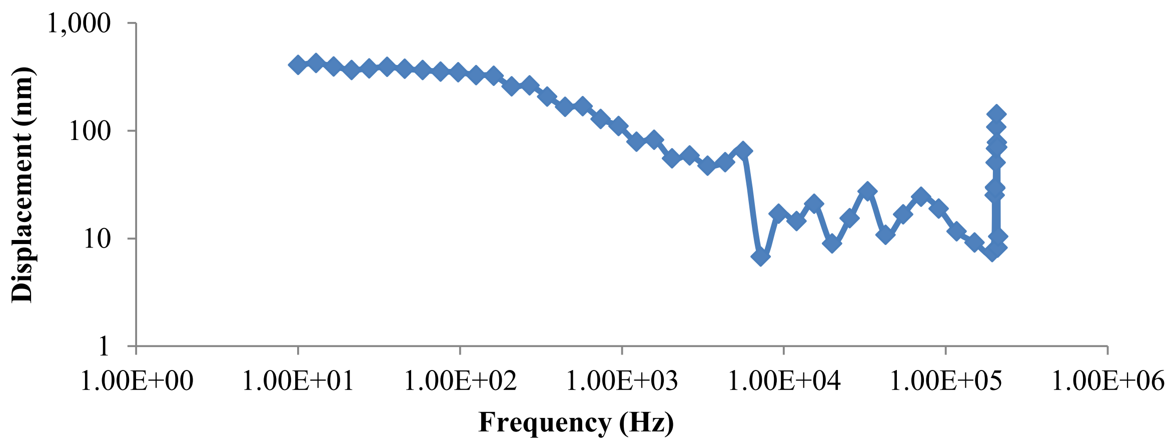

Fig. 2.17 (a) Frequency response of the CMOS-MEMS probe between 10 Hz and 250 kHz

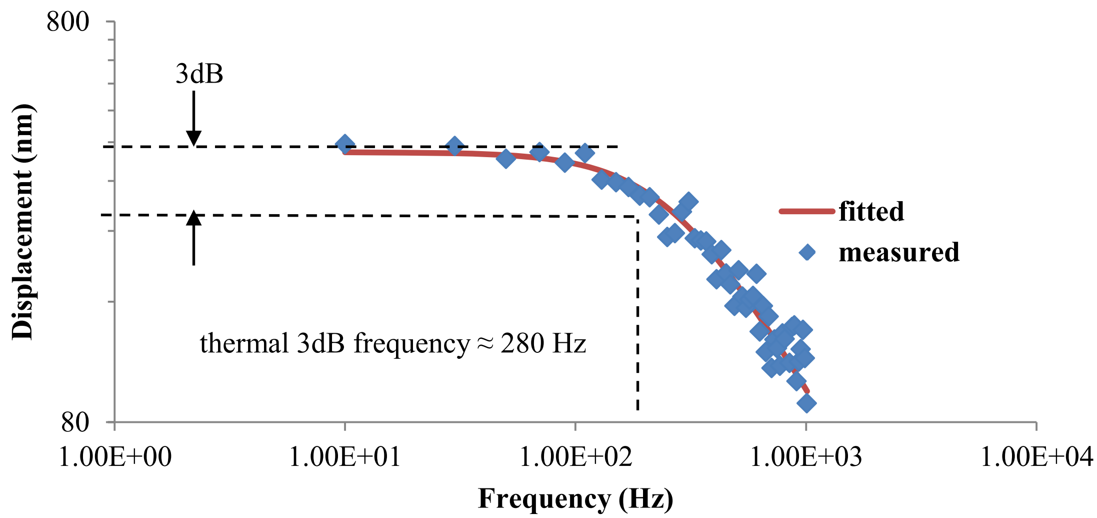

Fig. 2.17 (b): Dynamics of the ET driven CMOS-MEMS probe. The thermal cut-off frequency is 280 Hz.

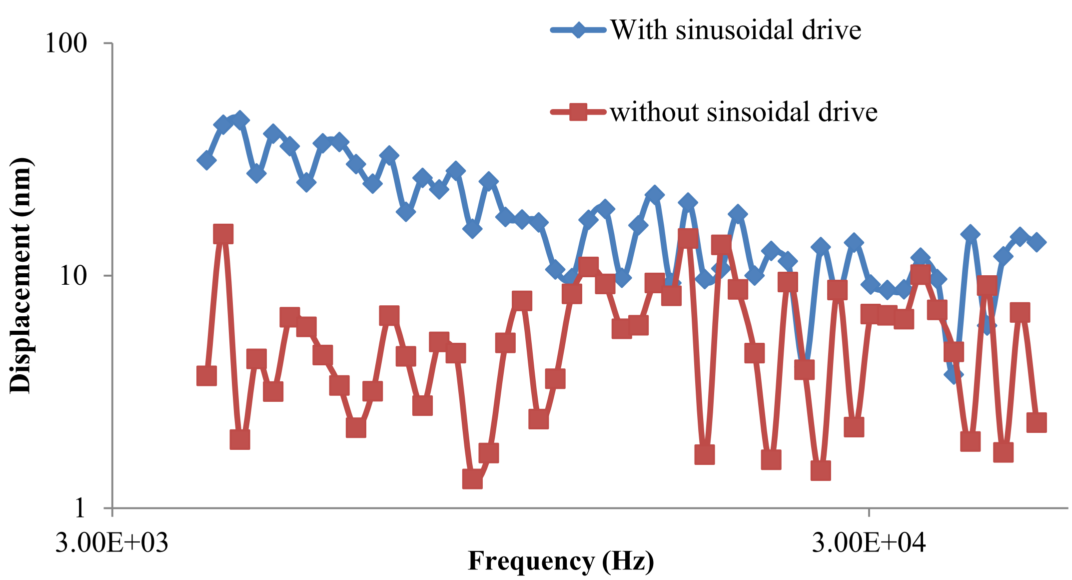

Fig. 2.17 (c) Frequency response of the CMOS-MEMS probe between 4 kHz and 50 kHz. No resonant peaks are identified in the range.

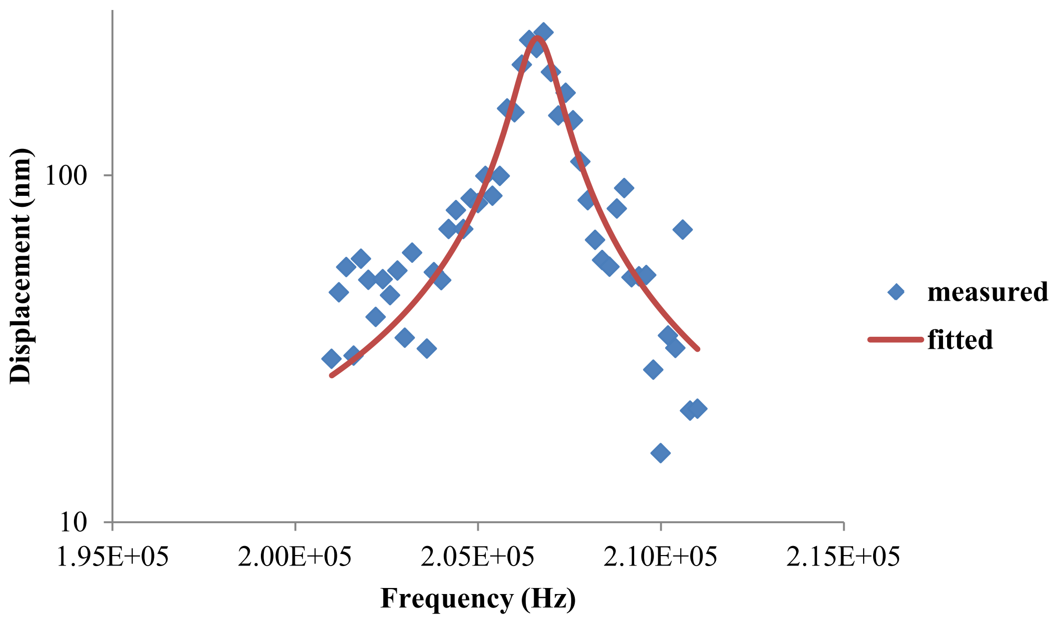

Fig. 2.17 (d) Dynamics of the ET driven CMOS-MEMS probe. The probe resonance frequency is 206 kHz, and the qualify factor is 180 in air.

Table 2-3 *Parameters of ET actuator dynamics of the CMOS-MEMS probe*

Parameters	Value	Description
C	131 nm/mW	Probe DC drive sensitivity
$\omega_{ET}/2\pi$	280 Hz	Thermal cut-off frequency
$\omega_r/2\pi$	206 kHz	Resonance frequency
Q	180	Quality factor

2.6 Discussion

Sufficient vertical stroke needed for parallel operation

In the parallel operation of a STM probe array, it is required all array probes be at a same distance above the sample substrate simultaneously and perform the scanning task. Therefore, each array probe needs to have sufficient vertical stroke range to cover not only the topography variation of the examined surface, but also the difference in relative height between each probe and the surface. Factors such as the process variation introduced in CMOS MEMS processing, the tip height variation among array probes and the substrate curvature contribute to the height variation among array probes.

Sources of height variation among probes

In STM characterization, the surface roughness of the sample is generally below 20 nm, so a vertical measurement range of 20 nm is assumed for a STM probe. Due to the process variation in residual stress gradient, the probes will each have different curl up upon structure release. For the 1D probe array fabricated in TSMC 0.35 µm process and used in the dual probe STM system, the standard deviation of curl-up heights is 160 nm. Variation of the tip height among array probes is estimated to be 20 nm. For a 6" SOI wafer, the bow/warp is smaller than 30 µm [45], which is translated to a height difference of 40 nm for two points spaced 100 µm apart on the wafer. As a conservative estimation, three standard deviations of all these factors that need to be compensated for should be no more than the half of the full stroke of a vertical ET actuated probe. Assuming a maximum vertical stroke of 2 µm, and a maximum spacing of $L \times 100$ µm between two outmost probes, we have:

$$3\sigma = 3 * \sqrt{\frac{20^2 + 160^2 + 20^2 + (40 * L)^2}{4}} = 1000 \ nm \tag{2. 21}$$

Therefore, L is derived as 16. It suggests that the maximum spacing between two outmost probes in a 1D array should be no more than 1.6 mm.

For the designed 1×5 CMOS MEMS probe array in TSMC 0.35 μm technology, the spacing between adjacent probe tips is 340 μm, with two outmost probes 1360 μm. A power of 15.2 mW provides a vertical stroke range of 2 μm for the ET actuated probe given the measured ET drive sensitivity is 131 nm/mW. Therefore, five probes in the 1D array will be able to be engaged on the examined surface at the same time for parallel operation.

Stepper concept for wafer-scale operation

To cover a wafer-scale characterization and nanofabrication, the concept of a wafer stepper can be introduced, where the wafer is moved back and forth and left and right under the probe array chip through the external actuator and motor so that the probe array can characterize the surface from one location to another.

2.7 Summary

A widely-spaced active CMOS MEMS conductive probe array platform qualified for STM mode imaging were designed and fabricated via TSMC 0.35 μm CMOS technology. A compliant cantilever structure was adopted for the CMOS MEMS probe in that it was easy to actuate with on-cantilever embedded microactuators and thus possible to be scaled to an array of probes. Electrothermal actuation was chosen to provide the vertical direction movement of the probe. A minimum cantilever stiffness of 26 N/m is required to avoid snap-in when the compliant probe is used as STM end-effectors. The designed active probe has a spring constant of 36 N/m, a thermal power drive sensitivity of ~131 nm/mW, a resonance frequency of 206 kHz and a thermal cut-off frequency of 280 Hz. The probe array is used in the dual-probe parallel STM imaging, as will be introduced in Chapter 4.

Chapter 3. SPM Tip Process on CMOS-MEMS Probe Array

Significance of SPM tips

Accompanied with the invention of SPM are a variety of techniques which are developed for fabricating SPM tips—mainly AFM and STM tips. Depending on the specific properties of the materials needed to be examined, the SPM tip materials need to be carefully selected so as to be a good indicator of examined properties. The tip geometry, such as shape, height and tip radius, is also desired to be precisely controlled to be suitable for different surface topography and contour requirement. In short, the SPM nanoscale tip fabrication is a complex combination of science and practical art.

Chapter content

In this chapter, the fabrication technology of STM tips on CMOS MEMS structures is described in detail, highlighting a batch STM tip integration process on CMOS MEMS chips. Section 3.1 reviews the various approaches to fabricating SPM tips and their integration on SPM probes, and particularly discusses the "Spindt tip" process in detail. Section 3.2 focuses on the development of a modified Spindt tip process, which is compatible with post-CMOS MEMS processing techniques and enables the batch fabrication of STM platinum tips on an array of MEMS cantilevers at one time. The Spindt platinum tip is capable of STM-based imaging and nanowire writing. In section 3.3, electron-beam induced deposition (EBID), a localized nanofabrication technique is introduced to directly fabricate platinum tips on MEMS probes, but one at a time. Although EBID is a serial process of making STM tips, it is a quite flexible and convenient technique and is used to make prototype tips on probe arrays.

3.1 SPM tip fabrication review

3.1.1 General SPM tip processes

STM tips:

STM tip materials

STM aims to produce atomic resolution. This atomic resolution originates from p_z or d_{z2} electron energy band states on the tip. Consequently, only a limited selection of tip materials can provide atomic resolution: d-band metals, for example, Pt, Ir, Pd, Rh, W, Mo; semiconductors that tend to form p-like dangling bonds, for example, Si [46]. Depending on specific applications, tip materials may vary. For example, in the spin-polarized STM techniques, high quality ferromagnetic STM tips are needed, so ordered equi-atomic MnNi is generally chosen [47].

STM tip geometry

Commercial STM tips are usually produced from W (tungsten) or Pt/Ir (platinum/iridium) alloy. The tips are rod-like, 2 – 3 cm in length and ~0.2 mm in diameter. They are required to have ultra-sharp tip end, with ideally one atom at its apex, because it is expected to accomplish atomic resolution images of studied surface in STM characterization.

STM tip preparation

There are two common methods for STM tip preparation, mechanically cutting wires at angles with a quality wire cutter and electrochemical etching [48]. The mechanical cutting method is mostly used in preparing Pt/Ir tips. The resulting tip shape has a very jagged apex that serves well in the examination of very flat surface like HOPG (Highly Ordered Pyrolytic Graphite), but gives irreproducible performance and poor stability on rough surfaces [49]. Cutting is a manual process, so the tip shape is not reproducible or controllable. Electrochemical etching is an economic and efficient way to fabricate extremely sharp tips that give better performance on more corrugated surface. A standard process flow can be established for electrochemical etching to guarantee tip geometry control and reproducibility [50], and can be readily modified to produce tips with specific needs. For example, when using STM in the electrochemical study of metal substrates in a liquid environment, a tip-coating step is added after electrochemical etching to cover the tip apex with insulating materials to minimize the effects of Faradaic current on the STM tunneling current [51].

AFM tips:

AFM tip materials

AFM tips are of great variety. Typically, these tips are made of silicon or silicon nitride. An additional coating such as Al, Pt, or diamond can be applied on the probe depending on the specific application requirements.

AFM tip via etching approach

AFM probes are generally batch fabricated through micromachining technology. The process steps include photolithography, dry and wet etching, and thin film deposition. The fabrication of sharp tips is generally an integral part of the AFM cantilever production process [52-43].The tip formation is a subtractive process. Fig. 3.1 shows a typical process of fabrication of an AFM cantilever [53, 54]. First, a layer of tip material and a layer of cantilever beam material are deposited on a handle wafer (Fig. 3.1 (a)). The thickness of the tip material typically ranges from 5 μm to 15 μm, depending on specific requirements. A shadow mask is then deposited and patterned to define the tip location (Fig. 3.1 (b)). A timed isotropic dry or wet etch is then applied to remove the tip material not covered by the shadow mask, resulting in sharp conical tips (Fig. 3.1 (c)). Further tip sharpening of the tips is possible, either via focused ion beam milling [55] or oxidation sharpening [56]. After removing the shadow mask (Fig. 3.1 (d)), Cantilever beams are then formed using reactive ion etching (Fig. 3.1 (e)). Backside of the handle wafer is then patterned and etched to release the cantilever structure (Fig. 3.1 (f)-(g)).

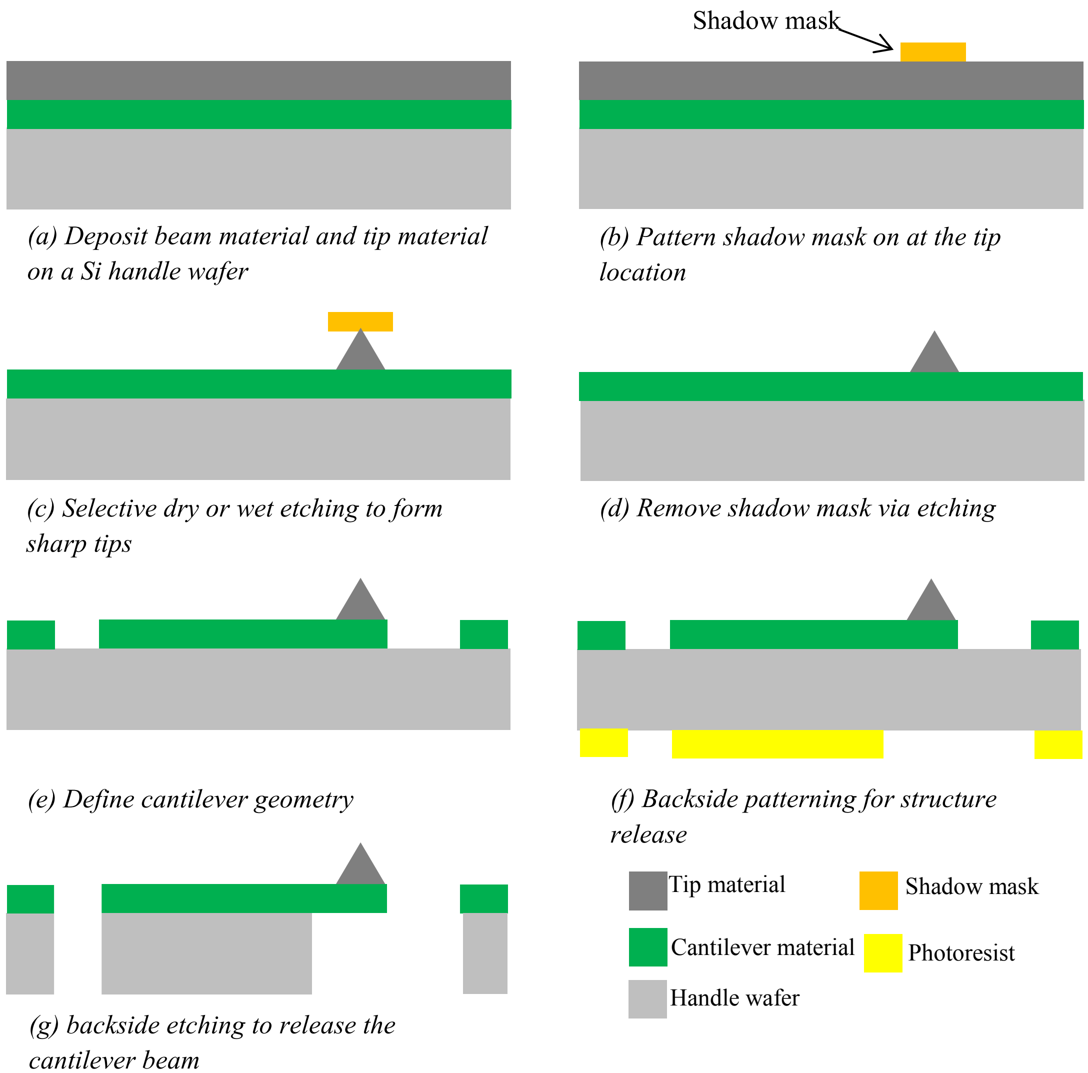

Fig. 3.1 Typical AFM tip formation mechanism [42, 43].

AFM tip via transfer

Recently, nanowires and nanotubes, particularly those made of carbon, are becoming more commonly used as AFM tips because of their extremely large aspect ratio and their chemical and mechanical stability [57]. In such cases, AFM cantilevers and nanotubes are prepared in separate processes, and then the nanotubes are transferred to the end of the cantilever through manual operation of micro-manipulators under the view of a SEM. This separate tip preparation process saves the sharp tips from being subjected to the etching involved in AFM cantilever fabrication, and is compatible with post-CMOS processing techniques.

3.1.2 Spindt tip process

Problems with previous tip process

The commonly used AFM tip processes, as introduced above, include several wet or dry etching steps. Due to the constraint imposed by the post-CMOS MEMS process, however, these tip fabrication methods are not easily implementable because the on-chip electronics and interconnect layers cannot survive various etching procedures. Separate tip fabrication with subsequent transfer of tips onto the SPM cantilevers, though implementable, is still a serial process for the time being. Furthermore, the transfer approach has a poor scalability to higher tip densities, and may be prone to manufacturing variation. Therefore, a direct fabrication of tips on CMOS-MEMS cantilevers is desired.

Benefits of Spindt tip process

To address this need, a so-called Spindt tip process stands out as a promising solution to manufacture STM tips on CMOS-MEMS structures. The Spindt tip process was invented by C. A. Spindt in 1968 [58]. The process was originally developed to make Mo tips and tip arrays as field-emitter cathodes. These field-emitter arrays have a variety of applications including flat panel displays, microwave amplifiers and x-ray tubes. One main advantage of the Spindt tip process is that a very sharp tip end with tip radius down to ~10 nm will naturally evolve during the material deposition; no extra tip-sharpening process such as wet-etching or ion-milling is needed. On-chip CMOS circuitry will not survive many of these common tip-sharpening processes. Moreover, the Spindt process is a batch process, and so is more scalable compared to serial tip processes like tip transfer or EBID. These qualities of the Spindt process make it an ideal candidate to fabricate sharp SPM metal tips on a CMOS chip.

Basic Spindt tip process

Fig. 3.2 shows the mechanism of how a sharp Spindt tip evolves. A shadow mask layer is first made on the substrate where the Spindt tip is to be manufactured. The shadow mask is a thin film mask, shown in Fig. 3.2 (a), with a series of patterned holes of certain aspect ratio, *t/d*, where *t* is the hole thickness and *d* is the hole diameter. Next, sputter or evaporative deposition from the tip source material onto the substrate is initiated. Because of the angular distribution, the material being deposited will not only land on the bottom of holes but also stick to and accumulate on the sidewalls. The opening on top of the hole gradually becomes narrower, leading to less and less tip material being able to go through the hole opening and reach the substrate, so that a cone-like structure forms in the patterned hole. Eventually, the hole is entirely pinched off by the deposition flux and the cone structure ends up with a very sharp tip at the apex.

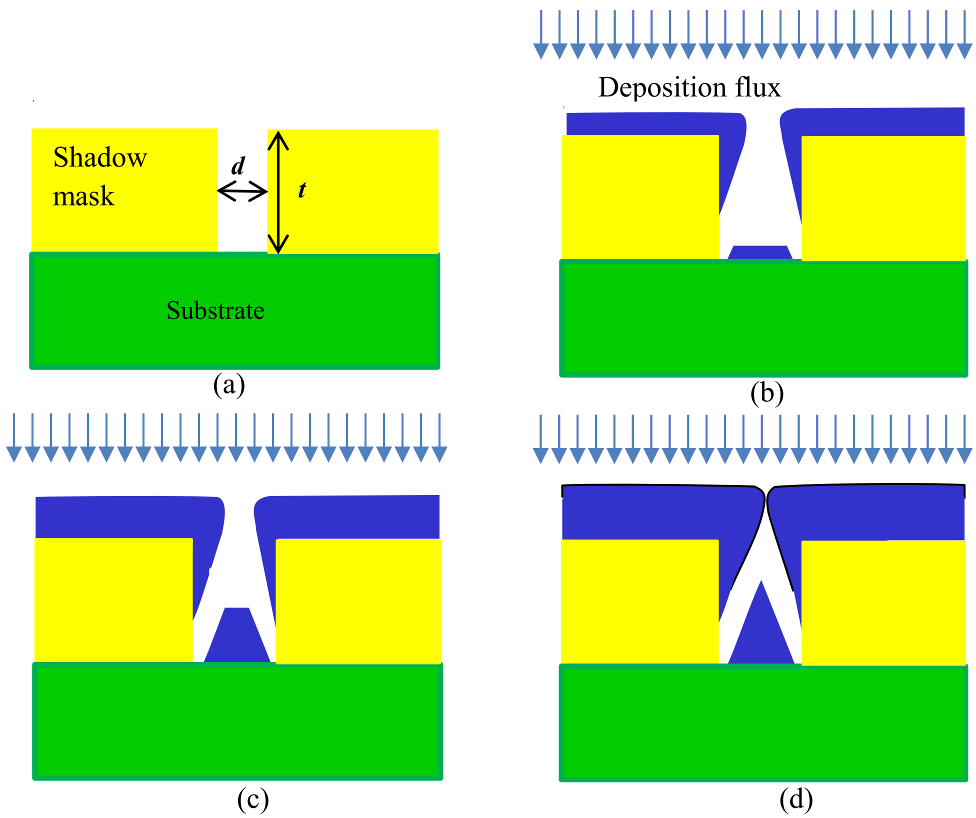

Fig. 3.2 Schematic of mechanism of Spindt process: (a) Fabrication of a shadow mask with patterned holes of designed aspect ratio on the Spindt tip platform; (b) to (d) Deposition of tip source material into the hole. With the opening of the hole gradually becoming narrower, the deposited material evolves into a cone-shape.

Factors affecting Spindt tip formation

Thin film growth models can be used to describe and simulate the growth mechanism of Spindt type tips [59]. Two major factors control the evolution of the morphology of the Spindt tip during the deposition: the incident angle distribution of the deposited material, which depends on the specific deposition methods, and aspect ratios of the patterned holes for the tip.

Sputtering *vs.* evaporation

Magnetron sputtering and e-beam (electron beam) evaporation are the two most commonly used metal thin-film deposition techniques in micro-fabrication. The major difference of these two techniques lies in their directionality, which is determined by the deposition conditions of the respective techniques. Table 3-1 shows the typical deposition parameters used for the two techniques in specific equipment. In magnetron sputtering, the ion-sputtered metal atoms assume a broad distribution of emergent angles from the target and transfer that incident angle distribution to the sample, as depicted in Fig. 3.3 (a). The high pressure in sputtering enhances the scattering between particles and further expands the angular distribution of particles incident on the substrate. In e-beam evaporation, the target source area is small compared to source-sample distance. The deposition pressure is much lower than in sputtering and consequently there is less scattering of atoms. Therefore the flux of evaporated material can be treated as collimated and the angular spread of the atoms is small.

These attributes suggest that, given a hole aspect ratio of *t/d*, more of the sputtered atoms in magnetron sputtering will be incident on sidewalls of the holes than reach the bottom of the holes. Only a small amount of material will land at the bottom of the hole to contribute to the tip formation, as illustrated in Fig. 3.3 (a) and shown in experiment in Fig. 3.4 (a). By comparison, in e-beam evaporation, a higher ratio of atoms are reaching within the hole to contribute to the tip formation than hit its sidewall to close the hole, to the extent that a sharp tip end forms at the closing of the hole, as shown in Fig. 3.2. So in the most Spindt tip process, e-beam evaporation is applied.

Table 3-1 *Deposition parameters in magnetron sputtering and e-beam evaporation*

Parameter	Magnetron Sputtering	E-beam evaporation
Equipment	Perkin Elmer 8L	Ultek E-beam evaporator
Target geometry	Circular, 6" in diameter	Circular, 1.1" in diameter
Target-substrate distance	2.5"	~40"
Chamber pressure	~5 mtorr	10^{-6} to 10^{-5} torr
Deposition rate for nickel	~7-8 Å/sec	~1 – 2 Å/sec
Substrate temperature	High	Low

Sputtering with collimator

A properly designed collimator may be placed in a sputtering chamber between the target and the substrate to serve as a directional filter that blocks the atoms whose incident angles deviate beyond a certain degree from the substrate normal. Sharp Spindt tips with around 1 μm tip height and around 1:1 aspect ratio can be manufactured via a collimated sputtering process, as reported in [60] and illustrated in Fig. 3.3 (b) and shown in experiment in Fig. 3.4 (b) and (c).

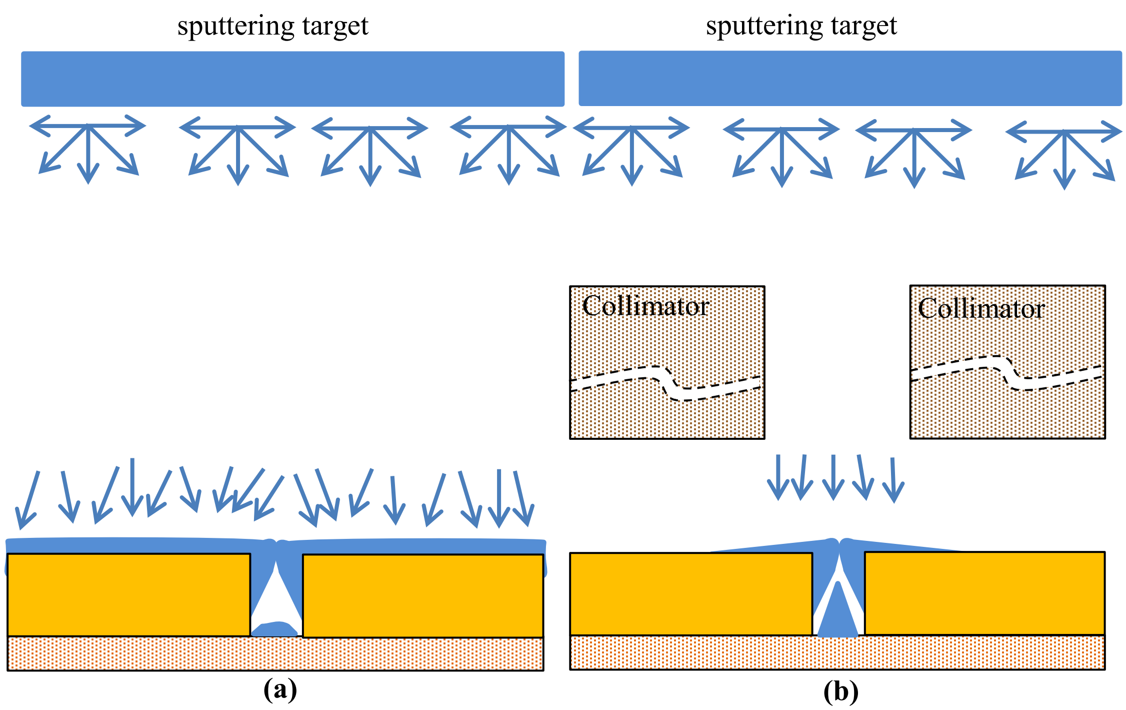

Fig. 3.3 Magnetron sputtering: (a) Without collimator; (b) With collimator.

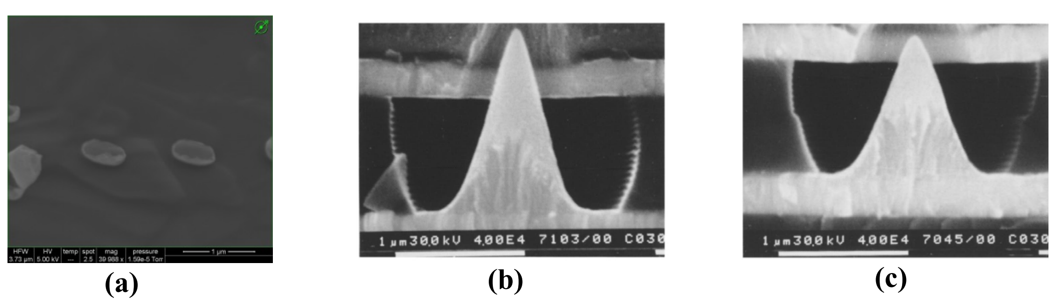

Fig. 3.4 Spindt tips via magnetron sputtering: (a) No collimator used, only a small amount of material results. (b) & (c) Collimators with different aspect ratios are used. Tips with different aspect ratios are created [60].

Hole aspect ratio effect

Once the deposition technique is chosen, the aspect ratio of the patterned holes will determine morphology of the tips. In Spindt's original approach, holes with *t/d* value of 3:1 were patterned on the shadow mask. Concerning the deposition configuration, two deposition flux were used: one flux from tip source materials was at normal incidence to the substrate to form the tip in the hole, while a second, auxiliary, flux made of selectively removable materials was deposited at a grazing incidence to the surface of the shadow mask to control the rate of the closure of the hole. The deposited film from the auxiliary flux was removed by the corresponding etchant after the tip deposition. Mo tips with tip height of ~1.5 μm and tip radius of 50 nm were obtained [61].

In the process reported in this thesis, no auxiliary flux is used. The optimum *t/d* to satisfy the requirements to make STM tips is presented in the next section.

3.2 Spindt tip material selection

Criteria of tip material selection

Choice of the tip material for the Spindt STM tip on CMOS MEMS probes is driven by several constraints. To be a qualified on-CMOS STM tip that is fabricated before the MEMS cantilever processing, the tip material(s) need to possess a good electron tunneling property and at the same time they have to survive the CMOS-MEMS SiO_2 DRIE and Si RIE. Pt, Pt-Ir and W are common STM tip materials that offer good tunneling property. Pt/Ir tips are used more often in air because the material is inert to oxidation and so provides more stable tunneling. In ultra-high vacuum (UHV) operation, W tips are most frequently used where oxidation is not a factor. In this work, Pt is chosen as the tip coating material for STM application because most of the experiments were conducted in the ambient environment. The Spindt process is also suitable to make W tips if that is desirable.

Composite tip structure

However, Pt may not be put on CMOS probes before the post-CMOS processing. First, Pt has an appreciable etch rate in SiO_2 anisotropic RIE. In the Plasma Therm 790 RIE system, the etch rate of Pt is around 50 nm/hour [25] (The etch rate of Pt in the STS Aspect Cluster RIE/AOE system was not measured). Secondly, Pt is a precious metal and it is not economical to deposit a few microns to make a thick tip. Ni (nickel) is chosen as the tip body material as it has low, though not zero, etch rate in SiO_2 anisotropic RIE and Si DRIE. As the last step in the microsystem fabrication, Pt is deposited after MEMS full structure release to coat the Ni tip, resulting in a Ni/Pt composite tip.

3.3 Modified Spindt tip process

Modified process overview

950 PMMA C7 (poly(methyl methacrylate), 950 stands for the molecular weight of the resins used in PMMA product) e-beam resist is adopted as the shadow mask on which the sub-µm tip holes are patterned in series via e-beam lithography techniques. E-beam evaporation is used to deposit Ni metal to make the body of the tips.

Section Contents

A suitable aspect ratio of tip holes is discussed in the first subsection. The full process flow of making passive MEMS and active CMOS-MEMS probes is then provided, where the tip manufacturing step is realized by the modified Spindt tip process with optimized parameters. The main purpose of fabricating custom Si-based passive MEMS probes with Spindt tips is to provide ample tips to verify the suitability of the tip material and geometry for STM operation before shifting to tip fabrication on active CMOS probes. The passive SPM probe fabrication technique may also be considered as supplementary to the current state of the art.

Spindt is a batch process

Due to the local unavailability of an advanced optical lithography instrument with sub-µm resolution, optical photoresist is not used as the shadow mask. However, the developed tip process can be extended to use of a photolithographic shadow mask. With an advanced optical lithography instrument, a number of sub-µm tip holes can be patterned with a single photomask and batch photolithography, followed by a single run of material deposition. So the developed e-beam process can be readily modified to a true “batch” tip process.

3.3.1 Effects of tip hole aspect ratio on tip morphology

Exp. Details on t/d study

To examine the effects of hole aspect ratio on tip morphology, holes of different diameters ranging from 100 nm to 500 nm are created on the shadow mask. The mask layer is a 1 μm-thick 950 PMMA C7 e-beam resist spun on the Al-coated test wafer. An adhesion layer of 5 nm-thick Ti is then deposited followed by 1 μm-thick Ni deposition. The PMMA is then lifted off in acetone to reveal the tips.

SEM images of tips

Fig. 3.5 shows the SEM images of the fabricated Spindt tips [62]. Ni tips develop in holes with diameters from 200 nm to 500 nm. At the location of holes of 100 nm in diameter, just a small trace of Ni is found, which suggests the very high aspect ratio of more than 10:1 causes the patterned holes to be closed off by the deposition flux so fast that very little Ni goes into the hole before it is completely sealed.

Determine hole diameter

Tips as sharp as 10 nm in radius are achieved in all three hole diameters: 300 nm, 400 nm and 500 nm. The 300 nm diameter holes have the highest aspect ratio and give shorter tips compared to lower aspect ratio holes. The 500 nm diameter holes produce tips as tall as 900 nm. This result occurs because deposition flux pinches off the higher aspect ratio holes faster than lower aspect ratio holes. In the final integrated process flow, holes with diameters of 400 nm and 500 nm are adopted because longer STM tips are desired.

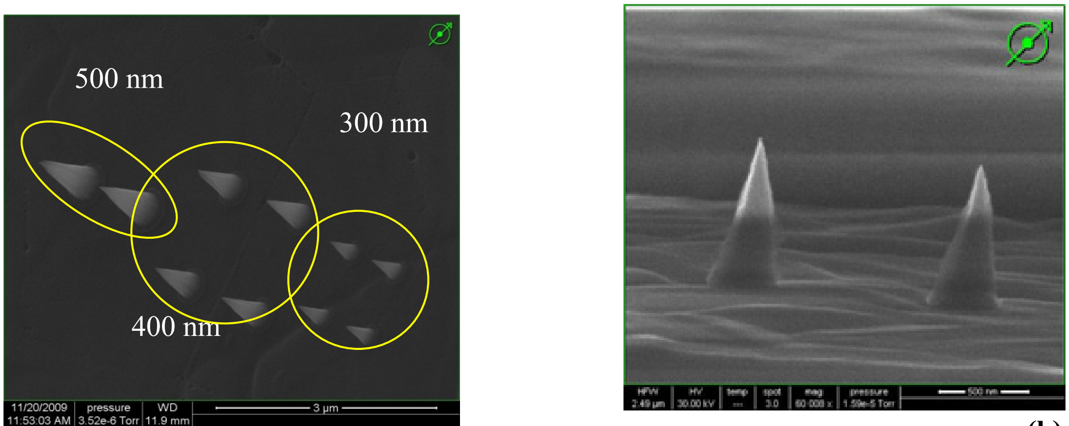

(a) **(b)**

Fig. 3.5 (a) Tips fabricated in PMMA holes of different size, with hole diameters ranging from 300 nm to 500 nm; (b) Tips resulting from PMMA holes with diameter of 500 nm.

3.3.2 Passive probes with Spindt tip

Passive probe process detail

Passive Si-based MEMS probes with integrated Spindt tips are designed and made. Fig. 3.6 shows the probe fabrication process. The process starts with a 300 µm-thick 4" Si wafer. A 1.4 µm-thick AZ5214 photoresist is first spun on the wafer and patterned. A 40-nm thick Ti and a 100 nm-thick Ni layer are then deposited via e-beam evaporation. The photoresist is then lifted off in acetone to reveal the probe cantilever geometry. The Ni tips are then fabricated on the probe cantilever end via the Spindt process. The probe structure is formed by front-side Si DRIE. The last step is to coat the probe wafer with 100 nm-thick Pt via DC magnetron sputtering. The detailed process follow of passive probe fabrication is provided in Appendix A.2. Fig. 3.7 (a) is the photo of probe wafer after finishing the front-side DRIE and coating of the Pt. 112 probes can be batch-fabricated on a 4" wafer. Fig. 3.7 (b) shows the SEM image of a single probe taken after the fabrication of the Spindt tip on the end of the probe cantilever.

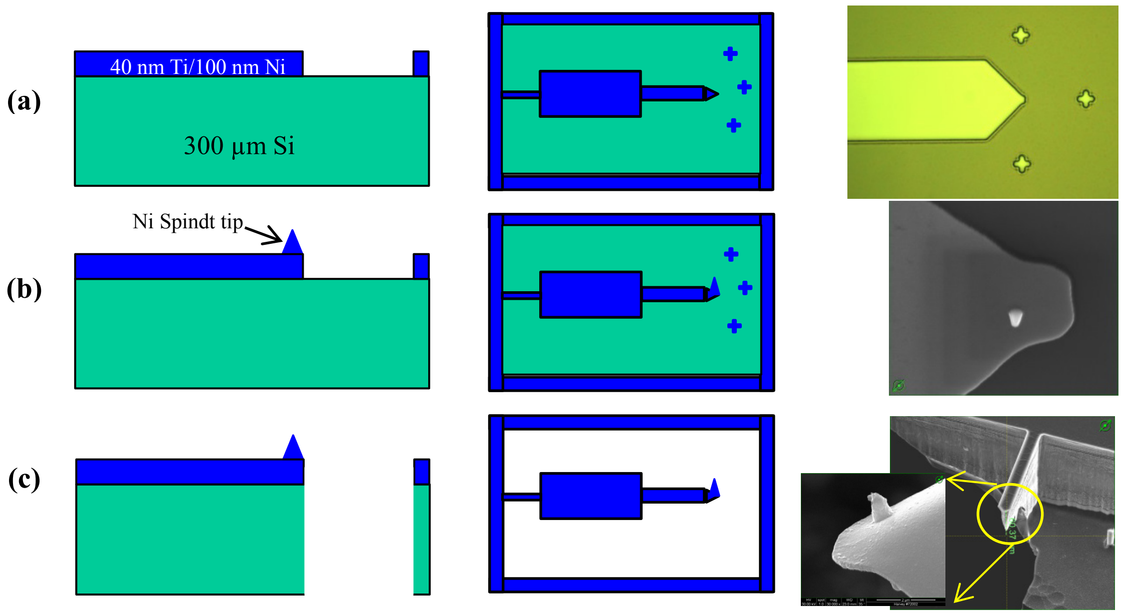

Fig. 3.6 Process flow for the Si-based MEMS probe with Spindt tip: (a) Pattern the Ni mask; (b) Fabricate Ni Spindt tip on probe end; (c) Front-side Si anisotropic DRIE to release the probe. The last step of flashing the probe wafer with Pt is not shown. Column 1 is the side view; column 2 is the top view; column 3 is the image of the fabricated probe.

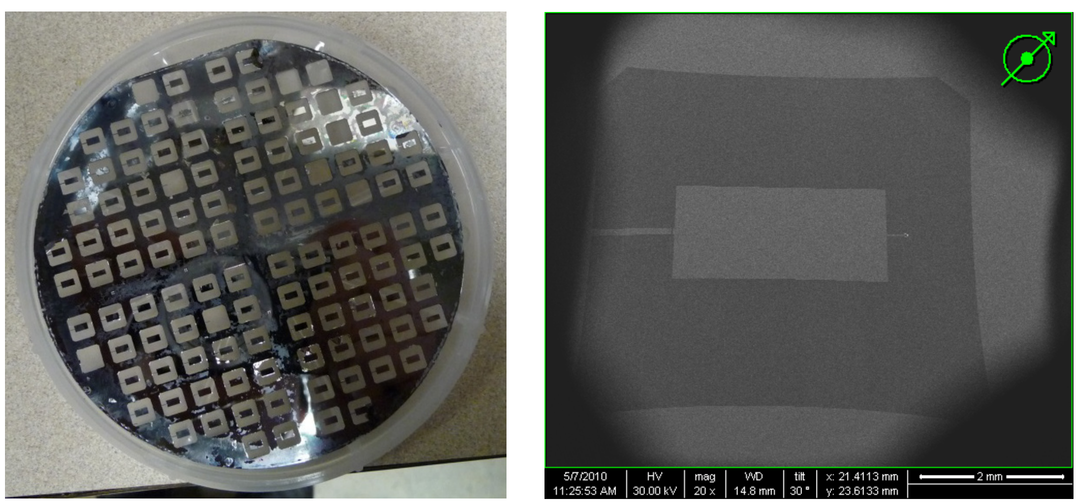

(a) (b)

Fig. 3.7: (a) 4" probe wafer with 112 passive MEMS probe; (b) SEM image of a single probe after Ni tip integration but before front-side Si DRIE.

STM via Spindt tips

One of the Pt-coated passive MEMS probes is mounted on a commercial SPM system to examine the functionality of the Ni-Pt Spindt tip. Fig. 3.8 is the STM image on Si (100) 2x1 reconstruction surface obtained in an ultra-high vacuum (UHV) RHK SPM system. The RHK SPM system is an ATM 350 SPM system designed and manufactured by RHK Technology (Troy, MI, USA) in cooperation with researchers from Carnegie Mellon University. Atomic-level resolution imaging is obtained, where the dimer rows are clearly observed with the ones on the adjacent terraces perpendicular to each other. Spindt tips are thus capable of performing the STM imaging task with atomic resolution in UHV.

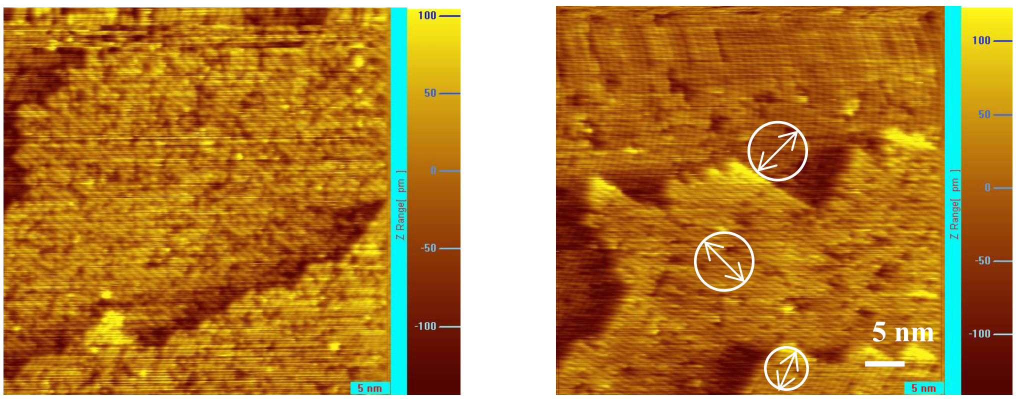

Fig. 3.8 STM images of Si (100) via Ni-Pt Spindt tips on passive MEMS probe. Dimer rows on adjacent terraces are perpendicular to each other.

3.3.3 Spindt tip process on CMOS-MEMS probe

General process:

Active probe fab flow

After the verification of Pt-coated Spindt tip as a qualified STM tip, the process is applied to make Spindt tips on CMOS-MEMS probes. Fig. 3.9 shows the schematic of the full process of fabricating CMOS-MEMS probes out of a CMOS chip. First, a partial oxide etch is performed to expose the top CMOS metal-4 layer that acts as the tip platform. A layer of 1 μm-thick PMMA e-beam resist is then applied and holes of approximately 400 nm in diameter are patterned via e-beam lithography. A 5 nm-thick adhesion layer and 1000 nm-thick Ni layer are deposited in the pre-patterned holes. The PMMA is then removed by lift-off. The CMOS-MEMS process then initiates with a silicon oxide dry etch via AOE (Advanced Oxide Etch) to form the MEMS sidewalls. Then, a timed DRIE into the silicon substrate creates an etch pit followed by a timed isotropic RIE to undercut and release the probe beams. The last step is flashing the sharp Ni tips with a layer of Pt. A sputter etch is performed before Pt sputtering to remove the oxide on Ni and on the exposed CMOS aluminum metallization. Pt deposition has to be constrained to the end of the MEMS beam and not extended to other parts of the chip to avoid electrical shorting of the on-chip circuitry. Two mechanical shadow masks, around 1.5 mm thick, are placed on each side of the tip platform area, directing the Pt flux within the tip area, as shown in Fig. 3.9 (h).

Key points in active probe process

Two issues prove crucial in the integration of Spindt tip on CMOS probes. One is the descum process after photolithography pattern and before deposition, the other is the adhesion material selection in Ni deposition on Al.

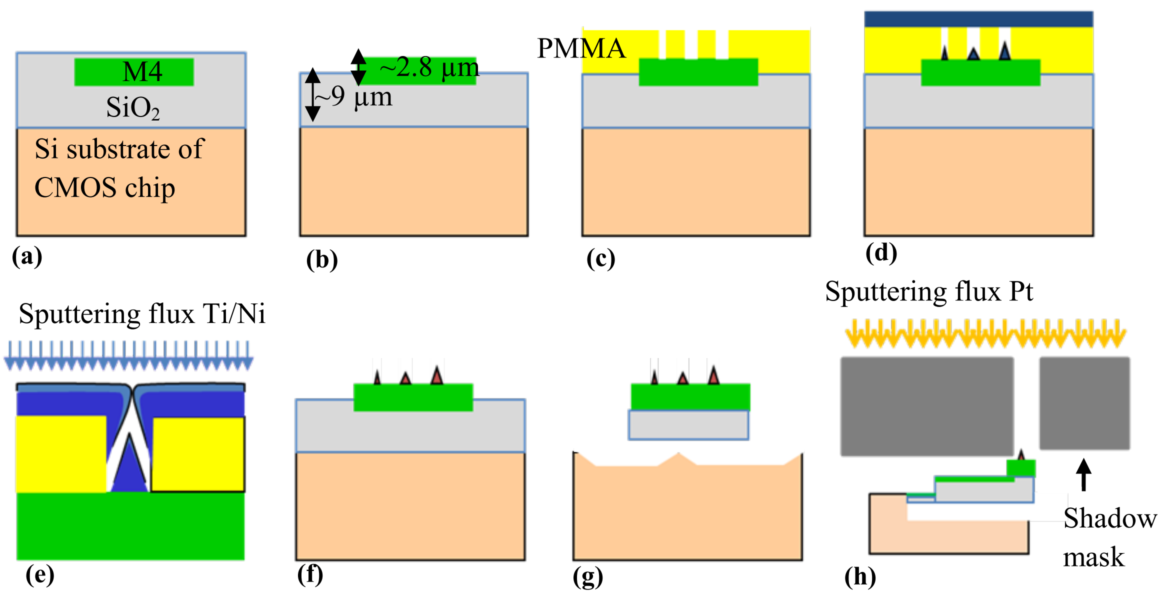

Fig. 3.9 Modified Spindt process for tip integration on CMOS chip: (a) Chip from foundry; (b) Partial oxide etching to expose M4; (c) E-beam lithography, holes of various sizes are made in PMMA; (d) ~1000 nm Ti/Ni tip deposition via e-beam evaporation, with (e) Enlarged deposition picture; (f)Lift-off; (g) CMOS-MEMS structure release; (h)Final flashing with a layer of Pt. Two shadow masks are put on chip to constrain the deposition direction.

Descum in Spindt tip process:

Descum function

The descum process is carried out on the patterned PMMA resist right before Ni deposition occurs. The descum step is a common practice in lift-off. It takes place after the photolithography and development, and the purpose is to remove organic films and residues such as resist remains on the bottom of the patterned area not stripped by the developer.

Isotropic oxygen ashing

In the general photoresist and e-beam resist descum process an isotropic oxygen plasma ashing is used. Yet it did not work completely for tip fabrication on the CMOS-MEMS chips. The success of Spindt tip fabrication on the CMOS chip is location dependent. Future migration to a wafer-scale process would eliminate this dependence.

Tip result from oxygen ashing

Fig. 3.10 shows a 5 mm by 5 mm test CMOS chip (TowerJazz 0.35 µm 4-metal CMOS technology) on which the Spindt tip fabrication was attempted on different places, and where oxygen plasma ashing via IPC barrel etcher was carried out to descum the PMMA resist. Fig. 3.10 (a) shows 3 by 3 arrays of patterns made on a bondpad comprising an 80 µm by 80 µm square of the top metal-4 layer. All patterns are at least 10 µm from the bondpad edge. Eight tips stay on the bondpad after lift-off. Fig. 3.10 (c) shows the location of a top metal-4 tip platform at the end of a probe cantilever. The hole pattern was very close to the edge of the platform, less than 2 µm away. No tips on this platform were found after lift-off, however. The descum step is believed to cause this yield issue.

Analysis of effects of oxygen ashing

This difference in effectiveness of descum via oxygen plasma ashing to clean tip holes on the CMOS chip can be accounted for by the topography of the tip platform on which the PMMA is spun. In the former case, an 80 µm by 80 µm surface area is sufficiently large for 1 µm-thick PMMA to be spun evenly. The patterned holes are straight down to the bottom of the tip platform, and so the oxygen plasma, though non-directional, is able to reach the bottom and fully remove any remaining PMMA residue. The deposited metal will land on the platform and remain after lift-off.

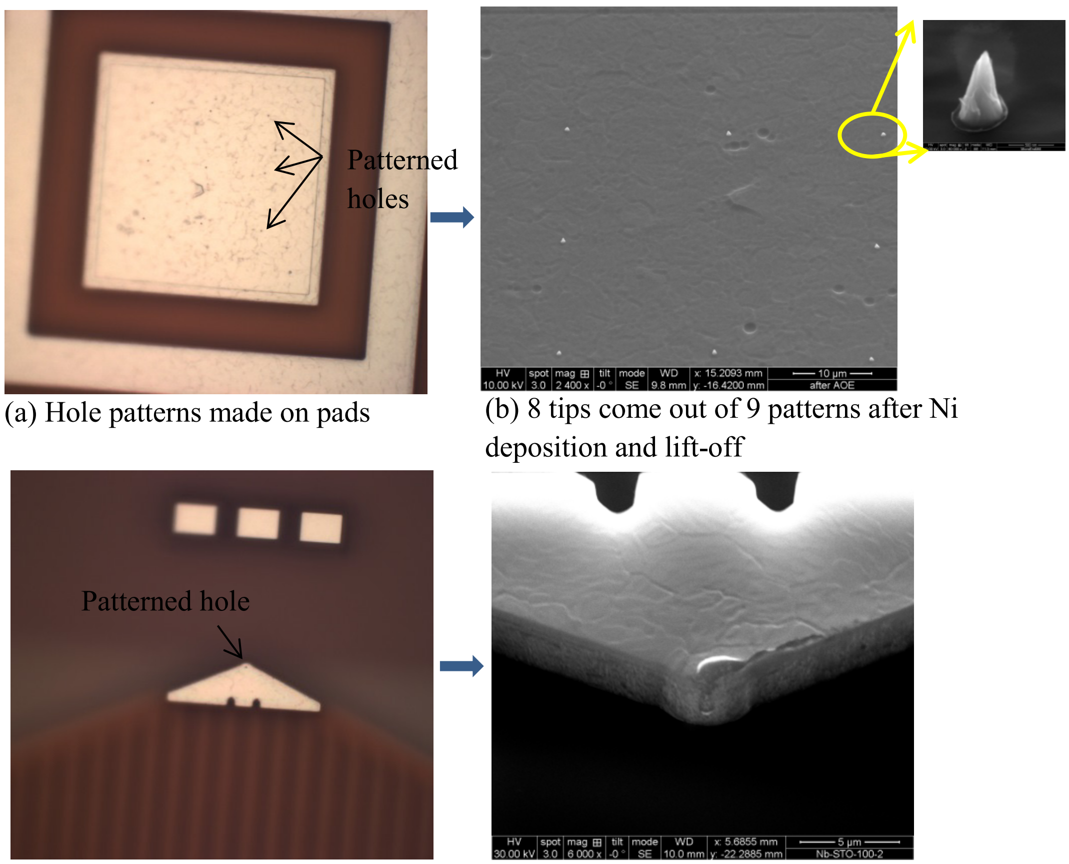

(a) Hole patterns made on pads

(b) 8 tips come out of 9 patterns after Ni deposition and lift-off

(c) Hole pattern made on the end of the MEMS cantilever

(d) No metal trace was found after Ni deposition and lift-off

Fig. 3.10 Effectiveness of Spindt tip processing with descum via oxygen plasma ashing at different locations of the CMOS chip

In the other case the designed metal-4 tip platform is of small area, where the very end is a circle of 5 μm in diameter, and the platform is around 3 to 4 μm higher than the surrounding oxide field, as measured by profilometer and shown in Fig. 3.11. The PMMA spun on the small platform is non-uniform, and the non-uniformity is worst near the circumference of the platform where the large step topography is located. Tip holes patterned near the circumference have a very irregular structure along the sidewall, which is believed to create a thicker than desired residue of PMMA that is not fully removed by the descum step. The deposited Ni lands on the PMMA remains and both layers are removed together in the lift-off step.

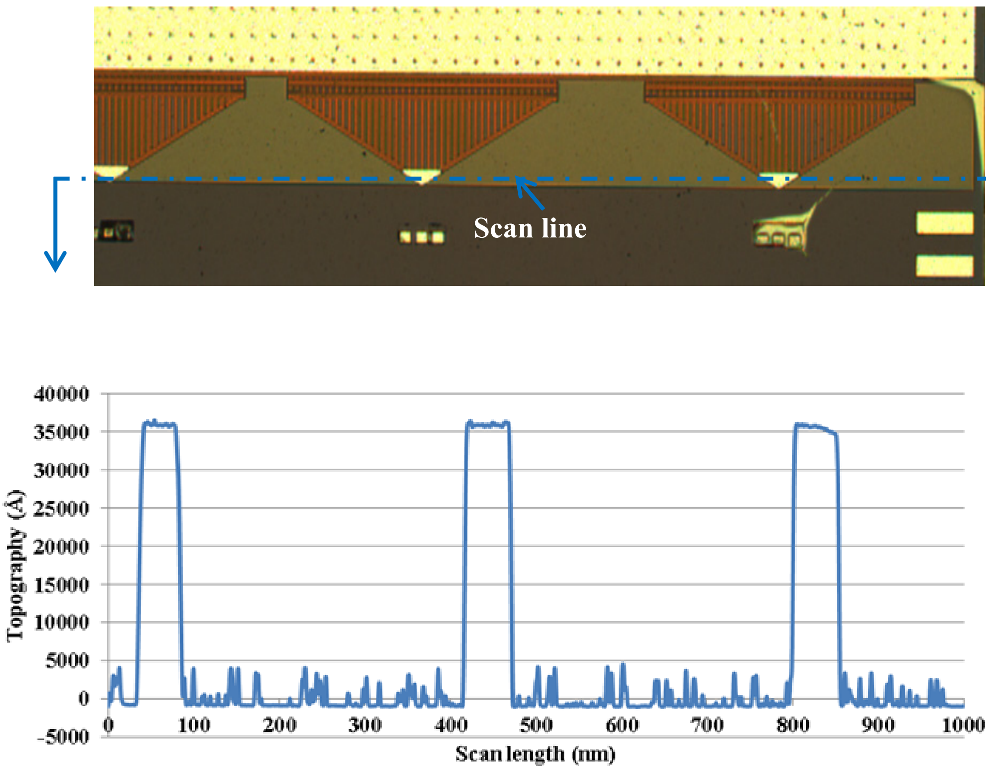

Fig. 3.11 Topography of CMOS chip surface surrounding metal-4 tip platform.

Alternative directional descum processes

To resolve the issue, two alternative directional descum processes were tested. The first is to subject the sample to a RF sputter etch using Ar ion to physically clean up the hole; the second is to use oxygen RIE (Plasma Therm 790 RIE) to provide a physical etch assist in the etch of the PMMA residue. Both of these processes work and the tips are found sitting on the probe end after lift-off, as shown in Fig. 3.12 (a), (b) and (c), respectively. The detailed descum processes can be found in appendix A.1.

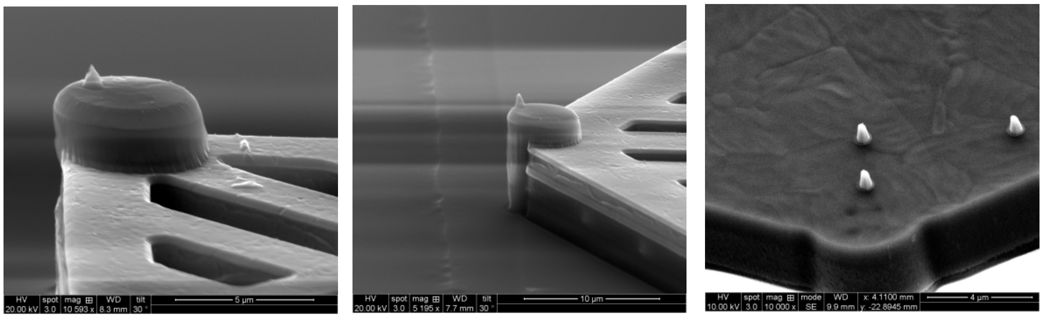

Fig. 3.12 Spindt tips stay on the end of the CMOS cantilevers after Ni deposition and lift-off when the chip is descumed via (a) & (b): RF sputter etch; (c) RIE using oxygen

Future study of descum

The preliminary study of three descum processes suggests that the directional RF sputter etch and oxygen RIE are more effective to descum the patterns with high aspect ratio and irregular geometry compared to non-directional oxygen plasma ashing. Further investigation is warranted, such as examination of the cross-sections of patterned holes on substrate with different topography and element analysis on the bottom of patterned holes after different descum processes to reach a more comprehensive conclusion.

__**Adhesion layer materials in Spindt tip process**__

Cr, not Ti is used as adhesion layer

When Ni is deposited on Al tip platform, an intermediate layer is pre-deposited. The purpose is to increase the adhesion between different materials. Ti was used at first as adhesion layer. Yet SF_6, which is one of the gas etchants in Si DRIE during the CMOS MEMS processing, attacks Ti. Fig. 3.13 shows such a case, where Ti/Ni tips made on CMOS probes survive the SiO_2 RIE, yet all are detached after Si DRIE. Cr (chromium) is not attacked by chemicals used in RIE process and acts as an appropriate adhesion layer for integrating the tip process with the CMOS-MEMS process.

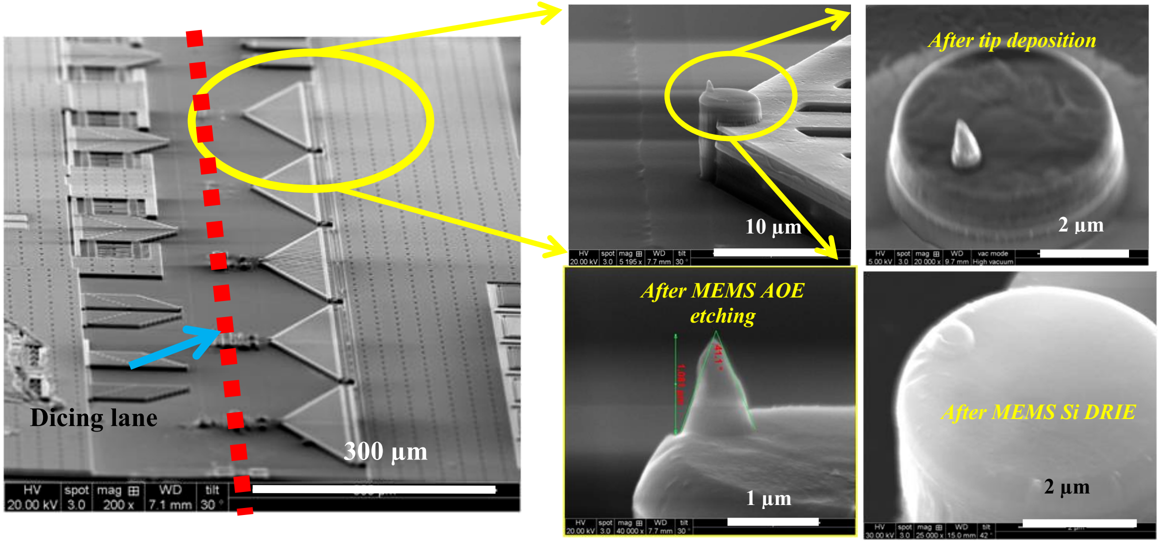

Fig. 3.13 Spindt tips using Ti as adhesion layer: (a) Afive-probe array on a CMOS chip with Spindt tips; (b) A probe end with Spindt tip; (c) to (e): Images of tips after each processing step. The tips are lost in the last step of Si DRIE.

Cr/Ni/Pt Spindt Tip examination

Cr/Ni tips on a CMOS substrate and prior to MEMS processing are shown in the top row of Fig. 3.14. After AOE to remove ~9 µm thick dielectric oxide layers, the tips were shortened by the reactive ion bombardment in the etch process, and the tip radius is around 50 nm, as shown in the second row of Fig. 3.14. After Si DRIE, fully released CMOS-MEMS probes with Spindt tips are shown in the third row of Fig. 3.14. No significant tip geometry change occurs. Tips flashed with 100 nm Pt are shown in the fourth row of the Fig. 3.14. An array of STM tips is made on an array of four CMOS MEMS probes at the same time, with a yield of 60%. Fig. 3.15 shows a typical element analysis of the Spindt tip via EDS (Energy Dispersive X-ray Spectroscopy). Pt and Ni are identified on the tip.

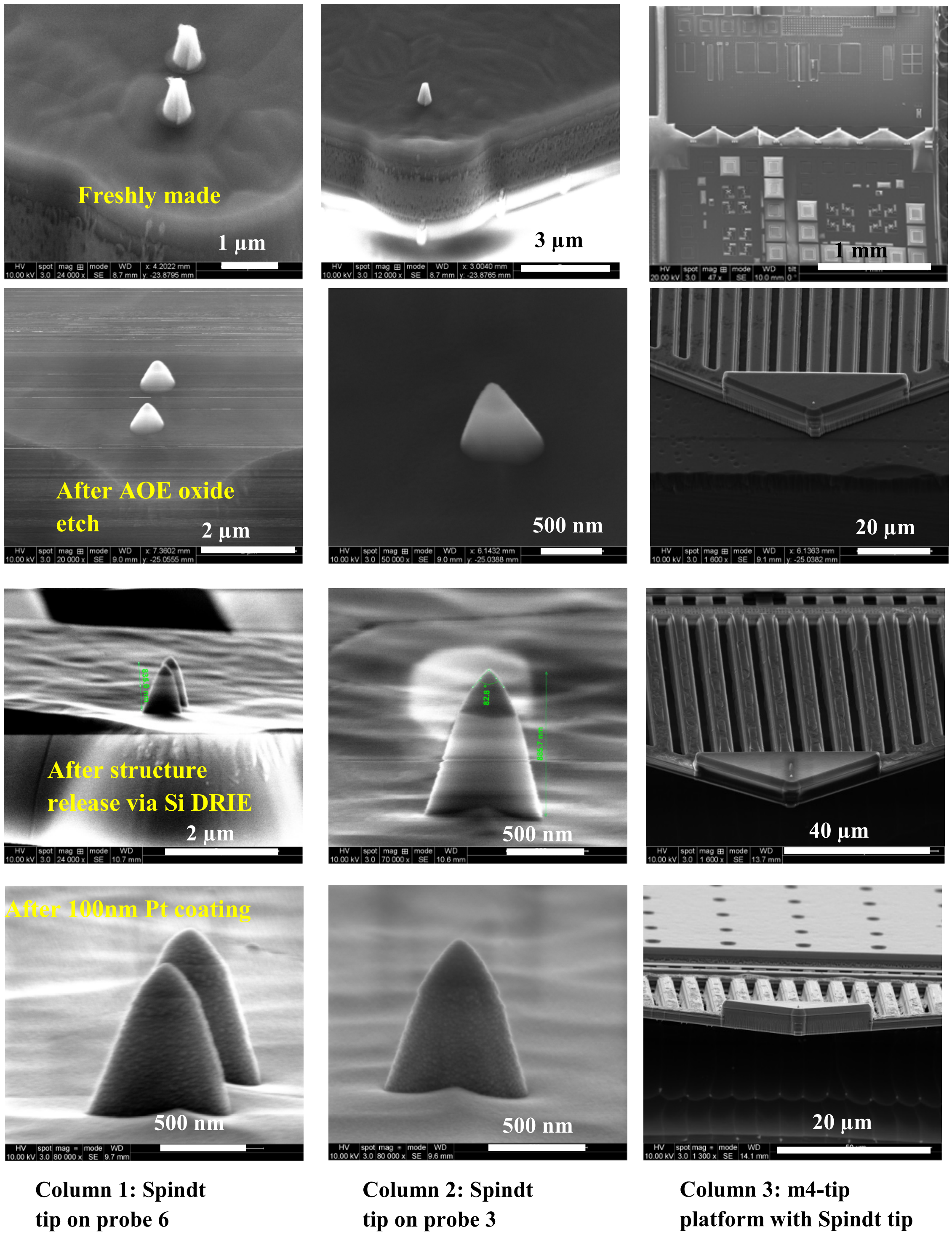

Fig. 3.14 Spindt tips after each step of processing.

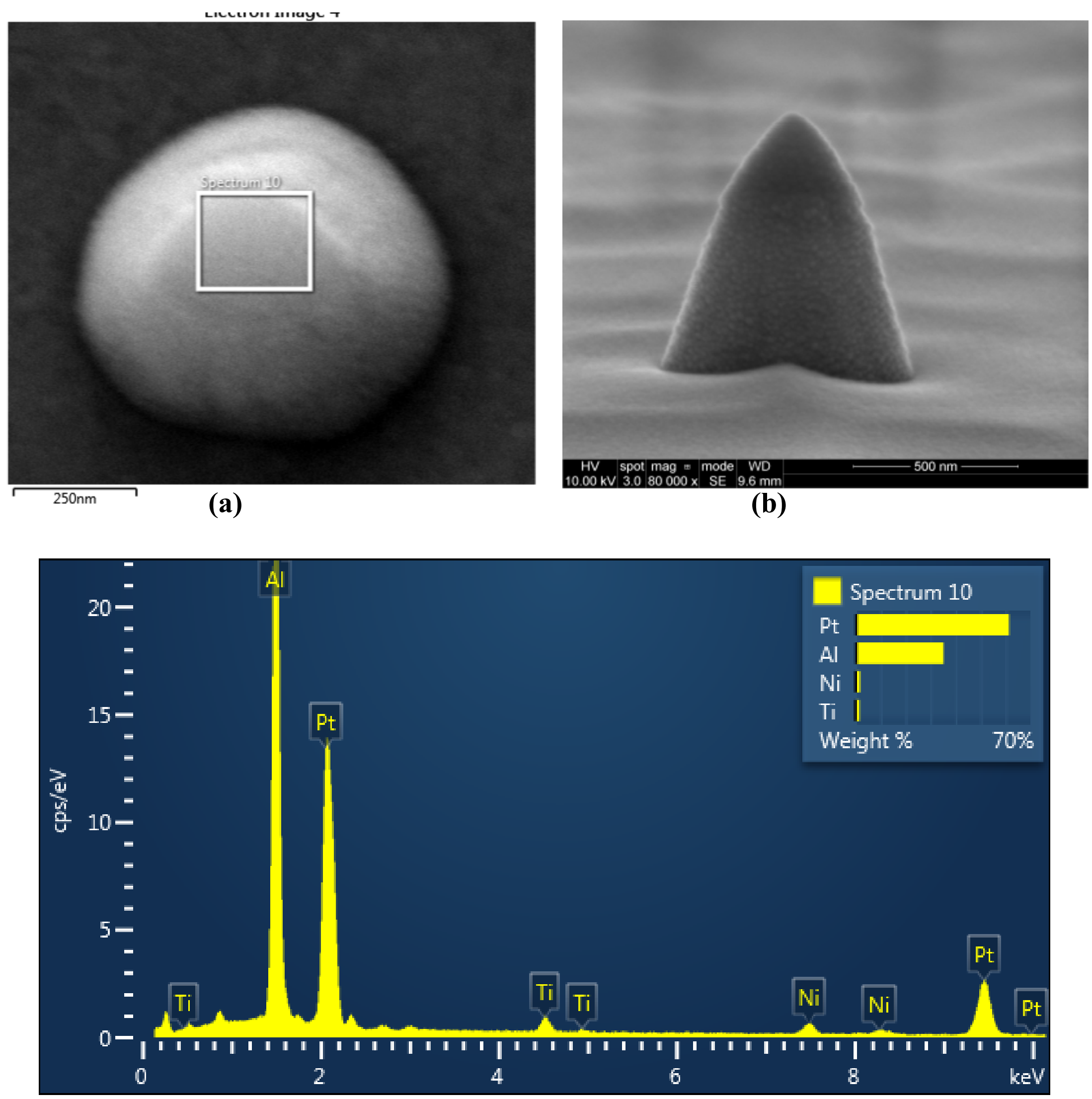

(c)

Fig. 3.15 Element analysis of the Spindt tips via SEM/EDX: (a) Scanning area. (b) Side view. (c) Scanning results.

STM imaging with Spindt tip on CMOS-MEMS probes

STM via CMOS MEMS probe

CMOS MEMS probes with Spindt tips are mounted on a commercial Veeco Dim3000 SPM system, for tip function verification. Fig. 3.16 shows an ambient STM image on the commercial calibration sample with a metal grating period of 278 nm, using a Spindt tip on a CMOS-MEMS probe. The tip before and after STM scanning is shown in Fig. 3.17. The tip was found crashed, with the Pt coating layer spread around the tip locations, but not lost after scanning. This damage is not believed to be because of the scanning itself, but it is very likely that they were damaged due to a misoperation during the manual alignment of the probe chip with the sample. The element analysis on tip platforms are shown Fig. 3.18, where the existence of platinum on the residue confirms that this residue is leftover from the smashed tip.

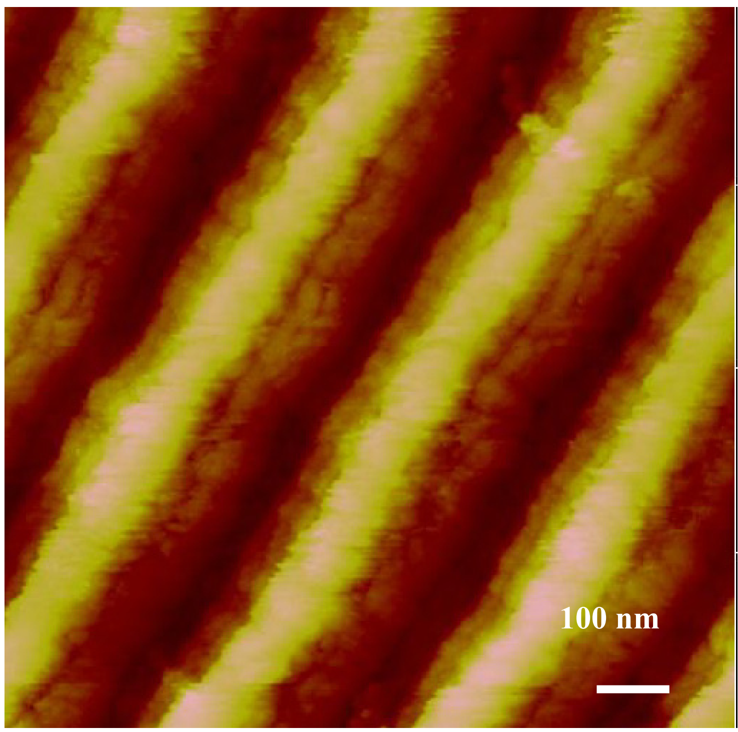

Fig. 3.16 STM images on gold calibration sample using integrated Ni-Pt Spindt tips on CMOS-MEMS probes.

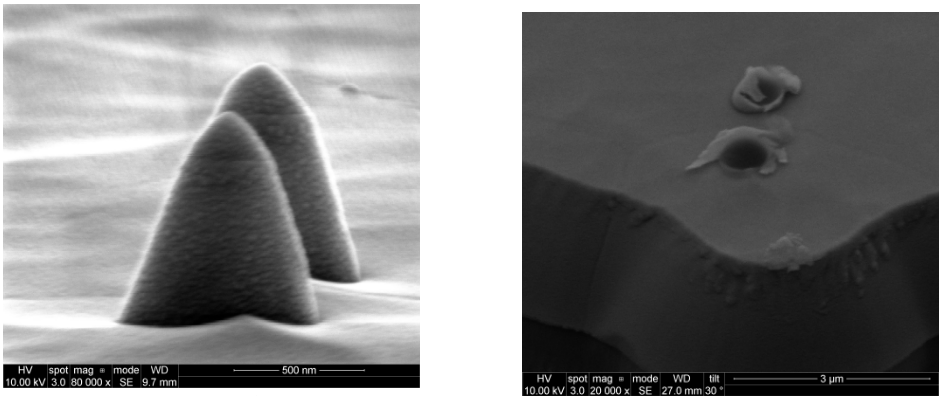

(a) Before scanning **(b)** After scanning

Fig. 3.17 Ni-Pt Spindt tips before and after STM imaging. The tip smashed against the sample is not due to scanning, but is likely due to manual error in chip-sample alignment operation via goniometer.

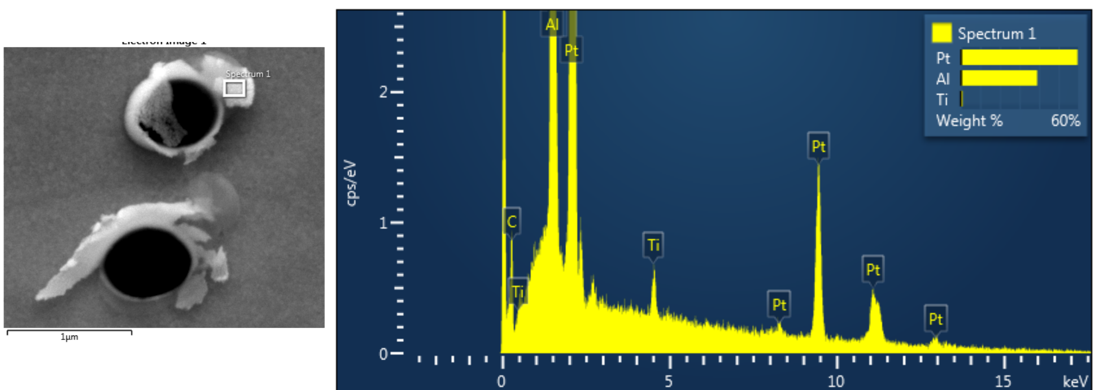

(a) **(b)**

Fig. 3.18 Element analysis of the Spindt tips via SEM/EDX (a) Scanning area, (b) Analysis results.

3.4 EBID tip

EBID intro

EBID is a highly localized and flexible deposition method, though limited to low throughput due to its serial nature. The EBID technique is capable of generating almost any shape of nano-structures by controlled scanning of the beam and has been used in making field-emission tips as well as SPM tips [63].The tip can be fabricated in any step in the processing. Commercialized EBID services are available, such as [64].

EBID process flow

In EBID, a precursor gas is introduced to a sample in the SEM chamber and only those gas molecules adsorbed on the substrate and within or directly around the irradiating coverage of the focused electron beam, with beam diameter of 2 to 5 nm and energy of 5 keV to 20 keV, are decomposed, resulting in the deposition of the non-volatile component and escape of the volatile component so that a nano-sized structure is formed on the irradiated regions of the surface. Fig. 3.19 is a schematic diagram of this process.

EBID resolution

Metalorganic Pt is chosen as the precursor for the STM Pt tip fabrication. In the process, the deposition area and thickness is preset in the EBID software. The resolution of EBID is affected by the vacuum chamber pressure, the size of electron probes, the energy of the electron beam that dissociates the gaseous precursors, and secondary electron emission characteristics that result from the interaction of electron probes with the substrate. The best resolution from EIBD is down to sub-nm [65], which is at least an order of magnitude smaller than the state-of-art photolithography technique.

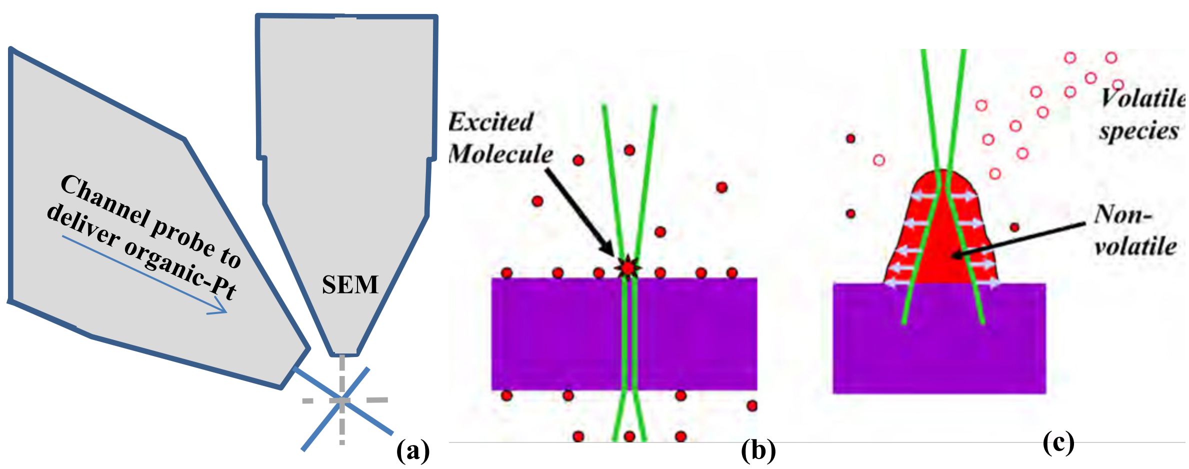

Fig. 3.19 EBID process [63]: (a) The channel probe delivers the organic-Pt compound to the sample surface which electron-beam focuses on. (b) and (c) The sharp tip end is formed when the metalorganic Pt compound is decomposed and the volatile species leave the deposited bulk.

Fig. 3.20 shows the SEM images of STM tips made on a commercial AFM probe via EBID. Fig. 3.21 shows the SEM images of the STM tips made on CMOS chips via EBID, with different e-beam scan areas. Tips with radius down to 10 nm are obtained.

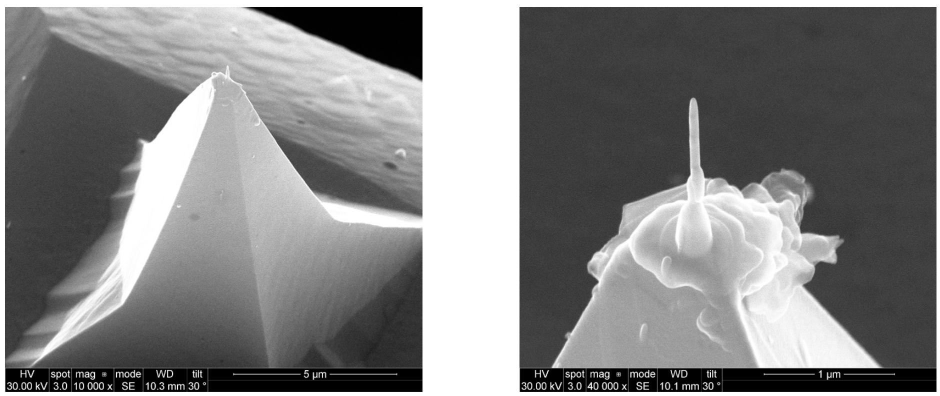

Fig. 3.20 EBID tips made on commercial AFM probe tips. They are capable of STM and AFM imaging task.

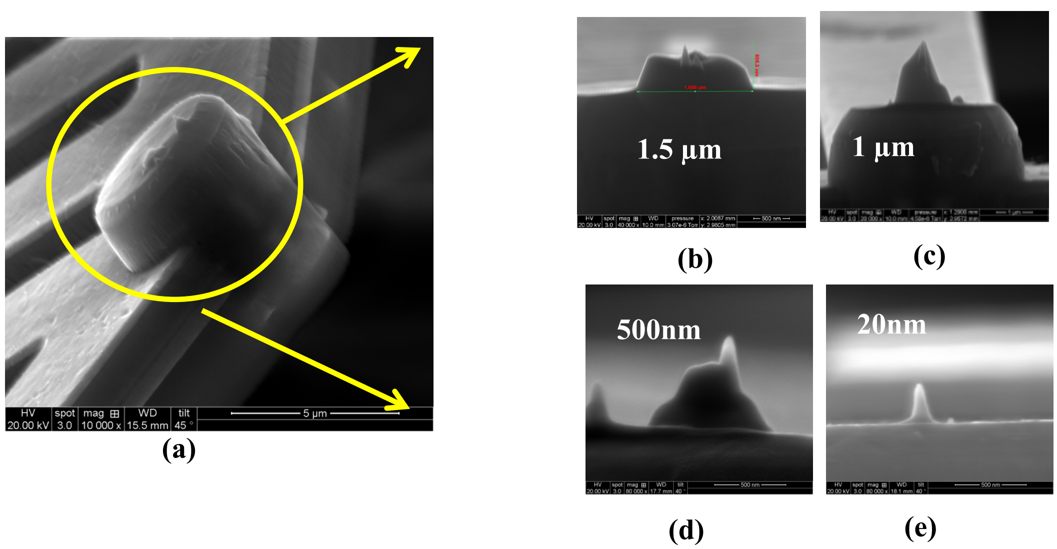

Fig. 3.21 EBID process (a) A metal-4 tip platform with EBID Pt tip on it. (b) to (e) EBID tips with different focused e-beam scan diameters.

High aspect ratio tip via EBID

Some strategies for parameter optimization were applied to obtain very high aspect-ratio SPM tips that can be used for examination of surfaces with high-aspect ratio features [66]. The developed tip shaping process adopts a "layer-by-layer" technique: a circular Pt layer of several μm^2 is first deposited on the CMOS metal-4 tip platform followed by a series of depositions on the same location, each with gradually shrinking e-beam writing area, as illustrated in Fig. 3.22.

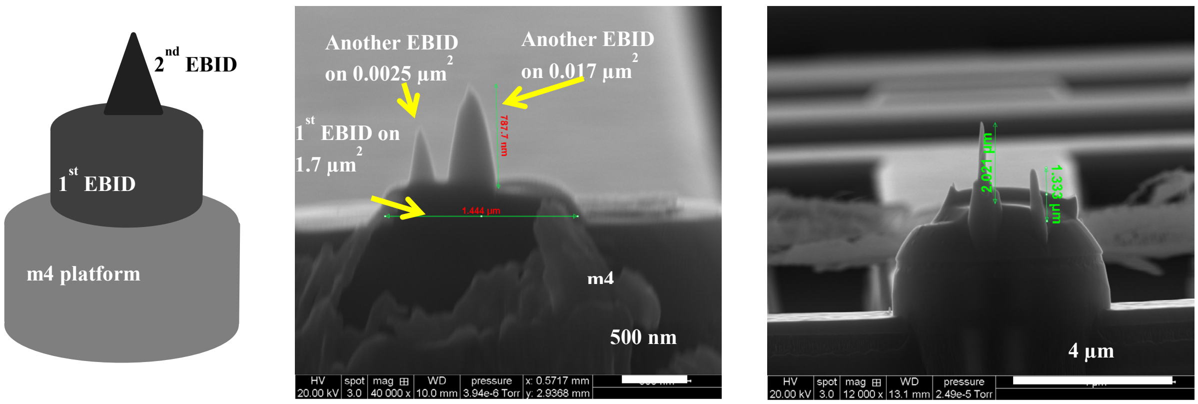

(a) (b) (c)

Fig. 3.22 High aspect ratio tips: (a) Schematic of a "layer by layer" EBID producing high aspect ratio tips; (b) and (c) Pt tips consisting of multi-layers on m-4 platform.

STM via EBID tips

The AFM probe with EBID tips was mounted on a commercial SPM system to verify its functionality. Fig. 3.23 (a) is the STM image of gold sample taken in ambient environment, on a Veeco Dim3000 system, where gold grains are clearly resolved. Fig. 3.23 (b) and Fig. 3.23 (c) were taken in ambient environment on the RHK SPM system. Fig. 3.23 (b) is an STM image of Ti. In Fig. 3.23 (c), a TiO_2 nanowire pattern was directly written on the Ti thin film via energized tunneling current in STM mode. These images are concrete proof that EBID-produced Pt tips are qualified SPM tips for imaging and nanoscale patterning.

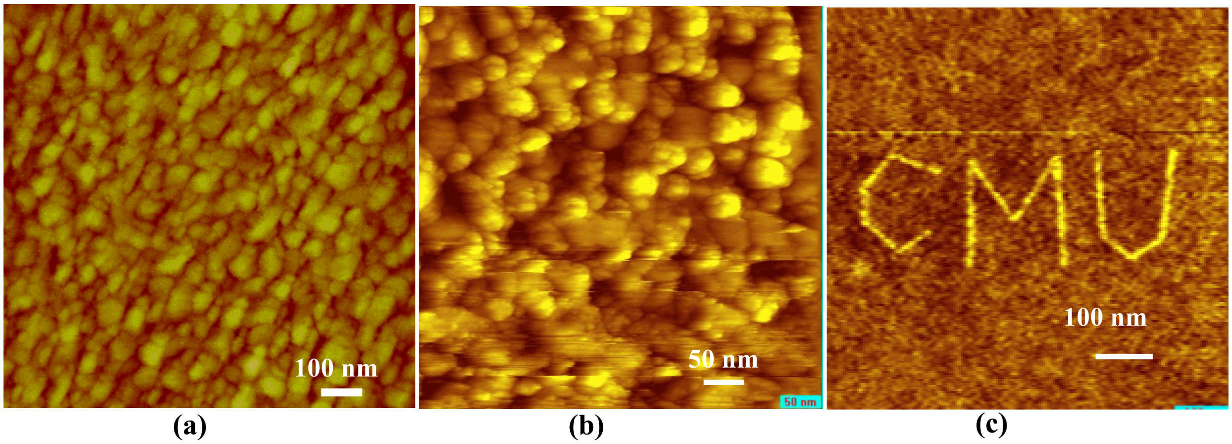

Fig. 3.23 STM imaging and writing using EBID tips on CMOS probes: (a) STM image of gold in environmental STM. Gold grains are well resolved; (b) STM image of titanium in an environmental STM; (c) STM image of a TiO_2 nanowire written on Ti surface. The line width is around 10 nm.

3.5 Summary

Based on the Spindt tip process, a modified tip fabrication process is developed that is compatible with post CMOS MEMS processing technique and enables batch fabrication of STM tips on CMOS MEMS probe arrays. An array of Ni/Pt composite tips were successfully manufactured on an array of CMOS MEMS probes via the modified Spindt process. These Spindt tips demonstrated the capability of performing the STM imaging both in UHV and ambient environment.

In parallel, a serial tip fabrication process based on EBID technique is developed to make Pt tips on CMOS MEMS probes. The EBID tips demonstrated the capability of performing the STM imaging and nanoscale patterning in ambient environment. EBID is a quite flexible and convenient technique and is used to make prototype tips on probe arrays.

Chapter 4 Dual Probe STM System

SPM features low efficiency

Since the invention of Scanning Tunneling Microscopy (STM) in 1982 by Bing and Rohrer, a series of scanning probe microscopy (SPM) techniques have been inspired by the invention and developed. Basically, SPM techniques make use of the interaction between the nano-scale sharp tip and the sample surface to study its local properties. An SPM probe interacts with the material's surface locally, point by point, and therefore provides direct information of material properties at the atomic and nano-scale that leads to an understanding of the material that is different from sample-averaged techniques such as spectroscopy and crystallography. Yet it is also this nature of reliance on localized interaction of SPMs that make it a much slower surface characterization approach than the sample-averaged techniques. It may require a few minutes to scan a few μm^2 area using SPM while it may only take a couple of seconds in an SEM.

Chapter content

Probe arrays are proposed, and developed in this thesis work, to overcome the disadvantage of the intrinsic drawback of slow spatial coverage with SPM. Multiple micro-probes can work in parallel on multiple areas of a surface so the speed of total surface characterization will be multiplied by the number of active probes. In this chapter, the design, construction and implementation of a dual-probe STM system is presented, using the widely-spaced CMOS-MEMS active probe array designed in chapter 2 as the prototype detectors. Section 4.1 reviews the principle of conventional STM. Section 4.2 describes the working principle of the multi-probe STM system, where the probes are equipped with individual feedback of their relative tip-sample position in order to perform the scanning and imaging tasks independently and simultaneously. Section 4.3 presents the stability analysis of STM feedback loops used in the dual-probe array system. Section 4.4 provides details of the design and fabrication of a custom calibration sample that is used in characterization of the dual-probe performance during parallel scanning. Section 4.5 describes the test bench setup and the probe array-sample alignment for the dual-probe system. The dual STM imaging on the custom calibration sample using the dual-probe system is presented in Section 4.6, verifying the functionality of the dual-probe array used for parallel STM operation.

4.1 Review of conventional scanning tunneling microscopy

Current-distance exponential relation in STM

STM is used to study surface topography and electronic structure that relies on the highly localized quantum tunneling between the STM tip and the material surface. When a STM tip is brought within sub-nm proximity to a sample surface, the electron wavefunctions in the tip and the electron wavefunctions in the sample surface overlap. The potential difference, V, between the tip and sample make electrons tunnel through the sub-nm gap and cause an electric current to flow. The tunneling current density is [67]

$$J_{TC} = \frac{e}{4\pi\hbar z^2}\left[2\bar{\phi}exp[-(4\pi z m_e^{0.5}/\hbar)/(2\bar{\phi})^{0.5}] - 2\bar{\phi}exp[-(4\pi z m_e^{0.5}/\hbar)/(2\bar{\phi}+2eV)^{0.5}]\right] \tag{4.1}$$

where $\overline{\phi}$ is the tunneling barrier height between two electrodes. $e = 1.6\times10^{-19}$ C, is the charge of an electron, $\hbar = 1.054\times10^{-34}$ J·s, is the Planck's constant, $m_e = 9.109\times10^{-31}$ Kg, is the mass of an electron, z is the separation between the tip and the surface. The tunneling current is obtained by integrating (4.1). A simplified expression of tunneling current is given by [68]

$$I = \zeta V exp\left(-1.025z\sqrt{\bar{\phi}}\right) \tag{4.2}$$

where ζ is a proportionality constant related to the local density of state at the Fermi level of the material. The tunneling current is exponentially dependent on the tip-sample separation. This exponential relationship makes the tunneling current an excellent indicator for sensing the tip-sample separation.

STM main component

The schematic view of a STM is shown in Fig. 4.1. The main components of a conventional scanning tunneling microscope include a scanning metal tip, a piezoelectric actuator, a scanning unit, a servo for vertical distance control of the tip and a computer for image display. The STM tip is used to sense the tunneling current between the tip and the sample. The tip is mounted on a piezoelectric actuator, which provides the motion of the tip in *x*-, *y*- and *z*-directions. The scanning unit dictates the *x*- and *y*- movement of the piezo actuator. The servo, or the feedback loop, is the core part of the STM system: it controls the motion of the piezo actuator in the *z*- direction. The STM image is constructed based on the *x*-, *y*- and *z*- motion of the tip, and displayed as $z(x, y)$.

STM operation modes

STM systems have two operation modes. The first is “constant height” mode. In constant height mode, the servo keeps the piezo actuator nearly still in the vertical direction and the variation of tunneling current during the tip scanning over the sample surface is recorded and translated to surface topography based on (4.2). The constant height mode can only be applied to a very flat sample surface because surface corrugations higher than about 5 to 10 Å will cause the tip to crash. The second mode is “constant current” mode. In constant current mode, the servo drives the peizo actuator to move up and down to keep the tunneling current nearly constant, and the change in the pizeo drive voltage is recorded and translated to surface topography. All of the STM studies in this thesis employ operation in constant current mode, except where otherwise stated.

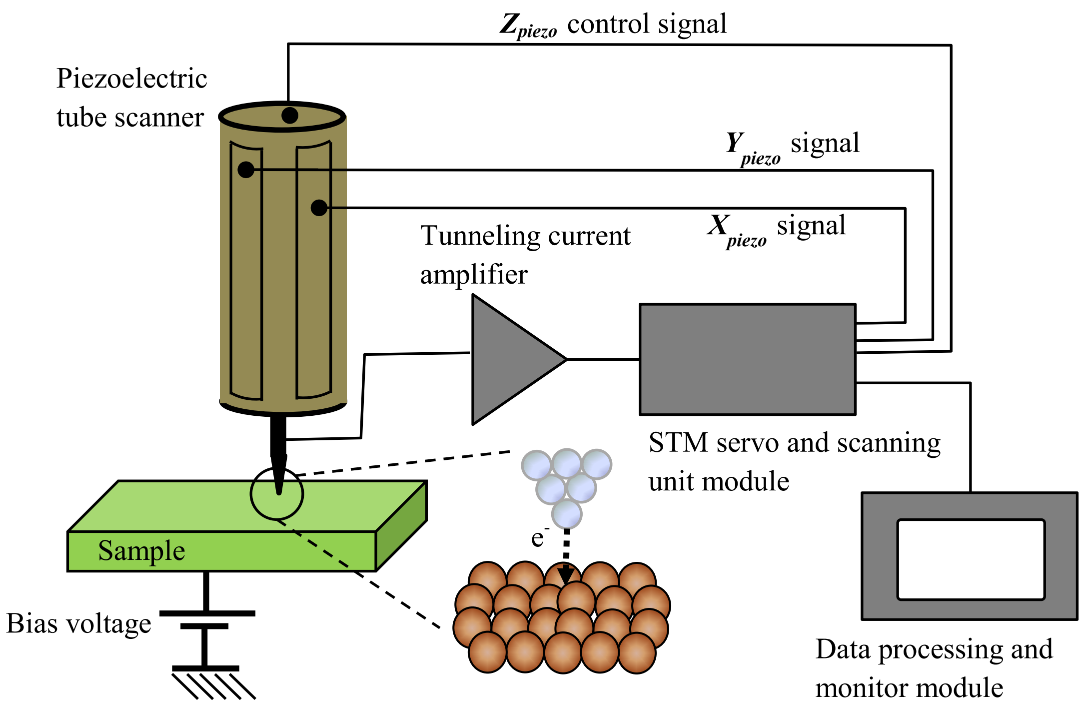

Fig. 4.1 The schematic view of a STM.

4.2 Working principle of dual-probe STM system

Multi servos for multi probes

In a conventional single-probe STM system, only one servo and one drive plant is needed to maintain a constant current between the tip and the sample surface during scanning, and the image is directly extracted from the drive voltage applied on the piezo actuator plant. In a multi-probe STM system, all the array probes need to scan the surface in parallel, each independently maintaining a constant tunneling current with the sample surface. This requires that each array probe should have its own drive plant and servo for a parallel and independent working mode.

System block diagram description

Fig. 4.2 shows a dual-probe array system block diagram that fulfills the task. A hierarchical dual servo system is designed for parallel STM operation with two probes on the chip. The multi-probe array chip is mounted on a piezoelectric actuator scanner head. Each of the array probes is equipped with its own servo. During the system operation, one of the dual probes acts as the "master" probe and is driven by the "master" actuator, which is the piezoelectric actuator in the present setup. The master servo controls the position of the probe chip and thus the master probe relative to the sample, and a constant current is maintained by the master feedback loop. The second, "slave" probe, is actuated by a bimorph electrothermal actuator embedded in the probe cantilever. The slave servo controls the position of the second probe relative to the sample while in the frame of reference of the master servo, and also maintains a constant tunneling current between the slave probe and the sample surface.

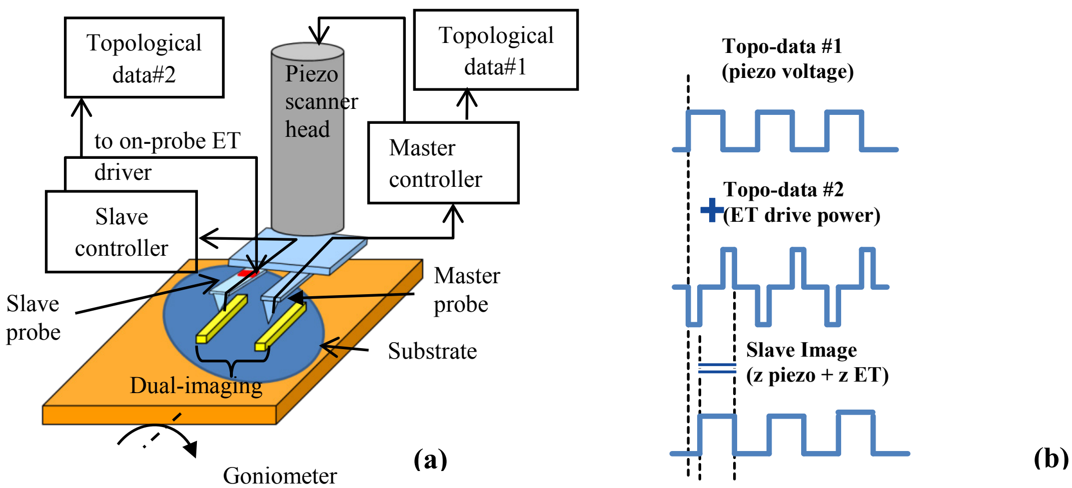

Fig. 4.2 (a) Schematic of master-slave dual probe array system. (b) Slave image constructed by the taking the weighted difference of two drive signals.

Dual image constructio n mechanism

For the image signal extraction, the variation of the drive voltage on the master piezo actuator follows the topography of the scanned area and so is directly converted to construct the image under the master probe. The slave electrothermal actuator has to compensate for not only the topography fluctuation under the slave probe, but also the full chip movement driven by the master actuator. The second image has to be extracted by taking the weighted difference of the master piezo voltage signal and the slave ET power signal to get the actual topography data, as notionally illustrated in Fig. 4.2 (b). In principle, the system can be extended to accommodate more slave probes with corresponding servos.

4.3 Compliant MEMS probe-based STM feedback system

Conventional STM feedback loop

Fig. 4.3 shows a conventional STM feedback loop model diagram. During STM operation, a bias voltage, typically ranging from 100 mV to 1 V, is applied to the sample. The tip is kept at a virtual ground by the current sensing circuit, so the tunneling electrons flow between the tip and the sample. The sensed tunneling current, after being converted to a voltage by a transimpedance amplifier (TIA), is compared with the set-point reference voltage value, V_0. The measured voltage is subtracted from the reference value, and this difference, called the actuating or error signal, is then fed to the controller, which in most cases is a proportional-integral (PI) controller. The controller output voltage is amplified by a high voltage (HV) amplifier and applied to the piezo actuator to drive the STM tip up and down to compensate for the surface height variation, $h(s)$. The tunneling gap is kept constant and a constant tunneling current is maintained. Therefore, the surface topography data can be constructed based on the voltage data that is applied on the piezo actuator. Table 4-1 summarizes the general terms and parameters commonly used in the STM feedback loop.

Cantilever dynamics involved in custom loop

In the conventional STM, an ultra-stiff metal tip is mounted on the piezo scan head and is used as the STM end-effector. In the custom dual-probe STM system, compliant MEMS cantilevers with finite stiffness are used. Compliant MEMS cantilevers are used because on-cantilever actuation mechanism is implemented for individual control of tip movement in the STM probe array. While an ultra-stiff tip will follow the exact movement of the piezo actuator, the displacement of the compliant cantilever will not move in exact synchronization with the actuators, either the piezo actuator or ET actuator, in the dual-probe system. Therefore, the cantilever dynamics must be included in the modeling of the probe feedback loops. In the following two subsections, the custom piezo actuator-driven and ET actuator-driven STM feedback loop models are built and analyzed, respectively, and the stability region of each feedback loop using a PI controller is obtained.

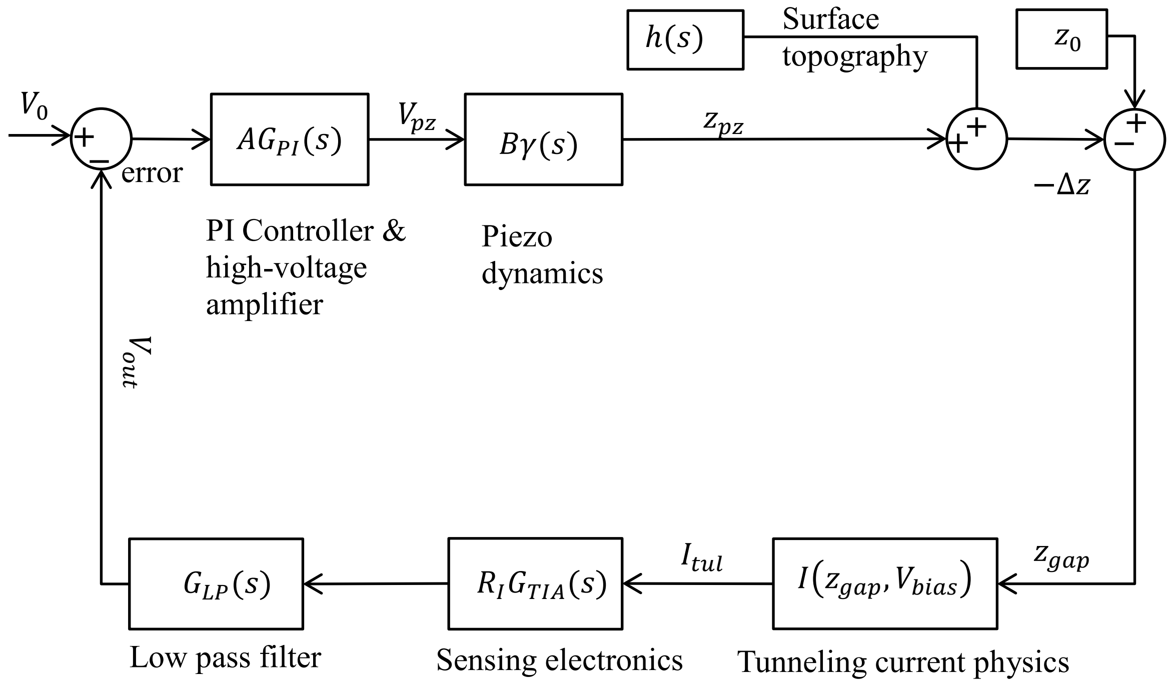

Fig. 4.3 A conventional STM feedback loop using a piezo actuator as the drive plant and an infinitely stiff metal tip as the STM end-effector.

Table 4-1 *General Terms and expressions used in the schematic of a STM feedback loop*

Terms	Description	terms	Description
$G_{TIA}(s)$	Transfer function of TIA	R_I	DC Gain of TIA
$G_{PI}(s)$	Transfer function of PI controller	A	DC Gain of high-voltage amplifier
$\gamma(s)$	Dynamics of the piezo actuator	B	Drive sensitivity of piezo actuator
I_0	Current set-point	V_0	Corresponding voltage set-point
I_{tul}	Actual tunneling current	V_{out}	Voltage output converted from tunneling current via current sensing electronics
$G_{LP}(s)$	Transfer function of low-pass filter	z_0	Equilibrium tip-sample separation @ $I_{tul} = I_0$, or $V_{out} = V_0$
z_{gap}	Actual tip-sample separation	V_{bias}	Tip-sample bias voltage
$h(s)$	Surface topography	$I(z_{gap}, V_{bias})$	Tunneling current physic model
V_{pz}	Pizeo drive voltage	z_{pz}	Pizeo displacement in vertical direction
$F(z_{gap})$	Tip-sample interaction force	k_{sc}	MEMS cantilever spring constant

4.3.1 Feedback Loop of the custom piezo actuator-driven STM system

Interaction force model involved in loop

During the STM operation, a variety of tip-sample interaction forces, discussed in chapter 2, are exerted on the tip when it is only a few angstroms above the sample surface during the scanning. While the interaction force has virtually no effect on a standard infinitely stiff STM tip with axial spring constant of around 10^7 N/m in the conventional STM system, this force will draw compliant CMOS-MEMS cantilevers towards the surface during STM scanning in the custom feedback loop that has a spring constant of 36 N/m. This displacement caused by the tip-sample interaction force contributes to the distance variation between the tip and the sample and so affects the tunneling current. Hence the model of interaction force exerted on the MEMS cantilever, constituting a minor feedback loop, needs to be added to the major STM feedback loop. The cantilever dynamics, $\beta(s)$, is also included. The full piezo actuator-driven feedback loop diagram is shown in Fig. 4.4.

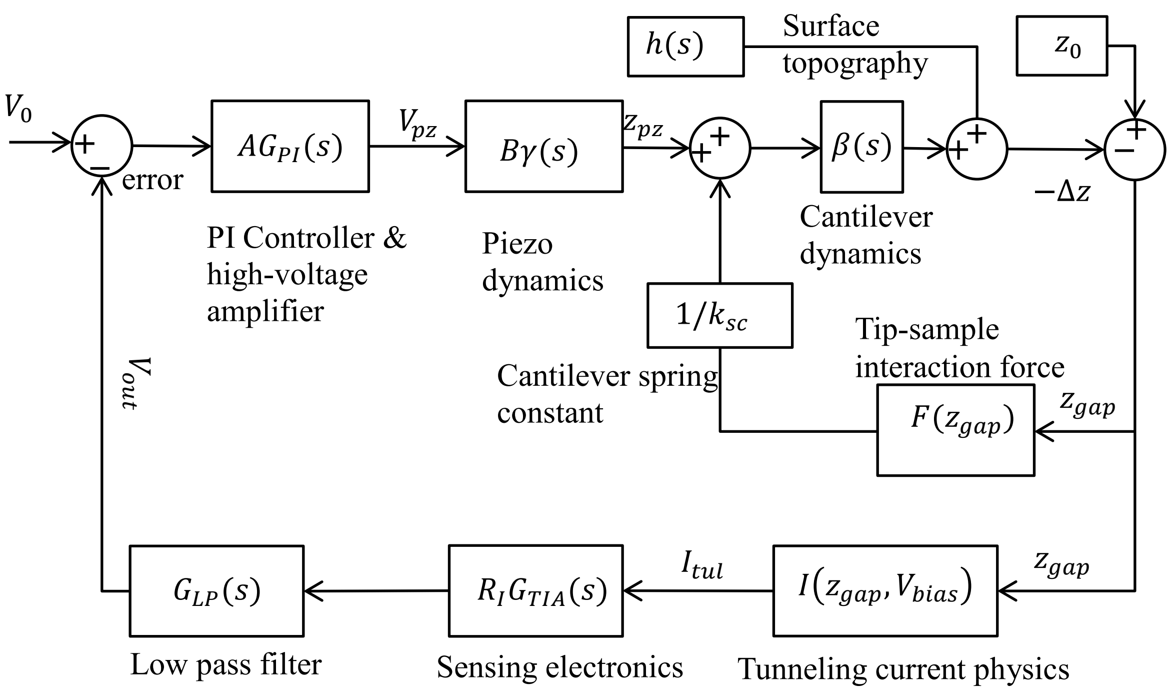

Fig. 4.4 A STM feedback loop using a piezo actuator as the drive plant and using a compliant AFM cantilever as the tip end-effector.

Loop linearization for stability analysis

To carry out the STM feedback loop stability analysis and design the controller for the feedback loop, a linear approximation to the nonlinear system is firstly made. Two nonlinear blocks are identified in the STM feedback loop: one is the tunneling current, which has a highly nonlinear exponential dependence on tip-sample separation and is common to all types of STM systems, and the other is the tip-sample interaction force, which is also nonlinearly dependent on tip-sample separation and is exclusive to the custom STM system where a compliant cantilever is used. Despite these two nonlinearities, the sample surface to be examined using STM is very flat in most scenarios, with surface roughness of only a few nm, so the fluctuation around the current set-point is very small. Therefore, it is reasonable to linearize these two blocks to find out the range of parameters for the controller. Later these parameters can be put in the nonlinear system model for the simulation and numerical verification of the completed design.

Linearization math

Assuming the STM system is working in constant current mode with a fixed bias voltage applied on the sample, the operating point is then defined as point O (z_0, I_0). I_0 is the current set point, the equilibrium point around which the system is linearized. V_0 is the corresponding voltage set point. z_0 is the corresponding equilibrium tip-sample distance that yields I_0. Then small excursions of the tip-sample separation about point O, Δz, will yield small changes in the tunneling current, ΔI, that are related by the slope at point O. Thus, the linearized distance-tunneling current relationship, expressed in its Laplace transform, is

$$I = I_0 + \Delta I(s) = I_0 + \left(\frac{dI}{dz}\right)_{z=z_0} \Delta z(s) \tag{4.3}$$

Similarly, the nonlinear dependence of tip-sample interaction force on the distance can also be linearized about point O, and expressed as

$$F = F_0 + \Delta F(s) = F_0 + \left(\frac{dF}{dz}\right)_{z=z_0} \Delta z(s) = F_0 + (k_{int})_{z=z_0} \Delta z(s) \tag{4.4}$$

where F_0 is the interaction force at the equilibrium point, and k_{int} is the interaction force gradient at point O, which is negative and is given by (2.11).

minor loop reduction

In addition to the linearization of two nonlinear blocks, an extra step is taken to reduce the minor feedback loop introduced by the tip-sample interaction to its equivalent open loop form so as to facilitate the loop analysis. For the minor loop in Fig. 4.4, the actual tip-sample separation, z_{gap}, is given by

$$z_{gap} = z_0 + \Delta z(s) \tag{4.5}$$

and

$$\Delta z(s) = -(h(s) + (\Delta z_{pz}(s) + \frac{\Delta F(s)}{k_{sc}})\beta(s)) \tag{4.6}$$

where $h(s)$ represents the variation of the sample topography and $\Delta z_{pz}(s)$ represents the variation of piezo displacement. The cantilever dynamics are expressed as

$$\beta(s) = \frac{{\omega_{ct}}^2}{s^2 + \frac{\omega_{ct}}{Q_{ct}} s + {\omega_{ct}}^2} = \frac{k_{sc}}{ms^2 + bs + k_{sc}} \tag{4.7}$$

where ω_{ct}, Q_{ct} are the resonance frequency and the quality factor of the MEMS cantilever in air, k_{sc} is the cantilever spring constant, m is the cantilever mass, and b is the damping coefficient. m and b can be derived from measurements using ω_{ct}, Q_{ct} and k_{sc} via

$$m = \frac{k_{sc}}{{\omega_{ct}}^2} \tag{4.8}$$

$$b = \frac{k_{sc}}{\omega_{ct} Q_{ct}} \tag{4.9}$$

Combining (4.4), (4.6) and (4.7) leads to:

$$\Delta z(s) = -(h(s) + \Delta z_{pz}(s) * \beta(s)) * \frac{ms^2 + bs + k_{sc}}{ms^2 + bs + k_{sc} - |k_{int}|} \quad (4.10\text{-a})$$

Let

$$\xi(s) = \frac{ms^2 + bs + k_{sc}}{ms^2 + bs + k_{sc} - |k_{int}|} \quad (4.11)$$

Then

$$\Delta z(s) = -(h(s) + \Delta z_{pz}(s) * \beta(s)) * \xi(s) \quad (4.10\text{-b})$$

Tip-sample interaction on loop expression

The term $\xi(s)$ in (4.11) represents the effect of the tip-sample interaction force on the feedback loop. $\xi(s)$ is equal to one when $k_{sc} \gg |k_{int}|$, *i.e.*, when an ultra-stiff cantilever or simply a standard STM metal tip is used, so the interaction force does not have to be taken into account in the conventional STM feedback loop as described in Fig. 4.3.

Linearized loop

Fig. 4.5 shows the final linearized reduced servo-loop block diagram, where the nonlinear tunneling current and interaction force model are replaced with their linearized counterparts, and the minor feedback loop introduced by the interaction force is replaced with its equivalent open loop form.

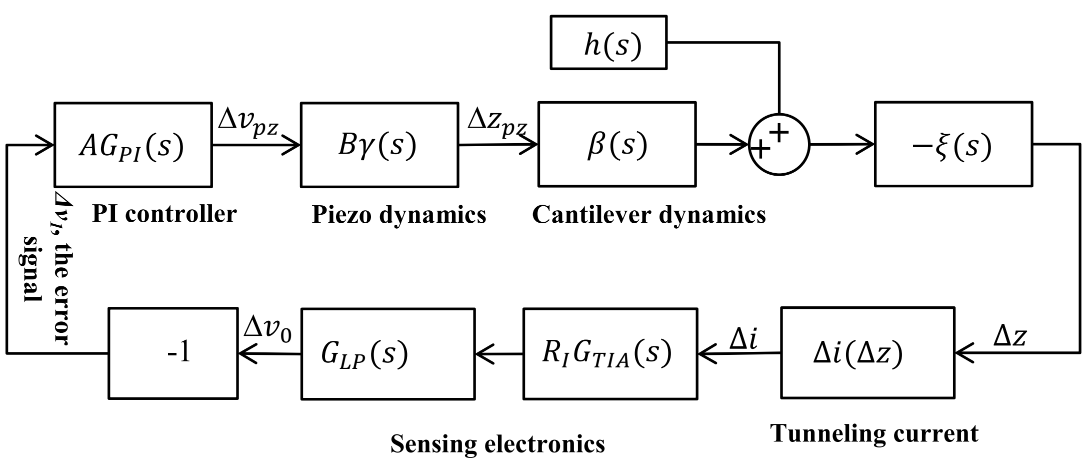

Fig. 4.5 Linearized reduced piezo-driven STM feedback loop using a compliant cantilever as the STM end-effector.

Derive loop transfer function

When the tip scans over the sample surface with a topography expressed by $h(s)$, the tip-sample distance changes and tunneling current changes accordingly in agreement with (4.3). The resultant current signal is then converted to a voltage signal by a TIA with a gain of R_I and a transfer function of $G_{TIA}(s)$, and then passes through a low-pass filter, $G_{LP}(s)$,

$$V = V_0 + \Delta v_0(s) = V_0 + R_I G_{TIA} G_{LP} \left(\frac{dI}{dz}\right)_{z=z_0} \Delta z \tag{4.12-a}$$

where $\Delta v_0(s)$ is the fluctuation in the output voltage signal.

Defining:

$$\alpha = -R_I \left(\frac{dI}{dz}\right)_{z=z_0}$$

Then (4.12-a) can be written as

$$V = V_0 + \Delta v_0(s) = V_0 - \alpha G_{TIA} G_{LP} \Delta z(s) \tag{4.12-b}$$

Next, the converted voltage signal, V, after comparison with the reference voltage set-point, V_0, produces the error signal, $\Delta v_1(s)$

$$\Delta v_1(s) = V_0 - V = -\Delta v_0(\mathrm{s}) \tag{4.12-c}$$

The error signal is fed into the controller and amplified, generating the actuating signal:

$$\Delta v_{pz}(s) = \Delta v_1(A G_{PI}) = \alpha A G_{TIA} G_{LP} G_{PI} \Delta z(s) \tag{4.13}$$

where $G_{PI}(s)$ is the transfer function of the PI controller, and A is the gain of the high voltage amplifier that follows the controller.

The fluctuation in the vertical displacement of the piezo actuator is

$$\Delta z_{pz}(s) = \Delta v_{pz}(s) B \gamma(s) = \alpha A B G_{TIA} G_{LP} G_{PI} \gamma(s) \Delta z(s) \tag{4.14}$$

where B and $\gamma(s)$ are the drive sensitivity and the dynamics of the piezo actuator, respectively.

Substituting (4.14) into (4.10-b) gives

$$\Delta z(s) = -(h(s) + \Delta v_{pz}(s) * B * \gamma(s) * \beta(s)) * \xi(s) \quad (4.10\text{-c})$$

Substituting (4.10-c) into (4.13) and solving for $\Delta z_{pz}(s)$ and $\Delta v_{pz}(s)$ leads to

$$\Delta z_{pz}(s) = -\frac{\alpha AB\gamma(s)\xi(s)G_{TIA}G_{LP}G_{PI}}{1 + \alpha AB\gamma(s)\beta(s)\xi(s)G_{TIA}G_{LP}G_{PI}} h(s) \quad (4.15\text{-a})$$

$$\Delta v_{pz}(s) = -\frac{\alpha AG_{TIA}G_{LP}G_{PI}\xi(s)}{1 + \alpha AB\gamma(s)\beta(s)\xi(s)G_{TIA}G_{LP}G_{PI}} h(s) \quad (4.15\text{-b})$$

Let

$$G_{pz}(s) = \alpha ABG_{TIA}G_{LP}G_{PI}\gamma(s)\beta(s)\xi(s) \quad (4.16)$$

then

$$T_{pz}(s) = \frac{\Delta z_{pz}(s)}{h(s)} = -\frac{G_{pz}(s)}{1 + G_{pz}(s)} = -\frac{\alpha ABG_{TIA}G_{LP}G_{PI}\gamma(s)\beta(s)\xi(s)}{1 + \alpha ABG_{TIA}G_{LP}G_{PI}\gamma(s)\beta(s)\xi(s)} \quad (4.17)$$

Close loop transfer function

$T_{pz}(s)$ is the closed-loop transfer function of the system. It is evident from (4.17) that the vertical displacement of the piezo actuator is following the sample surface topography with an opposite sign. It is justified that the surface topography is constructed from the piezo actuator displacement that is linearly dependent on the piezo drive voltage.

Cantilever stiffness requirement from a viewpoint of loop stability

As it can be seen from the linearized loop diagram, when the interaction force gradient was larger than the cantilever spring constant, a positive pole would be introduced in the loop and thus the loop becomes unstable. This is consistent with the conclusion in chapter 2 that the cantilever stiffness must be designed larger than the gradient of the interaction force to ensure system stability.

Open loop transfer function to determine system stability

For convenience, Table 4-2 summarizes the transfer functions used in the STM feedback loop, and Table 4-3 gives the values of the parameters used in the transfer functions. To study the feedback loop stability, the loop gain, (*i.e.*, the open-loop transfer function $G_{pz}(s)$ and is given by (4.16)) must be considered. For $T_{pz}(s)$ to be stable, the gain margin, G_M, has to be greater than zero. Systems with greater gain margins are more robust and can withstand greater changes in system parameters before becoming unstable. As a rule of thumb, for satisfactory STM performance the gain margin should be larger than 3 dB [69].

Obtaining stability region using PI controller

In the expression of $G_{pz}(s)$, $G_{PI}(s)$ is the transfer function of the PI controller that is to be designed. The transfer function of the PI controller is given in (4.18), where K_p is the proportional gain and K_I is the integral gain. During the scanning, the PI controller is the main functional block that can be *in-situ* adjusted to achieve a stable system. Because the tunneling barrier height, $\overline{\phi}$, determined by the specific type of tip and the sample and their surface conditions, is different in any specific STM characterization [70, 71], this *in-situ* adjustment capability of the PI controller is required to accommodate this uncertainty. To find the range of K_p and K_I to give a gain margin greater than zero to maintain a stable system, the value of K_I is swept and the value of K_p is found out with the aid of programming in the Matlab. The Matlab program script is listed in Appendix C.1. Other transfer functions and parameters in the feedback loop are kept unchanged during the simulation.

$$G_{PI} = K_p + \frac{K_I}{s} = K_p\left[1 + \frac{K_I/K_p}{s}\right] \tag{4.18}$$

Fig. 4.6 shows a series of $K_p - K_I$ curves at different tunneling barrier heights between the tip and the sample. The $K_p - K_I$ curve defines the region over which the system maintains stability. Any combination of (K_p, K_I) under the curve will make the system stable. An increasing tunnel barrier height gives a smaller stability region for the feedback loop, which can be accounted for by the larger slope of $I(z)$ at the equilibrium operating point, as shown in Fig. 4.7. The rate of change of tunneling current with tip-sample separation when the tunneling barrier height is 4 eV is twice as large as that at 1 eV.

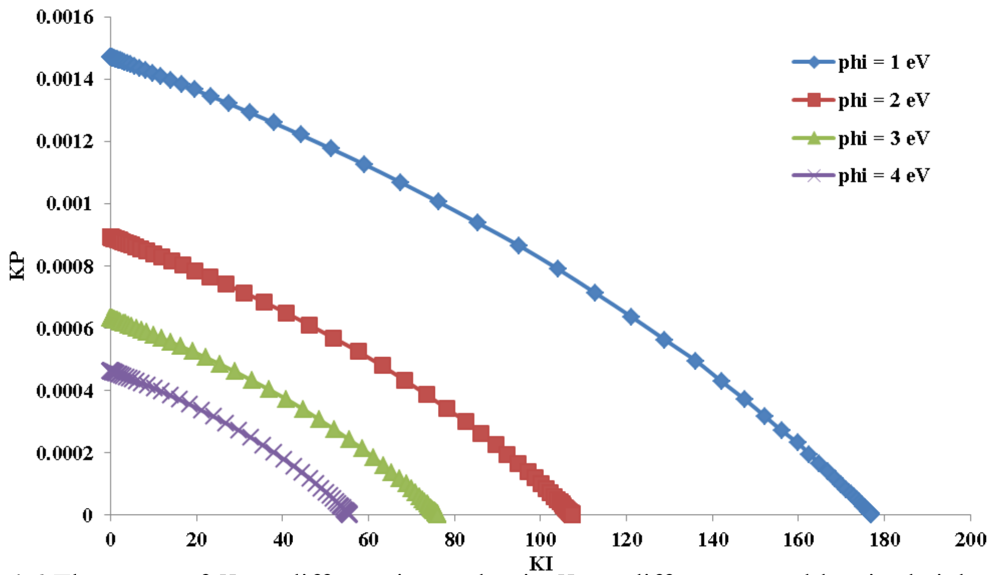

Fig. 4.6 The range of K_p at different integral gain K_I, at different tunnel barrier heights, for a piezo actuator driven STM system.

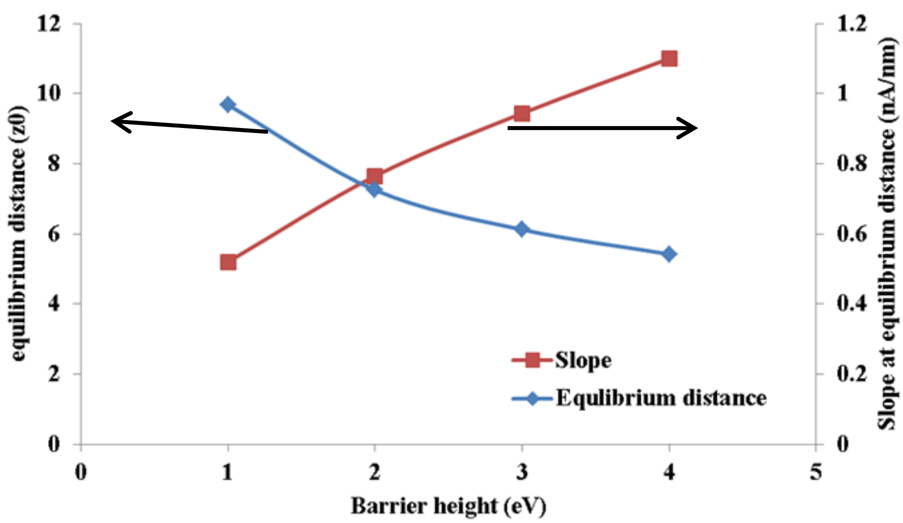

Fig. 4.7 Theoretical tip-sample distance and the (dI/dz) at the equilibrium point for different tunnel barrier height. The current set point is 0.5 nA.

Simulink model of the nonlinear system

The design of the PI controller is based on a linear approximation of the STM feedback loop. A full nonlinear simulation model of the STM feedback loop is built in MATLAB Simulink to evaluate the design. The model diagram is shown in Appendix C.2. Fig. 4.8 shows a representative simulated displacement of the piezo scanner when the tip is scanning across a virtual topography line. The virtual topography is a sinusoidal wave with a frequency of 100 Hz and peak-to peak amplitude of 0.5 nm. It can be seen from the curve that the piezo scanner tracks the topology variation of the virtual line. Given the characteristic interatomic distance of 5 Å of silicon, then a maximum scan rate of 50 nm/s can be achieved without losing the track of the atomic topology.

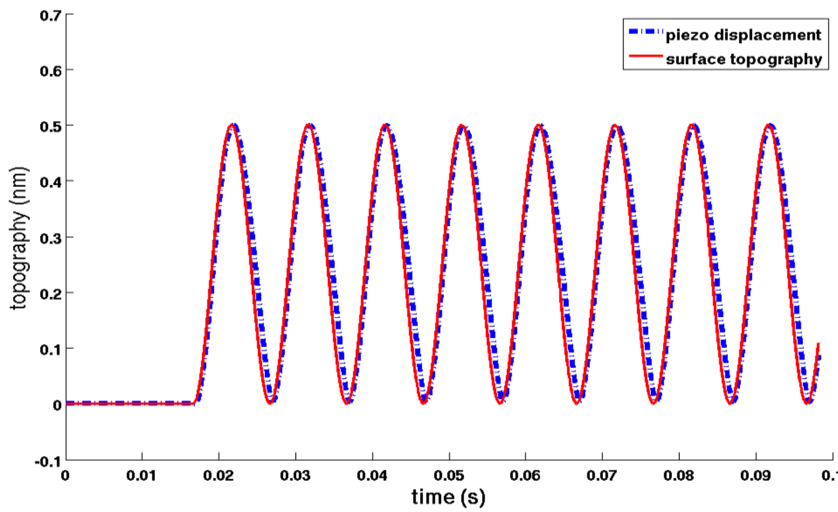

Fig. 4.8 A representative simulated piezo scanner displacement in a STM line scan. The current set point is 0.5 nA, the tunnel barrier height is 3 eV. $K_p = 1.1\times10^{-4}$, $K_I = 14.94$.

Experimental test

The $K_p - K_I$ curve that is obtained through the analysis of the linearized STM feedback loop and defines the stability working region is used to guide the parameter adjustment of the PI controller in the actual STM operation. The PID loop functional block embedded in HF2Li Lock-in Amplifier (Zurich Instruments, AG Switzerland) implements the PI controller in the feedback loop. The CMOS MEMS cantilever with an EBID Pt tip is used as the STM end-effector and the sample is an evaporated gold thin film on Si substrate. The piezo tube in the Veeco Dim3000 system is used as the piezo actuator drive plant. The scan area is limited to 1 nm.

Fig.4.9 shows a representative measured tunneling current where the current set-point toggles between 500 pA and 1 nA. The STM servo follows the current variation.

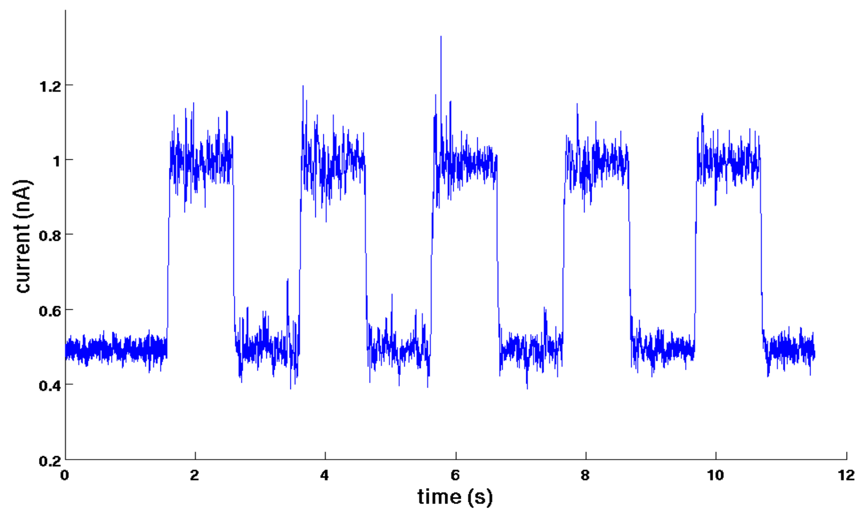

Fig. 4.9 A representative measured tunneling current in a piezo-actuator driven STM system. The current set point toggles between 500 pA and 1nA.. $K_p = 6\times10^{-3}$, $K_I = 85$.

It is found that a constant current is maintained when K_I is increased up to 160, which exceeds the stability region obtained using the theoretical tunnel height of 4 eV between the Pt and Au. It indicates that the actual tunnel barrier height must be well below the theoretical value. This agrees with the fact that the tunnel barrier height between the STM tip and the examined sample surface is much lower than the theoretical value when operated in the air where they have a high chance of being contaminated [37, 59]. Cleaning of the tip and the sample surface may be applied to remove these contaminants and a larger tunnel barrier height can be obtained. In this thesis, no tip or sample cleaning is performed, which, however, can be part of the future work. Nevertheless, it is validated that our custom STM system is able to be stabilized through the parameter adjustment of the PI controller in order to perform the STM imaging task.

4.3.2 Feedback loop of the custom ET actuator-driven STM system

Slave feedback loop

The slave MEMS probe in the dual STM system uses the ET actuator embedded in the cantilever to drive the vertical movement of the probe. Fig. 4.10 shows the STM feedback loop model where the ET actuator replaces the piezo actuator as the drive plant. The transfer function of the ET actuator is given by (2.20), and is also summarized in Table 4-2. In the STM application, the probe needs to be able to move up and down to cover the surface topography. Since the vertical movement range of the ET actuator is unidirectional, its position is centered in its travel range by a pre-actuation bias voltage, V_{ET0}. This arrangement provides room for voltage control of both upward and downward displacement, as shown in the loop diagram.

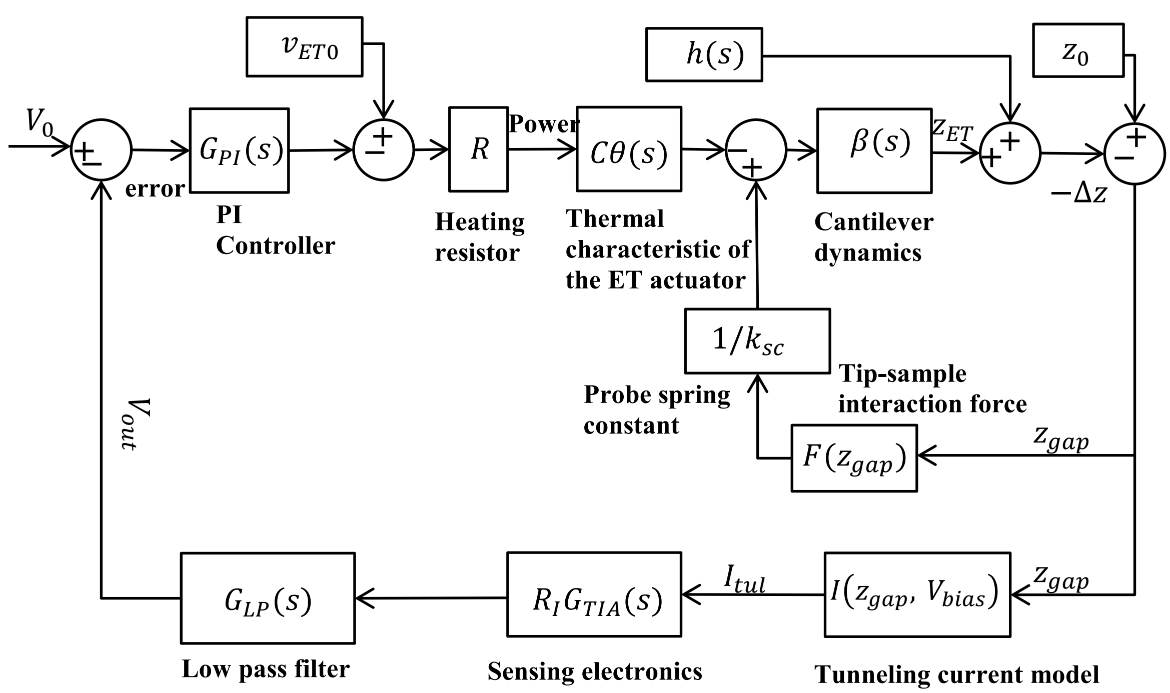

Fig. 4.10 STM feedback loop using the ET actuator as the drive plant and a compliant AFM cantilever as the tip end-effector.

Linearization math

While the displacement of the cantilever tip is linearly dependent on the ET drive power, the ET drive power is given by

$$P_{ET} = \frac{{V_{ET}}^2}{R_{ET}} \tag{4.19}$$

and has a nonlinear dependence on the drive voltage, V_{ET}, applied on the heating resistor, R_{ET}.

For the system stability analysis, this third nonlinear $P_{ET} - V_{ET}$ relationship is also linearized following the procedures presented in 4.3.1. Assume the STM system is operating at point O (z_0, I_0). The nonlinear dependence on the drive voltage of ET power can be linearized about point O, and expressed as

$$P_{ET} = P_{ET0} + \Delta P_{ET}(s) = P_{ET0} + \left(\frac{dP_{ET}}{dV_{ET}}\right)_{V_{ET}=V_{ET0}} \Delta v_{ET}(s) \tag{4.20}$$

where P_{ET0} and V_{ET0} are the drive power and the drive voltage at the equilibrium operation point. Define

$$\varsigma = \left(\frac{dP_{ET}}{dV_{ET}}\right)_{V_{ET}=V_{ET0}} = \frac{2V_{ET0}}{R}$$

Then

$$\Delta P_{ET}(s) = \left(\frac{dP_{ET}}{dV_{ET}}\right)_{V_{ET}=V_{ET0}} \Delta v_{ET}(s) = \varsigma \Delta v_{ET}(s)$$

Fig. 4.11 shows the linearized reduced feedback loop block diagram of the ET actuator driven STM system, where the nonlinear voltage dependence of the drive power is replaced with its linearized counterparts. The open-loop transfer function of the system, $G_{ET}(s)$, is represented as

$$G_{ET}(s) = \alpha\varsigma C\vartheta(s)\beta(s)\xi(s)G_{TIA}G_{LP}G_{PI} \tag{4.21}$$

The relation of the variation of the ET actuation power and the cantilever tip displacement with the sample topography are, respectively,

$$\Delta z_{ET}(s) = -\frac{\alpha\varsigma C\vartheta(s)\beta(s)\xi(s)G_{TIA}G_{LP}G_{PI}}{1+\alpha\varsigma C\vartheta(s)\beta(s)\xi(s)G_{TIA}G_{LP}G_{PI}}h(s) \tag{4.22-a}$$

$$\Delta P_{ET}(s) = \frac{\alpha\varsigma\xi(s)G_{TIA}G_{LP}G_{PI}}{1+\alpha\varsigma C\vartheta(s)\beta(s)\xi(s)G_{TIA}G_{LP}G_{PI}}h(s) \tag{4.22-b}$$

The closed-loop transfer function of the system, $T_{ET}(s)$, is

$$T_{ET}(s) = -\frac{\Delta z_{ET}(s)}{h(s)} = -\frac{G_{ET}(s)}{1+G_{ET}(s)} = -\frac{\alpha\varsigma C\vartheta(s)\beta(s)\xi(s)G_{TIA}G_{LP}G_{PI}}{1+\alpha AB\gamma(s)\beta(s)\xi(s)G_{TIA}G_{LP}G_{PI}} \tag{4.23}$$

Similar to the closed-loop transfer function of the piezo actuator driven STM system, the vertical displacement of the ET actuator is following the sample surface topography with opposite sign, so it is justified that the surface topography is constructed from the ET actuator displacement that is linearly dependent on the ET drive power.

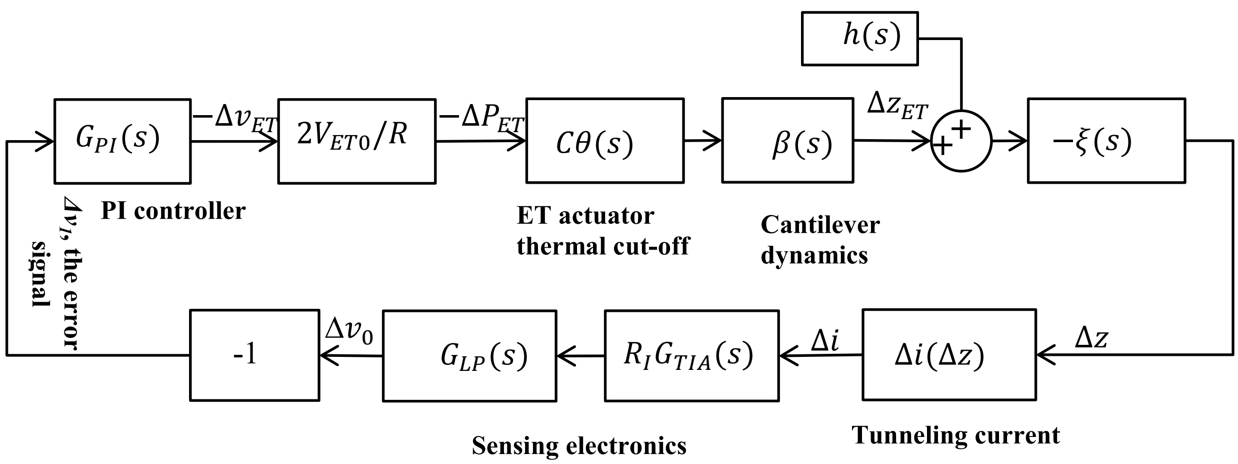

Fig. 4.11 Linearized reduced ET actuator-driven STM feedback loop using a compliant cantilever as the STM end-effector.

Obtain stability region using a PI controller

For the PI controller design of an ET actuator driven STM system, the value of integral gain, K_I, is swept and the range of proportional gain, K_p is found for maintaining the system stability. Fig. 4.12 shows a series of $K_p - K_I$ curves at different tunneling barrier heights between the tip and the sample. The $K_p - K_I$ curve defines the region over which the system maintains stable. Fig. 4.13 shows a root locus of the system showing the evolution of the closed loop poles with K_p at a fixed integral gain, $K_I = 347$. The closed-loop system is stable when $0.031<K_p<0.257$. This is unlike the stability region of a piezo actuator driven system, where there is only an upper limit of K_p at a given value of K_I. A full nonlinear simulation model of the STM feedback loop is built in MATLAB Simulink to evaluate the design. Fig. 4.14 shows a representative simulated displacement of the ET driven STM tip when it is scanning across a virtual line. It can be seen from the curve that the ET driven tip basically tracks the height variation of the virtual line.

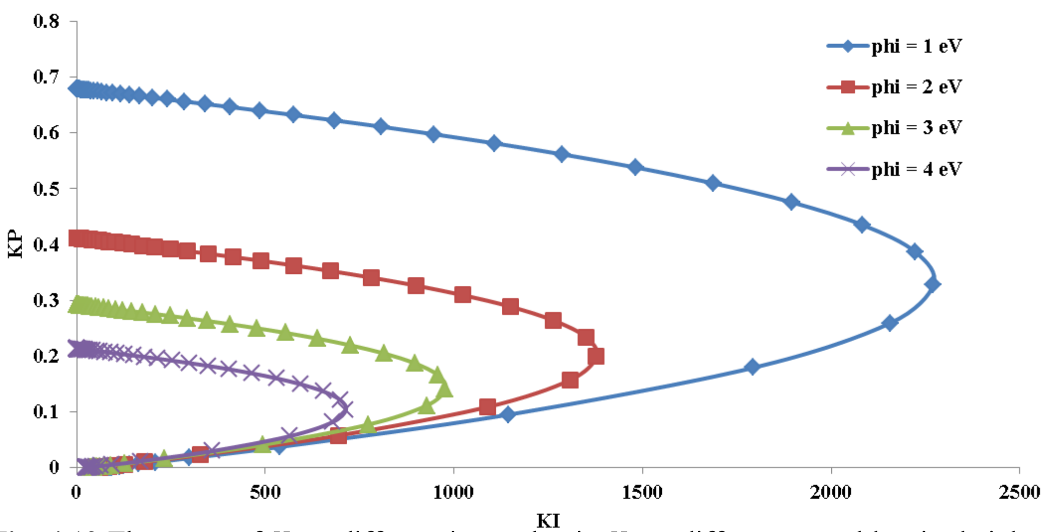

Fig. 4.12 The range of K_p at different integral gain K_I, at different tunnel barrier height, for a nET actuator driven STM system.

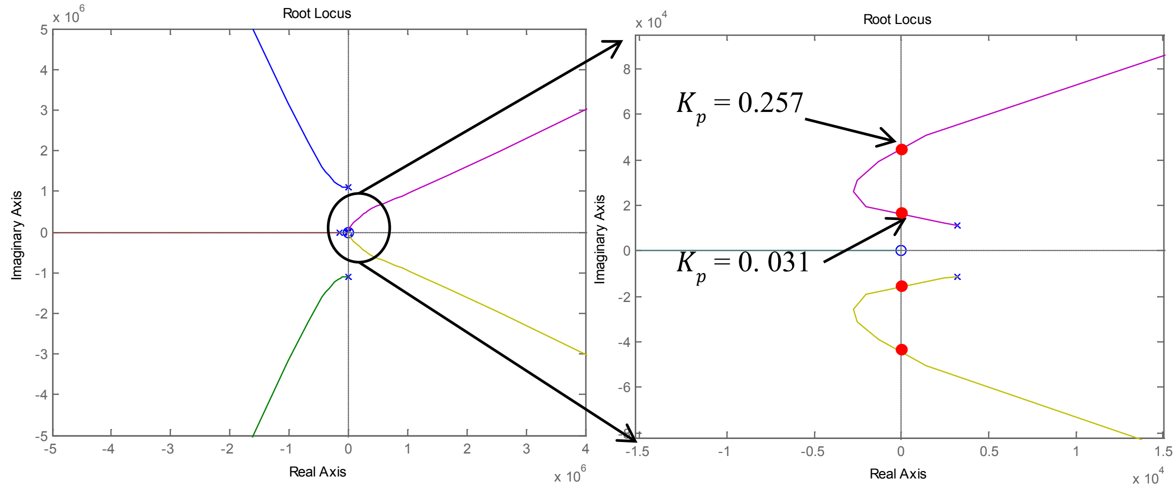

Fig. 4.13 A typical root locus showing the range of K_p to maintain system stability at a fixed $K_I = 347$ in an ET actuator driven STM system. The tunnel barrier height is 3 eV.

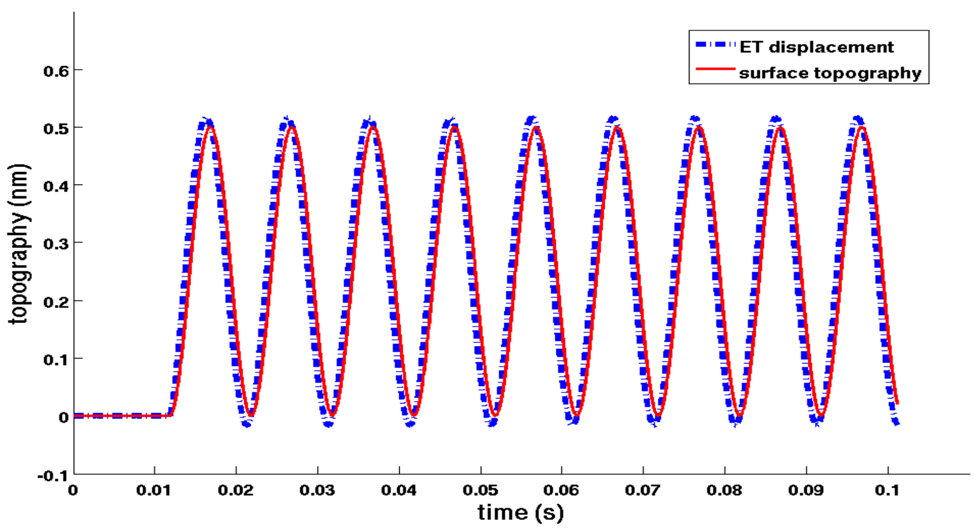

Fig. 4.14 A representative simulated ET actuator displacement in a STM line scan. The current set point is 0.5 nA, the tunnel barrier height is 3 eV. $K_p = 0.01$, $K_I = 100$

The obtained system stability region will be used as a guidance of parameter adjustment in the actual experiment. Construction of an independently running ET actuator-driven STM servo system will be part of future work to fully characterize the performance of the MEMS ET actuator as a plant in the STM feedback loop.

Table 4-2 *Transfer functions used in feedback loop stability analysis*

	Transfer function	Description
G_{TIA}	$G_{TIA} = \frac{\omega_{TIA}}{s + \omega_{TIA}}$	Transfer function of TIA
G_{LP}	$G_{LP} = \frac{\omega_{LP}}{s + \omega_{LP}}$	Transfer function of low-pass filter
G_{PI}	$G_{PI} = K_p + \frac{K_I}{s}$	Transfer function of PI controller
$\gamma(s)$	$\gamma(s) = \frac{{\omega_1}^2}{s^2 + \frac{\omega_1}{Q_1}s + {\omega_1}^2}$	Dynamics of the piezo actuator
$\beta(s)$	$\beta(s) = \frac{{\omega_2}^2}{s^2 + \frac{\omega_2}{Q_2}s + {\omega_2}^2}$	Dynamics of the MEMS cantilever
$\xi(s)$	$\xi(s) = \frac{ms^2 + bs + k_{sc}}{ms^2 + bs + k_{sc} - \lvert k_{int} \rvert}$	Represent Effect of tip-sample interaction force
$\vartheta(s)$	$\vartheta(s) = \frac{\omega_{ET}}{s + \omega_{ET}}$	Represent the thermal characteristics of the ET actuator

Table 4-3 *Parameters used in feedback loop simulation and stability analysis*

Parameters	Value	Description
ω_1	5.5 kHz	Resonance of the piezo actuator
Q_1	20	Quality factor of the piezo actuator
ω_2	206 kHz	Resonance of the MEMS cantilever
Q_2	180	Quality factor of the MEMS cantilever
ω_{TIA}	25 kHz	Bandwidth of the TIA
ω_{LP}	2 kHz	Bandwidth of the low-pass filter
α	0.5 V/nm ~ 1.1 V/nm	TIA output voltage change per nm change of z
A	10	Gain of the high voltage amplifier
B	17 nm/V	Drive sensitivity of the piezo actuator
C	131 nm/mW	Drive sensitivity of the ET actuator
V_{ET0}	5 V	Preset voltage of the ET actuator
R_{ET}	4.6 kΩ	Resistance value of the heating resistor
k_{sc}	36 N/m	Spring constant of the CMOS MEMS cantilever

4.4 Calibration sample fabrication

Custom sample design

To demonstrate the parallel scanning of the piezo actuator-driven probe and the ET actuator-driven probe of the dual-probe STM system, a custom calibration sample is made. Fig. 4.15 shows the schematic of the design of the custom calibration sample. A series of grating patterns with different orientations and periods are fabricated on the sample. The spacing between two neighboring gratings is set equal to that of two neighboring probes in the probe array. During the dual-probe STM imaging, one of the working probes can be made to land on an area bearing one type of pattern. The second probe will automatically scan on an area bearing a different type of pattern if it is directly adjacent to the first probe, or it will land on an area with no grating patterns if it is not next to the first probe. In both scenarios, two distinguishable topography images under different probes will be obtained in the parallel scanning of the dual probe system.

Process details of custom calibration sample

Fig. 4.16 shows the process of fabricating the calibration sample. The process starts with a 1" plain silicon wafer. 200 nm-thick 950 PMMA A4 e-beam resist is spun on the wafer. The gratings designed in NPGS software (JC Nabity Nanometer Pattern Generation system) is patterned on the resist via e-beam lithography in SEM. Next the periodic grating patterns in PMMA is transferred to the Si substrate via anisotropic etch in a Plasma-Therm 790 RIE system. After washing off the PMMA resist, a 5 nm-thick gold layer is deposited on the Si wafer via e-beam evaporation.

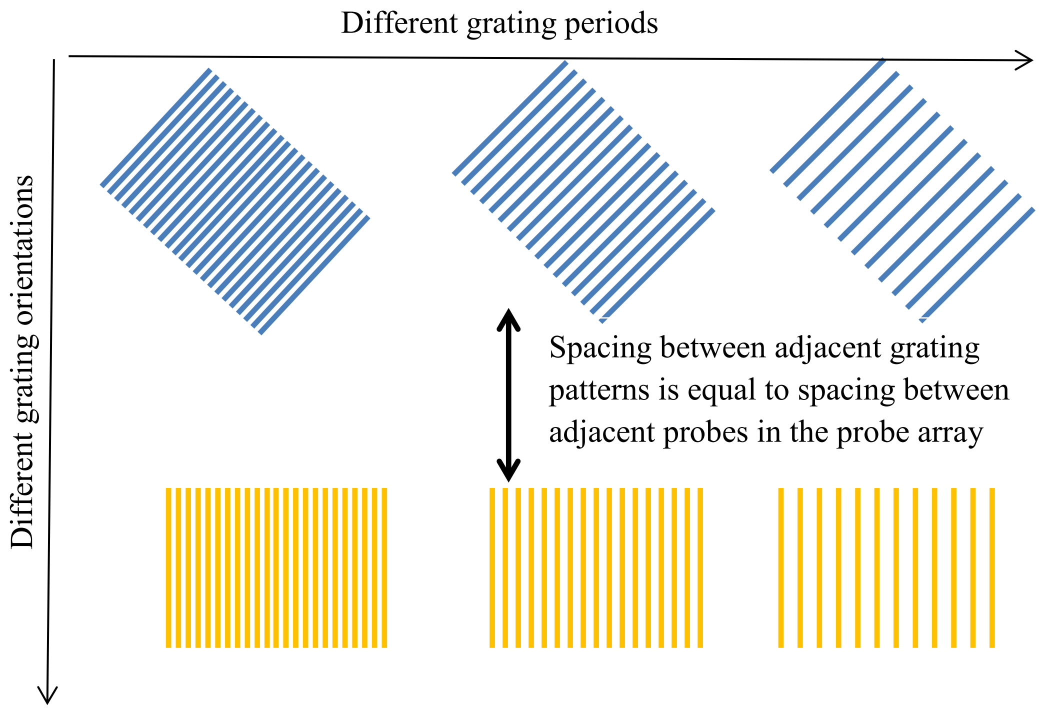

Fig. 4.15 Schematic of grating design on custom STM calibration sample for dual probe array system

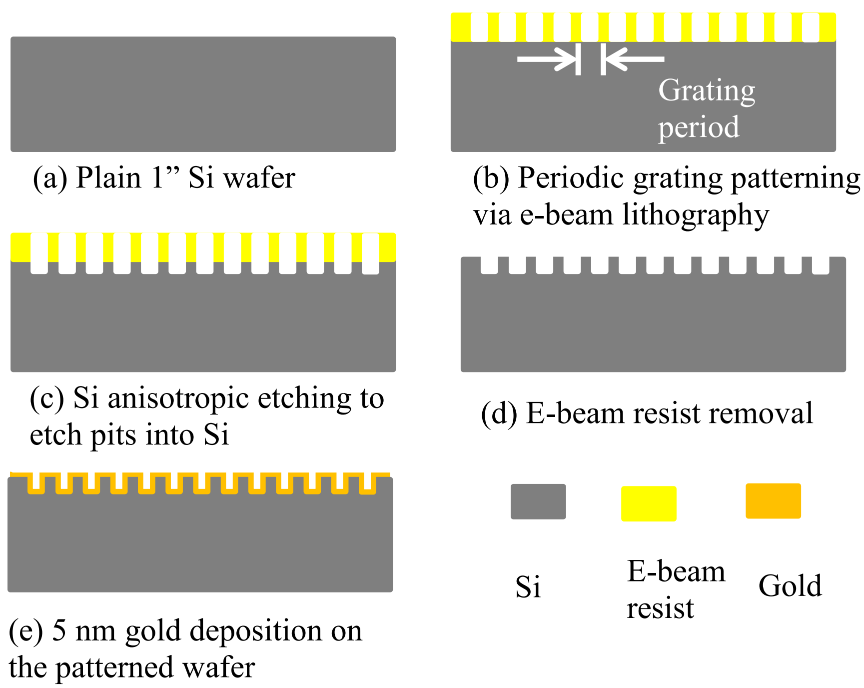

Fig. 4.16 Process of fabricating STM calibration sample with custom gratings.

Optical and AFM examination

The fabricated custom sample is examined by an optical microscope and AFM, as shown in Fig. 4.17. Fig. 4.17 (a) shows a representative optical image of the patterns. Fig. 4.17 (b) to (d) shows representative AFM images of the grating. The examined pattern has a grating period of 282 nm, and the step height is around 25 nm.

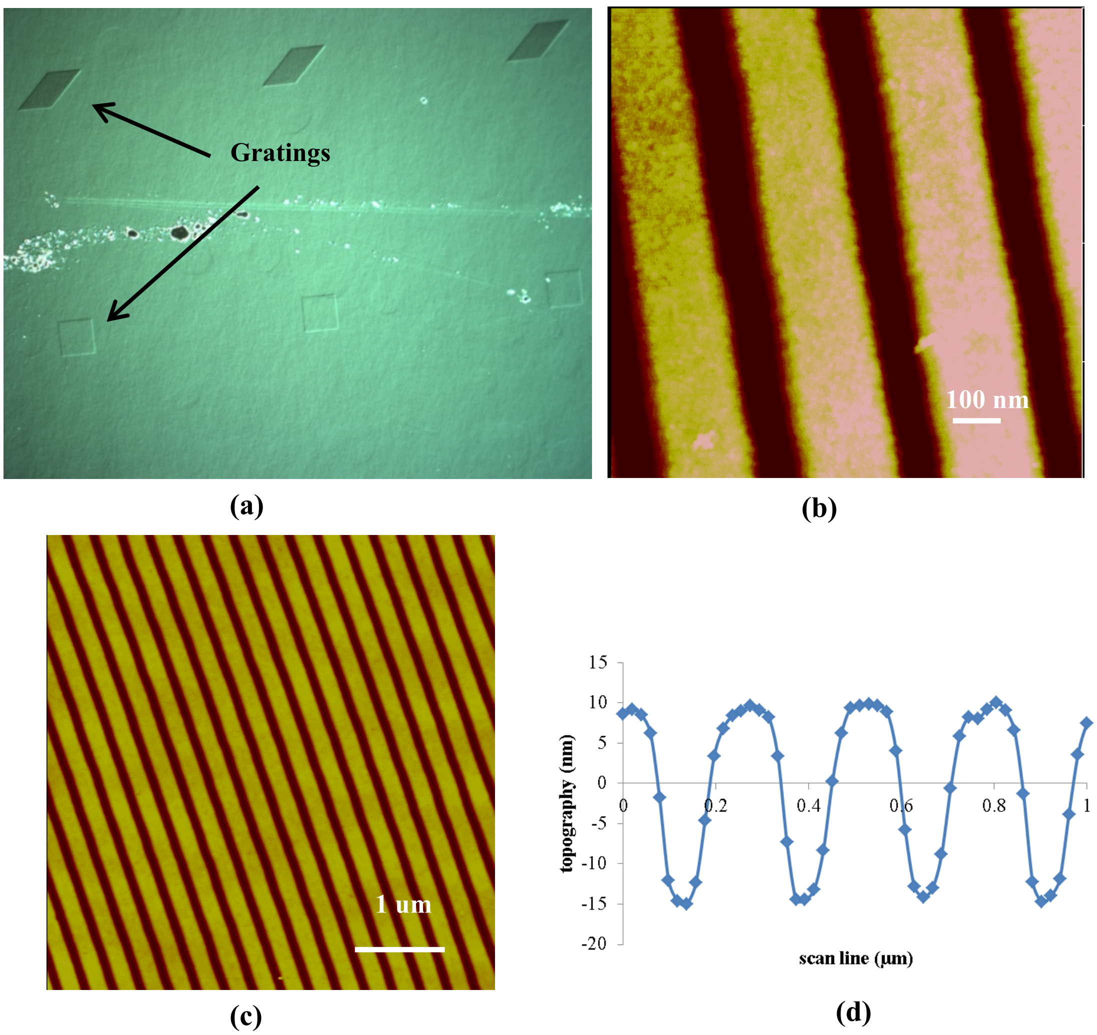

Fig. 4.17 Optical and AFM images of gratings: (a) Optical image. (b) & (c) AFM images. (d) A line topography across the gratings.

4.5 Instrumentation of a dual probe array system

4.5.1 Experimental setup

Testbench description

To build a dual-probe STM system, A Veeco Dim3000 SPM system is used as the test bench. The physical experimental setup of the dual-probe STM system is described in Fig. 4.18. The Veeco SPM test bench provides a vibration-isolation stage and a coarse approach unit to bring the STM tips from millimeter-scale separation to within the tunneling distance of the sample surface. The multi-probe STM chip has an ET drive for each probe and external control circuit for each active probe (two probes for these experiments). In the custom test bench, the probe array chip is mounted on the piezo-tube scan head with the Veeco system, and the piezo-tube is utilized to provide the *x*-, *y*- and *z*- movement of the whole chip, acting as a "master" drive. Each array probe has its respective ET actuator which acts as a "slave" drive to provide the vertical *z*- movement of individual probes. The dual probes are each equipped with a custom STM servo for their independent vertical displacement control. The servo electronics, including the TIA, PI controller, and low pass filter is realized by analog electronics and implemented on printed circuit boards (PCB) that were designed and made by Yingying Tang in our TBN research group [72]. The design of the circuit schematics is documented in Appendix D.

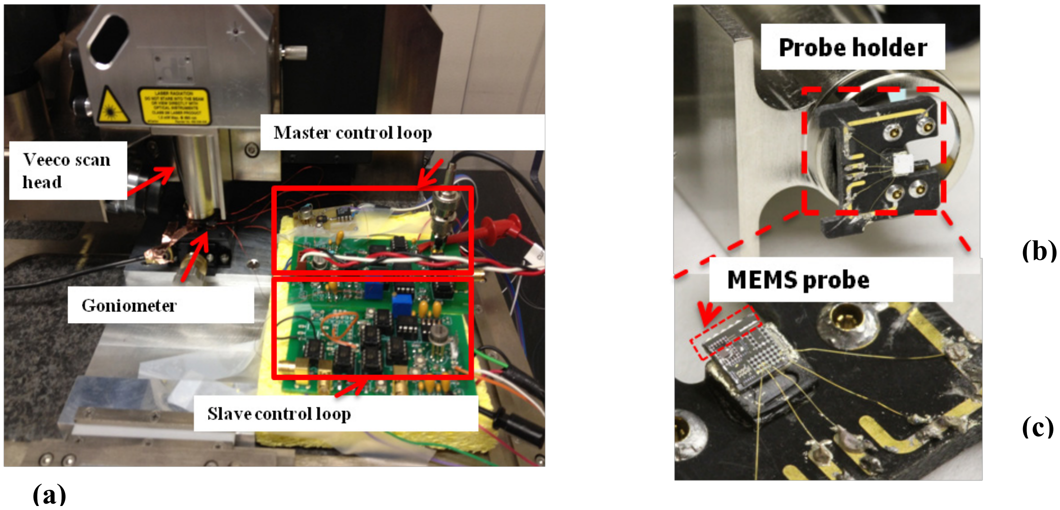

Fig. 4.18 Dual probe array STM setup: (a) Ambient Veeco system with mounted probe array and external control electronics. (b) & (c) Zoom-in photos of probe arrays.

4.5.2 Probe chip-sample alignment

Probe-sample alignment procedures

An instrumentation challenge in the dual-probe STM system is the alignment between the array probes and the sample surface. Because all the array tips have to be within a tunneling working distance of the sample surface at the same time when they are performing the parallel STM scanning, the probe chip and the sample surface must be well aligned. Because the mounting of the probe chip on the scan head and the mounting of the sample on the stage are done manually, the required parallelism between the probe chip and the sample surface is not immediately achieved. A manually operated macro-goniometer is introduced to resolve this issue. The goniometer used in the test bench is a Newport Lower GON40-L Goniometric stage with a 12.7 mm travel actuator (model: AJS100-0.5K), having a travel range of ±5˚ and a drive sensitivity of 5 arcsec/µm.

Fig. 4.19 shows the mechanism of the chip-sample alignment via the goniometer. The sample substrate is mounted on the goniometer. The probe array alignment procedures are as follows:

a. The goniometer is first intentionally tilted by 1˚ to 2˚ towards the master probe so that the master probe will be the closest to the sample surface. The optical microscope with the Veeco SPM system can measure the levelness of the sample and the probe chip and estimate sample-chip misalignment based on which the degree of the pre-tilt is adjusted.

b. Pre-actuate the slave probe and then start the probe to sample coarse approach process to bring the master tip within the tunneling distance to the sample surface so that the master servo is initiated. The master probe will be the first and the only probe that enters the tunneling zone and start tunneling once the coarse approach process is done. The current amplifier output of the master loop should be fluctuating around the current set point.

   The slave servo is turned on after the master probe is engaged. At this point the slave probe is still far away from the sample surface and so no tunneling occurs between the slave probe and the sample, as can be read from the zero current amplifier output.

c. Before the goniometer is adjusted, the probe chip is lifted up by a few microns from the sample surface via the motor on the scan head until no tunneling current is detected from the master probe. This lift-up step raises all STM tips high enough above the surface to make room for the goniometer rotation and is to prevent the STM tips from being damaged during the goniometer adjustment.

d. The goniometer is manually adjusted by around 0.01˚ tolerance of planarity with the slave probe.

e. Lower down the probe chip via the motor to check if both master and slave probes are within the tunneling distance at the same time, *i.e.*, if both master and slave current amplifiers have a non-zero output reading. Generally one iterative step of rotation of the goniometer is not sufficient to align the probe chip and the sample surface, and the slave current amplifier still has a zero output reading.

f. Repeat step c through e until both master and slave current amplifier have a non-zero and constant output reading, which should agree with the current set-point. At this point both probes with their independent z-actuators are then locked to the appropriate tunneling current distance simultaneously during the scanning, as illustrated in Fig. 4.19, and each servo-loop maintains a constant tunneling current, respectively.

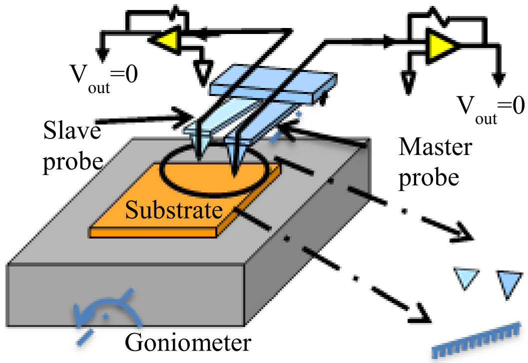

(a): the goniometer is pre-tilted towards the master probe;

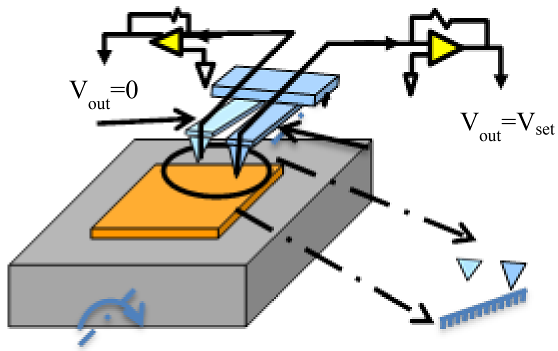

(b): the master probe is engaged to the surface via coarse approach while the slave probe is not;

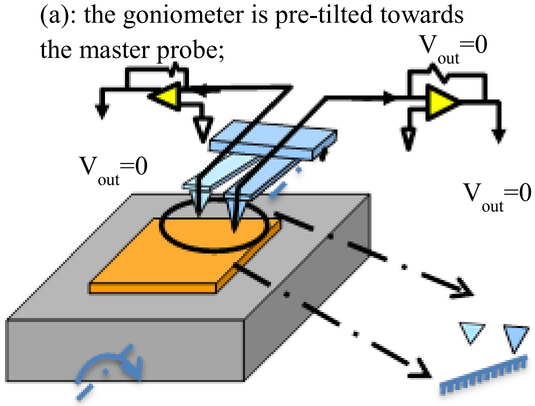

(c): the probe chip is lift up off the surface to make a room for goniometer rotation

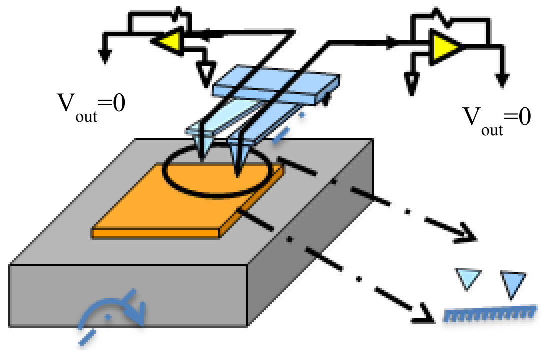

(d): the goniometer is fine adjusted towards the slave probe;

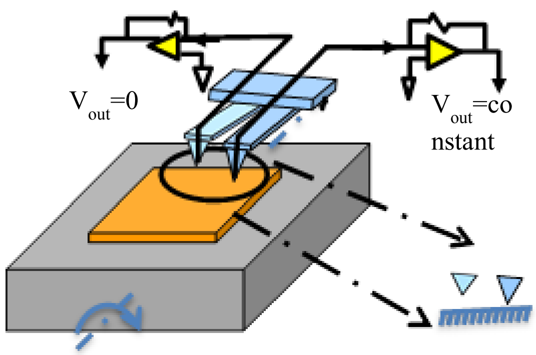

(e): lower down the probe chip to check both TIA output. The slave probe gets closer to the sample, but still out of tunneling range;

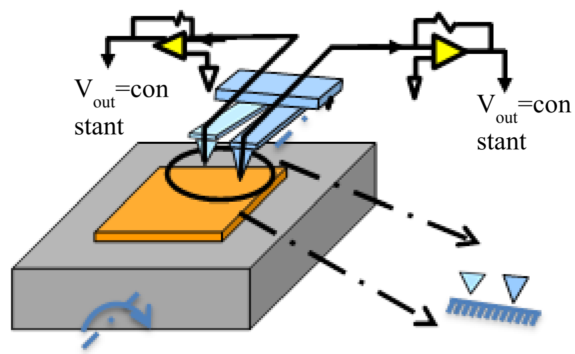

(f): repeat step (c) through (e) until both TIA outputs are non-zero and constant. The two probes are now both locked to the appropriate tunneling distance simultaneously and starts parallel scanning

Fig. 4.19 Procedures for probe chip – sample surface alignment via a macro-goniometer

4.6 Dual STM probe imaging implementation

Test description

Two probes among a 1D CMOS-MEMS arrays were used for dual STM scanning, as shown in Fig. 4.20. The master probe is located at the corner of the chip. This corner probe is a passive probe without an on-cantilever actuation mechanism. A probe on the edge of the probe chip is generally chosen as the master probe because it is easy to make the probe on the edge to be the one that is closest to the sample substrate by an intentional tilt of the sample towards this probe via the goniometer. One of the five probes that have an ET actuator is chosen as the slave probe. In this specific test, the active probe on the other end of the chip is used as the slave probe. In practice, any two of the active array probes can be selected for performing the dual STM imaging task. The custom calibration sample presented in section 4.4 is used for dual-probe STM system verification. A data acquisition board (NI DAQ 6009, National Instruments, Austin, TX) is used for data recording from the master and slave probe.

Tunneling current examinatio
n

In the experiment, the dual probes are first aligned and engaged with the sample surface, as described in section 4.5. The master and the slave probe perform the parallel scanning in the constant current mode. Fig. 4.21 shows an example of the master and slave currents during the parallel scanning. Both probes have tunneling current fluctuating around the set-point of 0.7 nA that is maintained through each probe gap by their respective servos.

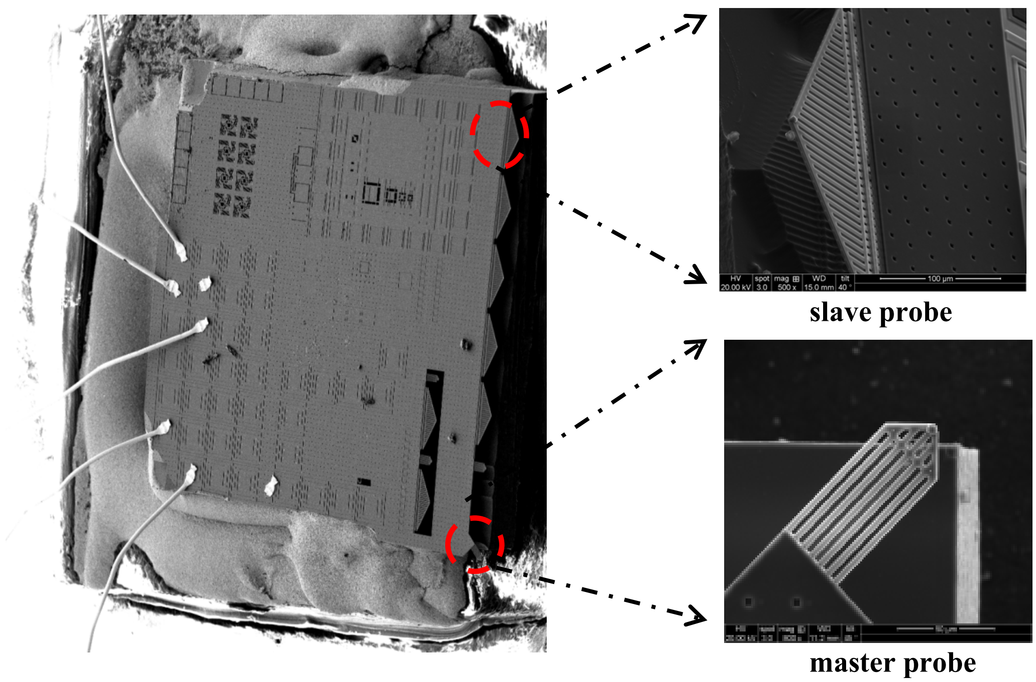

Fig. 4.20 SEM images of the master and slave probes used in the dual probe system

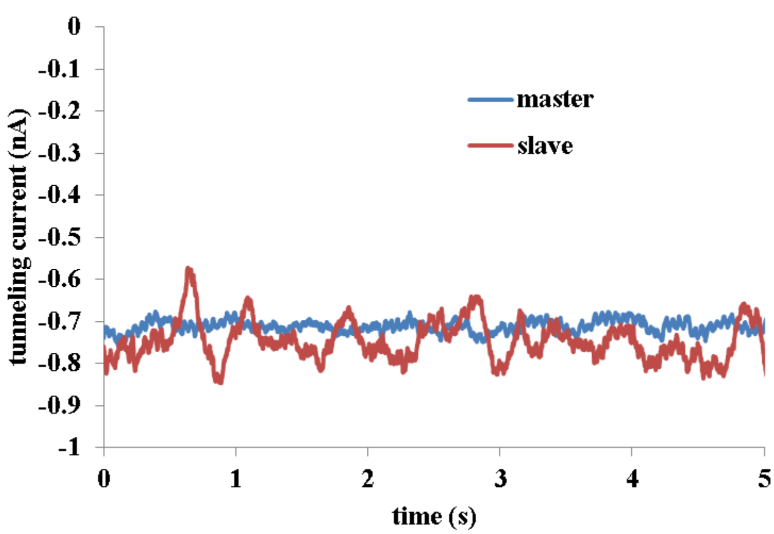

Fig. 4.21 Master current and slave current during parallel STM scanning

Two types of tests are carried out to examine the functionality of the dual-probe array STM system. In the first test, the response of two feedback loops in the dual scanning is examined when the whole probe chip is moved up and down over the sample surface by the external motor in the Veeco SPM system. The scan region is limited to 1 nm so there is virtually no topography variation under the probes.

Description of 1st test

Fig. 4.22 shows the test results. Five characteristic regions are identified in the system response. In region A the motor keeps still. Both the master piezo drive and the slave ET drive voltages maintain constant. In region B, the motor moves the probe chip towards the surface, so the master feedback loop responds correspondingly: the piezo drive voltage is lowered to extract the probe chip away from the surface. In region C, the motor moves the probe chip up, so the piezo drive voltage is increased to extend the probe chip to the surface. At the end of region C, the piezo drive voltage reaches its maximum of 130 V and saturates. In both region B and C, the slave ET drive voltage keeps constant, which is expected because the change in the gap between the slave tip and the sample is already cancelled out by the master feedback loop. Starting in region D, the motor continues to raise the probe up to the extent beyond the range that the master feedback loop can compensate for, so the master piezo drive voltage saturates and stops at a constant voltage of ~130 V. the master current also drops from the constant value to zero. The slave feedback loop starts to respond, lowering the ET drive voltage to extend the slave probe towards the sample surface to maintain a constant current. At the end of region D, the probe chip is raised out of the range of the slave feedback loop too, hence the slave drive voltage saturates and the slave current also drops to zero. In the final region E, the probe chip is raised further, but both the master and the slave drive voltages saturate, and both currents are zero. The test results suggest that two feedback loops are working in parallel properly.

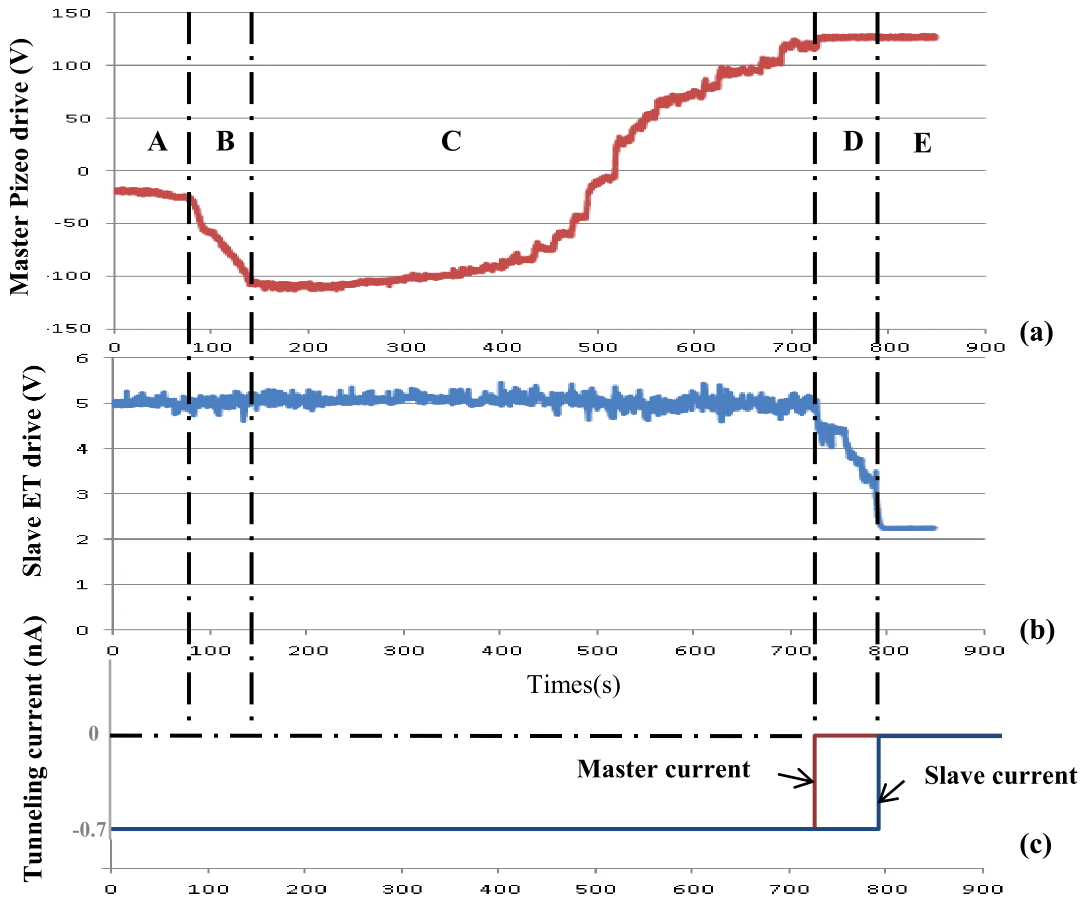

Fig. 4.22 Response of the master and slave drive voltages to a forced change of distance between the full probe chip and sample by the external motor: (a) Master piezo drive. (b) Slave ET drive. (c) A schematic showing current evolution.

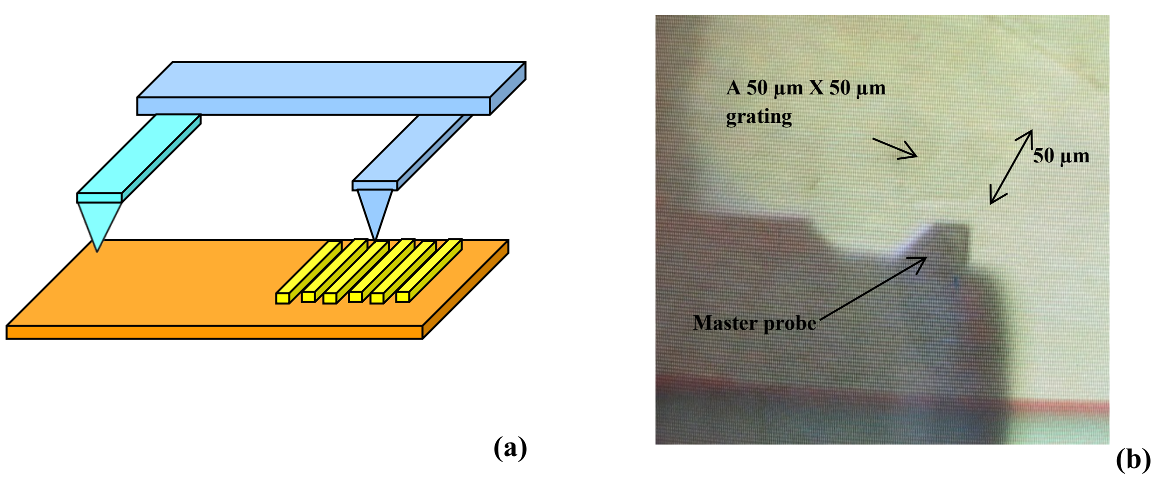

Fig. 4.23 (a) A schematic illustrating a scenario where one probe scan on the grating while the other scan on a flat surface. (b) A photo showing a MEMS probe scanning near a grating on the calibration sample. The grating and the probe is well identified in the picture.

Description of 2nd test

In the second type of test, the dual probes are scanning on the custom calibration sample for parallel image acquisition. Table 4-4 gives the experimental conditions. The custom gratings on the calibration sample can be manually moved under either the master probe or the slave probe, as illustrated in Fig. 4.23. Patterns under the two probes are intentionally designed to be different to identify the two simultaneously obtained images. Fig. 4.23 (b) shows an example photo where the master probe is scanning just next to a 50 µm × 50 µm grating area.

Table 4-4 *Scan parameters used in dual imaging recording*

Parameters	Value	note
Scan bias	100 mV ~ 200 mV	Varies depending on surface conditions
Scan rate	2.5 s/line	
Sampling rate	512 data/sec/channel	Two channels for two drive voltage recording

In the first scenario, the master probe falls on the pattern while the slave probe is scanning on an unpatterned area. Fig. 4.24 shows the obtained dual images. The image processing scripts are documented in Appendix C.3. Fig. 4.24 (a) shows the image under the master probe, constructed from the piezo drive voltage. The pattern has a period of around 280 nm. Fig. 4.24 (b) is the slave image built from the ET drive power applied on the slave probe. Although scanning on an area with no grating pattern, the image shows a grating that corresponds with that in the master image. This is expected because the slave feedback loop responds not only to the surface topography under the slave tip but also to variation of the vertical displacement of the master piezo drive. Therefore,

$$C\Delta P_{ET} = h_{sl-st} + \Delta z_{pz} = h_{sl-st} + B\Delta v_{pz} \tag{4.24-a}$$

where ΔP_{ET} is the ET power fluctuation in the slave feedback loop, and C is the ET drive sensitivity. $C\Delta P_{ET}$ is the addition of the fluctuation of actual surface topography, h_{sl-st}, and the fluctuation of piezo displacement, Δz_{pz}. So the actual surface topography is

$$h_{sl-st} = C\Delta P_{ET} - B\Delta v_{pz} = B(\Delta P_{ET}/\delta - \Delta v_{pz}) \tag{4.24-b}$$

where δ is the ratio of piezo actuator drive sensitivity to ET actuator drive sensitivity. In chapter 2, this ratio is *in situ* characterized. In the characterization, STM is working constant current mode using a CMOS MEMS probe equipped with an on-cantilever vertical ET actuator. Different drive powers are applied on the ET actuator to vertically displace the probe tip. The drive voltage on the piezo actuator responds accordingly to counteract this displacement in order to maintain a constant current. It is concluded that the travel distance caused by change of the drive voltage of 1 V on the piezo scanner is equivalent to that caused by change of drive power of 0.129 mW on the ET actuator, *i.e.*, δ=0.129 mW/V, as shown in Fig. 2.15. The actual topographical slave image is shown in Fig. 4.24 (c), obtained from the weighted difference of two drive signals. The grating pattern disappears on this difference image, leaving behind only the real features under the slave probe.

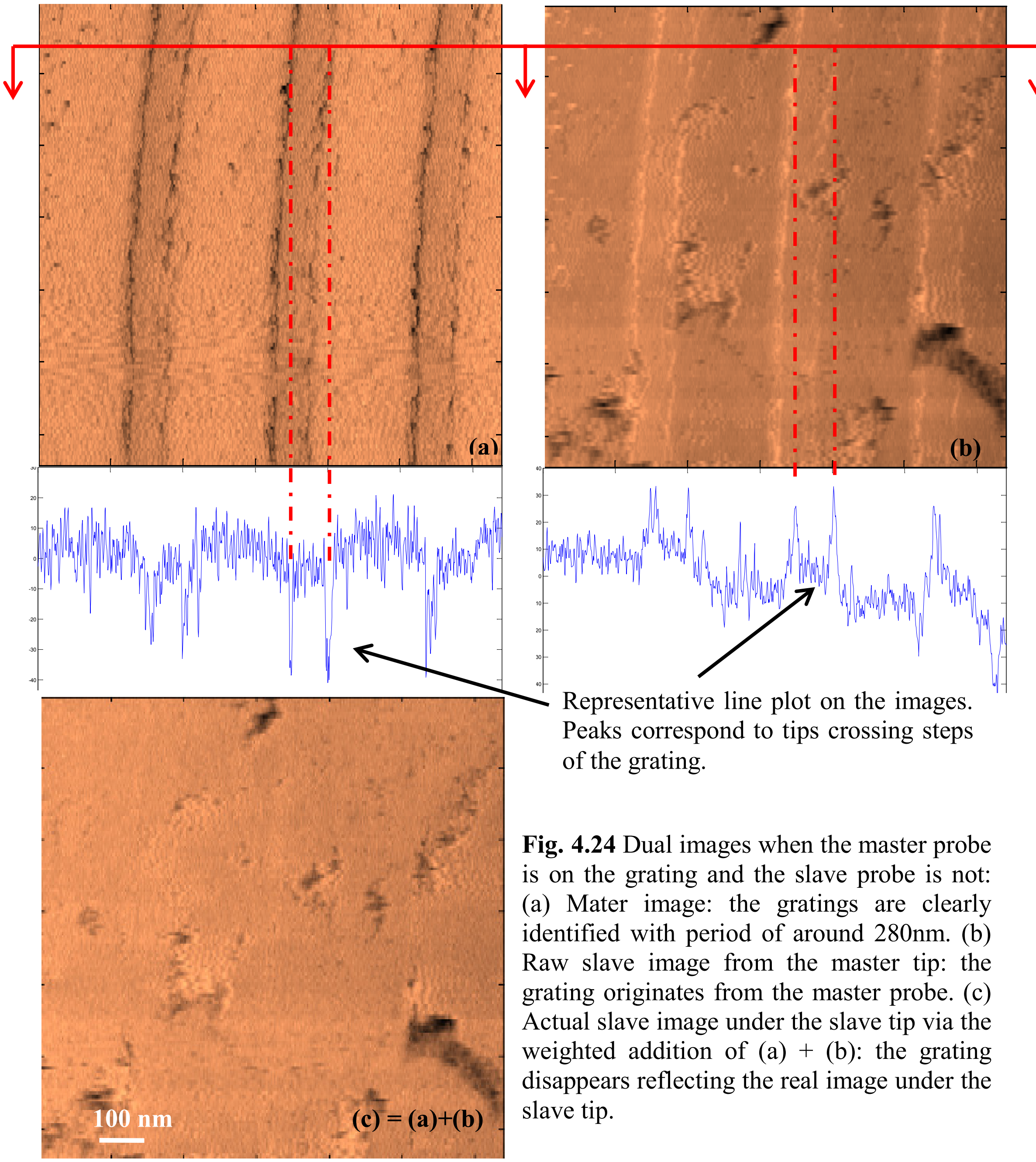

Fig. 4.24 Dual images when the master probe is on the grating and the slave probe is not: (a) Mater image: the gratings are clearly identified with period of around 280nm. (b) Raw slave image from the master tip: the grating originates from the master probe. (c) Actual slave image under the slave tip via the weighted addition of (a) + (b): the grating disappears reflecting the real image under the slave tip.

In a second scenario, a grating is moved under the slave probe while the master probe is scanning on an area without gratings. Fig. 4.25 shows the obtained STM images. No grating patterns appear on the master image. In the slave image of Fig. 4.25 (b), a grating with a period of 560 nm is identified. Fig. 4.25 (c) shows the difference slave image where the grating is preserved. The step height is not well resolved, though, due to poor tip quality. Fig. 4.26 shows the SEM images of Pt tips on the MEMS probe before and after the scanning. The tip crashed during the scanning, which accounts for the poor quality of obtained images. The gold grains are not resolved in the obtained STM images.

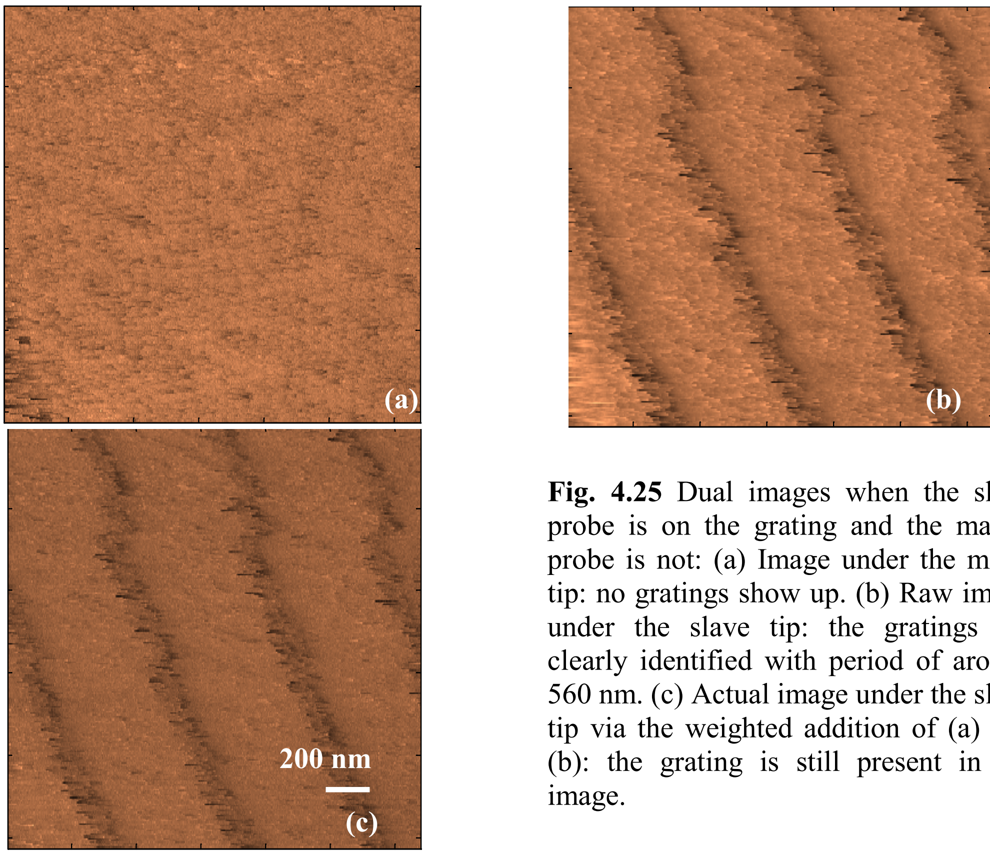

Fig. 4.25 Dual images when the slave probe is on the grating and the master probe is not: (a) Image under the mater tip: no gratings show up. (b) Raw image under the slave tip: the gratings are clearly identified with period of around 560 nm. (c) Actual image under the slave tip via the weighted addition of (a) and (b): the grating is still present in the image.

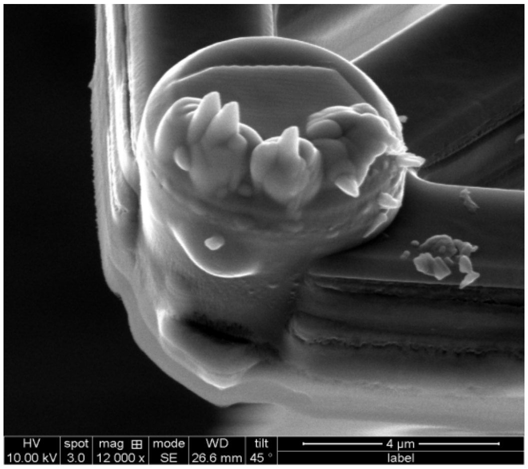

(a)

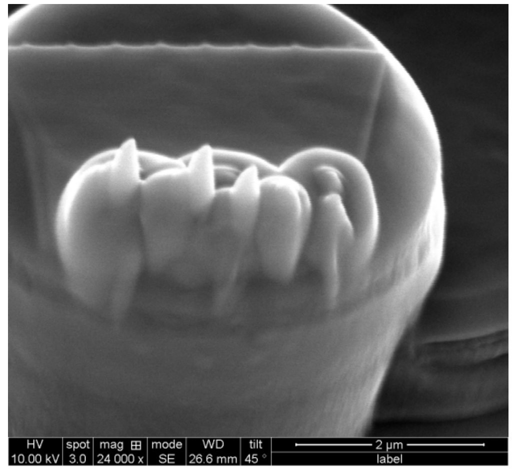

(c)

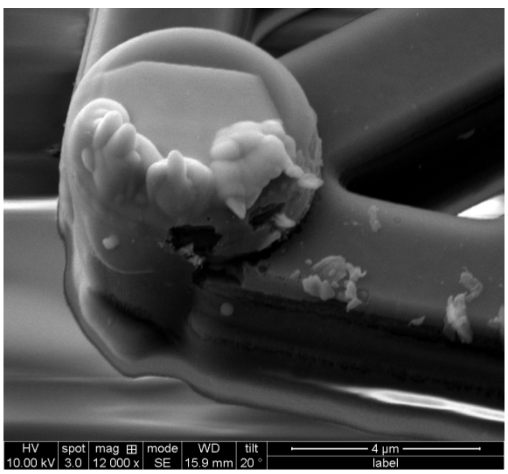

(b)

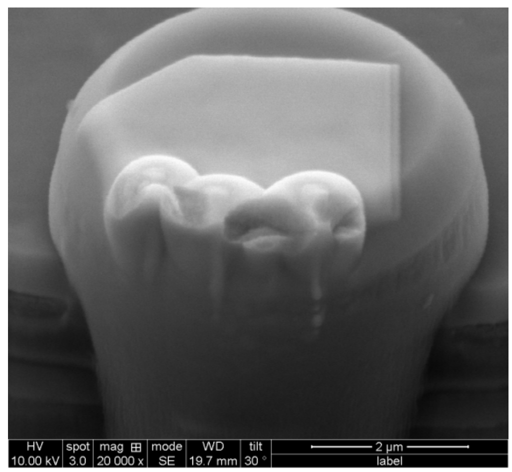

(d)

Fig. 4.26 (a) & (b): EBID STM tips of the master probe before and after the STM imaging. (c) & (d): EBID STM tips of the slave probe before and after the STM imaging.

Both the master probe and the slave probe are able to identify the custom grating on the custom calibration sample, proving the validity of dual-probe STM system.

4.7 Summary

A dual-probe STM system is built based on a commercial Veeco Dim3000 SPM system. Stability analysis of the custom piezo actuator-driven and the ET actuator-driven feedback loops is performed. Different from a conventional STM system where an ultra-stiff metal tip is used as a STM end-effector, a compliant MEMS cantilever is applied in the dual probe system; hence its dynamics and tip-sample interaction force are included in the feedback loop modeling. In both feedback loops, a PI controller is implemented. The stability region is obtained based on analysis of a linearized STM feedback loop, which gives a guidance of the adjustment of proportional gain and integral gain during the experiment.

The custom grating calibration sample was successfully employed to verify the functionality of a hierarchically driven dual-STM servo system. Two simultaneous STM images were obtained, where the pseudo-features on the raw slave images introduced by the master servo are successfully removed by differencing the image signals. The measured drive sensitivity relationship between the ET actuator and the piezo actuator provides the weighting factor for this difference, validating the fundamental understanding of the system operation.

Chapter 5. MEMS Proximity Sensor and Micro-Goniometer

Probe array scaling

In the current version of CMOS-MEMS STM probe arrays, adjacent probes are spaced around 340 μm apart. By comparison, the lateral travel range of a commonly used piezoelectric actuator is less than 100 μm. Furthermore, the scanning range of a single STM probe is generally limited to within only a 10 μm x 10 μm area in practice to achieve nanometer-scale and/or atomic resolution. Therefore it is desirable that the spacing between array probes be scaled to the same order of magnitude so the multiple scanned images can be merged and so that batch-fabricated nanostructures via different probes can be connected to make devices. In addition, a scaled version of an active MEMS probe array may find application in micro-handling and nanostructure manipulation and characterization [73, 74].

Introducing ancillary on-chip goniometer

The scaling of STM probe arrays brings about the idea of introducing an on-chip alignment mechanism for tip-substrate parallelization. For the widely spaced STM probe array system covered in chapter 4, this alignment was realized by making use of the optical microscope on the Veeco SPM system and a macro-goniometer. When the spacing between array probes is scaled down to tens of microns, it is possible to build an on-chip micro-goniometer which offers a platform to hold an array of probes. It serves to provide the *in situ* fine adjustment of relative height among these probes above the sample surface. A probe chip with integrated alignment mechanism will also facilitate its operation in an ultra-high-vacuum (UHV) system where external alignment tools are not readily implementable.

Chapter content

In this chapter, the on-CMOS chip alignment mechanism is introduced, which consists of a pair of on-chip substrate proximity sensors and a micro-goniometer. Section 5.1 reviews some on-chip electrothermal proximity sensing structures and introduces the design of probe cantilever-based electrothermal proximity sensors. The proximity sensors are to provide an estimate of the overall parallelism between the probe chip and the sample surface so a coarse alignment can be made. Section 5.2 presents the design of a micro-goniometer holding a scaled probe array, where the actuation mechanism of the goniometer also exploits the electrothermal approach.

5.1 Electrothermal probe sensor for chip position sensing

Misaligned probe array operation

When a one-dimensional (1D) probe array chip is manually mounted on the SPM scan head to perform the multi-probe scanning task on a sample, the probe array chip will not be in parallel with the sample surface: The angular misalignment between the two is around 2° and one corner of the chip is closer to the sample surface than the other. As the probe chip approaches the surface, the array probes placed between two corners of the chip cannot simultaneously reach within the actuation working distance to the surface, *i.e.*, one array probe may touch the surface first while other array probes are still a distance away from the surface.

Capacitive and ET position sensors

On-chip position sensors are introduced to estimate the distance and non-parallelism between the probe chip and the sample surface. Two of the most common MEMS-based position-sensing techniques are capacitive sensing [75,76] and thermal sensing [77,78]. When the distance or overlap between two concerned objects is changed, both the capacitance and the thermal conductance may change. It is by the detection of capacitance or temperature variation of the concerned objects that their relative position and displacement is evaluated.

ET position sensor adopted

Both capacitive sensing and thermal sensing are comparatively easy to be implemented in CMOS MEMS-based design and fabrication. In this work, a thermal proximity sensor is designed to fulfill the task of estimation of the separation and parallelism between the CMOS probe chip and the examined sample surface.

5.1.1 Thermal position sensor: an introduction

ET position sensor mechanism

Heat transportation between two objects, when they are separated by a macroscopic distance, is slow and often negligible. When the distance between the two objects are reduced to the scale of a few microns, the heat transportation will be very sensitive to variation of the distance and overlap area between them: the cold object acts as a heat sink, drawing much more heat flow from the heated object than when they stand far away from each other. This perturbation of the objects' local thermal environment as a function of distance/overlap area can be used as a position sensing signal: it can assess the displacement and relative position between the two objects, or the topography of one object when the other raster scan over it.

Previous work on ET sensor

Several groups have exploited the idea of using heat flow to measure proximity. Kim et al. [79] employed a self-heated silicon cantilever probe to perform topographical measurements, as shown in Fig. 5.1 (a), where the variation of probe-sample separation in the vertical direction follows the sample topography and is translated into the temperature fluctuation of the heated probe. The resolution in the vertical direction was found to be 1-3 nm. Lantz, et al. [77] in IBM research Zurich introduced the application of ET sensors as displacement sensors to measure the horizontal displacement of an *x/y* scanner where the sample mounted, as shown in Fig. 5.1 (b). The sensor chip is placed on top of the scanner, and the spacing between them is about 5 µm. When the scanner moves horizontally, it changes the overlap area between the scanner and the ET sensor and hence the temperature of the heater on the sensor. Using two sensors in a differential configuration, they demonstrated a resolution of 2.1 nm in a 10 kHz bandwidth with a dynamic range of more than 100 µm. In the work reported in this thesis, on-chip ET probe position sensors are used as proximity sensors to estimate the non-parallelism of the CMOS probe array and the sample surface, based on which a macro-goniometer is used to align the probe array and the sample surface.

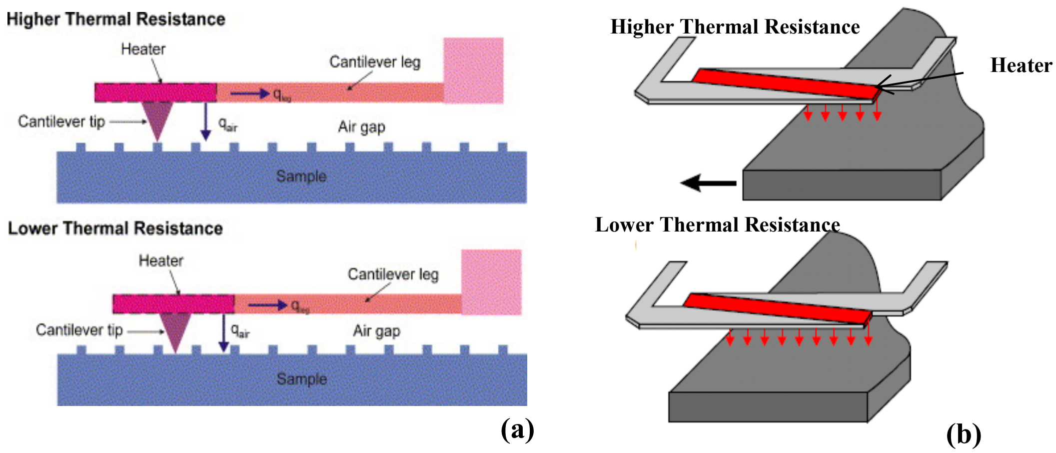

Fig. 5.1 Thermal position sensing based on the variation of: (a) Heated tip-sample separation [79]. (b) Heated cantilever-sample overlap area [77].

5.1.2 On-chip ET proximity sensor design

ET sensor structure

Cantilever probe geometry and its derivatives, among others, are frequently adopted as the basic structure to realize a MEMS thermal proximity sensor. Fig. 5.2 illustrates the conceptual design of an on-chip probe thermal proximity sensor. It is a cantilever-suspended micro-heater. A resistor with a large thermal coefficient of resistance (TCR) is embedded at the end of the ET probe, which has dual functions: as an electric heater element and as a sensor to detect the temperature change of the probe.

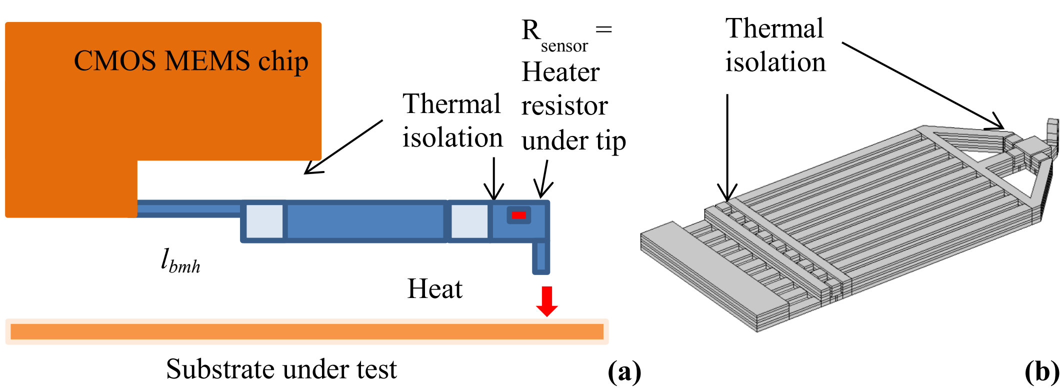

Fig. 5.2 Schematic design of the probe thermal position sensor: (a) Side view. (b) 3D view.

Tip structure of the ET proximity sensor

Via structures in tip to lower thermal resistance

A CMOS metal-2 to metal-4 tungsten via structure, with a total area of ~1µm^2 per via is made above the polysilicon heater resistor to decrease the thermal resistance from the bottom heater to the tip apex of the ET probe sensor end. It serves to enhance the heat transfer to the substrate heat sink when the ET probe gets close to it and hence enhances its sensitivity. The via structure is illustrated in Fig. 5.3.

The thermal resistance between the heater resistor and top metal-4 is roughly estimated as follows. Without metal-2 to metal-4 vias, the thermal resistance, $R_{nvia,}$ is contributed by three oxide layers, four metal layers and vias connecting the polysilicon heater and metal-1:

$$R_{nvia} = \frac{1}{\kappa_{via}} \frac{l_{01}}{A_{via}} + \frac{1}{\kappa_{ox}} \frac{l_{12} + l_{23} + l_{34}}{A_{tip}} + \frac{1}{\kappa_{Al}} \frac{l_1 + l_2 + l_3 + l_4}{A_{tip}} \tag{5.1}$$

where κ_{ox}, κ_{via} and κ_{Al} are thermal conductivities of silicon oxide, tungsten vias and aluminum metal layers, respectively, A_{via} is the total via area, A_{tip} is the metal-4 tip area, l_i (i=1 to 4) is metal thickness, and $l_{j,j+1}$ (j=1 to 3) is the oxide or via thickness between two neighboring metals,. Particularly, l_{01} is the distance between the polydilivon heater and the metal 1. With metal-2 to metal-4 vias, the thermal resistance, R_{via}, is contributed by one oxide layer between metal-1 and metal-2, four metal layers and vias through metal-2 to metal-4 plus those connecting the polysilicon heater and metal-1:

$$R_{via} = \frac{1}{k_{via}} \frac{l_{01} + l_{23} + l_{34}}{S_{via}} + \frac{1}{k_{ox}} \frac{l_{12}}{S_{tip}} + \frac{1}{k_{Al}} \frac{l_1 + l_2 + l_3 + l_4}{S_{tip}} \tag{5.2}$$

Using the values provided in Table 5-1, R_{nvia} is around 4.53×10^5 K/W, while R_{via} is around 1.26×10^5 K/W. Therefore, the thermal resistance is more than three times lower when a metal-2 to metal-4 via structure is introduced.

Table 5-1 *Parameters used in estimation of thermal resistance of ET proximity sensor*

Parameters	Value	Description
κ_{ox}	1.4 W/(m·K)	Thermal conductivity of silicon oxide
κ_{via}	174 W/(m·K)	Thermal conductivity of Tungsten
κ_{Al}	237 W/(m·K)	Thermal conductivity of aluminum
l_i *(i=1,2,3)*	0.635×10^{-6} m	Metal thickness
l_4	2.8×10^{-6} m	Metal thickness
l_{01}	0.65×10^{-6} m	Distance between polysilicon and metal-1
$l_{j,j+1}$ *(j=1,2)*	0.95×10^{-6} m	Dielectric layer thickness
l_{34}	2×10^{-6} m	Dielectric layer thickness
A_{tip}	6.25×10^{-12} m^2	Metal-4 tip area
A_{via}	1×10^{-12} m^2	Via total area

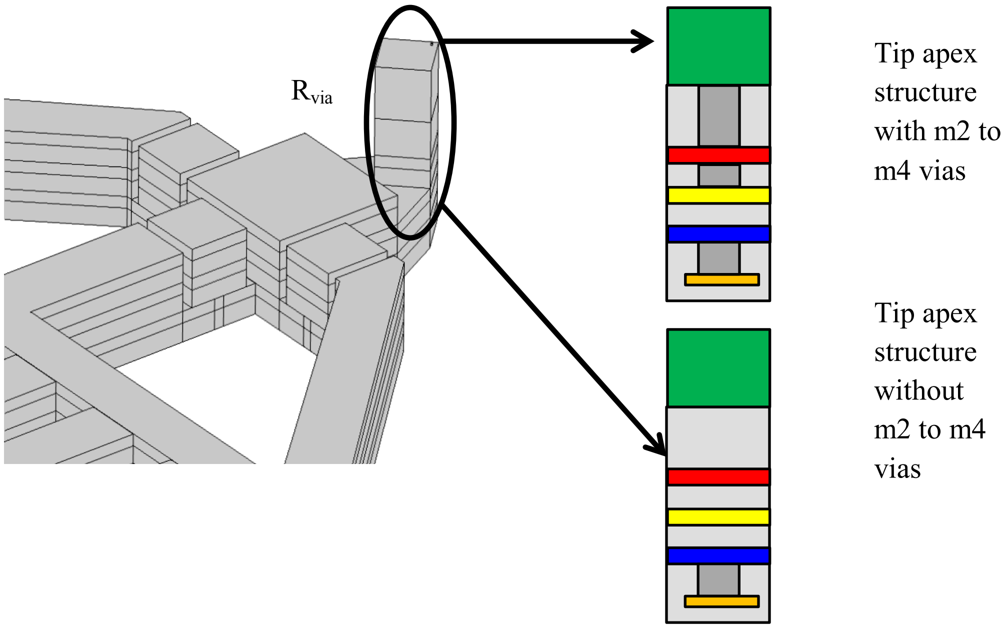

Fig. 5.3 The structures of tip apex of the ET probe sensor, with and without metal-2 to metal-4 via structure.

FEM model to examine the thermal sensor performance

A three-dimensional finite element modeling (FEM) of the heat transfer between the ET probe sensor and the sample in air, based on the Fourier's law of heat conduction, is performed in COMSOL to examine the temperature variation of the heater resistor with tip-sample separation. The sample was an Au-coated Si substrate. The heater resistor provides a constant heat power of 1.65 mW. Joule heat is generated causing a local temperature increase at the probe-end with respect to that of the environment. The highest temperature of the ET probe occurs at the location of the heater resistor and is defined as the probe temperature. The simulation result is shown in Fig. 5.4. When the ET sensor stands isolated from the substrate, the main heat loss is through the cantilever beams down to the CMOS chip body. As the heated ET probe approaches the substrate surface, it will provide a significant heat conduction channel through air due to the proximity of the surface, thus increasing the heat loss and lowering the temperature of the pre-heated ET probe, as evidenced by the simulation.

FEM confirms effectiveness of via structure

The sensitivities of the two sensor structure designs are also compared (*i.e.,* with and without the underlying vias). When the ET sensor stands over 30 µm away from the substrate, the temperature difference between two sensor structures is small, no more than 0.5 K, *i.e.*, the presence of this metal-2 to metal-4 via structure between the tip end and the polysilicon heater has little effect on the probe temperature. This is understandable because most heat generated at the tip end is directed down the cantilever into the CMOS chip body, while the heat loss through air is small. As the tip end approaches the substrate, more heat will be conducted through air from the tip end to the substrate. The metal-2 to metal-4 vias, acting as a 'fast channel for heat flow', will expedite this process and increase the sensitivity to tip-sample separation change of the tip temperature. When the tip-sample distance drops down to 1 µm, the temperature of the sensor with metal-2 to metal-4 via structure is 491 K, with a displacement sensitivity of 4.1 K/µm, By comparison, the temperature of the sensor without metal-2 to metal-4 via structure is 493 K, with a displacement sensitivity of 2.8 K/µm. Therefore, the tip structure with metal-2 to metal-4 vias is adopted in the ET proximity sensor design.

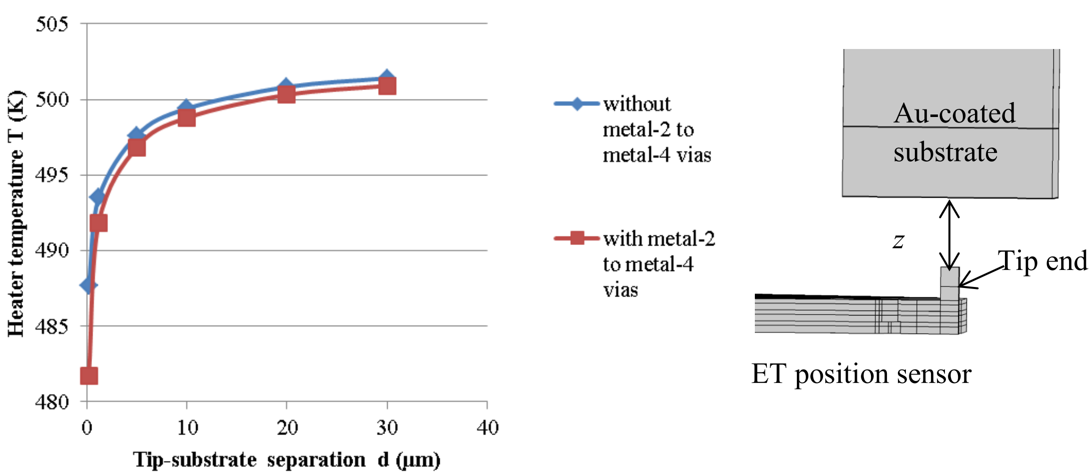

Fig. 5.4 Simulated temperature of the heater resistor *vs.* tip-substrate separation with and without metal-2 to metal-4 via structure.

ET proximity sensor for estimation of tip-sample separation

Analyze heater resistance vs. tip-sample separation relationship

A single ET proximity sensor on the probe chip can be used to estimate the separation between the chip and the sample substrate. In the actual test, usually a constant voltage or a constant current is applied to the heater resistor and the resistance is monitored, from which the tip-sample separation is estimated. Therefore, the relationship between the fluctuation in heater resistance and the variation of tip-sample separation needs to be known. A small signal analysis is used to obtain the relationship. Assume tip-sample separation is x_0. A constant voltage of V_0 is applied to the heater resistor, resulting in a current flow of I_0 and a temperature of T_0. A small fluctuation around x_0, Δx, causes a fluctuation in heater temperature, ΔT, and a fluctuation in heater resistance, ΔR. ΔR can be expressed as

$$\Delta R = R'(T_0)\Delta T \tag{5.3}$$

where $R'(T_0)$ denotes the slope $R(T_0)$ evaluated at T_0. $R(T)$ represents the heater resistance *vs.* temperature relationship and can be obtained experimentally.

The heater temperature, T, is the function of heating power, P, and tip-sample separation, x. Therefore, T can be expressed as:

$$T(P, x) = P \times S_{TP}(x) + C_0 = \frac{V_0^2}{R} \times S_{TP}(x) + C_0 \tag{5.4}$$

where C_0 is the temperature of the environment where the test is conducted. $S_{TP}(x)$ is the thermal resistance of the ET proximity sensor, denoting the temperature variation by change of a unit power dissipated in the heater at a given tip-sample separation, x. This relationship can be measured experimentally.

Then, a small perturbation in temperature, ΔT, caused by a fluctuation in tip-sample separation around x_0, Δx, be expressed as

$$\Delta T(P,x) = \Delta(P \times S_{TP}(x) + C_0) = \Delta(P) \times S_{TP}(x_0) + P_0 \Delta(S_{TP}(x)) \tag{5.5-a}$$

where:

$$\Delta(P) \times S_{TP}(x_0) = S_{TP}(x_0)\left(-\frac{V_0^2}{R_0^2}\right)\Delta R = S_{TP}(x_0)(-I_0^2)\Delta R \tag{5.5-b}$$

and

$$P\Delta\big(S_{TP}(x_0)\big) = P_0 \frac{\partial S_{TP}(x)}{\partial x}\Delta x\bigg|_{x=x_0} \triangleq P_0 S'_{TP}(x_0)\Delta x \tag{5.5-c}$$

Substituting (5.5) into (5.3) and rearranging to solve for the relationship of resistance *vs.* tip-sample separation yields:

$$S_{\tilde{R}\tilde{x}}(x_0) = \frac{\Delta R}{\Delta x} = \frac{R'(T_0)P_0 S'_{TP}(x_0)}{1 + (V_0^2/R_0^2)R'(T_0)S_{TP}(x_0)} \tag{5.6}$$

where $S_{\tilde{R}\tilde{x}}(x)$ is a sensitivity that relates the fluctuation of tip-sample separation and the fluctuation of the heater resistance, in mks units of Ω/m.

Since

$$\Delta I = \Delta\left(\frac{V}{R}\right) = \left(-\frac{V_0}{R_0^2}\right)\Delta R = \left(-\frac{I_0}{R_0}\right)\Delta R \tag{5.7}$$

where the actuator voltage, V, is held constant at V_0. Substitution of (5.6) into (5.7) gives:

$$S_{\tilde{I}\tilde{x}}(x_0) = \frac{\Delta I}{\Delta x} = -\frac{I_0}{R_0}\frac{R'(T_0)P_0 S'_{TP}(x_0)}{1 + (V_0^2/R_0^2)R'(T_0)S_{TP}(x_0)} \tag{5.8}$$

where $S_{\tilde{I}\tilde{x}}(x)$ is the tip-sample distance sensitivity of the current, in mks units of A/m.

Similarly, when a constant current, I_0, is applied to the heater resistor and the voltage is monitored, the relationship between the voltage fluctuation and the variation of tip-sample separation is

$$S_{\tilde{V}\tilde{x}}(x_0) = \frac{\Delta V}{\Delta x} = I_0 \frac{R'(T_0)P_0 S'_{TP}(x_0)}{1 - I_0^2 R'(T_0)S_{TP}(x_0)} \tag{5.9}$$

where $S_{\tilde{V}\tilde{x}}(x)$ is the tip-sample distance sensitivity of the voltage, in mks unit of V/m.

Larger sensitivity at smaller tip-sample separation

The simulated relationship between the thermal resistance of the ET proximity sensor system and the tip-sample separation, $S_{TP}(x)$, and its slope, $S'_{TP}(x)$, is shown in Fig. 5.5. A gold-coated sample is used in the simulation. As the tip-sample separation decreases, the thermal resistance also decreases, as expected. The slope variation is much greater with the separation change, from 0.036 K/mW/µm at a separation of 25 µm to 7.4 k/mW/µm at a separation of 0.5 µm.

Assume a constant current of 1 mA flowing through a heater resistor with R = 2195 Ω. Assume the heater resistor has a TCR of −1200 ppm/K and is constant in the operation range. Then $R'(T_0)$ = R × TCR = −2.6 Ω/K. $S_{\tilde{R}\tilde{x}}(x)$ is calculated using (5.6), and the result is shown in Fig. 5.6.

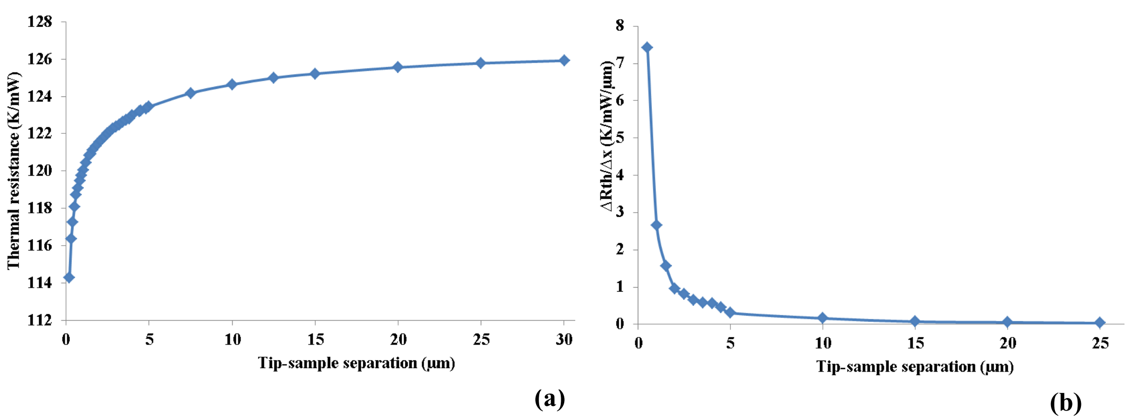

Fig. 5.5 (a) Thermal resistance of the ET proximity sensor system *vs.* tip-sample separation. (b) Rate of change of the thermal resistance *vs.* tip-sample separation.

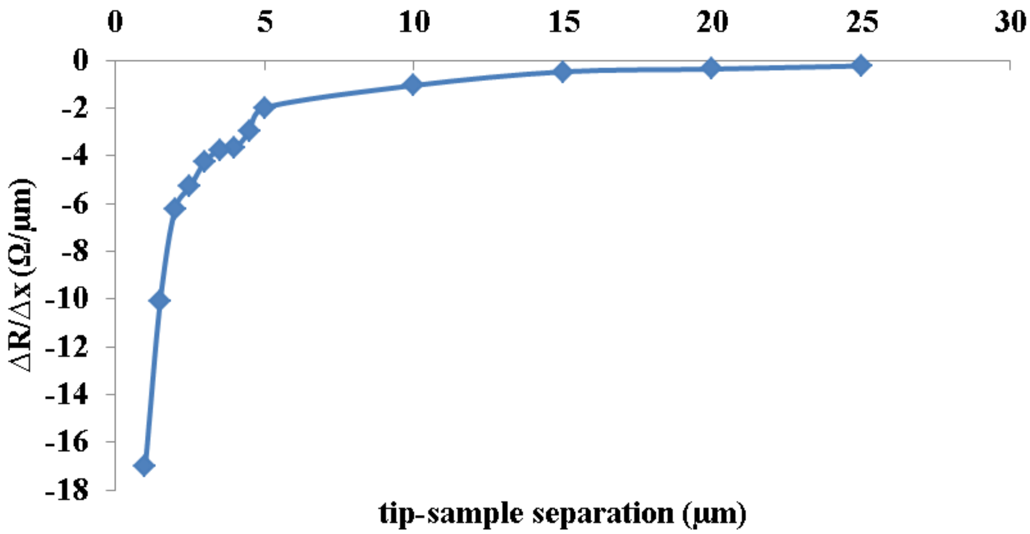

Fig. 5.6 Derived sensitivity to tip-sample separation of heater resistance.

Derivation of noise in heater sensor

The resolution of the ET proximity sensor can also be analytically obtained at different tip-sample separations. For an electrothermal proximity sensor, heater resistor thermal noise, or Johnson noise, and conductance fluctuation noise are two major noise sources. Thermal noise is generated by the collisions of agitated charge carriers, electrons in most cases, in the resistor. Thermal noise is 'white' noise, with a nearly constant power spectral density throughout the frequency spectrum. The thermal noise power spectral density (PSD), denoted by S_J in units of Ω/Hz, is

$$S_J = 4k_B TR/I_0^2 \tag{5.10-a}$$

where k_B is the Boltzmann constant, T is the temperature, R is the heater resistance and I_0 is the heater current. The thermal noise over a bandwidth, Δf, is

$$\sqrt{\int_{f_0}^{f_0+\Delta f} S_J\, df} = \sqrt{4k_B TR\Delta f/I_0^2} \tag{5.10-b}$$

The conductance fluctuation noise has a $1/f$ spectrum. Hooge presented an empirical formulation that describes this $1/f$ noise [80]. The corresponding PSD, denoted by S_H in units of Ω/Hz, is given by

$$S_H = \frac{\alpha R^2}{Nf} \tag{5.11-a}$$

where α is an dimensionless parameter. N is the total number of carriers in the resistor. Assuming the heater resistor has a width of w_s, a length of l_s and a thickness of t_s, and that the carrier concentration is N_c, then

$$N = N_c \times (l_s \times w_s \times t_s) \tag{5.12}$$

The $1/f$ noise over the noise band from f_0 to f_1, is:

$$\sqrt{\int_{f_0}^{f_1} S_f df} = \sqrt{\frac{\chi R^2}{N} \ln\left(\frac{f_1}{f_0}\right)} \tag{5.11-b}$$

The total resistance noise, $\sqrt{\overline{R_n^2}}$, is:

$$\sqrt{\overline{R_n^2}} = \sqrt{\frac{4k_B T R_0}{I_0^2}\Delta f + \frac{\chi R^2}{N} \ln\left(\frac{f_1}{f_0}\right)} \tag{5.13}$$

An estimation of resistance noise is estimated using the parameters values listed in Table 5- 2. The resistance thermal noise is 2×10^{-4} Ω, while the $1/f$ noise is 0.06 Ω. Therefore, Hooge $1/f$ noise is the dominant noise in the operation of the ET sensors.

The resolution of the ET sensor is obtained by dividing the noise by the sensitivity, as shown in Fig. 5.7. A resolution of 0.9 nm is achieved at a heated tip-sample separation of 0.5 μm. This indicates that ET cantilever sensors can also be used as a surface topography sensor with high resolution.

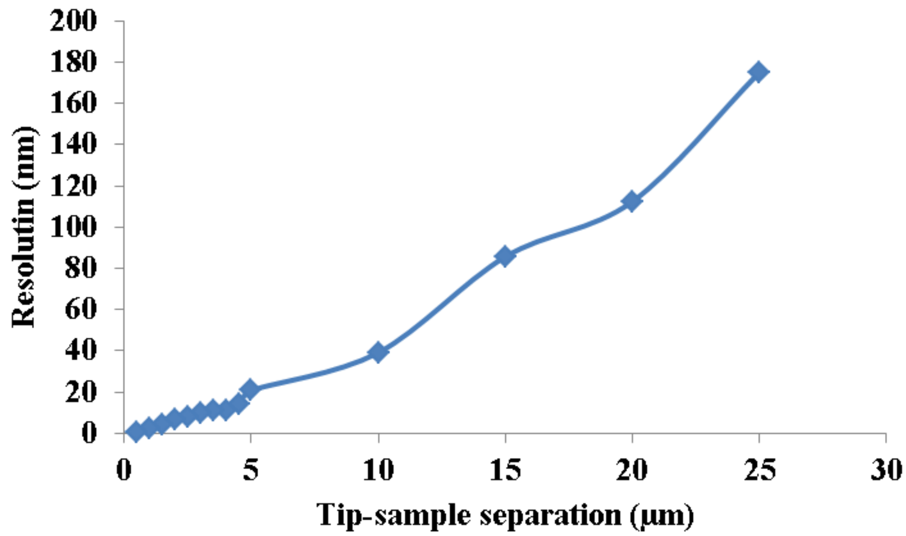

Fig. 5.7 Derived ET sensor sensitivity *vs.* tip-sample separation

Table 5- 2 *Parameters used in the estimation of resistance noise*

Parameters	**Value**	**Description**
R	2195 Ω	Heater resistance
I_0	1×10^{-3} A	Sourced current magnitude
k_B	1.38×10^{23} JK^{-1}	Boltzmann constant
T	500 K	Resistor temperature during sensing
N_c	1×10^{17} cm^{-3}	corresponds to a resistivity of ~0.03 Ω·cm
w_s	2 μm	Resistor width
l_s	2 μm	Resistor length
t_s	0.28 μm	Resistor thickness
α	10^{-5}	Hooge factor
Δf	1000 Hz	Noise bandwidth of thermal noise
f_1/f_0	1000 Hz	Integration bandwidth of $1/f$ noise

Sebastian et al. [81] adopted a systems approach to model the ET probe sensors as position sensors. The variation of tip-sample separation is regarded as a perturbation to the ET sensor-based thermal system. A similar heater current vs. tip-sample separation relationship to (5.8) is obtained. The method of experimentally identifying $R(T)$ and $S_{TP}(x)$ is also presented.

The change of the heater resistance in response to tip-sample separation is used to estimate the ET probe tip-sample separation when the probe chip approaches the sample.

Effect of bimorph bending in the ET proximity sensor

Bimorph bending affects tip-sample separation

During SPM operation, a motor drive is used in the approach of the probe chip with on-chip ET proximity sensors to the sample surface. The variation of ET tip-sample separation is translated from the displacement of the motor drive. This variation of tip-sample separation, however, is not exactly equal to the displacement of the motor drive. This is due to the bimorph beam in the ET proximity sensor structure shown in Fig. 5.2. During the approach of the probe chip and the sample, both the hot tip end and the bimorph beams on the sensor cantilever structure will get close to the sample, therefore the temperature will change on both the tip and the bimorph structure. The temperature fluctuation of the bimorph beams leads to its curvature variation and the displacement of the ET sensor tip. Hence the variation of tip-sample separation, Δx, consists of two parts: the displacement attributed to the motor drive, Δx_{md}, and the displacement attributed to the bimorph beam bending, Δx_{bph},

$$\Delta x = \Delta x_{md} + \Delta x_{bph} = \Delta x_{md}\left(1 + \frac{\Delta x_{bph}}{\Delta x_{md}}\right) \triangleq \Delta x_{md}(1 + \beta) \tag{5. 14}$$

where β denotes the sensor tip displacement caused by the bimorph bending per unit change of the displacement of the motor drive. When the motor drive moves the probe chip away from the sample, the temperature of the bimorph increases, and the bimorph will bend upwards, in the direction away from the sample. Therefore, the actual tip-sample separation increase is larger than the displacement of the motor drive, *i.e.*, $\beta>0$.

In the calibration test of the sensitivity of ET proximity sensor, the measurable quantity is the displacement of the motor drive. The bending of the bimorph can be measured by other sensing mechanism such as the integrated piezoresistive sensors [82]. Therefore, the actual tip-sample separation sensitivity is

$$\frac{\Delta R}{\Delta x} = \frac{\Delta R}{(1+\beta)\Delta x_{md}} \tag{5. 15}$$

The actual tip-sample separation sensitivity is slightly larger than the sensitivity that is derived based on the displacement variation of the motor drive.

<u>ET proximity sensor for estimation of probe chip-sample parallelism</u>

Operation of on-chip proximity sensors

ET proximity sensors are also used to measure the misalignment of the probe chip with the sample. It is achieved by placing two thermal probe proximity sensors on the two corners of a 2.4 mm by 2.4 mm CMOS probe array chip. The spacing between two sensor tips is around 2.4 mm. A 1D array of five probes lies in between the two proximity sensors. Fig. 5.8 illustrates the leveling methodology using the two ET probe proximity sensors. Equal power is applied to each of the probe-end resistive heaters on the ET probe proximity sensors. Due to the non-parallelism between the chip and the sample, the ET probe on one corner of the probe chip will be closer to the sample surface than its counterpart on the other corner. The two probes will have different amounts of heat conduction through the air, where the closer probe gets cooler than the farther one. Accordingly, the temperature difference is reflected in the difference in the electrical resistances of the heaters on the two probes. It is this resistance difference that conveys the non-parallelism between the chip and the sample surface.

The sample is mounted on a macro-goniometer and assumes an angle, θ, relative to the probe chip, assuming the left proximity sensor is closer to the sample, as shown in Fig. 5.8. Probe chip–sample misalignment of 0.024° or less is targeted in the alignment process through the combination of ET proximity sensor pairs and the goniometer. A misalignment of 0.024° indicates a 21 nm height difference between two array probes spaced at 50 μm. This height difference is around one tenth of the designed vertical travel range of an ET-actuated array probes that will be introduced in the next section and hence can be cancelled out by the vertical displacement of the array probes by themselves. A further reduction of misalignment is possible, but not necessary. Global probe array chip alignment is accomplished as follows:

(a) A constant current, I_0, is applied to the heaters of two ET proximity sensors. Assume the left side of the chip is closer to the sample. The probe chip with two pre-heated ET probe proximity sensors approach the sample surface via the motor, 1 μm per step. The positioning sensitivities, $S_{\tilde{R}\tilde{x}}(x)$, of both sensors need to be monitored, to estimate the tip-sample separation for each sensor. The approach process is kept until the tip of the left proximity sensors is 1 μm or less above the surface, estimated by $S_{\tilde{R}\tilde{x}}(x)$. This step provides a reference point at which the lowest point of the probe chip and the sample is around 1 μm. Adjustment of the motor and the goniometer during the alignment procedures should be based on this reference point so that chip will not touch the surface. Two cases may arise at this point. In the first scenario, the right sensor is also within 1 μm above the surface, which indicates the difference in the relative height above the sample surface between two probes is smaller than 1 μm, or the probe chip-sample misalignment is smaller than 0.024°, hence the alignment task is accomplished. In the second scenario, which is more likely to happen, the tip of the right probe is still very far from the sample, $S_{\tilde{R}\tilde{x}}(x) \approx 0$. Assuming an initial misalignment of 2° (θ = 2°), the right sensor tip will be around 83 μm from the sample surface. In this case, it is identified which corner of the probe chip is closer to the sample surface, but the exact misalignment angle cannot be determined, since the distance sensitivity of the proximity sensor, $S_{\tilde{R}\tilde{x}}(x)$, is very small when the tip is more than 20 μm from the sample surface;

(b) The probe chip is raised to make room for the goniometer adjustment. An initial rotation of 1° is applied. Then step (a) is repeated and the proximity sensor that is closer to the sample is determined.

(c) Two cases may arise at this point. The first scenario is the same as that in (b), where both sensors are within 1 μm above the sample surface, and the alignment task is done. In the second scenario, if it is still the left sensor that is closer to the sample, repeat step (b), keeping the 'step length' of the rotation at 1° per adjustment. The adjustment is kept until either: (1) the first scenario occurs, i.e., both proximity sensors is within 1 μm above the sample; or (2) the goniometer is over adjusted resulting in that the right sensor is closer to the sample surface, at which point the misalignment between the probe chip and the sample surface will be smaller than the 'step length' of the goniometer, *i.e.*, 1°.

(d) In case step (c) ends up with the second scenario, repeat step (b) and (c), except for that a rotation step equal to one half of the previous 'step length', is applied to the goniometer. The adjustment will end up with either: (1) both proximity sensors being within 1 μm above the sample and the alignment task is done, or (2) the goniometer being over adjusted and the left sensor is closer to the sample again, at which point the misalignment between the probe chip and the sample surface is further reduced, smaller than the current 'step length' of rotation.

(e) Step (d) is repeated, until either: (1) both proximity sensors being within 1 μm above the sample and the alignment task is done, or (2) the 'step length' of rotation is decreased to 0.024°. In both cases the misalignment between the probe chip and the sample surface is reduced to smaller than 0.024°.

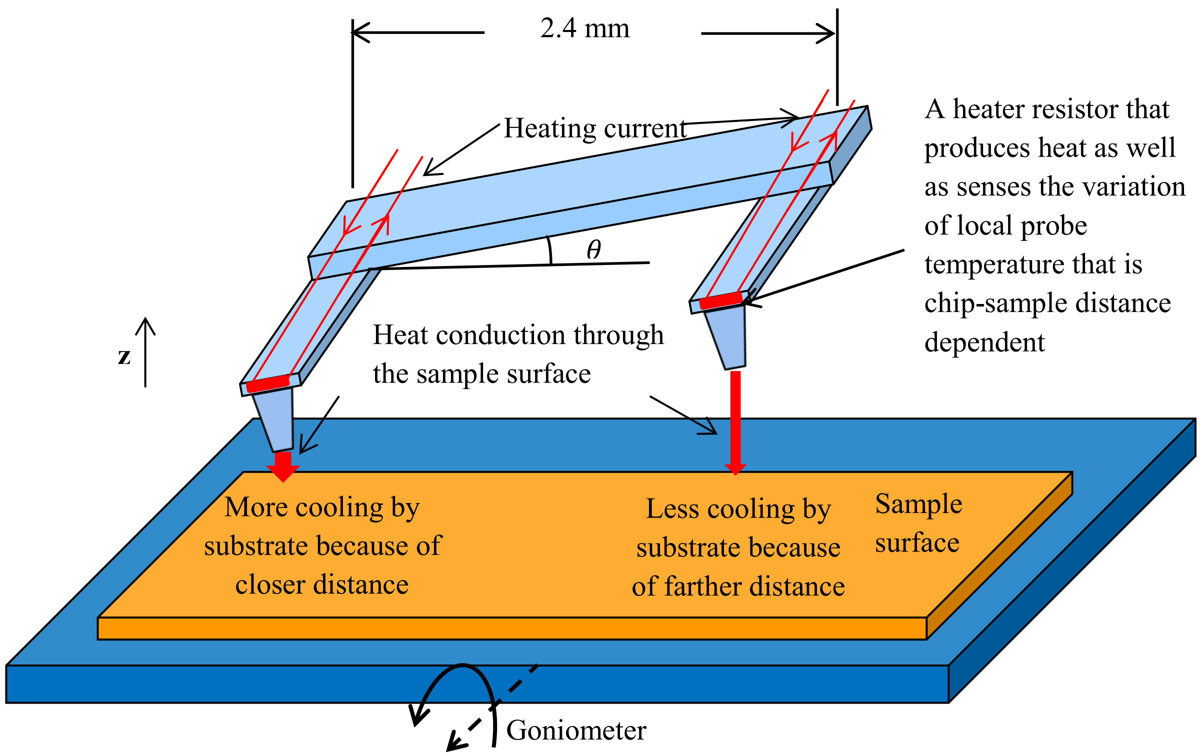

Fig. 5.8 Schematic of the on-chip ET position sensor illustrating its working principle.

5.1.3 Characterization of ET probe proximity sensor

Brief description of ET sensor deign technology

The ET probe proximity sensor design is implemented in the TowerJazz 0.35 μm SiGe BiCMOS process followed by the post-CMOS MEMS processing. As described in Chapter 3, the CMOS chip from the foundry is later processed with an anisotropic oxide etch, and then a directional silicon etch followed by an isotropic silicon etch to undercut the structure for the release. Tips on the probe cantilever array are later deposited using EBID, but this step is omitted in the characterization reported in this chapter.

SEM of sensor structures

Fig. 5.9 (a) and (b) shows the SEM images of the released ET probe proximity sensors on the CMOS chip. Two sensors are placed on two corners of the chip, between which lies a 1 × 5 probe array. Fig. 5.9 (c) shows the layout design details at the ET probe end. The tip end is embedded with an unsilicided polysilicon resistor with a high sheet resistivity of around 1100 Ω/sq, which is referred to as an “HP” resistor in the TowerJazz process. The “HP” resistor has a temperature coefficient of resistance (TCR), measured around −1200 ppm/K [25], which is large relative to other CMOS resistors and is favorable for high sensor temperature sensitivity. The locations of the thermal isolation structures are indicated in the image. These structures thermally isolate the tip from the CMOS substrate. The base of the cantilever looks similar to the ET actuated probes, however the actuation heater is not used in this device.

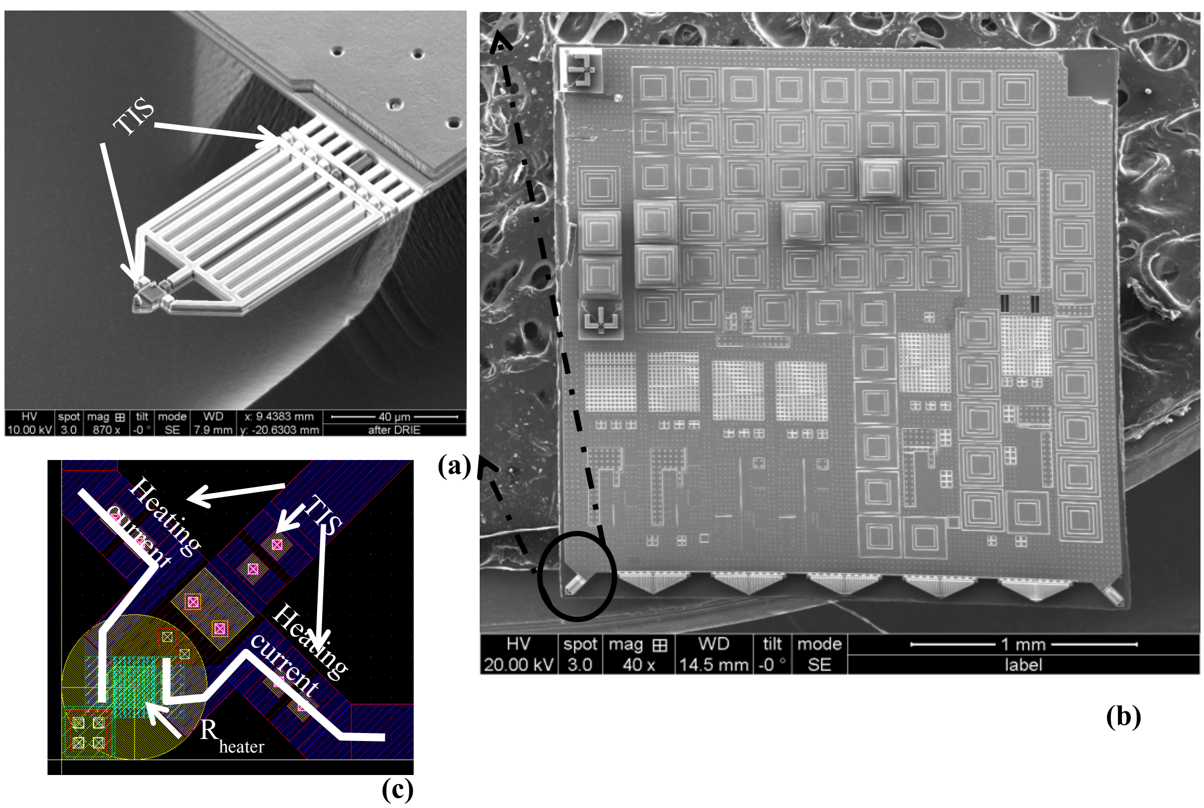

Fig. 5.9 SEM images of the ET probe sensor: (a) The ET probe sensor on one corner of the chip. (b) A full CMOS chip on which the ET probe sensor are placed. (c) Layout showing structure details of the ET sensor.

Test bench setting

Fig. 5.10 shows the custom test-bench used to characterize the ET probe proximity sensor. The global probe array chip is mounted on a motor that is able to move the chip in a large range of 50 mm in the x, y and z directions. A gold-coated silicon substrate is put on a piezostage, with a minimum step of movement of 1 nm and a travel range of 200 µm in the x, y and z directions. The probe chip is first moved to within the range of the piezostage travel distance via the motor, and then the sample is brought up step by step towards the probe chip via the piezostage. The heater resistance is recorded at every step change.

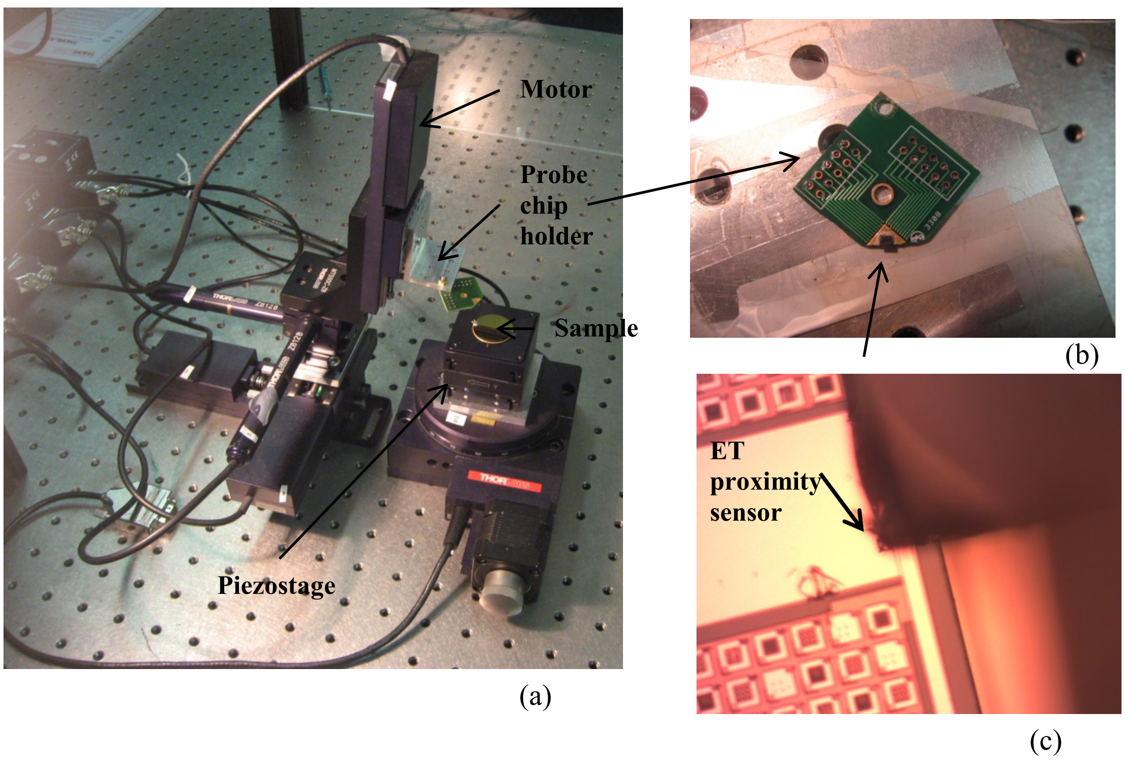

Fig. 5.10 The test-bench setup for characterization of the ET probe position sensor: (a) Motor and piezostage. (b) Probe holder with probe chip. (c) Top view of the ET probe position sensor over the sample surface.

Determine RT heater resistance

The resistance of the polysilicon heater of the ET probe proximity sensor at room temperature (RT) in air was first determined and used as the reference resistance. The ET probe stood isolated, centimeters away from the substrate. A constant current sourced by a current sourcemeter was passed through the tip heater resistor to provide the heating power. The heater resistance was measured at different heating powers. With the current increased up to 100 μA, the resistance kept constant, around 2193.9 Ω. Therefore, the RT resistance of the heater is defined to be 2193.9 Ω. At current level lower than 100 μA, the temperature change of the heating resistor arising from the generated joule heat was below the resolution of the resistance measurement setup. When the current was further increased, the resistance started to go down, indicating that the temperature rise started to fall within the measurement resolution. The resistance reduced to 1645 Ω at a source current of 1 mA.

R measured at low heating power in approach

The measurement of the heater resistance was then carried out as the ET probe was moved towards the sample. Fig. 5.11 (a) shows the heater resistance change when a constant current of 100 μA passes through the heater resistor. The *x*-axis of the plot stands for the displacement of the piezostage towards the ET probe. The resistance stays at a constant value of 2193.9 Ω until the piezostage moves up by 70 μm, at which point the resistance starts to rise. The resistance curve ascends gradually and reaches a plateau of 2195.8 Ω at a piezostage displacement of 87 μm, at which point the tip and the sample come into contact, and does not increase any further with further upward movement of the piezostage. The total resistance change is 1.9 Ω, corresponding to a temperature decrease of 0.7 K.

R measured at high heating power in approach

By comparison, with a current of 1 mA flowing through the heater resistor, its resistance starts with 1645.4 Ω when it is away from the substrate, and ends up with 1690 Ω as the two get into contact, corresponding to a temperature decrease of 17.3 K, as shown in Fig. 5.11 (b). The resistance does not reduce to its RT value upon contact, which means the tip is still hot. A much larger increase of the heater resistance indicates that by applying a higher power during ET probe tip-sample approach, the positioning sensitivity is enhanced.

Plot of $\Delta R/\Delta x$ vs. tip-sample separation

The rate of change of the resistance of the heater resistor at different ET probe tip-sample separations is constructed based on the data of Fig. 5.11 (b) where 1 mA current passes through the resistor, and is shown in Fig. 5.12. The resistance has a jump of 21 Ω at a piezostage displacement of 78 μm, which is defined as the tip-sample contact point, *i.e.*, zero separation. A further resistance increase from 1690 Ω to 1695 Ω beyond 78 μm is due to the tip pushing against the substrate and the accompanied improvement in heat conduction. The body of the probe also moves closer to the sample surface after tip contact, further enhancing the air conduction. This after-contact resistance change is not shown in Fig. 5.12. When the tip-sample distance is larger than 10 μm, the measured resistance change is smaller than 3 Ω/μm. As the tip-sample distance decreases to ~ 1 μm, the resistance change increases to 12 Ω/μm. Because of the high sensitivity of the ET probe proximity sensor when it is 1 μm or less above the sample surface, it will be easy to identify when the sensor enters sub-micron range above the sample surface. When both ET sensors, spaced 2.4 mm apart, enter sub-micron range above the sample surface via the alignment adjustment of the macro-goniometer, the non-parallelism between the probe-chip and the sample surface will be reduced to below 0.024°.

To evaluate the point of contact between the tip and the sample as defined by the resistance jump of the heating resistor during the ET proximity sensor's approach to the sample surface, a layer of gold can be deposited on the cantilever end of the ET proximity sensor. The resistance between the cantilever tip and the sample will be monitored during the tip-sample approach. When the tip and sample get in contact, the tip-sample resistance will be reduced to a few ohms, providing an "absolute" point of contact, which can be used to calibrate the point of contact as defined using ET proximity sensor. Alternatively, a dedicated piezoresistive sensor can be integrated on the cantilever to detect the probe bending, arising from either temperature variation or probe-sample contact. With reduced step length, more data should be taken to have a more accurate measurement of sensitivity and resolution of the ET proximity sensor. This constitutes part of the work in the future.

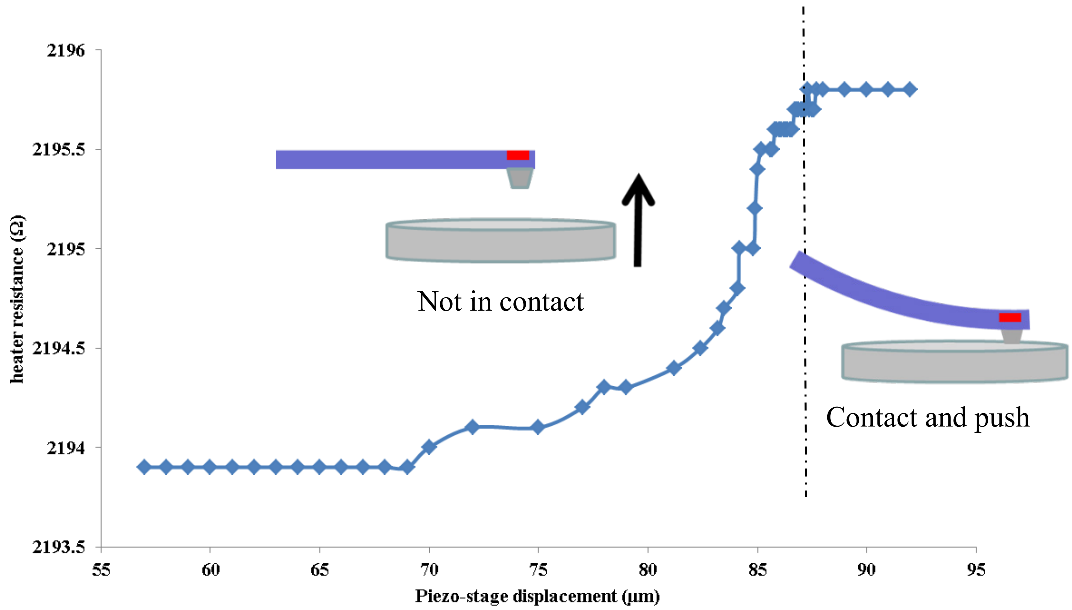

(a)

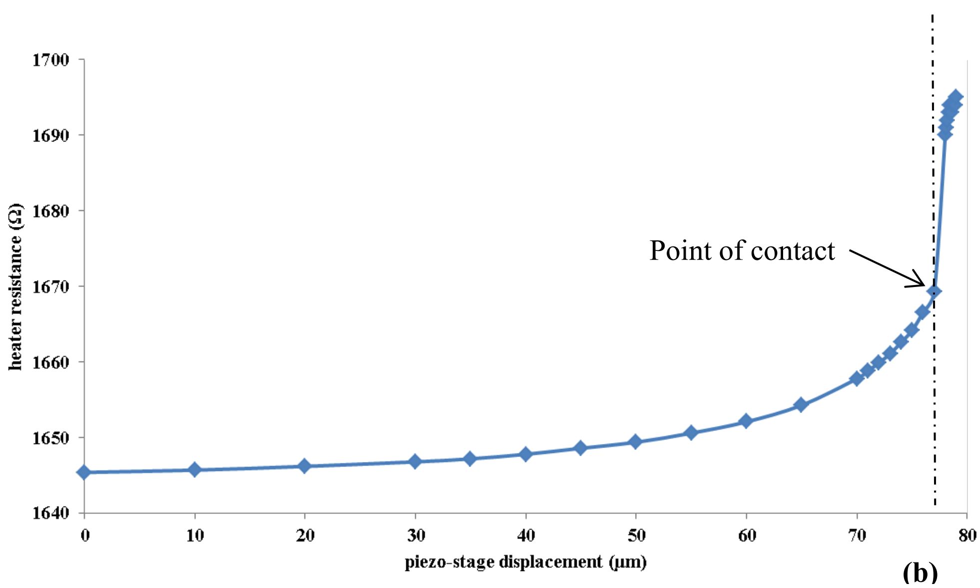

(b)

Fig. 5.11 Heater resistance *vs.* piezo-stage displacement at different current supply: (a) 100 µA. (b) 1 mA.

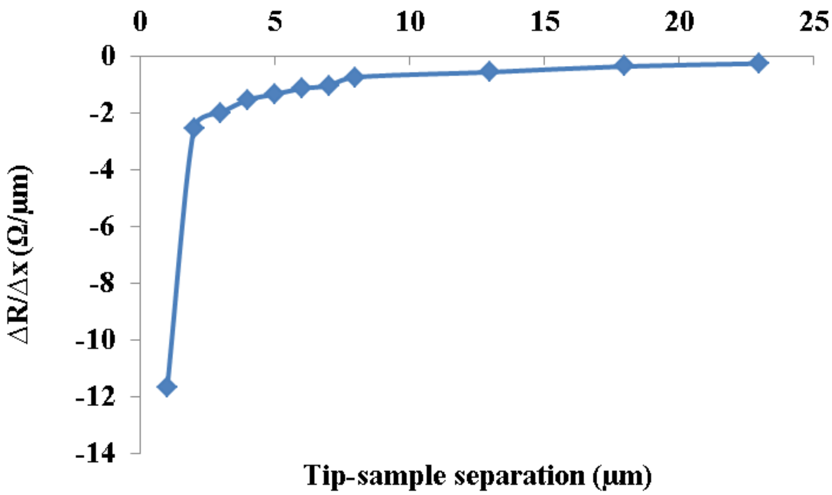

Fig. 5.12 Resistance change of the heater in the ET probe sensor *vs.* the probe tip-sample separation.

Angular accuracy of ET sensor

Given the spacing of ~2.4 mm between two sensors on the CMOS chip, a positioning accuracy of 1 µm corresponds to a non-parallelism of 0.024°. Therefore, after an adjustment by the on-chip ET proximity sensor pair and a macro-goniometer with a travel range of 10° and resolution of 0.001°, the non-parallelism of the probe chip and the sample substrate will be reduced to the order of magnitude of 0.024°. As mentioned previously, a probe chip–sample misalignment of 0.024° indicates a 21 nm height difference between two array probes spaced at 50 µm, and hence can be compensated for by the active ET-actuated array probes that have a designed vertical travel range of 200 nm. Alternatively, this remained misalignment may also be further realized by an on-chip micro-goniometer, which is introduced in the next section.

5.2 On-chip MEMS micro-goniometer

Introduce goniometer

An on-chip micro-goniometer, like its macroscale counterpart, is to provide an adjustment of the angular direction of the objects that are placed on it. When the spacing of STM array probes is scaled down to tens of microns, it becomes possible to place an array of probes on a micro-goniometer. The goniometer achieves fine angular adjustment to compensate for height difference and cantilever curl-up difference among array probe tips caused by process variations, as well as the remaining probe chip-sample non-parallelism after the coarse angular adjustment.

5.2.1 Design

Goniometer structure

The schematic design of the on-chip micro-goniometer is shown in Fig. 5.13. The micro-goniometer consists of two separate "trunk cantilevers" which can be individually actuated, a leveling beam connecting to (bridging) the trunk cantilevers through two twist beams, and an array of active SPM finger probes placed along the leveling beam, with a spacing of 15.1 μm between two neighboring finger probes. Similar to the widely-spaced array probes, the micro-goniometer also adopts electrothermal actuation as its driving approach.

Goniometer working mechanism

When the two trunk cantilevers are unevenly heated, *i.e.*, different drive powers are applied on two ET actuators, the two trunks will have different vertical *z* displacements, so one end of the leveling beam will be elevated higher than the other end, and the relative height among finger probes is therefore changed. When landing above the surface for scanning, the leftmost and rightmost finger probes in the 1D array can be made within the tunneling distance above the surface at the same time through this relative height adjustment through the goniometer. The height of other finger probes relative to the surface will be adjusted via the on-probe ET actuators of themselves to compensate for tip-to-tip height difference introduced by the manufacturing variation.

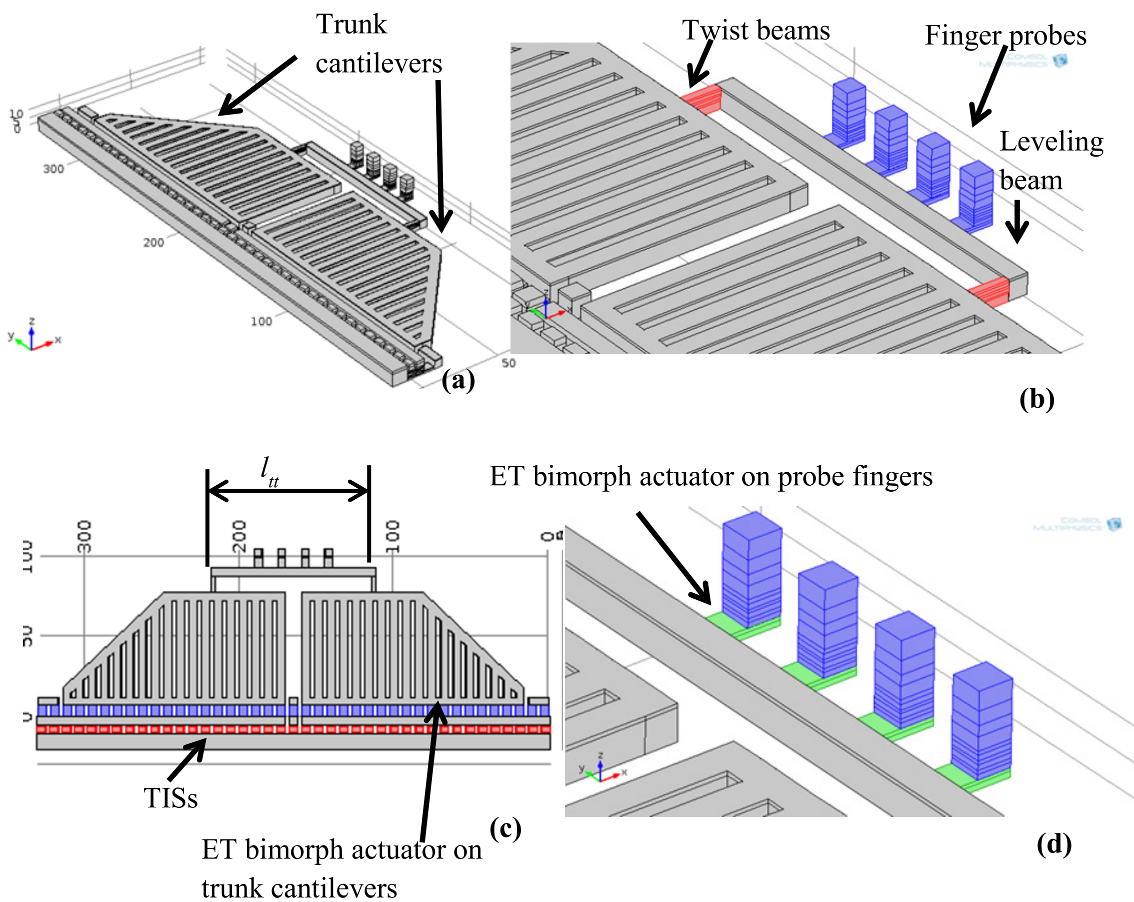

Fig. 5.13 Schematic design of an on-chip micro-goniometer with scaled finger probe arrays: (a) Main body structure. (b), (c) and (d) Images showing the structure and component details on the goniometer.

Geometry sizing through force analysis

For sizing, the micro-goniometer is first subjected to a force analysis to study the relationship between the tilt of the leveling beam and the goniometer geometry. Fig. 5.14 shows the free-body diagram of the goniometer when an external force, F, is applied on the end of the twist beam attached to the right trunk cantilever, at point D, located on the boundary between the twist beam and the leveling beam. The leveling beam at that point is lifted up accordingly. A reaction torque is exerted on each twist beam, and the rotation angle of the twist beams is equal to the tilt of the leveling beam. This logic assumes the leveling beam is designed to be much stiffer than the twist beams. This assumption will be verified late in this section. Fig. 5.14 (b) depicts the free-body diagram of the leveling beam: it is subjected to a pair of equal and opposite forces, F_C and F_D, exerted by the two twist beams, and two "pure" torques of the same direction exerted by the two twist beams. The force couple on the leveling beam, F_C and F_D, for which the amount of the net force is zero, produces a net torque that counteracts the sum of the "pure" torques. Since F_C and F_D are equal in magnitude, F_L is used to represent their magnitude. Fig. 5.14 (c) depicts the free-body diagram of the twist beams: each is subjected to a pair of moment, τ_L. Fig. 5.14 (d) shows the resultant tilt of the leveling beam.

As depicted Fig. 5.14 (d), a force of F_C is applied on the left trunk by the leveling beam, and a total force of $(F - F_D)$ is applied on the right trunk. Therefore, the displacement situated at the end of the left trunk cantilever, at point C, and that of the right cantilever, at point D, respectively, are:

$$Z_c = \frac{F_C}{k_z} \tag{5.16}$$

$$Z_D = \frac{F - F_D}{k_z} \tag{5.17}$$

where k_z is the spring constant of a single trunk cantilever.

At equilibrium, the total torque, τ, resulting from the tilt of the leveling beam and exerted on two twist beams is

$$\tau = 2 * \tau_L = F_L l_{tt} \tag{5.18}$$

where l_{tt} is the spacing between two twist beams.

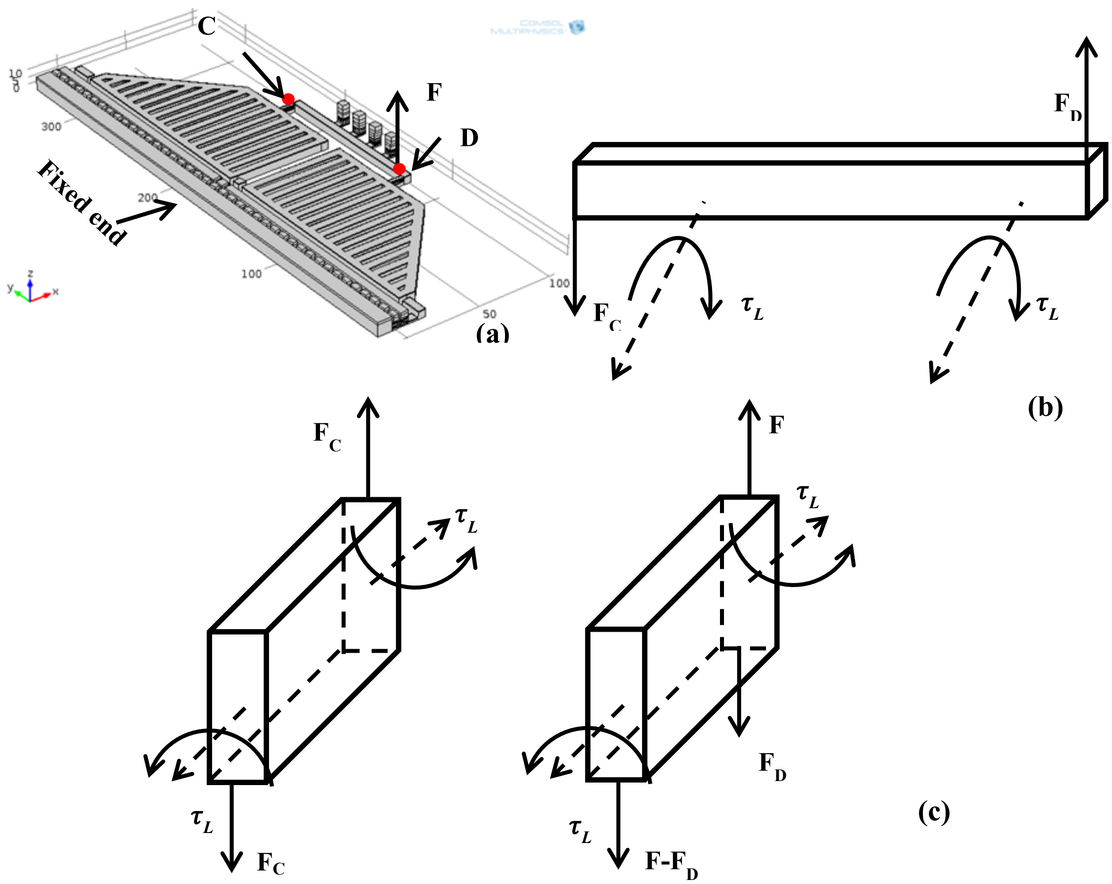

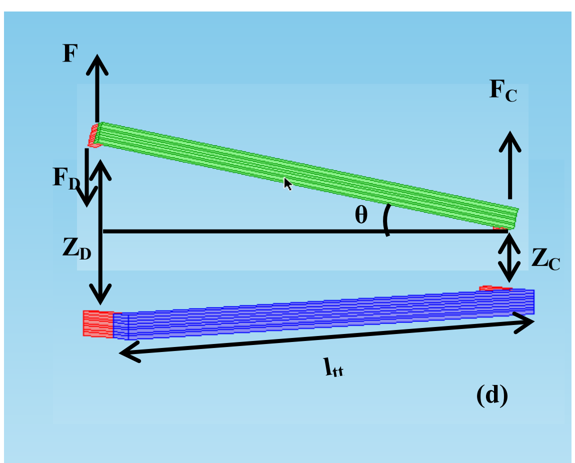

A total force of (F-F_D) is applied on the right trunk, resulting in a displacement of Z_D, and a total force of F_C is applied on the left trunk, resulting in a displacement of Z_C. Since Z_D and Z_C are not equal, the leveling beam tilts.

Fig. 5.14 Free-body diagram of the goniometer: (a) The micro-goniometer subjected to an external force, F. (b) The resulted forces and moments exerted on twisted beams. (c) The tilt of the leveling beam due to the twist.

So the twist angle, θ, is calculated as

$$\theta = \frac{\tau_L}{k_\theta} = \frac{F_L l_{tt}}{2k_\theta} \tag{5.19}$$

where k_θ is the torsion constant of one twist beam, and is given by

$$k_\theta = \frac{GJ}{l_{tw}} = \frac{EJ}{2(1+\upsilon)l_{tw}} \tag{5.20}$$

G, E, υ, J and l_{tw} are the shear modulus, Yong's modulus, Poisson's ratio, torsional spring constant and the length of the twist beam, respectively.

For a rectangular beam with a section dimension of 2a by 2b where a≥b, J is given by

$$J_{rec} = ab^3\left[\frac{16}{3} - 3.36\frac{b}{a}\left(1 - \frac{b^4}{12a^4}\right)\right] \tag{5.21}$$

On the other hand, θ, the twist angle of the twist beams, is equal to the tilt of the leveling beam, and is expressed as

$$\theta = \frac{Z_D - Z_c}{l_{tt}} \tag{5.22}$$

Combine (5. 3) to (5. 9) and solve for F_C, F_D and θ, we obtain

$$F_C = F_D = F_L = \frac{F}{\frac{{l_{tt}}^2 k_z}{2k_\theta} + 2} \tag{5.23}$$

$$\theta = \frac{F}{l_{tt}k_z + \frac{4k_\theta}{l_{tt}}} \tag{5.24}$$

Determine optimum spacing

For a given geometry of the trunk cantilever, an optimum distance between the two twist beams, l_{tt}, exists for the maximum tilt. The maximum value of θ at a fixed external force, F, occurs when the denominator of (5.24) is the minimum, which is found by differentiating the denominator and equal it to zero. The optimum value of l_{tt} is

$$l_{tt} = \sqrt{\frac{4k_\theta}{k_z}} \tag{5.25}$$

Substituting (5.25) into (5.24), the maximum tilt is

$$\theta_{max} = \frac{F}{4\sqrt{k_\theta k_z}} \tag{5.26}$$

Examine length of twist beam that affects both kz and $k\theta$

For a larger tilt, a smaller product of k_θ and k_z is desired. There are several constraints, however, in the sizing of the goniometer. First, the CMOS design rules and post MEMS processing places a constraint on the thickness and the width of the twist beams. In the first generation of design, the top metal of the twist beams is chosen to be metal-4, so the thickness of the twist beams is fixed, determined by the adopted CMOS process of the foundry, which is around 5.4 µm in TowerJazz 0.18 µm SiGe BiCMOS technology. The minimum structure width dictated by the MEMS design rule is 1 µm. A width of 2 µm is decided for the twist beam to avoid possible breaking during MEMS structure release. A trade-off has to be made in determining the length of the twist beam. Following (5.20) and (5.24), a larger twist beam length is desired for smaller torsion constant and the resultant larger tilt degree. As stated in Chapter 2, however, minimum probe stiffness is required for a single probe to perform STM operation. A simplified beam model of the trunk cantilever is built to evaluate the effect of the twist beam length, l_{tw}, on the trunk cantilever stiffness, k_z, the torsion constant of the twist beam, k_θ, and their product, $k_\theta k_z$. Fig. 5.15 shows the simplified geometry of a single trunk cantilever. It consists of three parts: a metal-1 bimorph beam, a metal-4 extension beam and a metal-4 twist beam. The total length of the trunk, l_{tot}, is set to be 97 µm; the length of the metal-1 beam bimorph ET actuator, l_{m1}, is set to be 7 µm; the width of the metal-1 beam and that of the metal-4 extension beam, w_{tk}, is 95 µm. These three sizes are chosen comparable to the length of the active CMOS MEMS probe in chapter 2. The length of the twist beam, l_{tw}, is varied and k_z, k_θ and their product, $k_\theta k_z$, is examined. As shown in Fig. 5.16, with increasing twist beam length, the probe stiffness decreases and the twist beam torsion constant increases. The product of these two quantities decreases with the twist beam length. Therefore, the length of the twist beam should be as large as possible to maximize the twist angle. The minimum required trunk stiffness is determined by the number of finger probes on the goniometer that will be operating in parallel. For the operation of a single probe, the overall stiffness of the goniometer, $2k_z$, should be larger than 26 N/m. Table 5-3 summarizes the values of parameters used in the evolution of k_θ and k_z.

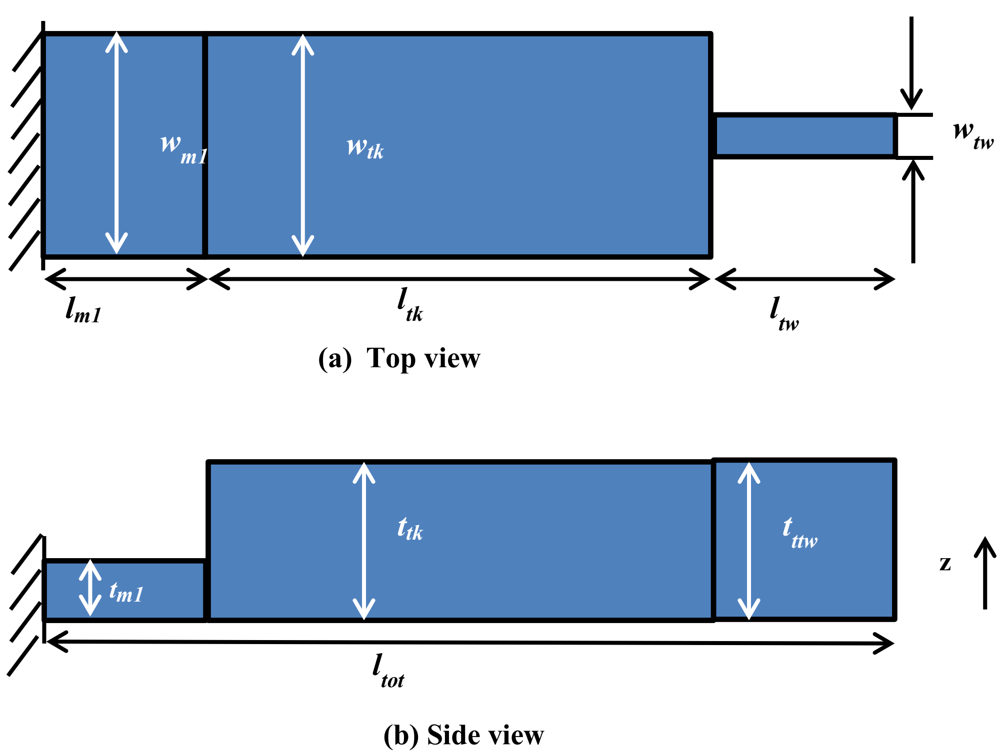

Fig. 5.15 Simplified geometry of a trunk cantilever of the micro-goniometer.

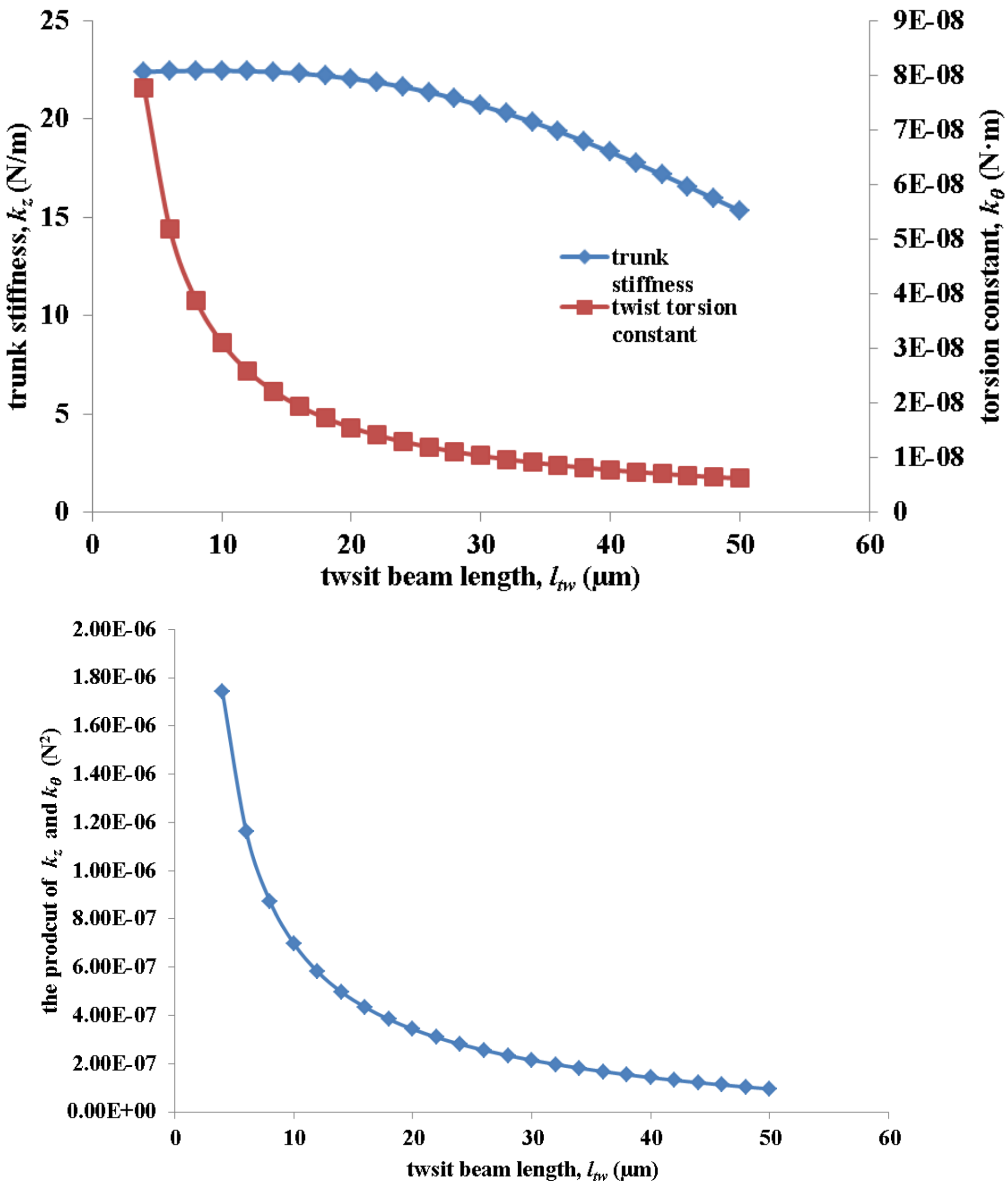

Fig. 5.16 (a) The variation of the trunk stiffness, $\boldsymbol{k_z}$, and the twist beam torsion constant, $\boldsymbol{k_\theta}$, with the twist beam length, $\boldsymbol{l_{tw}}$. (b) The variation of the product, $\boldsymbol{k_\theta k_z}$, with $\boldsymbol{l_{tw}}$.

Table 5-3 *Parameters used in the estimation of trunk spring constant, k_z, and twist beam torsion constant, k_θ*

Parameters	**Value**	**Description**
t_{tw}	5.4 µm	Twist beam thickness
t_{tk}	5.4 µm	Extension metal-4 beam thickness
t_{m1}	1.38 µm	Bimorph metal-1 beam thickness
w_{tw}	2 µm	Twist beam width
w_{tk}	95 µm	Extension metal-4 beam width
w_{m1}	95 µm	Bimorph metal-1 beam width
l_{tw}	Vary	Twist beam length
l_{tk}	Vary	Extension metal-4 beam length
l_{m1}	7 µm	Bimorph metal-1 beam length
l_{tot}	97 µm	Total length of the trunk cantilever
E	70 GPa	Young's modulus
ν_{ox}	0.17	Poisson's ratio of SiO_2
ν_{Al}	0.35	Poisson's ratio of Al

In the first generation of goniometer design, the length of the twist beam is 9.9 µm and that of the extension metal-4 beam is 80 µm, so the spring constant of a single trunk cantilever is around 20 N/m. This probe stiffness guarantees the stable STM operation of one finger probe. By reducing the total length and/or increasing the width of the trunk cantilever, stiffer probe can be realized for operation of more probes in parallel.

Given the selected values of the trunk cantilever sizing and using the Poission's ratio of Al and SiO_2, 0.35 and 0.17, respectively, the upper and lower limit of the optimum spacing between the twisted beams is calculated to be 76 µm and 81 µm, respectively.

In the geometry sizing of the leveling beam, the length of the leveling beam is 105 µm, equal to the spacing of the two twist beams. The thickness of the leveling beam is 5.4 µm, which is same as that of the twist beam. As stated previously, an assumption is made that the rotation angle of the twist beams is equal to the tilt of the leveling beam. For this assumption to be valid, the width of the leveling beam needs to be large enough so that the contribution of the bending of the leveling beam to the total tilt is small compared to the contribution of the rotation angle of the twist beams. Fig. 5.17 shows the free-body diagram of the leveling beam. The boundary conditions of the beam are the fixed-guided end configuration. The shape function of the beam is

$$z_{lel} = \frac{F_L x^2 (3l_{tt} - 2x)}{12(EI)_{lel}} \tag{5.27}$$

And the slope of the beam is

$$s_{lel} = \frac{F_L x (l_{tt} - x)}{2(EI)_{lel}} \tag{5.28-a}$$

The maximum slope of the beam occurs at the middle point of the beam, *i.e.*, when $x = l_{tt}/2$:

$$s_{lelx} = s\left(\frac{l_{tt}}{2}\right) = \frac{F_L {l_{tt}}^2}{8(EI)_{lel}} \tag{5.28-b}$$

The ratio of the bending of the leveling beam to the rotation angle of the twist beams is obtained by dividing (5.28-b) by (5.19), and evaluated using the values of the parameters in Table 5-3:

$$\frac{s_{lel}}{\theta} \leq \frac{s_{lelx}}{\theta} = \frac{k_\theta l_{tt}}{4(EI)_{lel}} = \frac{3k_\theta l_{tt}}{(Ew_{lel}t_{lel}^3)} \approx \frac{0.85}{w_{lel}} \tag{5.29}$$

In the current design, the width of the leveling beam is 5.1 μm, so $s_{lelx}/\theta = 0.17$. A larger width of the leveling beam can be chosen to reduce the ratio.

FEM and analytical result

Fig. 5.18 shows change of the tilt angle of the goniometer when a force of 100 μN is applied to the end of one of the trunk cantilevers, derived from the analytical calculation and the FEM simulation in COMSOL, respectively. The maximum twist occurs when two twist beams is around 78 μm apart as predicted by FEM, which verifies the analytical result.

Geometry in practical design

In the practical design, the spacing between the two twist beams is chosen to be 105 μm. It is chosen so since the tilt at the spacing of 105 μm is 1.38°, only 4% smaller than the tilt of 1.42° at the spacing of 78 μm, but a longer leveling beam may hold more finger probes.

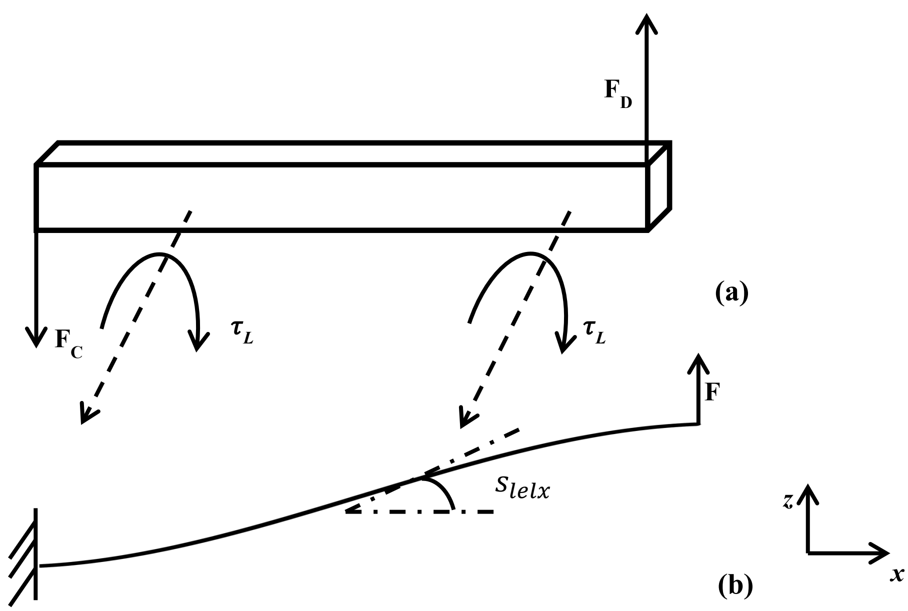

Fig. 5.17 (a) The free-body diagram of the leveling beam; (b) The deflection shape of a fixed-guided the beam subjected to a force, F.

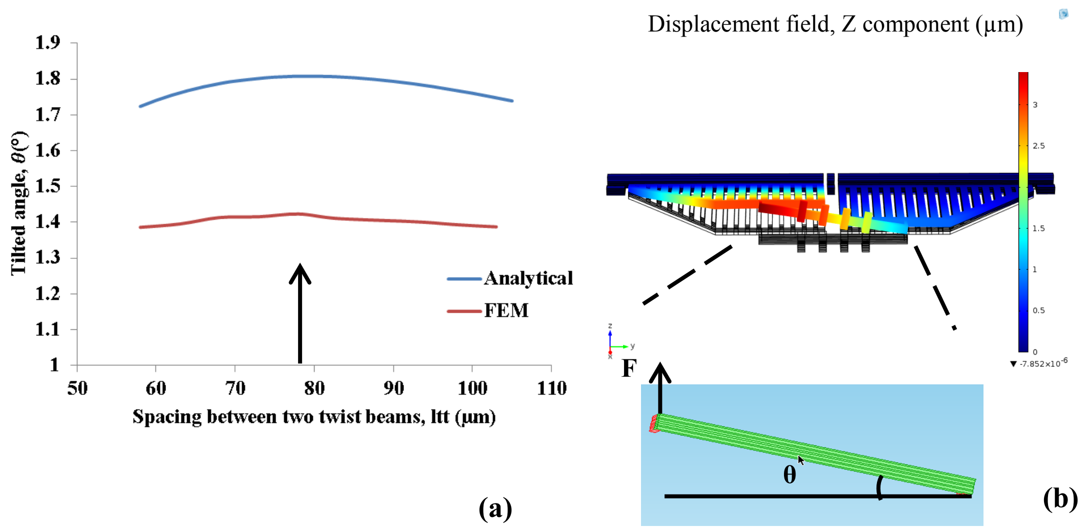

Fig. 5.18 (a) Tilt angle of the leveling beam *vs.* the spacing between two twist beams when a force of 100 µN is applied on one side of the goniometer. (b) A 3D simulated image showing the tilt of the goniometer. The displacement of the goniometer is scaled by 10 times for a better visualization of the tilt of the leveling beam.

FEM to examine tilt at different powers

3-D multi-physics (coupled structural and thermal) FEM simulation in COMSOL is used to examine the tilt of the leveling beam when one of the trunk cantilevers of the goniometer is driven at different ET powers. Since the ET actuators on the CMOS chip can be heated up to 525 K without producing damages [83], the trunk cantilever is heated to a similar level of temperature to examine the maximum possible tilt. A tilt of 1.09º is achieved when the trunk cantilevers is heated to 539 K while the other is kept unheated, which will be sufficient for the fine adjustment of the relative height among finger probes.

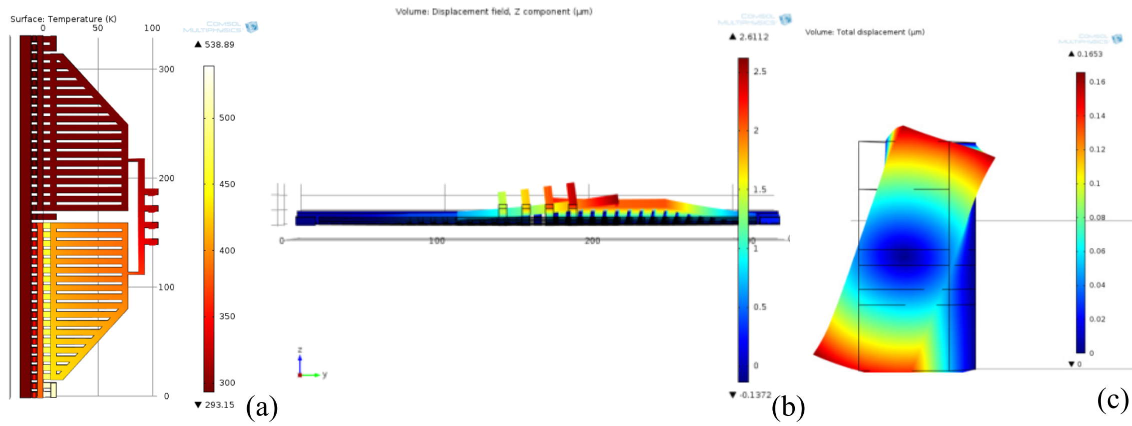

Fig. 5.19 FEM of the micro-goniometer when unevenly heated: (a) The ET actuator on one trunk cantilever is heated to 539 K. (b) The leveling beam twist due to the height difference between two trunk cantilevers. The tilt is 1.09°@539 K. (c) Cross-section of the twist beam showing its rotation.

Like the widely-spaced array probes, the small finger probes in the array on the micro-goniometer are individually addressable, equipped with their own ET bimorph actuator and current sensing electronics.

5.2.2 Characterization of micro-goniometer

Structure release description

The design of the micro-goniometer with a scaled version of CMOS-MEMS probe array is implemented via TowerJazz 0.18 μm SiGe BiCMOS technology. The CMOS chip is processed with an anisotropic oxide etch to etch the CMOS oxide stack, which is about 13 μm thick. Then a ~10 μm directional silicon DRIE is performed followed by a ~10 μm isotropic silicon etch to undercut the structure for the release.

SEM and Wyko images@ fresh chip

Fig. 5.20 shows the SEM images of the released goniometer. An array of four finger probes is located along the leveling beam. A Veeco WYKO NT3300 white-light interferometer is used to examine the height profile of the goniometer, as shown in Fig. 5.21. The four finger probes have a 3.2 μm upward tip deflection above the top metal-6 main chip body. The deflection difference among finger probes is smaller than 100 nm. Fig. 5.22 shows the height profile of the leveling beam with no power applied to the actuators. The height difference between the highest point and the lowest point on the leveling beam is small, around 0.25 μm, corresponding to a curvature of around 1.79×10^{4} μm^{-1}.

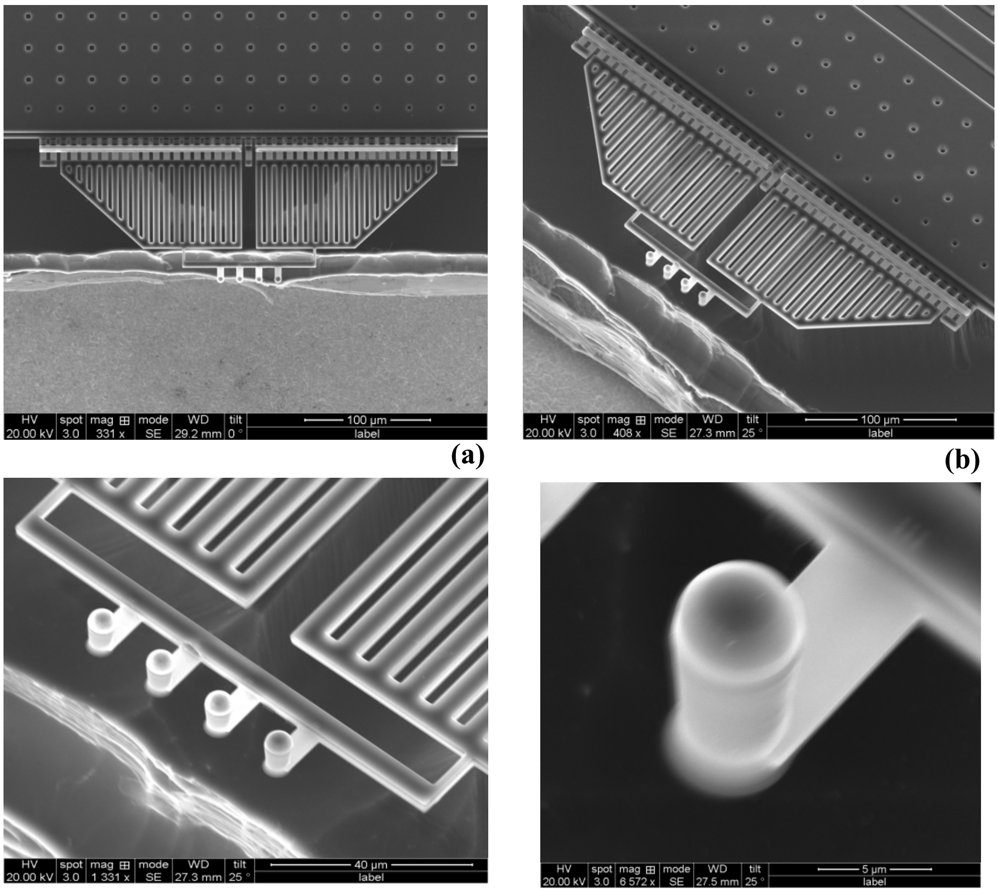

(a) (b)

(c) (d)

Fig. 5.20 SEM images of micro-goniometer: (a) Top view. (b) Tilted view. (c) Leveling beams with finger probe array. (d) A single finger probe.

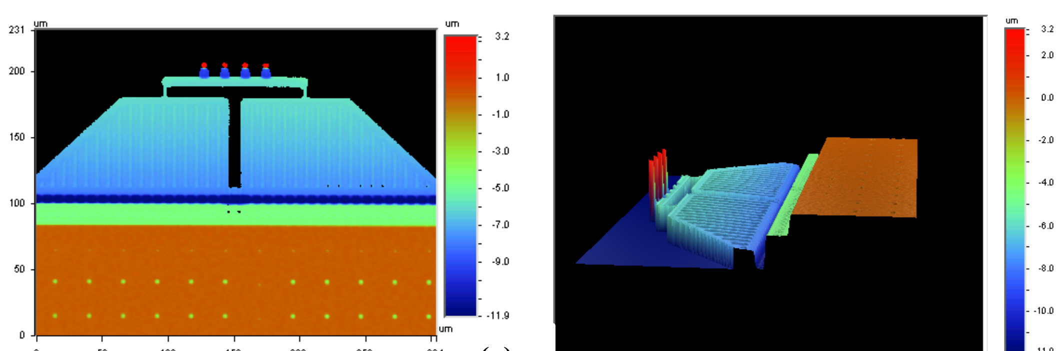

(a) (b)

Fig. 5.21 Fresh released goniometer profile taken on the WYKO interferometer: (a) 2D contour. (b) 3D contour.

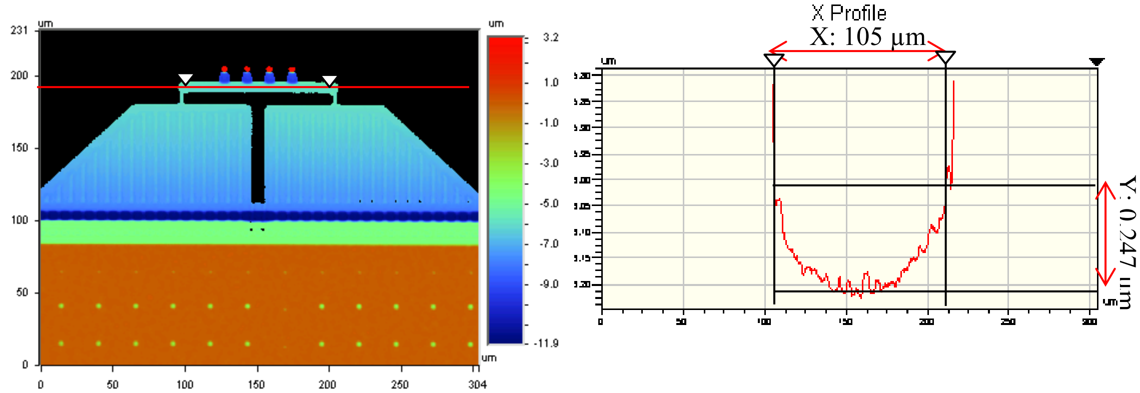

Fig. 5.22 The height profile of the leveling beam upon structure release. The leveling beam is relatively straight, with a small but measurable curvature.

Tilt-power relation

Different drive powers were applied on two trunk cantilevers to measure the tilt of the leveling beam. It is found that a critical power exists. Below the critical power, the tilt of the leveling beam has a linear dependence on drive powers, and the deformation is reversible, *i.e.,* the trunk cantilevers on the goniometer recover their original shape. Above the critical power, the leveling beam is not straight anymore but bends. Furthermore, irreversible deformation of the probe structure occurs, *i.e.*, the leveling beam tilt remains after the power has been removed.

To facilitate the description, it is defined that when the left trunk is higher than the right one the tilt angle is positive, and when the left trunk is lower than the right one the tilt angle is negative. Left and right are defined relative to the image in Fig. 5.22.

Working region of reversible deformation

Tilt vs power relationship

The test started with a freshly released goniometer device. The drive power was applied on the right trunk cantilever of the goniometer, while the left trunk was not powered. The power was varied between 0 W and 32.2 mW and never went beyond this range. Fig. 5.23 (a) shows the variation of the tilt angle with the power. The tilt angle is linearly dependent on the power and has a drive sensitivity of 0.038°/mW. Fig. 5.24 shows a case when a drive power of 32.2 mW is applied on the right trunk cantilever. The leveling beam tilt is 1.19°.

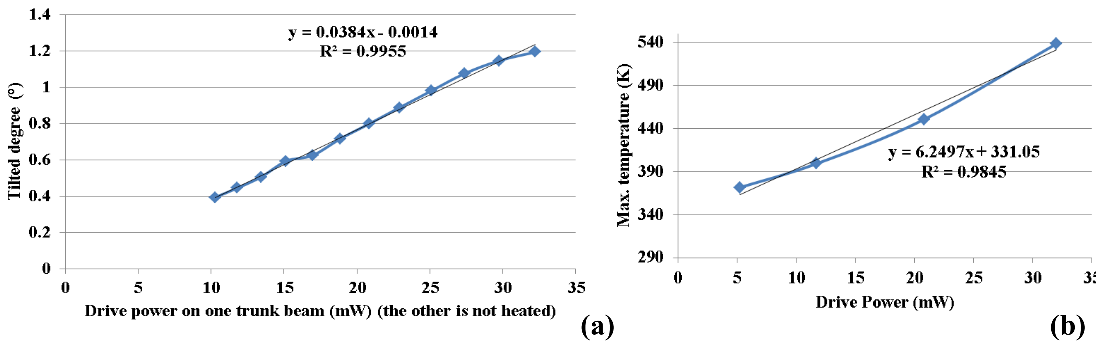

Fig. 5.23 (a) The tilt of the leveling beam *vs.* the drive power. (b) The maximum temperature on the goniometer *vs.* the drive power. The drive power is only applied on the right trunk cantilever. The goniometer had no previous heating history.

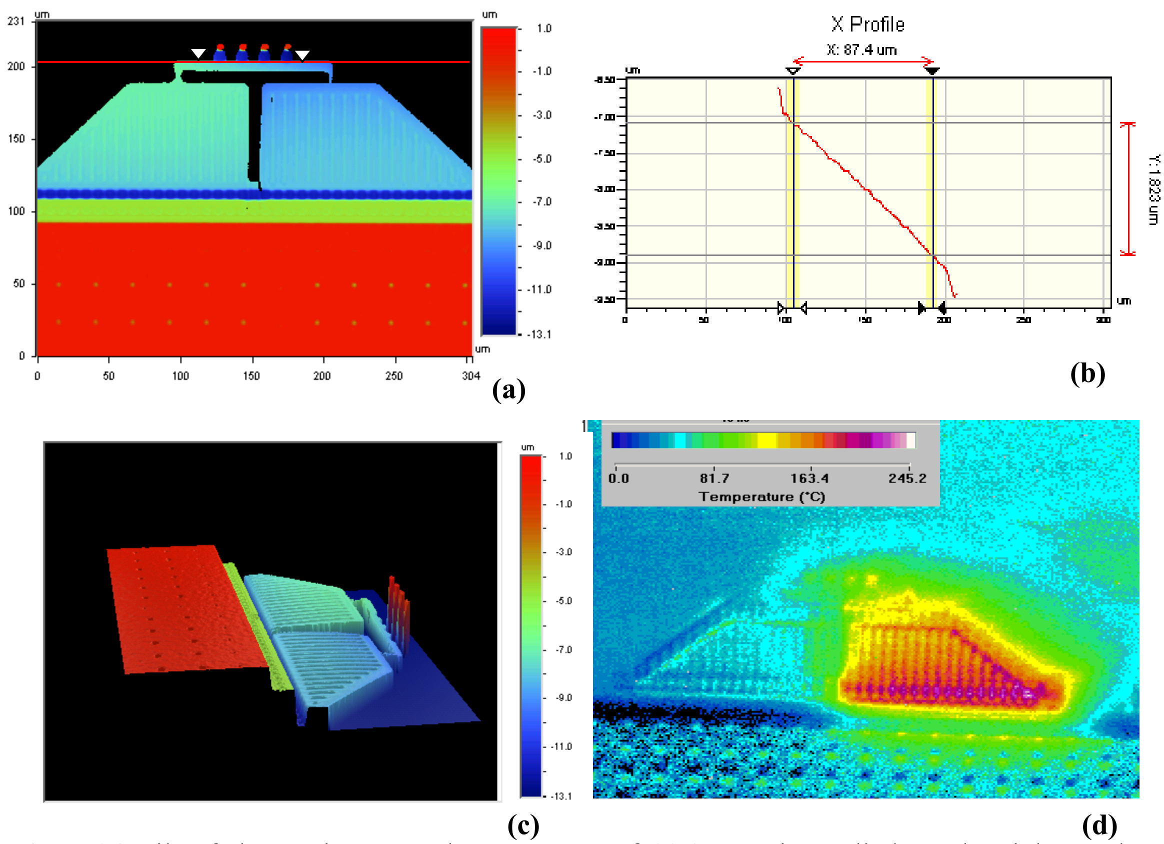

Fig. 5.24 Tilt of the goniometer when a power of 32.2 mW is applied on the right trunk cantilever: (a) 2D contour. (b) The tilt of the leveling beam. (c) 3D contour. (d) Temperature distribution on the goniometer.

The temperature of the micro-goniometer under different drive powers was examined using an infrared microscope. Fig. 5.24 (d) shows the temperature distribution of the goniometer when the right trunk cantilever is driven at 32.2 mW. The maximum temperature on the goniometer occurs at the bimorph actuator, around 518 K. The maximum temperature is linearly dependent on the power, as shown in Fig. 5.23 (b), and has a drive sensitivity of 6.2 K/mW.

No deformation below critical power

Little irreversible deformation, smaller than 100 nm, is left on the goniometer structure after the drive power up to 32.2 mW has been applied and then removed, as demonstrated in Fig. 5.25. An operation window is then defined where the tilt of the leveling beam has a linear dependence on the supplied power and no irreversible deformation occurs. This window provides a tilt range of ±1.19°.

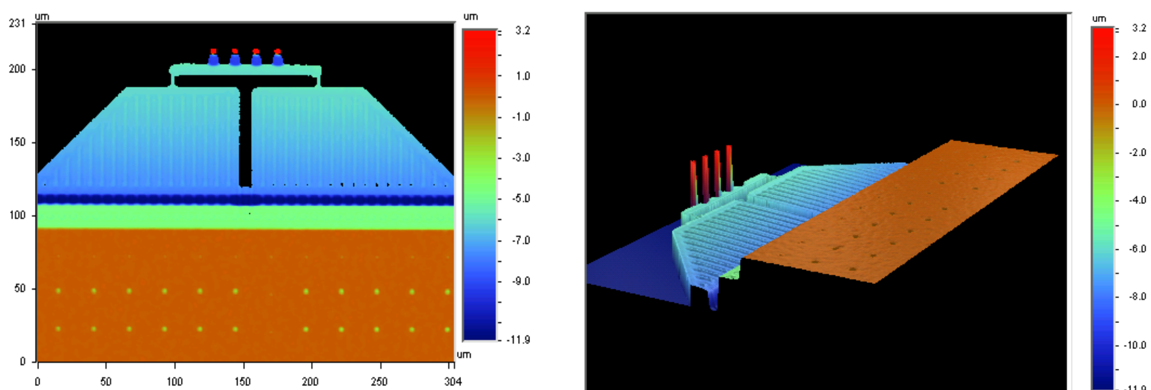

(a) (b)

Fig. 5.25 Goniometer profile after a power of 32.2 mW is applied on the left trunk cantilever and removed: (a) 2D contour. (b) 3D contour. Compared to the fresh goniometer, the irreversible deformation left after the heating history is smaller than 100 nm.

Working region of irreversible deformation

Leveling beam bends@ high power

When the drive power applied on the bimorph drive is above a critical point, the cantilever beam is not straight anymore, but bends and the tilt angle of the leveling beam cannot be well defined. Fig. 5.26 shows an example when a power of 66.7 mW is applied on the right trunk.

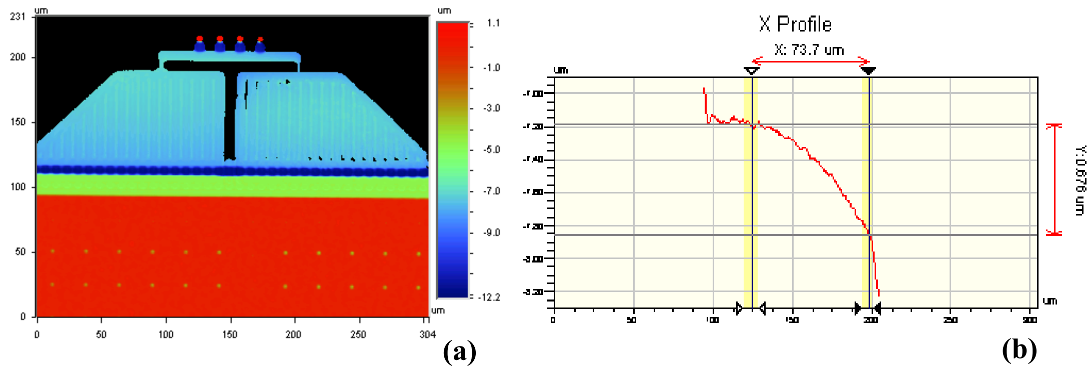

Fig. 5.26 Tilt of the goniometer when a power of 66.7 mW is applied on the right trunk cantilever: (a) 2D contour. (b) The tilt of the leveling beam. The leveling beam is not straight anymore but bends.

Discovery of irreversible deformation

Furthermore, irreversible deformation is introduced after a high drive power is applied and then removed from the trunk cantilever. It is found that the right trunk cantilever, which bends downwards upon heating and assumes a lower position than its left counterpart, restores to a higher position, resulting in a negative tilt angle. Fig. 5.27 shows a case where a power of 66.7 mW is applied on the right trunk cantilever and then removed. A tilt of −1.22° results.

Irreversible deformation dependence on power and time

To examine the time and power dependence of irreversible deformation, a freshly-released goniometer with no previous heating history and hence no irreversible deformation was chosen for test. A fixed drive power was applied to its right trunk cantilever, maintained for different durations and the leftover deformation was measured after the power was removed. The process is like “annealing”, heating the material to above a critical temperature, maintaining for a certain amount of time and then cooling. Fig. 5.28 (a) shows the evolution of the tilt of the leveling beam with “annealing” time at three different drive powers. At a fixed power, the tilt angle increased with the “annealing time”, showing a logarithmic time response with the time increasing up to 1000 s. Fig. 5.28 (b) shows the tilt angle dependence on the power. Irreversible deformation occurs at around 28.4 mW, as extrapolated from the graph. No higher power than

66.7 mW was applied on the trunk cantilever during the test to avoid any possible overheating and damage to the goniometer structure.

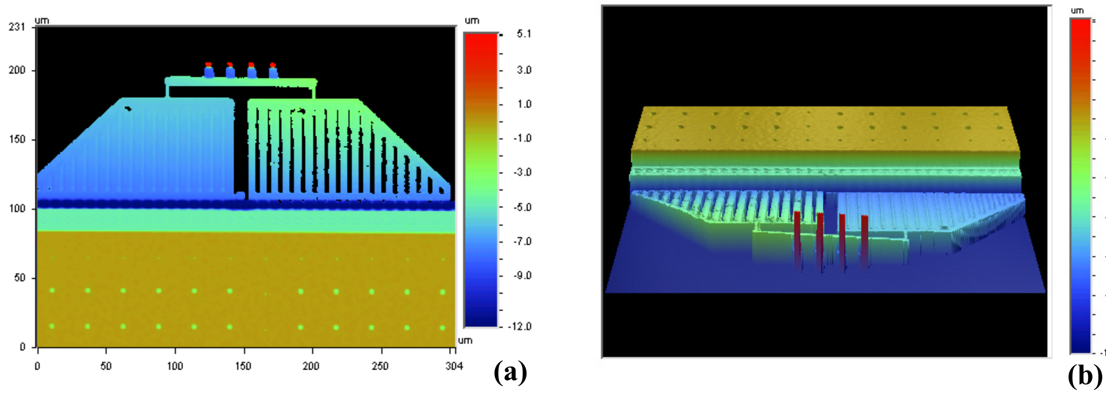

Fig. 5.27 Irreversible deformation on the goniometer after a drive power of 66.7 mW is applied on the right trunk cantilever and removed: (a) 2D contour. (b) 3D contour.

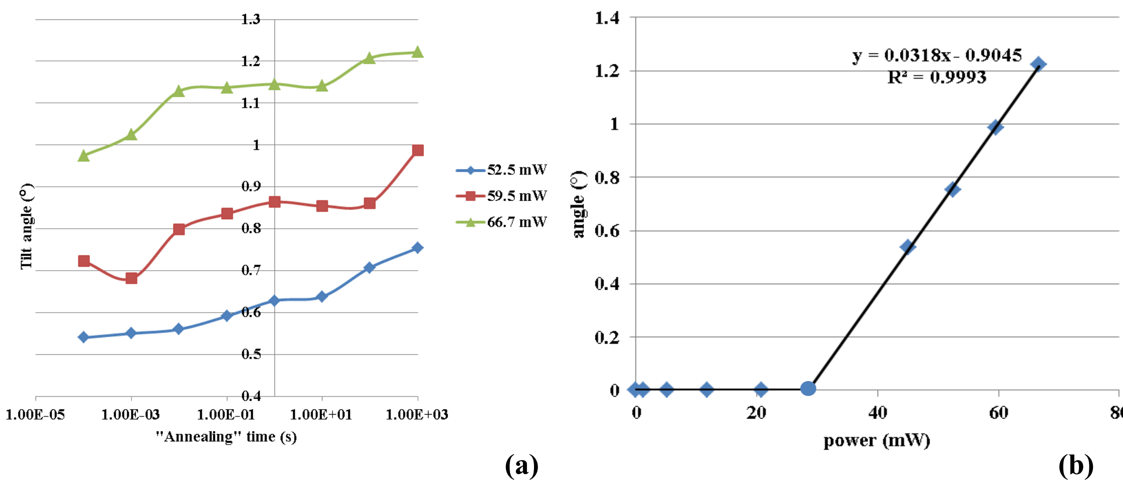

Fig. 5.28 (a) Permanent tilt angle *vs.* annealing time at different powers. (b) Permanent tilt angle at different powers with a fixed annealing time of 1000 s.

Explanation for irreversible deformation

The study of Sinha and Sheng [84] may account for the occurrence of irreversible deformation on the trunk cantilever of the goniometer after a high power is applied on the Al-SiO_2 bimorph actuators and then removed. They reported the temperature dependence of stress in Al films on SiO_2 substrate. In their study, Al thin films of different thicknesses were subjected to several heating and cooling cycles. They found that the tensile stress in the Al film with thickness below 1 μm had a significant increase after the first thermal cycling and cooled to room temperature (RT). Further temperature cycling had little effect on final RT stress in the film. It was pointed out that an order-of-magnitude increase in the grain size and grain-boundary-assisted diffusional creep occurred in the Al film during the first heating cycle, which led to an increase in tensile stress after cooling. Similar process may occur to the 0.5 μm thick Al film in the Al-SiO_2 bimorph structure on the goniometer. The grain growth and the creep that develop during the first heating cycle will lead that the freestanding Al-SiO_2 has a larger upward displacement after cooling to RT, as is observed in the characterization test of the goniometer.

Advantage of irreversible deformation

A permanent tilt angle can be introduced by an asymmetrical annealing of the ET bimorph actuators of two trunk cantilevers. This capability indicates that only a one-time application of power is needed to set a desired tilt angle, which is favorable in terms of power consumption. Another benefit of having the goniometer power off during STM operation is that the thermal coupling between the ET actuated goniometer and ET-actuated finger probes is eliminated.

Re-examine tilt vs power relation after irreversible deformation

An additional test was taken to reexamine the relationship between the tilt angle and the power on the right trunk cantilever, where the test was performed on the goniometer with the leveling beam having an irreversible tilt of −1.22°. The drive power varied between 0 W and 52 mW, smaller than the maximum power of 66.7 mW that was ever applied on the goniometer to avoid introducing further irreversible deformation. Fig. 5.29 shows the variation of the tilt angle with the power. The tilt angle is nearly linearly dependent on the power and has a drive sensitivity of 0.033°/mW. Particularly, the tilt angle recovers to zero at around 37.4 mW, as interpolated from the graph.

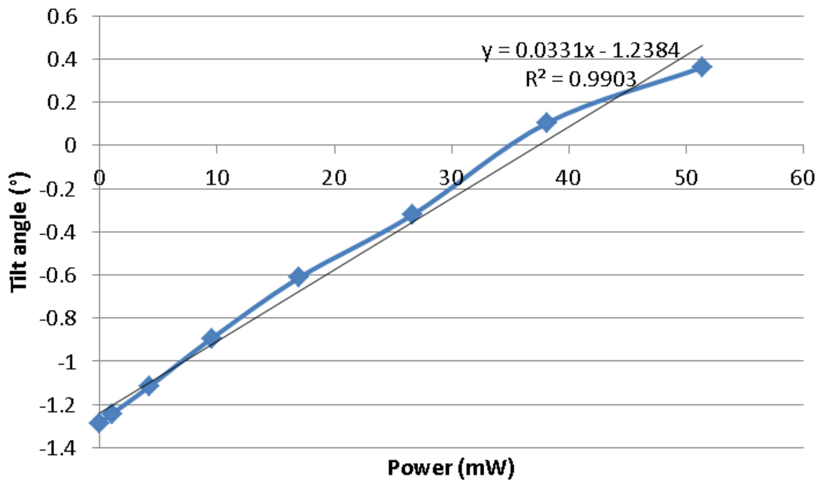

Fig. 5.29 The tilt of the leveling beam *vs.* the drive power on the right trunk cantilever. No power was applied on the left cantilever. The goniometer has an irreversible tilt of −1.22° at zero power.

The performance of the bimorph ET actuator of the finger probes was not characterized because the embedded polysilicon heater failed—resistance increasing to an infinite level—after the MEMS structure release. Further tests need to be done to figure out the causes and solutions.

5.3 Summary

The on-chip ET probe proximity sensor has a positioning accuracy of 1 μm or better when it is used to estimate the chip-sample separation. The on-chip micro-goniometer has an irreversible tilt degree of −1.22° when one of its trunk cantilevers is subjected to a thermal annealing process at 66.7 mW for 1000 s. Their combination should be able to minimize the misalignment between the probe array and the sample to the extent that all array probes will be able to perform the STM imaging in parallel. The capabilities of an integrated system need to be verified in the *in situ* alignment in future work beyond this thesis.

Chapter 6. Conclusion and Outlook

In this thesis work, active CMOS-MEMS probe arrays are developed to work in non-contact STM mode intended for parallel imaging and batch nanofabrication. A prototype hierarchical dual CMOS-MEMS probe STM system is built and demonstrated parallel STM imaging for the first time. Section 6.1 summarizes the main contribution of the thesis work, the active conductive CMOS-MEMS probe array design, the batch STM tip fabrication process on CMOS MEMS structure, the construction of the dual STM servo system, and the on-chip electrothermal proximity sensor pair and micro-goniometer. Section 6.2 presents several respects of the multi CMOS-MEMS probe STM system that need further improvement and discusses the direction of future work.

6.1 Conclusion

This thesis work first presents the design and fabrication of a widely-spaced active CMOS-MEMS conductive probe array platform qualified for STM mode imaging and nanofabrication. A compliant cantilever structure is adopted for the CMOS-MEMS probe in that it is easy to actuate with on-cantilever embedded microactuators and thus possible to be scaled to an array of probes. Electrothermal actuation is chosen to provide the vertical direction movement of the probe because of its easy implementation in CMOS MEMS and large displacement range. The analysis of the various interaction forces between the probe tips and the examined sample surface in STM operation, including VDW force, ES attractive force and meniscus force, is provided. These interaction forces are of attractive nature in the working distance regime of STM, and could make compliant probe cantilever jump into contact if they are not stiff enough. The minimum required probe stiffness is estimated to be 26 N/m for a specific ambient STM operation where the STM tip is platinum and the examined sample is gold, and is used as the mechanical stiffness design specification required of a qualified compliant STM probe. To satisfy the stiffness requirement, the designed probe is 330 μm wide, and so the probe array is called "widely-spaced". The designed active probe has a spring constant of 36 N/m, a thermal power drive sensitivity of ~131 nm/mW and a stroke of 2 μm at a power consumption of 15.3 mW, which is sufficient for each probe in the 1×5 probe array to cover the general topography of a STM sample plus the process variation of self-curl up among array probes.

High quality STM tips are desired in STM operation as the tip quality plays a dominant role in STM image quality and minimum feature size that can be achieved in tip-based nanofabrication. Based on the Spindt tip process developed in 1968, a custom STM tip fabrication process is developed in this thesis that is compatible with post CMOS MEMS processing technique and enables batch fabrication of STM tips on CMOS-MEMS probe arrays. Commonly used SPM tip processes on compliant cantilevers are of subtractive nature, where tips are fabricated out of a layer of thin film that involves several etching steps. They are not easily implementable for tip fabrication on CMOS chips because the on-chip electronics and interconnect layers cannot survive various etching procedures. By comparison, the Spindt tip process is an additive and etch-free process, and can make multiple tips on multiple locations at one time, which makes it a good approach to manufacture STM tips on CMOS-MEMS structures. The Spindt process takes place before the MEMS structure release, so the tip material needs to survive post CMOS MEMS processing. A Ni/Pt composite is chosen as the STM tip material. Ni rather than Pt is chosen as the tip body material that are made on the CMOS chip before the structure release as it has low etch rate in SiO_2 anisotropic RIE and Si DRIE. Pt, though having a good electron tunneling property, has an etch rate of around 50 nm/hour in SiO_2 anisotropic RIE. To obtain tips capable of good tunneling, Pt is deposited after the MEMS full structure release to coat the Ni tips, resulting in Ni/Pt composite tips. Pt is chosen as the tip coating material for STM application in this work because most of the experiments were conducted in the ambient environment. The final coating layers can also be other materials such as W or MnNi, depending on the specific samples to be examined and/or the specific environment where STM characterization takes place.

In the modified batch tip process, the tip holes patterned in the shadow mask for tip growth have a height of 1 μm and diameter of 400 nm to 500 nm. The determined geometry of the holes has two advantages. The first advantage is that the size of the holes is well above the resolution of the current state-of-the-art optical lithography, 22 nm. Therefore, tip holes can be patterned with a single photomask and batch photolithography, followed by a single run of tip material deposition. So the process can be classified as a true ‘batch’ tip process. The second advantage lies in the reduction of complexity of material deposition configuration. The aspect ratio of the tip holes is optimized for the selected material deposition approach, e-beam evaporation, and freshly made Ni Spindt tips with radius down to 10 nm are fabricated without using auxiliary deposition flux or collimators. The integrated composite Ni-Pt tips on the CMOS MEMS probes, *i.e.*, the Ni Spindt tips coated with 100 nm thick Pt, have a tip radius of around 50 nm. The composite Ni-Pt tips are able to resolve the atoms of Si (100) surface when used to perform the STM imaging in an ultra-high vacuum environment, and are able to resolve the grains of gold surface in an ambient environment, demonstrating their functionality as STM end-effectors.

A serial EBID process is developed in parallel with the batch Spindt process in order to create rapid-prototype STM tips on CMOS MEMS probes. EBID is a flexible and convenient technique that is capable of generating almost any shape of nano-structures in any step in the processing. The drawback is that EBID is a serial process, *i.e.*, only one structure can be made at a time. Using metalorganic Pt as the precursor, the EBID technique has made STM Pt tips on released CMOS-MEMS probes with tip radius down to 10 nm. The EBID Pt tips are able to resolve the grains of gold and titanium surface when used to perform the STM imaging in an ambient environment, and are able to fabricate the TiO_2 nanowire on the titanium thin film, demonstrating their functionality as STM end-effectors. In this work, EBID technique, instead of Spindt process, is used to make prototype tips on array probes that are used for dual-probe STM imaging. When only two STM tips are needed to be made on dual probes, it costs the serial EBID technique half an hour to complete the process, much more time efficient than the batch Spindt tip process that involves several hours' labor work on e-beam lithography, material deposition and lift-off process. Nevertheless, when ten or more STM tips need to be fabricated on a multiple STM probe array, the Spindt tip process should be adopted.

Different from a conventional STM feedback loop where ultra-stiff tips are used as end-effectors and piezo-actuators as drive plants, relatively compliant CMOS-MEMS probe cantilevers and electrothermal actuators are used in the custom STM feedback loops in the multi-probe STM system. Models of the custom piezoelectric actuator-driven STM feedback loop and ET actuator-driven STM feedback loop complete the necessary infrastructure for the loop stability analysis. A same conclusion is reached from the perspective of STM feedback loop stability analysis that the cantilever stiffness must be larger than the interaction force gradient so no positive poles will be introduced in the loop to make it unstable.

A hierarchically driven dual-STM servo system is created for the parallel operation of two CMOS-MEMS array probes. The system contains a 'master' servo and a 'slave' servo. The master servo is a piezoelectric actuator-driven STM feedback system. The probe chip is mounted on the piezoelectric actuator, so the master piezo servo controls the vertical position of the probe chip and thus the position of the master probe relative to the sample. The piezo actuator also provides the *x*- and *y*- movement of the whole chip. The “slave” servo is an ET actuator-driven STM feedback system. The ET actuator is embedded in the probe cantilever and provides the *z*-movement of the probe, so the slave ET servo controls the vertical position of the slave probe relative to the sample while in the frame of reference of the master servo. In principle, the system can be extended to accommodate more slave probes with corresponding servos.

Using the hierarchically driven dual-servo system to perform parallel STM scanning on known features of a custom calibration sample, two simultaneous STM images were obtained. Real features under the master tip were immediately identified in the master image that is directly constructed from the master piezo-drive signals. In the raw slave image directly constructed from ET drive-signals, features were identified to be an addition of the features under the slave tip and that under the master tip, which was expected because the slave servo responded not only to the topography variation under the slave tip but also to the vertical displacement of the master piezo actuator. By converting master and slave drive voltage signals to topography variation signals and differencing the signals, pseudo-features on the raw slave image introduced by the master servo were successfully removed, leaving behind the real features under the slave tip. The fundamental understanding of the hierarchical system operation was therefore validated.

One technical challenge in the parallel operation of STM probe array is the alignment of multiple tips with the examined sample surface. In the current work, an external optical microscope is used to estimate the misalignment between the probe chip and the sample and a macro-goniometer is used to adjust the angle between them. Meanwhile, an on-chip ET probe proximity sensor pair and ET actuator-driven micro-goniometers together with a second generation of scaled probe array is developed. The ET probe proximity sensors are used to measure the separation and misalignment between the probe chip and the sample. Two ET proximity sensors are placed on the two corners of a 2.4 mm × 2.4 mm CMOS probe array chip, between which lies a 1D probe array. The single proximity sensor has a sensitivity of ~ 12 Ω/μm at a tip-sample separation of 1 μm and a positioning accuracy of 1 μm or better. When a pair of ET sensors, spaced 2.4 mm apart, enters sub-micron range above the sample surface at the same time via the alignment adjustment of the macro-goniometer, the non-parallelism between the probe chip and the sample surface will be reduced to below 0.024°. In the widely-spaced probe array, a probe chip–sample misalignment of 0.024° indicates a ~600 nm height difference between the leftmost and rightmost probes spaced 1.36 mm apart, and can be compensated for by the ET-actuator driven probe tips that have a vertical travel range of 2 μm. In the scaled probe array, a probe chip–sample misalignment of 0.024° indicates a ~21 nm height difference between the leftmost and rightmost probes spaced 50 μm apart, and can be compensated for by the ET-actuator driven probe tips that have a designed vertical travel range of 200 nm.

The ET micro-goniometer is to provide an adjustment of the angular direction of the scaled probe array that is placed on it. A permanent tilt angle up to 1.22° can be introduced on the micro-goniometer by asymmetrical annealing of the two trunk cantilevers of the goniometer. Therefore, a desired tilt angle may be achieved without supplying continuous heating power, which is favorable in terms of power scaling for a large system. The approach to set a permanent tilt angle also avoids thermal coupling between the ET actuated goniometer and ET-actuated finger probes. The integrated micro-goniometer will facilitate the probe chip – sample alignment where external alignment tools are not readily implementable such as in an UHV SPM system.

In summary, the contributions of this PhD research work are as follows:

- A compliant active CMOS-MEMS cantilever structure with required probe stiffness is developed for STM operation.
- A batch STM Ni/Pt tip fabrication process on CMOS-MEMS probes is established for the first time. The CMOS MEMS probes with integrated Ni/Pt composite tips are capable of STM imaging and nanopatterning.
- A hierarchical dual servo STM system is constructed. Two STM images are obtained simultaneously by having two CMOS-MEMS probes in a 1D probe array perform the STM scanning in parallel.
- On-chip electrothermal proximity sensors and micro-goniometers are designed that will be used to assist the probe chip-sample substrate alignment in future work. The positioning accuracy of the proximity sensor is 1 μm. The micro-goniometer has a range of tilt of around 1.2°.

6.2 Future Work and Directions

One issue with the currently developed widely-spaced CMOS-MEMS probe arrays is that the spacing between two neighboring array probes is 340 μm, much larger than the lateral travel range of a common piezoelectric actuator – 86.7 μm in Veeco Dim3000 system and 5 μm in RHK SPM system – that provides the system with two degrees of freedom in the x- and y-directions. A smaller scan area is required where nanometer scale or atomic resolution is need. A scaled active probe array should be developed, where the probe spacing is reduced to at least the lateral travel range of the piezo actuator so multiple scanned images with desired resolution can be merged and so that batch-fabricated nanostructures via different probes can be connected to make devices.

In this thesis a scaled prototype tip array with an on-chip micro-goniometer is developed, where electrothermal actuation is adopted for individual probe actuation. Two problems need to be addressed to realize the parallel operation of the scaled probe array. The first issue is the thermal cross-talk among array probes during parallel operation due to their close proximity. Future effort is warranted in two respects. One is an improved structure design, such as adding thermal isolation structures between finger probes to alleviate this coupling issue; the other is to quantify the exact thermal cross-talk among probes and include it in the servo design for array probes.

The second problem is the stiffness requirement of the probes. For a single compliant MEMS cantilever, the cantilever spring constant of ~26 N/m is required to avoid snap-in during STM operation. The micro-goniometer developed in chapter 5 has a spring constant of ~40 N/m. This stiffness is just enough for one array probe on the goniometer to perform STM operation. Snap-in would occur if two or more probes were to operate in parallel. A stiffer probe structure can be designed to have more probes work in parallel. Another approach to this issue is to explore an advanced controller mechanism that may overcome the snap-in during the STM operation when the spring constant of the probe is smaller than the tip-sample force gradient.

With respect to tip-based characterization and nanofabrication, the size and shape of the SPM tip plays an important role in control of the geometry of the manufactured nanostructures. Fig. 6.1 (a) and (b) shows an example of STM-based TiO_2 nanowires written using a Pt/Ir tip in CMU TBN group [85]. Fig. 6.1 (c) shows the STM tip geometry before writing, and Fig. 6.1 (d) shows the STM tip geometry after writing 302 lines. No significant tip geometry change occurred. For Spindt tips on CMOS MEMS probes, they have a Ni-Pt composite structure, where only a 100-nm thick Pt coats the tip. Tip wear will be a primary concern using these tips. How long these tips can be used for a continuous operation to make nanostructures of controlled sizes needs to be quantified.

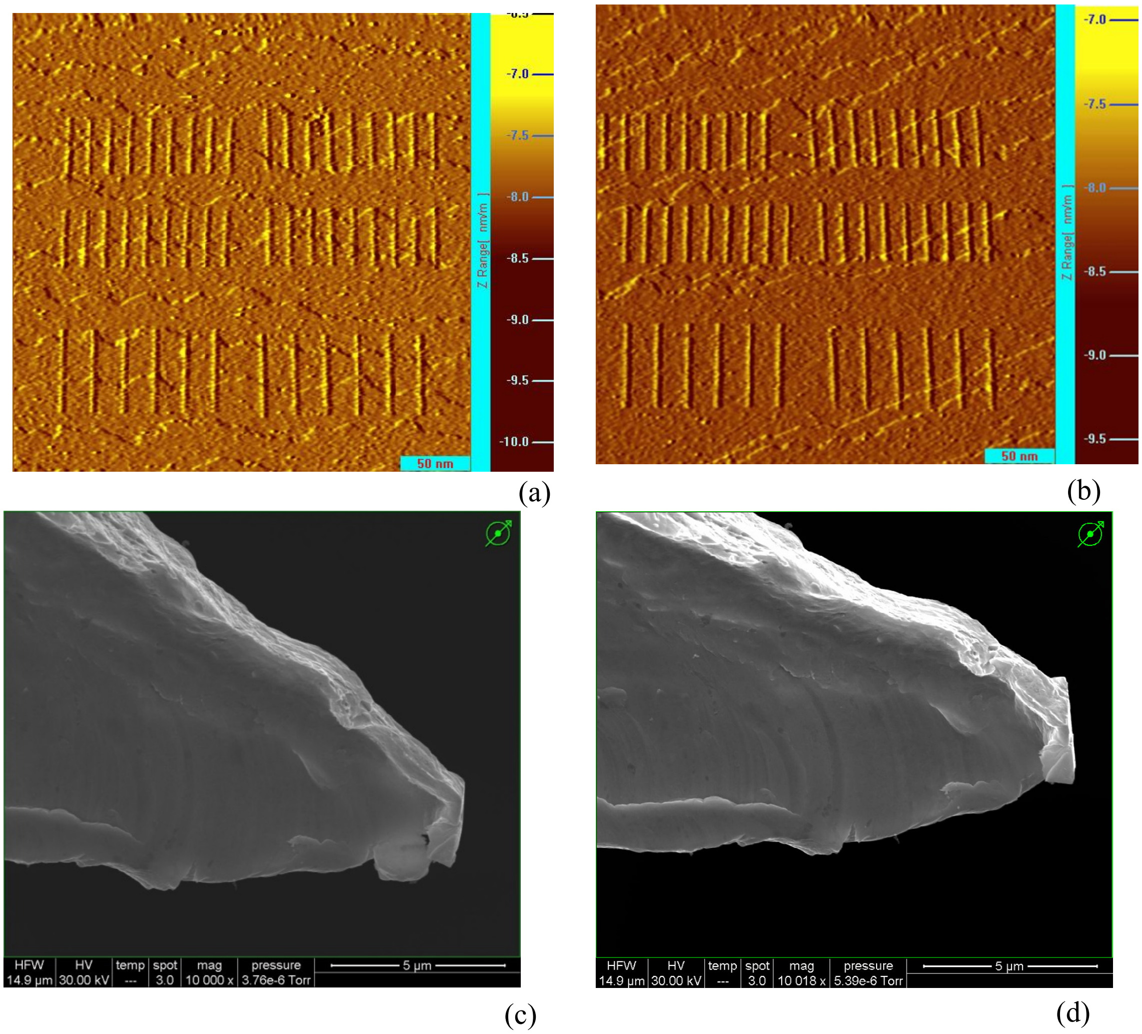

Fig. 6.1 STM-based fabrication of TiO_2 using a Pt/Ir tip: (a) & (b) TiO_2 naowires written on Ti thin film [85]; (c) Pt/Ir tip before use; (d) Pt/Ir tip after writing 302 lines.

SPM-based local nano-oxidation of Ti has been demonstrated using compliant MEMS cantilevers. The tip-fabricated Ti-TiO_x junction has a low barrier height and lateral configuration, which makes it an attractive structure component in such devices as metal-insulator-metal diodes and single electron transistors [85]. In this thesis work, local oxidation of Ti has been demonstrated using a CMOS MEMS probe and a piezo actuator-driven STM system. The feature width of TiO_2 nanowire down to 20 nm was achieved. The nanofabrication on the Ti surface using an ET actuator-driven STM system and the parallel nano-fabrication using multi-probe STM system is yet to be demonstrated.

On the system level, a full multi-probe STM system would have to be developed for system compactness and maneuverability to be widely adopted for use. The current dual-probe STM system is built on a commercial Veeco Dim3000 SPM system. The system provides a coarse approach unit for STM tip-sample substrate engagement and a piezoelectric actuator as the drive plant in the master servo in the dual-servo STM system. However, there are two major technical drawbacks associated with the current instrumentation. First, in the prototype system, wires are used to make the electrical connection between the probe chip holder and external electronics. The process has to be repeated whenever a chip replacement is needed, which costs great amount of time. Such wiring introduces noise and adds to system fragility. By comparison, in the regular use of commercial SPM systems like the Veeco Dim3000 SPM system, typically four pins on the piezo-actuator scanner head are used for electrical connection, and the pin holes on the probe holder are connected to the terminals of the tunneling current sensing circuitry on the holder. After the SPM probe is mounted on the probe holder, simply plugging the pins into the holes on the SPM probe holder will accomplish the electrical connection between the on-probe holder circuitry and the external circuitry. The second major technical drawback is that currently the control electronics unit, data acquisition unit and data processing unit are discrete. The images are not real-time displayed but rather are post-processed. Prototype future system meant for practical use must be automated for ease of use.

To address these issues, it is envisioned that a custom automated SPM system can be built. In the custom system, a scan head with multiple pin holes and a probe chip holder with multiple pins for electrical connections need to be developed. The on-chip STM servo electronics can be designed and integrated with MEMS probes. An automatic alignment between the probe chip and the sample can be achieved through the on-chip ET proximity sensor pair and micro-goniometer. Software and hardware can be developed for multiple imaging processing and display.

Some primary work has been done in tip-based nanofabrication (TBN) group at Carnegie Mellon University for the future realization of a custom automated multi-probe SPM system. Onur Ozcan [86] developed a custom automated SPM control system that can switch between AFM mode and STM mode *in-situ* to allow for SPM operation on heterogeneous surfaces. The custom system can also manipulate the path of SPM probes in an arbitrary way. For example, the "CMU" pattern in Fig. 3.20 is written using this custom system. Weihua Hu built the physical model of quantum tunneling effect in STM, and fabricated Ti/TiO_x/Ti nano junctions based on SPM tip-based nanofabrication [85]. Yingying Tang designed on-chip STM servo electronics. The on-chip transimpedance amplifier for tunneling current measurement achieves a gain of 88 MΩ with a bandwidth of 40 kHz and input referred noise current of as low as 25 fA/√Hz [87].On-chip STM servo electronics have been developed, with a TIA bandwidth of ~1.5 MHz and the feedback system's closed-loop bandwidth of ~80 kHz. The imaging speed of a single CMOS-MEMS probe in a STM system with a bandwidth of 80 kHz will reach up to 80 µm/s for a lateral resolution of 1 nm. Lower resolution requirements will allow even higher speed. CMOS MEMS probes with integrated polysilicon piezoresistive sensors were developed with a theoretical resolution of 1 nm [25], which has the potential to be used as an AFM tip end-effector. AFM probes are able to characterize features with vertical height variations up to a few microns, which constitutes an essential compliment to STM probes whose working range is only tens of nm. The realization of both AFM and STM with CMOS MEMS probes will pave a way for the construction of a multi-scale multi-resolution CMOS-MEMS based SPM hybrid system.

In 2008, Tseng [88] proposed a preliminary roadmap for tip-based nanofabrication that consists of six metrics. One of the metrics that is related to MEMS probe array-based TBN are the feature fabrication rate, *i.e.*, number of structures/minute/tip with an array of tips. It is expected that a thirty-tip array can be built and 60 nanostructures/minute/tip can be achieved. CMOS MEMS provides an approach of high integration of electronics and MEMS cantilever tips that can facilitate future automation and parallel probe operation. Based on the current accumulation of knowledge, experience and accomplishments contributed by the TBN members, a 1x30 CMOS-MEMS probe array is eminently achievable and such a future design would be expected to fulfill a first-generation demonstration of parallel nanofabrication.

Appendix A –Process Flows

A.1 Process flow of Spindt tip fabrication on CMOS-MEMS probes

a. Partial oxide etch. A partial directional oxide etch is performed on a 5 mm by 5mm CMOS chip using plasma Therm 790 RIE system to expose the top CMOS metal layer, metal-4 in the case of Jazz 0.35 μm technology and TSMC 0.35 μm technology. All metals below top metals are still covered by the dielectric oxide layer.

b. Mounting. The probe chip is then mounted on a 1" wafer using 120°C heat release tape. The 5 mm by 5 mm chip is too small to sit tightly on the spinner, therefore a carrier 1" wafer is used to assist the photoresist spinning.

c. E-beam resist spin. 1 μm thick PMMA is spun the chip. 950 PMMA C7 is used in the processing, with a pre-spin speed of 600 rpm, 13 sec, and a spin speed of 5000 rpm, 50 sec. the chip is then baked at 180 °C on the hotplate for 2 minutes.

d. E-beam lithography. The probe chip is then patterned via e-beam lithography. The tip hole patterns are designed in NPGS software (JC Nabity Nanometer Pattern Generation system) and are patterned on the resist via e-beam lithography in SEM (FEI Sirion 600 SEM). The diameters of the patterned hole range from 100 nm to 500 nm. The dosage of e-beam used to expose the patterns on PMMA is independent of PMMA thickness, which is approximately 700 $\mu C/cm^2$. A fine adjustment of dosage may be necessary if the pattern feature size and/or pattern spacing is small.

e. Development. The chip is developed in the blends of methyl-iso-butyl-ketone (MIBK) and isopropyl alcohol (IPA) (ratio of 1:3), 30 s, rinsed by IPA 15 s, and de-ionized (DI) water 15 s, successively;

f. Descum process. The developed chip is descumed to clean the surface. three types of descum process are used in cleaning the surface:

Descum type	Recipe	Equipment
Oxygen Ashing	O_2, 1 torr, 100 W power, 1 min	IPC Barrel Etcher
RF Sputter Etch	Ar, 5 mtorr, 70 W power, 10 min	Perkin Elmer 6J Sputtering system
Reactive Ion Etching	O_2, 10 mtorr, 20 W power, 30 sec	Plasma Therm 790 RIE

Non-directional oxygen ashing is able to fully clean the bottom remains in the PMMA holes which are patterned on "large areas" of the sample surface, *i.e.,* areas large enough to have a uniform PMMA coverage after spin. This is evidenced by the fact that the deposited Spindt tips are found on these "large areas" after lift-off.

Oxygen ashing does not work on the top metal-4 tip platform, *i.e.*, no tips are found after lift-off on the tip platform of the probe chip that experienced descum via oxygen ashing. The patterned probe chips that are subjected to either a RF sputter etch or O_2 RIE before deposition have Spindt tips on the tip platform after lift-off, as evidenced in chapter 3.

g. Ni tip deposition. The descumed probe is transferred to Ultek e-beam evaporator. 5 nm-thick Cr followed by 800 to 1000 nm Ni is deposited on the patterned probe chip. Refer to B.1 for deposition details.

In this step, the Ni source for evaporation is custom designed and ordered. It is done so because there are not suitable crucibles to hold Ni during e-beam evaporation: most of the widely used crucibles either made of alumina, fabmate or graphite, crack during the e-beam evaporation. Nickel's magnetic permeability will affect the electron beam's focus and steering it in unpredictable ways and the beam spitting and hitting the crucible. In most cases the crucible cracks during the stage of temperature ramping, before reaching the melting point of Ni. The geometry of the custom Ni source follows the size of commercial 7cc crucibles so that it can directly fit into the hearth (crucible holder) in the chamber of the Ultek e-beam evaporator so no crucible is needed. It performs well in the evaporator.

h. Lift-off. The probe chip is put into acetone for lift-off. The lift-off time generally takes three days. No ultrasonic vibration is used in helping lift-off to avoid that tips may be shaken off. The chip is further cleaned via oxygen ashing to remove PMMA remains. The power and time for oxygen ashing is 200 W to 250 W, 10 min, respectively.

i. Chip dicing. The 5 mm by 5 mm CMOS probe chip with integrated Spindt tips are diced to four 2.5 mm by 2.5 mm chips, on Kulicke & Soffa 782-6 dicing saw. A line of marks is designed on the CMOS chip to guide the chip dicing, as shown in Fig. A. **1** (a). The spacing between the mark line and the CMOS cantilever end is 50 µm. Fig. A. **1** (b) shows an example of the CMOS chip after dicing.

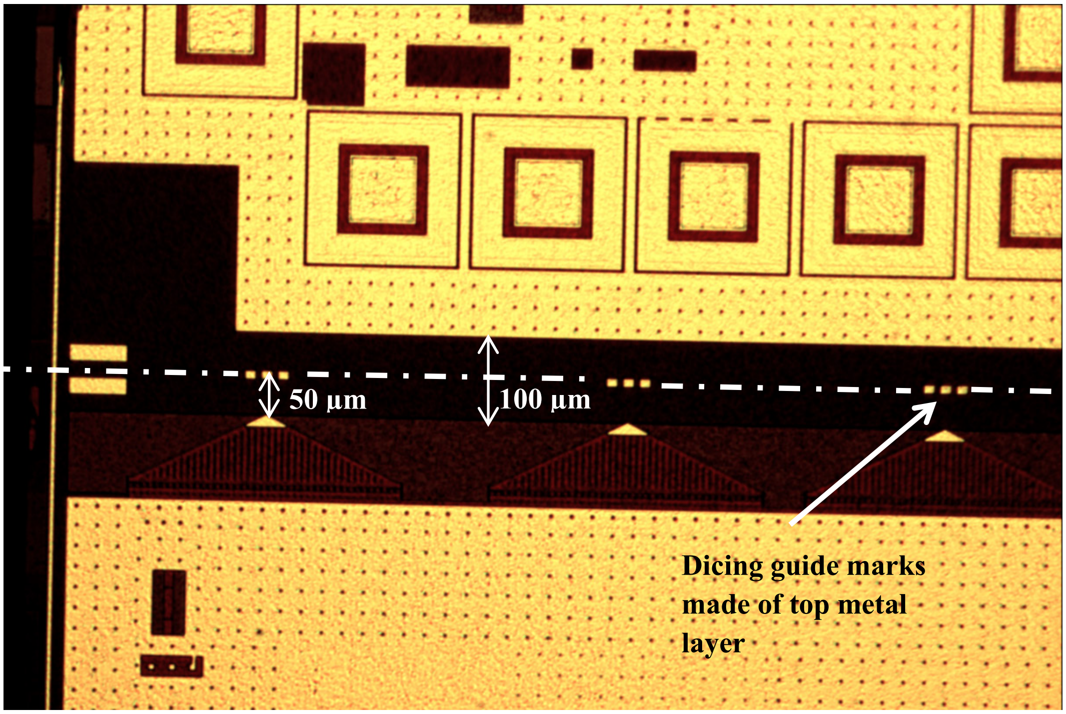

(a)

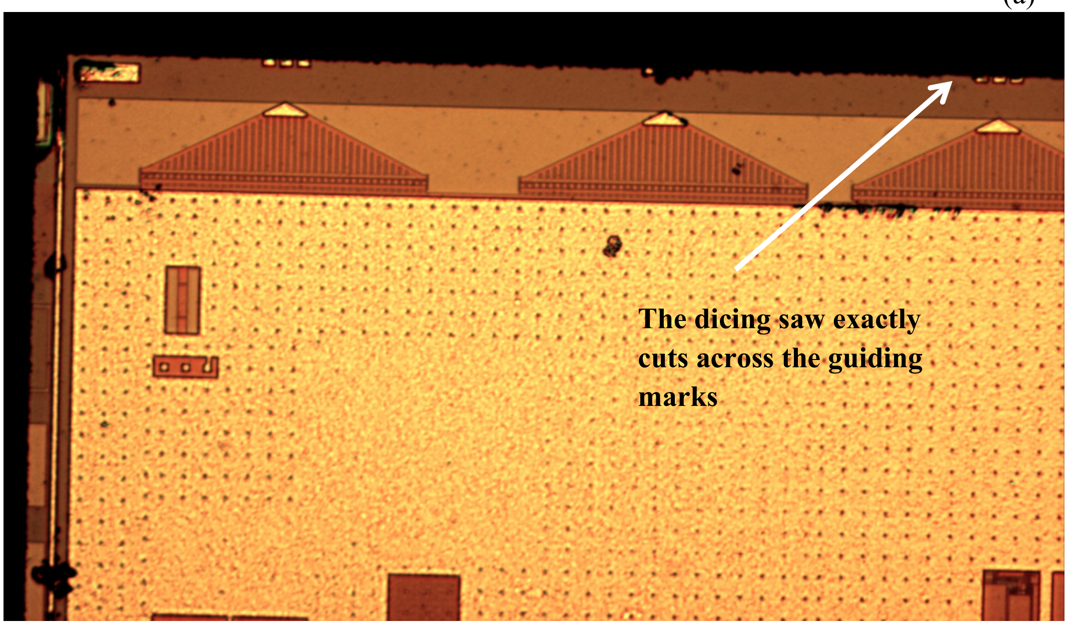

(b)

Fig. A. 1 (a) The dicing guide line on a 5 mm by 5 mm CMOS chip. (b) A diced CMOS chip

This type of dicing saw has an affected span of 60 – 80 µm, the area that the debris produced in the dicing may cover. So a layer of photoresist is applied on the probe chip before dicing to protect the tips. Instead of the general practice of manually pasting the photoresist on the chip to be diced, a layer of photoresist AZ4210 is spun on the chip to avoid damaging the tips on the chip. The photoresist is washed off after dicing.

j. Dielectric silicon oxide etching. The quadrant of the chip that has CMOS MEMS probe is then subjected to anisotropic oxide etch in STS Aspect Cluster RIE/AOE system. During the oxide etch, the top-most metal layers acts as an etch mask to define the MEMS structures.

k. Silicon etching. The probe chip is then fully released by Si DRIE in the STS ICP RIE system. It is a two-step process, first a ~20 μm anisotropic etch followed by 15 to 20 μm isotropic etch, depending on specific MEMS structures. An extra isotropic etch of Si can be performed to undercut the silicon under the cantilever, but care should be taken because extra etch may also attack the tungsten vias on the MEMS structures leading to electrical failure.

l. Mounting shadow masks. Mounting two shadow masks above the probe chip. Shadow mask covers most part of the chip so only the cantilever end is exposed to the sputtering. It helps direct the deposited flux only through the gap and constrain it on the cantilever end.

   The probe chip is first mounted on a carrier wafer using silver paste as the glue. Heat release tape is not suggested because the later RF sputter etch process on the chip could sputter the plastic tape and makes it redeposit on the chip and damage the tips and MEMS structures.

Two pieces of shadow masks, around 15 mm long, 7 mm wide, 1.5 mm thick, are prepared. They are then manually put on either side of the probe cantilever end under the optical microscope. The gap between the two masks is sub-mm.

m. Platinum coating. 100 nm Pt then deposited on the probe chip to coat the Spindt Ni tip, in Perkin Elmer 6J Sputtering System. A RF sputter etch is performed first to eliminate the oxide on the tip and tip platform.

A.2 Process flow of fabrication of passive probes with Spindt tip

a. Pattern probe geometry via photolithography. The process starts with a 300 μm-thick 4'' Si wafer. AZ5214 is used as negative photoresist (PR) to pattern the wafer with probe geometry mask, on Karl Suss MA56 contact aligner with a Lamp power of 10 mW/cm^2. Table A-1 gives the pattern process details:

Recipe of using AZ5214 as negative photoresist

Op. type	Recipe	Note
HMDS spin	600 rpm, 5 sec, 4000 rpm, 45 sec	
PR spin	600 rpm, 5 sec, 4000 rpm, 45 sec	PR thickness: ~1.4 μm
Baking	90 °C, 1 min on hotplate	
Exposure	2.5 sec with probe mask	Lamp power: 10 mW/cm^2
Baking	115 °C, 1 min on hotplate	
Flood exposure	10 sec with a transparent mask	Lamp power: 10 mW/cm^2
Development	1.2 min	AZ 400K developer: DI water = 1:4

b. Ni deposition. 40 nm Ti and 100 nm Ni is deposited on the patterned silicon wafer via e-beam evaporation, followed by lift-off. (Refer to Appendix B.1 for recipe)

c. Spindt tip deposition. This process flow is similar to steps *c* – *h* used in making Ni Spindt tips on CMOS-MEMS probes in Appendix A.1. Because the local topography variation around the region of cantilever end where the tips are to be made is small, around 100 nm, the e-beam resist coverage is quite uniform. Hence the descum process is not critical, and oxygen plasma ashing is sufficient to clean the residue at the bottom of the tip holes.

d. AZ 4620 protection layer. A layer of 10 µm-thick photoresist AZ4620 is applied on the wafer and patterned, using the same probe geometry mask as in step *a*. The photoresist acts as a protection layer in anisotropic Si DRIE, covering Ni tips and probe cantilever geometry. The exposure is carried out on Karl Suss MA6 contact aligner, with a lamp power of 5 mW/cm^2. The recipe is as follows:

Recipe of spinning AZ4620 photoresist

Op. type	Recipe	Note
HMDS spin	600 rpm, 5 sec, 4000 rpm, 30 sec	
PR spin	600 rpm, 9 sec, 3000 rpm, 30 sec	PR thickness: ~10 µm
Baking	90 °C, 40 min, oven baking	
Exposure	16 min with probe mask	Lamp power: 5 mW/cm^2
Development	15 min	AZ 400K developer: DI water = 1:4

e. Wafer mounting. Since the probe wafer will experience an anisotropic Si DRIE that will etch through the wafer to form the cantilever structure, the probe wafer is mounted on a carrier wafer before the etch process.

f. An anisotropic Si DRIE is performed to etch through the 300 µm-thick wafer. The anisotropic etch rate for Si is 1 µm/s – 2 µm/s, depending on equipment conditions. The process is divided to three to four runs and the Si etch rate is examined during the intervals so that the etching time can be properly determined.

g. Platinum coating. A 100 nm-thick Pt is deposited on the probe wafer to coat the Spindt Ni tips as well as the probe cantilevers, in Perkin Elmer 6J Sputtering System. One probe wafer that contains 112 probes.

The batch-fabricated probes can be picked up one by one from the probe wafer for use.

Appendix B –Process Recipes

B.1 Ultek E-beam Evaporator Deposition Conditions

Cr/Ni recipe

Parameters	Cr	Ni
Base pressure	1×10^{-6} to 2×10^{-6} mtorr	
Power supply	5.95 kV	
Evaporation rate	1 Å/sec to 2 Å/sec	
Beam current	~65 mA	~160 mA
Film thickness	100 Å	10000 Å

Ti/Pt recipe

Parameters	Ti	Pt
Base pressure	1×10^{-6} to 2×10^{-6} mtorr	
Power supply	5.95 kV	
Evaporation rate	1 Å/sec to 2 Å/sec	
Beam current	~70 mA	~200 mA
Film thickness	As required	

B.2 Perkin-Elmer 6J Deposition Conditions

Sputter etch recipe

pressure	RF power	Target voltage	Ar flow	time
5 mtorr	60 W to 70 W	500 V	25 sccm	600 sec

DC magnetron sputtering recipe

Parameters	Ti	Au	Pt
Table spacing	2.5″		
pressure	5 mtorr		
Ar flow	25 sccm		
Power	100 W	50 W	50 W
Pre-sputter time	600 sec	60 sec	120 sec
Deposition rate	~2 Å/sec	~8 Å/sec	~4 Å/sec

Appendix C – Scripts and Code

C.1 K_p – K_I relations in stability analysis of custom STM feedback loops

In the STM feedback loop, a PI controller is implemented. The values of the proportional gain, K_p, and of the integral gain, K_I, can be *in-situ* modified during the imaging to determine the optimum scan conditions. These Matlab m-files are to find out the maximum value of K_p at any given K_I that maintains system stability. The K_p – K_I curve defines the stability region of the STM feedback loop.

Two m-files are included in this section. One is for a piezo actuator-driven STM feedback loop, the second if for an ET actuator-driven STM feedback loop.

```
%Examination of Kp-KI relations of a piezo actuator-driven STM

%barrier height phi = 3 eV, tip radius r = 20 nm

clear all
clc

%Piezo dynamics: plant1
wr=5.5e3*2*pi; %Piezo resonance in z-direction
Q=20; %Piezo quality factor
plant1_num = 17*wr^2; %piezo sensitivity 17 nm/V
plant1_dnm=[1 wr/Q wr^2];
plant1 = tf(plant1_num,plant1_dnm);

%cantilever dynamics: plant2
wr_c=206e3*2*pi; %cantilever resonance in z-direction
Q_c = 180; %Cantilever quality factor
k_sp=36; % Spring constant nN/nm
m=k_sp/(wr_c^2); %cantilever mass kg
b= (k_sp/wr_c)/Q_c; %damping coefficient
k_es=10.5; % interaction force gradient @ 3eV r = 20 nm

plant2_num = [wr_c^2];
plant2_dnm=[1 wr_c/Q_c wr_c^2];
plant2 = tf(plant2_num,plant2_dnm);

%transfer function including tip-sample interaction
cant_num=[k_sp];
cant_dnm=[m b k_sp-k_es];
cant=tf([k_sp], [m b k_sp-k_es]);

BW_TIA = 2*pi*25e3; % TIA bandwidth
BW_BUF = 2000*2*pi; %Low pass filter
```

```
V_tunl = 0.944;% linearized distance sensitivity of current
TIA = tf(BW_TIA, [1 BW_TIA]); % TIA tranfer function
LP = tf(BW_BUF, [1 BW_BUF]);  % LP tranfer function

K_HV = 10; % Gain of high voltage amplifier

sp = (0:8/100:8)'; % Sweep range
length_sp = length(sp);
P = zeros(length_sp,1);  % Proportional gain: KP
IP = zeros(length_sp,1); % Integral gain: KI
P2 = zeros(length_sp,1);
I = zeros(length_sp,1);  % KI/KP
varg = 6.8e-4/300;  %variable gain

for n=1:length_sp
    I(n) = power(10,sp(n));
    PI_num = [1 I(n)];
    PI_dnm = [1 0];
    PI = tf(PI_num,PI_dnm); % PI transfer function
    %Uncompensated system transfer function
    LPG_uc = K_HV*plant1*cant*V_tunl*TIA*LP;
    %Compensated system transfer function
    LPG = K_HV*plant1*cant*V_tunl*TIA*varg/10*LP*PI;
    [Gm, Pm]=margin(LPG);
    P(n) = Gm*varg/10; %Maximum KP
    IP(n) = I(n)*P(n); %The value of KI
end
figure (1)
plot(IP, P);
xlabel('Integral gain KI','FontSize',12,'FontWeight','bold','Color','k')
ylabel('Proportional gain KP','FontSize',12,'FontWeight','bold','Color','k')
```

```
%Examination of Kp-KI relations of a custom ET actuator-driven STM

%barrier height phi = 3 eV, tip radius r = 20 nm

clear all
clc

%cantilever dynamics: plant2
z_ds = 131;% ET drive sensitivity 131 nm/mW
wr_c=206e3*2*pi; % Cantilever resonant frequency
Q_c = 180; %Cantilever quality factor
k_sp=36; % Spring constant N/m
m=k_sp/(wr_c^2); %cantilever mass kg
b= (k_sp/wr_c)/Q_c; %damping coefficient
k_es=10.5; % interaction force gradient

%cantilever transfer function
plant2_num = [wr_c^2];
plant2_dnm=[1 wr_c/Q_c wr_c^2];
plant2 = tf(plant2_num,plant2_dnm);

%transfer function including tip-force interaction
```

```
cant_num=[k_sp];
cant_dnm=[m b k_sp-k_es];
cant=tf([k_sp], [m b k_sp-k_es]);

R_ht = 4.6; %Heating resistor:kohm
V_et = 5; % V, center drive voltage

BW_TIA = 2*pi*25e3; % TIA BW.
BW_BUF = 2000*2*pi; % LP BW.
ET_BUF = 280*2*pi;  % ET thermal cut-off frequency
V_tunl = 0.944; % linearized distance sensitivity of current

TIA = tf(BW_TIA, [1 BW_TIA]);
LP = tf(BW_BUF, [1 BW_BUF]);
ET_off = tf(ET_BUF, [1 ET_BUF]);

%Uncompensated system transfer function
LPG_uc =z_ds*ET_off*cant*V_tunl*TIA*LP*(2*V_et/R_ht);


sp = (0:8/100:8)'; % Sweep range
length_sp = length(sp);
P = zeros(length_sp,1); % Proportional gain: KP
IP = zeros(length_sp,1); % Integral gain: KI
I = zeros(length_sp,1);
varg = 6.8e-4/300;  %variable gain
for n=1:length_sp
    I(n) = power(10,sp(n));
    PI_num = [1 I(n)];
    PI_dnm = [1 0];
    PI = tf(PI_num,PI_dnm);
    %Compensated system transfer function
    LPG = z_ds*ET_off*cant*V_tunl*TIA*LP*(2*V_et/R_ht)*PI*varg/10;
    [Gm, Pm]=margin(LPG);
    P(n) = Gm*varg/10;
    IP(n) = I(n)*P(n);
end

figure (1)
plot(IP, P);
xlabel('Integral gain KI','FontSize',12,...
       'FontWeight','bold','Color','k')
ylabel('Proportional gain KP','FontSize',12,...
       'FontWeight','bold','Color','k')

%Generalized root locus to find out the region of KP at given
%KI to maintain system stability
%extract coefficients of numerator N(s) and denominators D(s)
%of uncompensated sys N(s)/D(s).
[LPGuc_num LPGuc_dnm] = tfdata(LPG_uc, 'v');
LPGuc_num_tf = tf(LPGuc_num, 1);
LPGuc_v2_num = [LPGuc_num, 0]; %the coeff. of s x N(s)
sN = tf(LPGuc_v2_num, 1); % the transfer function of s x N(s)
sD_cft = [LPGuc_dnm, 0]; %the coeff. of s x D(s)
sD = tf(sD_cft, 1); % the transfer function of s x D(s)
LPGuc_v2_dnm_tf = IP(40)*LPGuc_num_tf+sD; % KI x N(s) + s x D(s)
```

```
LPGuc_v2_dnm = tfdata(LPGuc_v2_dnm_tf, 'v');
LPG_v2 = tf(LPGuc_v2_num, LPGuc_v2_dnm); %converted system

figure (3)
rlocus(LPG_v2) %the stability region can be found out on root locus
```

C.2 Simulink models of custom STM system

Two STM feedback loop models are built in the Simulink® in Matlab®. Fig. C.1 and Fig. C.2 shows the feedback loop models of the piezo actuator-driven STM system and the ET actuator-driven STM system, respectively. The transfer functions of piezo actuator dynamics, MEMS cantilever dynamics, TIA, low pass filter, PI controller are given in table 4-1 in Chapter 4. Two Matlab scripts are given in this section. The script for the calculation of the tunneling current between the STM tip and the sample is contributed by Weihua Hu. The script for the calculation of tip-sample interaction force is based on the model presented in Chapter 2.

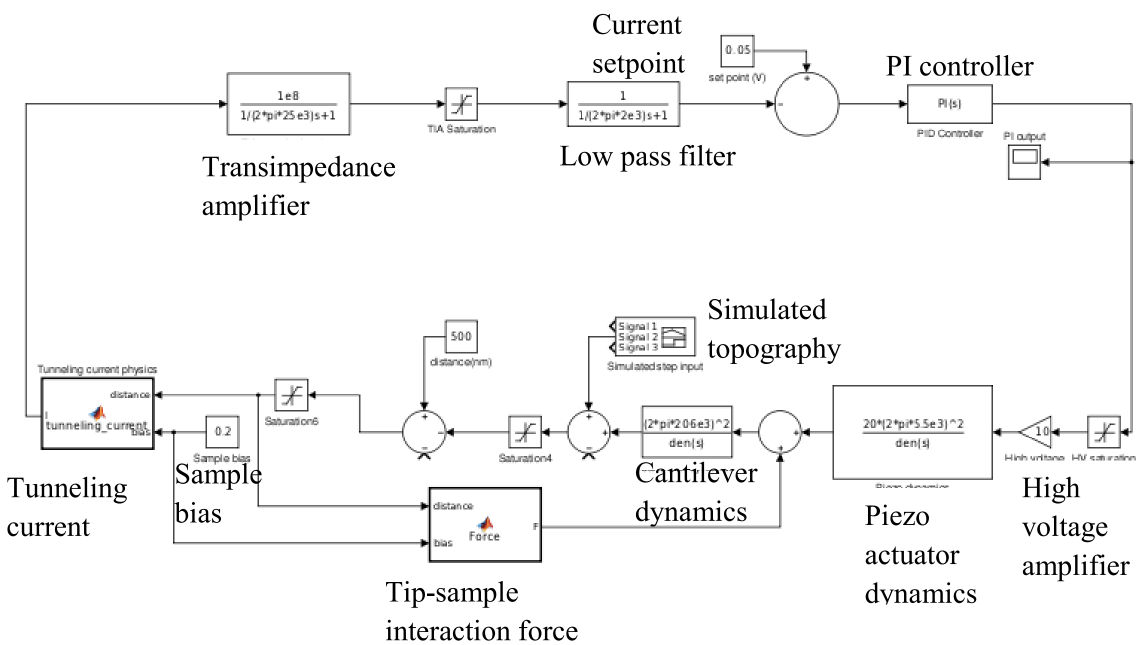

Fig. C.1 Block diagram of piezo actuator-driven STM system in Simulink

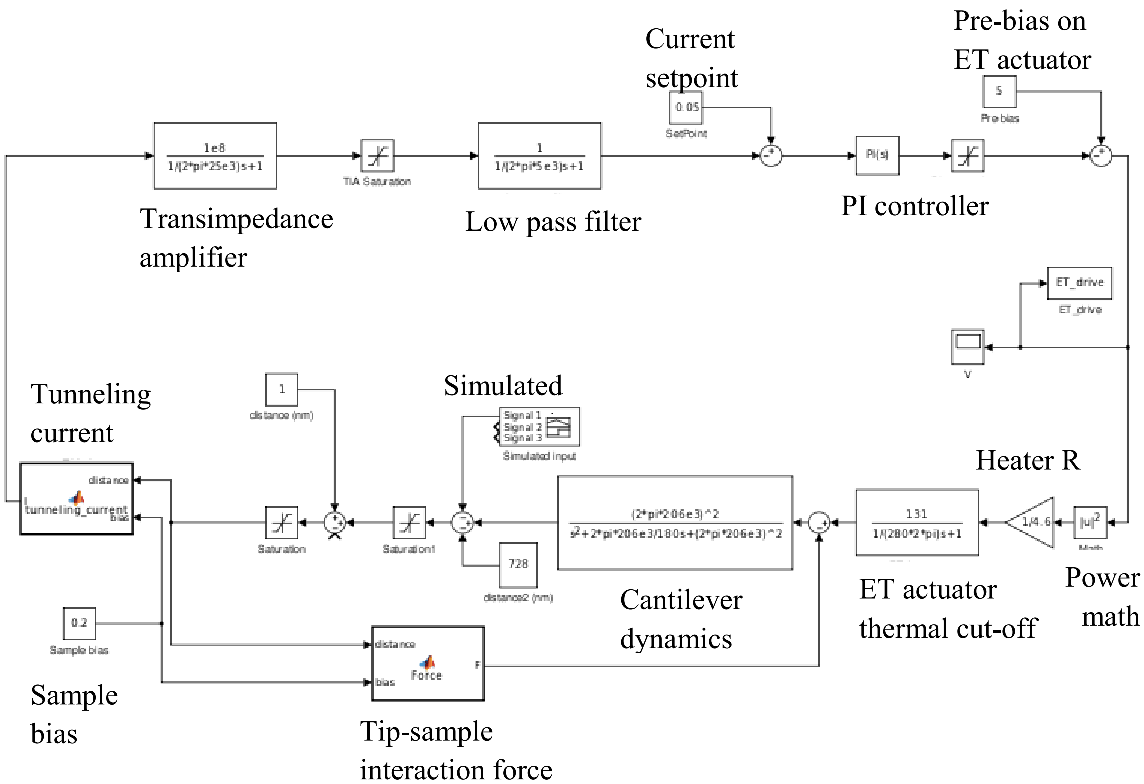

Fig. C.2 Block diagram of ET actuator-driven STM system in Simulink

Script for calculation of tunneling current between a STM tip and a sample surface:

```
%Calculation of tunneling current

function I  = tunneling_current(bias,distance)% V is the bias voltage and
d_nm is the distance between the tip and the substrate
%% define parameters %%
V = bias;
phi_0=3; % tunnel barrier height
R = 20*1e-9; % radius of the tip
d_0 = distanc*1e-9; % tip-substrate separation
x_0 = 0; % tip center
delta_x = 0.1e-10; % increasement in radial direction
q = 1.6e-19; % the charge of electron
h = 6.63e-34; % planck constant
m = 0.91e-30; % mass of electron
if d_0<0.288e-9
    I = 1e-6;
else
%% Simmons' model %%
I = 0; % initial value to be 0
for i = 1:80
    x = x_0 + i*delta_x;
    y = x^2/(2*R);
    d = d_0 + y;
```

```
    if (V<=phi_0)
    phi_bar = phi_0*q - q*V/2;
    beta = 1; % defined in Simmons' model
    delta_z = d;
else
    phi_bar = phi_0*q/2;
    beta = 23/24; % defined in Simmons' model
    delta_z = d*phi_0/(V);
end
    J_0 = q/(2*pi*h*beta*delta_z^2);
    A = (4*pi*beta*delta_z*sqrt(2*m))/h;
    J = J_0*(phi_bar*exp(-A*phi_bar^0.5)-(phi_bar+q*V)*exp(-
A*(phi_bar+q*V)^0.5));
    delta_S = 2*pi*x*(sqrt(1+(x/R)^2))*delta_x;
    I = I + J*delta_S;
end
I=min(1e-6, I);
end
```

Script for calculation of the interaction force between a STM tip and a sample surface:

```
%Calculation of tip-sample interaction force

function F  = Force(distance, bias)% V is the bias voltage and d_nm is the
distance between the tip and the substrate
%% define parameters %%
Vb = bias; %bias [V]
ep =8.854e-12; % dielectric constant
r = 20*1e-9; % radius of the tip; 10nm [m]
d = distance*1e-9; % tip-substrate separation [m]
Ah = 200e-21; % Hamaker constant [J]
sigma = 0.288e-9; %Interatomic distance
gama = 0.073; % surface tension [N/m]
theta = cos(59.3/180*pi); % contact angle of water meniscus
hmd = 0.2; % humudity
t = -0.54/log(hmd); % curvature of the water meniscus
sp = 36 % cantilever spring constant

%% Force model %%
if d>sigma
F_es = 80*pi*ep*Vb^2*r^2/(d*(d+r)); % ES force
else
F_es = 80*pi*ep*Vb^2*r^2/(sigma*(sigma+r)); % upper bound of ES force
end
F_vdw = Ah*r/(6*sigma^2)*((sigma/d)^2-1/30*(sigma/d)^8); % VDW force
F_men = 4*pi*gama*r*theta*(1-d/(2*t*theta))*(d<2*t*theta); % meniscus force
F = (F_es+F_vdw+F_men)/sp*1e9;
```

C.3 Image processing in dual-probe STM Imaging

In the dual-probe STM imaging, the piezo drive voltage and the ET drive voltage are recorded using a NI DAQ 6009 and Labview SignalExpress for DAQ. The data are imported in Matlab for image processing and plotting.

In the dual-probe STM system, two images are obtained simultaneously. The topographical image under the master tip is constructed from the piezo drive voltage. The raw topographical image under the slave tip is constructed from the ET drive power. The actual topographical image under the slave tip is obtained from the weighted difference of the master piezo drive voltage signal and the slave ET power signal.

```
%Imaging processing of the dual probe STM system

clc
clear all
close all

%Import data of piezo drive voltage
rawdata_mp=importdata('V_piezo_31.mat');

%Import data of ET voltage storage storage
rawdata_sp=importdata('V_ET_31.mat');


%Build image matrix
line = 128; %the number of lines in a STM image, can be 128/256/512.
fwd_mp=zeros(line,1280); %Each line contain 1280 data
fwd_mp_pf=zeros(line,1280);
fwd_sp=zeros(line,1280);
fwd_sp_end = zeros(line,1280);
bck_mp=zeros(line, 1280);
bck_mp_pf=zeros(line,1280);
bck_sp=zeros(line,1280);
bck_sp_end = zeros(line,1280);

%put the drive voltage data from the 'raw_data' to image matrix
for i=1:line
    %master piezo drive voltages*17.
    %The sensitivity of piezo is 17 nm/V
    fwd_mp(i, :)=-rawdata_mp((2*i-2)*1280+1:(2*i-2)*1280+1280)*17;
    %Line planefit to estimate the slope of the sample
    p=polyfit(1:1280,fwd_mp(i,:),1);
    cos_theta=1/sqrt(1+p(1)^2);
    %Planefit data
    fwd_mp_pf(i,:)=(fwd_mp(i,:)-(p(1)*(1:1280)+p(2)))*cos_theta;
```

```
    bck_mp(i, :)=-rawdata_mp(2*i*1280:-1:2*i*1280-1280+1);
    p=polyfit(1:1280,bck_mp(i,:),1);
    cos_theta=1/sqrt(1+p(1)^2);
    bck_mp_pf(i,:)=(bck_mp(i,:)-p(1)*(1:1280)-p(2))*cos_theta*17;

    %Slave ET drive voltage
    temp_sp=rawdata_sp((2*i-2)*1280+3:(2*i-2)*1280+3+1279);
    %Calculate the mean ET drive voltage in a line scan
    V_center = mean(temp_sp);
    %Calculate the ET drive voltage fluctuation around V_center
    rawdata_sp_var = temp_sp - V_center;
    %Calculate ET power fluctuation in a line scan
    pwr_var = 2*V_center*rawdata_sp_var/4.6;% heater R=4.6 kohm
    %ET drive sensitivity is 17 nm/V * 0.129 V/mW.
    %Refer to Chapter 2 for how to obtain ET drive sensitivity in-situ
    %in STM scanning
    fwd_sp(i, :)=pwr_var*(17/0.129);
    %actual slave iamge = raw master image + raw slave image
    fwd_sp_end(i, :)=fwd_sp(i,:)+fwd_mp_pf(i,:);

    temp_sp=rawdata_sp(2*i*1280+3-1:-1:2*i*1280-1280+3);
    V_center = mean(temp_sp);
    rawdata_sp_var = temp_sp - V_center;
    pwr_var = 2*V_center*rawdata_sp_var/4.6;
    bck_sp(i, :)=pwr_var/0.129*17;
    bck_sp_end(i, :)=bck_sp(i,:)+bck_mp_pf(i,:);
end

%Image plot
figure (1)
colormap(copper);
imagesc(fwd_sp);

figure (2)
colormap(copper);
imagesc(fwd_sp_end);

figure (3)
colormap(copper);
imagesc(fwd_mp);

figure (4)
colormap(copper);
imagesc(fwd_mp_pf);

figure (11)
colormap(copper);
imagesc(bck_sp);

figure (12)
colormap(copper);
imagesc(bck_sp_end);

figure (13)
```

```
colormap(copper);
imagesc(bck_mp);

figure (14)
colormap(copper);
imagesc(bck_mp_pf);
```

Appendix D – STM Servo Electronics on PCB

D.1 Master Servo Electronics

In the master-slave dual-servo STM system in Chapter 4, the servo electronics, is realized by analog electronics and implemented on printed circuit boards (PCB) that were designed and made by Yingying Tang in our TBN research group at CMU.

In the master servo, piezo actuator on a Veeco Dim3000 SPM system is used as the drive plant. Fig. D.1 shows the system block diagram. The system includes a transimpedance amplifier (TIA), a variable gain amplifier (VGA), a PI controller and a high voltage amplifier. Three functional blocks, TIA, VGA and PI controller, are implemented on PCB. The high voltage amplifier is a commercial piezo driver/power amplifier (Trek Model PZD350, Trek, INC.) Detailed schematics of TIA, VGA and PI controller are shown Fig. D.2. The component values used in the electronics are listed in Table D-1.

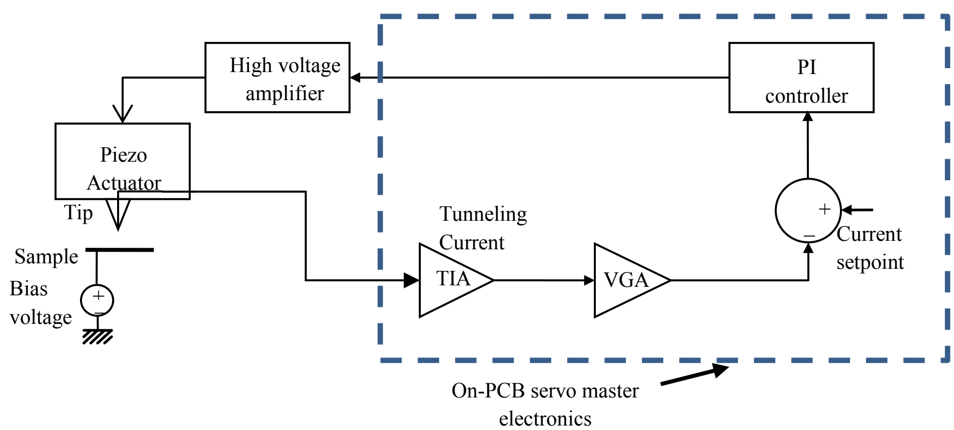

Fig. D.1 Block Diagram of a single probe piezo actuator-driven STM system

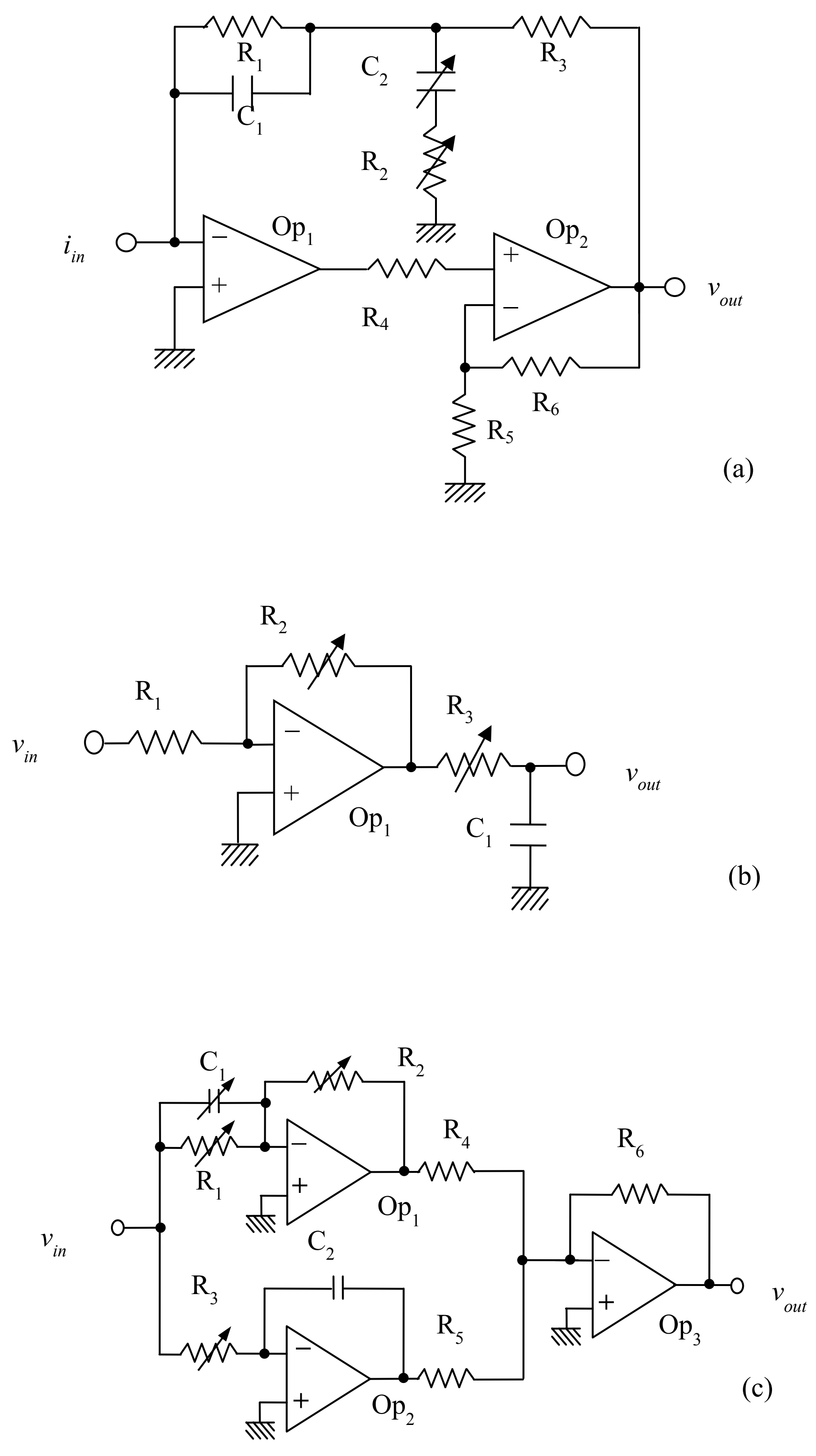

Fig. D.2 Detailed schematics of off-chip control electronics: (a) TIA; (b) VGA; (c) PI controller.

Table D-1 *Values of components used in master servo*

	Component	Value	Note
TIA	Op1	OPA111	Low noise amplifier
	Op2	Op27	
	R1	100 MΩ	
	R2	0-100 kΩ	Potentiometer
	R3	1 MΩ	
	R4	1 kΩ	
	R5	10 Ω	
	R6	1 kΩ	
	C1	1 pF	
	C2	47-57 pF	
VGA	Op1	OP27	
	R1	10 kΩ	
	R2	0-100 kΩ	Potentiometer
	R3	0-100 kΩ	Potentiometer
	C1	1 nF	
PI Controller	Op1	OP27	
	Op2	OP27	
	Op3	OP27	
	R1	0-200 kΩ	Potentiometer
	R2	0-200 kΩ	Potentiometer
	R3	0-200 kΩ	Potentiometer
	R4	10 kΩ	
	R5	10 kΩ	
	R6	10 kΩ	
	C1	0-5 nF	
	C2	0-5 nF	

D.2 Slave servo electronics

In the slave servo, ET actuator is used as the drive plant. Fig. D.3 shows the block diagram of the salve servo. The slave servo is similar to the master servo and yet has several exclusive features. First, since the vertical movement range of the ET actuator is unidirectional, its position needs to be centered in its travel range by a pre-actuation bias voltage, V_{ET0}, to provide room for voltage control of both upward and downward displacement, as shown in the loop diagram. Secondly, the relationship between the vertical displacement of the slave probe, Z_{ET}, and the ET drive voltage, V_{ET0}, is

$$z_{ET}(V_{ET}) = CP_{ET} = C\frac{{V_{ET}}^2}{R} \tag{D-1}$$

where P_{ET} is the ET drive power. It can be seen that the displacement is not a monotonic function of the drive voltage. To be used in the feedback loop, the sign of the ET drive voltage must be kept unchanged, either always positive or always negative to keep the function $z_{ET}(V_{ET})$ monotonic. In the testbench, the pre-actuation voltage, V_{ET0}, is set to be positive, so the output voltage of the PI controller must be kept smaller than V_{ET0} to keep V_{ET} always positive. To this end, a saturation unit is added following the PI controller. Fig. D.4 shows the saturation unit. The saturation unit consists of a current limiting resistor and a diode. When v_{in} is smaller than the threshold voltage of the diode, v_{th}, which is around 0.7 V in our case, the diode is off, so the output voltage, v_{out}, follows input voltage, v_{in}. When v_{in} is larger than v_{th}, the diode is on and v_{out} is clamped at v_{th}. Therefore, the maximum output of the saturation unit is 0.7 V. the pre-actuation voltage needs to be set larger than 0.7 V to keep V_{ET} positive at all the time so that the slave STM servo work properly. In the actual experiment, the pre-actuation voltage is set around 5 V.

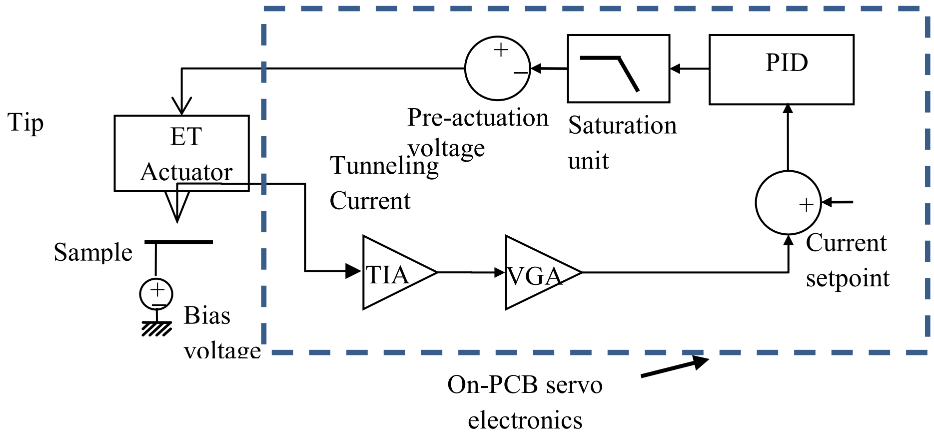

Fig. D.3 Block Diagram of a single probe ET actuator-driven STM system

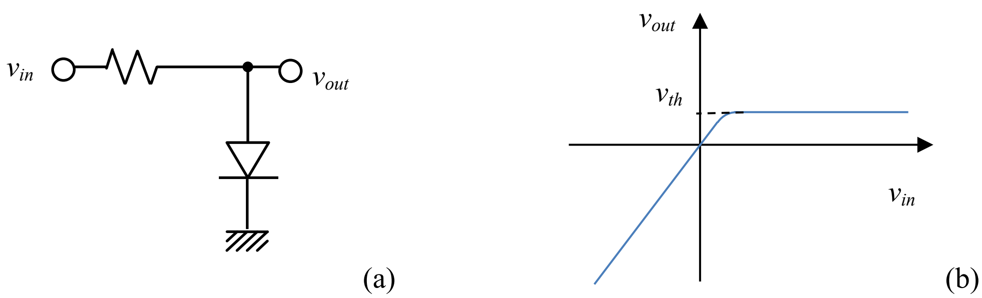

Fig. D.4 Block Diagram of a single probe ET actuator-driven STM system

Appendix E – Characterization of the Piezo and ET drive sensitivity

In chapter 2, the probe ET drive sensitivity is *in situ* characterized during the STM scanning. It is concluded that the travel distance caused by change of 1 V drive voltage on piezo scanner is equivalent to that caused by 0.129 mW drive power on ET actuator. The numerical value of the drive sensitivity of two actuators are then respectively measured and compared.

To measure the drive sensitivity of a piezo actuator on Veeco Dim3000 SPM system, a gold-coated silicon wafer with a step height of 110 nm, measured by the KLA Tencor P-15 Profilometer, is used as a calibration sample. The SPM system is working in AFM tapping mode, where the probe scans the step on the sample back and forth. The scan area is 20 μm by 20 μm and the scan speed is 4 μm/s. The piezo voltage in the z-direction is recorded. Fig. E.1 (a) shows the AFM image of the step height. Fig. E.1 (b) shows the recorded piezo-voltage across the step. The voltage difference of two planes, ΔV, is measured as ~6.6 V. The z-direction drive sensitivity of the piezo actuator is therefore calculated as 17 nm/V. Using the ratio of the drive sensitivities of two actuators, the drive sensitivity of the ET actuator on the CMOS MEMS probe is 131 nm/V.

The CMOS MEMS probe mounted on a Veeco AFM probe holder, as shown in Fig. E.2 (a), is used in the independent measurement of the ET drive sensitivity. The probe holder is the same as that is used to hold the CMOS MEMS probe chip in STM operation. A WYKO NT3300 white-light interferometer is used to examine the curl-up of the probe under different drive power. Fig. E.2 (b) shows an example of probe curl up at a drive power of 3.44 mW. Fig. E.2 (c) shows the vertical displacement dependence on the drive power. The measured drive sensitivity is 112 nm/mW, which is lower than the derived ET sensitivity from the piezo drive sensitivity.

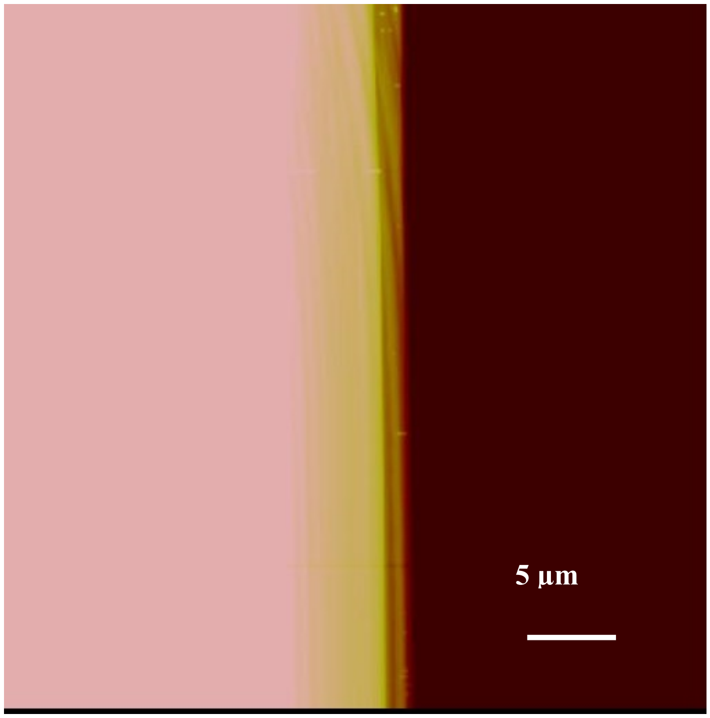

(a)

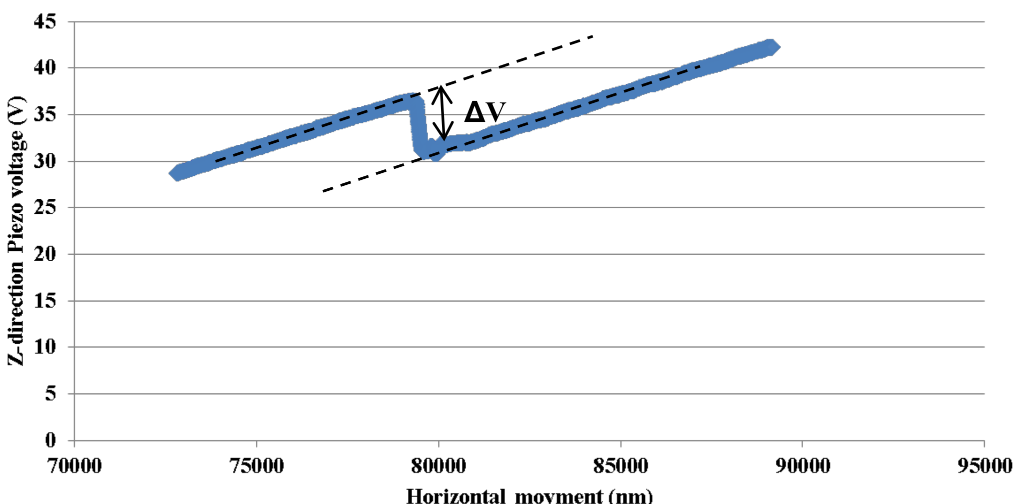

(b)

Fig. E.1 (a) AFM image of the calibration sample, the step is clearly identified. (b) The z-direction piezo voltage variation along the step.

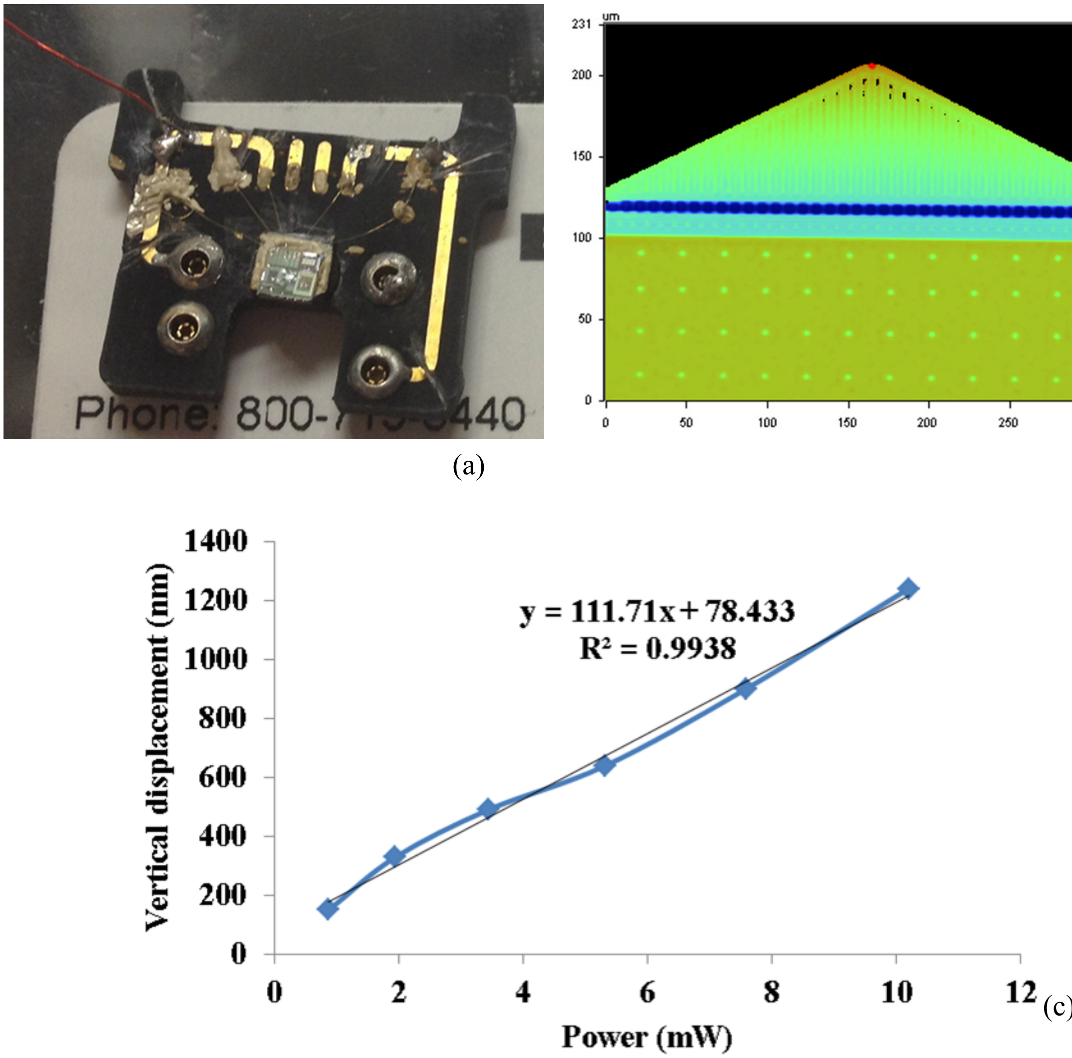

Fig. E.2 (a) the active CMOS MEMS probe mounted on the AFM probe holder. (b) Interferometer images of the CMOS MEMS probe at a drive power of 3.44 mW. (c) The vertical displacement *vs.* ET drive power. The ET drive sensitivity is 112 nm/mW.

A discrepancy exists in the ET drive sensitivity between that converted from the piezo drive sensitivity and that from the direct measurement under the interferometer. When the ET actuator-driven STM cantilever scans the surface, the ET actuator is close to the sample surface that acts as a heat sink, so it is expected that the ET actuator will have lower drive sensitivity compared to when it stands alone. The measurement gave an opposite result, however. In the two tests two different ET-actuated MEMS cantilevers were used, so their different heating history could be one cause of the discrepancy. Further characterization of the ET drive sensitivity needs to be done to account for the discrepancy.

References

[1] D. Wang, L. Tsau, K. L. Wang, P. Chow, “Nanofabrication of thin chromium film deposited on Si(100) surfaces by tip induced anodization in atomic force microscopy”, *Appl. Phys. Lett.*, vol 67, pp. 1295 – 1297, 1995.

[2] W. Ye, P. A. Martin, N.Kumar, S. R. Daly, A. A. Rockett, J. R. Abelson, G. S. Girolami, J.W. Lyding, “Direct Writing of Sub-5 nm Hafnium Diboride Metallic Nanostructures” , *ACS Nano.*, vol, 11, pp. 6818 – 6824, 2010.

[3] E. E. Ehrichs, S. Yoon, and A. L. de Lozanne, “Direct writing of 10 nm features with the scanning tunneling microscope”, *Appl. Phys. Lett.,* vol 53, pp. 2287 – 2289, 1998.

[4] M. J. Rost, et al., “Scanning probe microscopes go video rate and beyond”, *Rev. Sci. Instrum.*, vol. 76, pp. 053710, 2010.

[5] J. A. Stroscio, W. J. Kaiser, *Scanning tunneling microscopy*, Method of Experimental Physics, vol.27, Academic Press, INC., 1993

[6] W. A. Hofer, A. S. Foster, A. L. Shluger, “Theories of scanning probe microscopes at the atomic scale”, *Rev. Modern Physics*, 75:1287–1331, October 2003.

[7] A. A. Tseng, A. Notargiacomo, T. P. Chen, “Nanofabrication by scanning probe microscope lithography: A review”, *J. Vac. Sci. Technol. B*, vol. 23, pp. 877 – 894, 2005.

[8] S. C. Minne, G. Yaralioglu, S. R. Manalis, J. D. Adams, J. Zesch, A. Atalar, C. F. Quate, “Automated parallel high-speed atomic force microscopy”, *Appl. Phys. Lett.*, vol. 72, pp. 2340 – 2342, 1998.

[9] K. Wilder, h. T. Soh, A. Atalar, C. F. Quate, “Hybrid atomic force/scanning tunneling lithography”, *J. Vac. Sci. Technol. B*, vol. 15, pp. 1811 – 1817, 1997.

[10] X. Wang, C. Liu, “Multifunctional Probe Array for Nano Patterning and Imaging”, *Nano Lett.*, vol. 5, pp. 1867 – 1872, 2005.

[11] J. Lee, T. Beechem, T. L. Wright, B. A. Nelson, S. Graham, W. P. King, “Electrical, thermal, and mechanical characterization of slicon microcantilever heaters”, *J. MEMS*, vol. 15, pp. 1644 – 1655, 2006.

[12] H. Hu, H. Cho, S. Somnath, A. F. Vakakis, W. P. King, “Silicon nano-mechanical resonators fabricated by using tip-based nanofabrication”, *Nanotechnology*, vol. 25, pp. 275301, 2014

[13] B. Lee, S. Somnath, W. P. King, “Fast nanotopography imaging using a high speed cantilever with integrated heater-thermometer”, *Nanotechnology*, vol. 24, pp. 014001, 2014

[14] S. Somnath, H. J. Kim, H. Hu, W. P. King, “Parallel nanoimaging and nanolithography using a heated microcantilever array”, *Nanotechnology*, vol. 25, pp. 275301, 2014

[15] S. Hafizovic, D. Barrettino, T. Volden, J. Sedivy, K. Kirstein, O. Brand, A. Hierlemann, “Single-chip mechatronic microsystem for surface imaging and force response studies”, *PNAS*, vol. 101, pp. 17011 – 17015, 2004.

[16] A. Pantazi, A. Sebastian, P. Bachtold, et al., “Probe-based ultrahigh-density storage technology”, *IBM J. RES. & DEV.,* vol. 52, pp. 493 – 511, 2008.

[17] M. Despont, U. Drechsler, R. Yu, H. Pogge, P. Vettiger, “Wafer-scale Microdevice Transfer/Interconnect: Its application in an AFM-based Data-Storage System”, *J. MEMS*, vol. 13, pp. 895 – 901, 2004.

[18] J. L. Arlett, E. B. Myers, M. L. Roukes, “Comparative advantages of mechanical biosensors”, *Nature Nanotechnology*, vol. 6, pp. 203 – 215, 2011.

[19] X. Bai, H. Hou, B. Zhang, J. Tang, “Label-free detection of kanamycin using aptamer-based cantilever array sensor”, Biosens. Nioelectron., vol. 56, pp. 112 – 116, 2014.

[20] M. Favre, J. Polesel-Maris, T. Overstolz, P. Niedermann, S. Dasen, G. Gruener, R. Ischer, P. Vettiger, M. Liley, H. Heinzelmann, A. Meister, “Parallel AFM imaging and force spectroscopy using two-dimensional probe arrays for applications in cell biology”, *J. Mol. Recognit.*, vol. 24, pp. 446 – 452, 2011.

[21] F. Loizeau, M. Favre, T. Akiyama, S. Gautsch, A. Meister, R. Smajda, P. Vettiger, G. Weder, N. F. de Rooij, “2D Cantilever array with spherical tips for parallel force spectroscopy on cancerous cells”, *Proc. Transducers’13 conference*, pp. 1186 – 1189, 2013.

[22] J. Liu, M. Noman, J. Bain, T. Schlesinger and G. Fedder, “CMOS-MEMS probes for reconfigurable IC’s”, *Proc. IEEE MEMS’08 conference*, pp. 515 – 518.

[23] P. Gilgunn, *SOI-CMOS-MEMS electrothermal micromirror arrays*, Ph.D. thesis, Carnegie Mellon University, 2010.

[24] H. Yang, M. S. Bakir, “3D Integration of CMOS and MEMS using Mechanically Flexible Interconnects (MFI) and Through Silicon Vias (TSV)”, *Proc. ECTC 2010*, pp. 822 – 828.

[25] J. Liu, *CMOS-MEMS probes*, Ph.D. thesis, Carnegie Mellon University, 2010.
[26] S. C. Minne, S. R. Manalis, C. F. Quate, “Parallel atomic force microscopy using cantilevers with integrated piezoresistive sensors and integrated piezoelectric actuators”, *Appl. Phys. Lett.*, vol. 67, pp. 3918 – 3920, 1995.
[27]S. C. Minne, G. Yaralioglu, S. R. Manalis, J. D. Adams, J. Zesch, A. Atalar, C. F. Quate, “Atomic force microscopy for high speed imaging using cantilevers with an integrated actuator and sensor”, *Appl. Phys. Lett.*, vol. 66, pp. 871 – 873, 1998.
[28] E. C. M. Disseldorp, F. C. Tabak, A. J. Katan, M. B. S. Hesselberth, T. H. Oosterkamp, J. W. M. Frenken, W. M. van Spengenc, “MEMS-based high speed scanning probe microscopy”, *Rev. Sci. Instrum.*, vol. 81, pp. 043702, 2010.
[29] S. D. Senturia, *Microsystem design*, Kluwer Academic Publishers, 2002.
[30] A. Toantranont, V. M. Bright, “Micromachined thermal multimorph actuators fabricated by multi-users MEMS process”, *IEEE ICIT'02*, pp. 941 – 943, 2002.
[31]M.J. Sinclair, “A high force low area MEMS thermal actuator”, *Proceedings of Intersociety Conference on Thermal and Thermomechanical Phenomena in Electronic Systems*, pp. 127 – 132, 2000.
[32] J. H. Comtois, M. A. Michalicek, C. C. Barron, “Electrothermal actuators fabricated in four-level planarized surface micromachined polycrystalline silicon”, *Sensor Actuator A*, pp. 23 – 31, 1998.
[33] X. Wang, C. Liu, “Multifunctional Probe Array for Nano Patterning and Imaging”, *Nano Lett.*, vol. 5, pp. 1867 – 1872, 2005.
[34] S. Timoshenko, “Analysis of bi-metal thermostats”, *J. Opt. Soc. Am.*, vol. 11, pp. 233 – 255, 1925.
[35] R. Wiesendanger, *Scanning Probe Microscopy and Spectroscopy*, Cambridge University Press, 1994.
[36] B. Cappella, G. Dietler, “Force-distance curves by atomic force microscopy”, *Surf. Sci. Rep.*, vol. 34, pp 1 – 104, 1999.
[37]S.Hudlet, M. Saint Jean, C. Guthmann, J. Berger, “Evaluation of the capacitive force between and an atomic force microscopy tip and a metallic surface”, *Eur. Phys. J. B*, vol. 2, pp. 5 – 10, 1998.
[38]D. Y. Abramovitch, S. B. Andersson, L. Y. Pao, G. Schitter, “A tutorial on the mechanisms, dynamics, and control of Atomic force Microscopes”, *Proc. American Control Conference*, pp. 2488 – 3502, 2007.
[39] J. N. Israelachvili, *Intermolecular and Surface Forces*, third edition, Elsevier Science, 2011.
[40] J. Y. Park, S. Maier, B. Hendrksen, M. Salmeron, “Sensing current and forces with SPM”, *Materials Today*, vol. 13, pp. 38 – 45, 2010.
[41] C. M. Mate, R. Erlandsson, G. M. Mcclelland, S. Chiang, “Direct measurement of normal force during scanning tunneling microscope imaging of graphite”, *Surf. Sci.*, vol. 208, pp. 473 – 486, 1989.
[42] P. J. Gilgunn, J. Liu, N. Sarkar, G. K. Fedder, “CMOS-MEMS lateral electrothermal actuators”, *J. MEMS*, vol. 17, pp. 103 – 114, 2008.
[43] J. Reinke, G. K. Fedder, T. Mukherjee, “CMOS-MEMS 3-bit digital capacitors with tuning ratios greater than 60:1”, IEEE Trans. Microwave Theory Tech., vol. 59, pp. 1238 – 1248, 2011.
[44] S. Timoshenko, J.N.Goodier, *Theory of Elasticity*, third edition, McGraw-Hill, 1970.
[45] SVM, www.svmi.com/silicon-wafers/silicon-insulator-wafers/, accessed August 4th, 2014.
[46] C. Julia Chen, “Role of tip material in scanning tunneling microscopy”, *Mat. Res. Soc. Symp. Proc.*, vol. 159, pp. 289 – 292, 1990.
[47] S. Murphy, J. Osing, I. V. Shvets, “Fabrication of submicron-scale manganese–nickel tips for spin-polarized STM studies”, *Appl, Surf. Sci.*, vol. 144, pp. 397 – 500, 1999.
[48] C. J. Chen, *Introduction to Scanning Tunneling Microscopy,* Oxford University Press, 1993.
[49] J. Garnæs, F. Kragh, K. A. Mørch, A. R. Thölén, “Transmission electron microscopy of scanning tunneling tips ” *J. Vac. Sci. Technol. A*, vol 8, pp. 441 – 444, 1990.
[50] Y. Khan, H. Al-Falih, Y. Zhang, T. Ng, B. S. Ooi, “Two-step controllable electrochemical etching of tungsten scanning probe microscopy tips”, *Rev. Sci. Instrum.*, vol. 83, pp. 063708, 2012.
[51] E. Abelev, N. Sezin, and Y. Ein-Eli, “An alternative isolation of tungsten tips for a scanning tunneling microscope”, *Rev. Sci. Instrum.*, vol. 76, pp. 106105, 2005.
[52] T. R. Albrecht, S. Akamine, T. E. Carver, C. F. Quate, “Microfabrication of cantilever styli for the atomic force microscope”, *J. Vac. Sci. Technol. A*, vol. 8, pp. 3386 – 3396, 1990.
[53] C. Liu, R. Gamble, “Mass-producible monolithic silicon probes for scanning probe microscopes”, *Sensor Actuator A*, vol. 71, pp. 233 – 237, 1998.
[54] H. Shin, *Fabrication of atomic force microscope probes integrated with electrodes for micro four-point probe and SECM-AFM*, PhD thesis, Georgia Institute of Technology, 2006.

[55] A. P. Janssen, J. P. Jones, "The sharpening of field emitter tips by ion sputtering", *J. Phys. D.*, vol. 4, 118 – 123, 1971.
[56] R. B. Marcus, T. T. Sheng, "The oxidation of shaped silicon surfaces", *J. Electrochem. Soc.*, vol. 129, pp. 1278 –1282, 1982.
[57] S. Akita, H. Nishijima, y. Nakayama, F. Tokumasu, K. Takeyasu, "Carbon nanotube tips for a scanning probe microscope: their fabrication and properties", *J. Phys. D: Appl. Phys.*,, vol. 32, pp. 1044 – 1048, 1999.
[58] C. A. Spindt, "A thin-film field-emission cathode", *J. Appl. Phys.*, vol. 39, pp. 3504 – 3505, 1968.
[59] H. Lee, Y. Park, J. Kim, J. Choi, J. Kim, "Investigation of the formation mechanism of Spindt-type cathode by simulation and experiments", *J. Vac. Sci. Technol. B*, vol. 17, pp. 547 – 551, 1999.
[60]G. N. A. van Veen, B. Theunissen, K. van de Heuvel, R. Horne, A. Burgmans, "Collimated sputter deposition, a novel method for large area deposition of Spindt type field emission tips", *J. Vac. Sci. Technol. B*, vol. 13, pp. 478 – 481, 1995.
[61] C. A. Spindt, I. Brodie, L. Humphrey, E. R. Westerberg, "Physical properties of thin film field emission cathodes with molybdenum cones", *J. Appl. Phys.*, vol. 47, pp. 5248 – 5263, 1976.
[62] Y. Zhang, S. Santhanam, J. Liu, G. K. Fedder, "Active CMOS-MEMS AFM-like conductive probes for field-emission assisted nano-scale fabrication", *Proc. MEMS'10 conference*, pp. 336 – 339, 2010.
[63] A. A Tseng, *Nanofabrication: Fundamentals and Applications*, World Scientific Publishing Co. Pte. Ltd, 2008.
[64]Nanoelectrotec, http://nanoelectrotec.com/index.html, accessed April 20th, 2014.
[65] W. F. van Drop, B. van Someren, C.W. Hagen, P. Kruit, P. A. Crozier, "Approaching the resolution limit of nanometer-scale electron beam-induced deposition", *Nano Lett.*, vol. 5, pp. 1303 – 1307, 2005.
[66] Y. Zhang, Y. Tang, L. R. Carley, G. K. Fedder, "Active CMOS-MEMS conductive probes and arrays for tunneling-based atomic-level surface imaging", *Proc. Transducers'11 conference*, pp. 2446 – 2449, 2011.
[67] J. G. Simmons, "Electric tunnel effect between dissimilar electrodes separated by a thin insulating film", *J. Appl. Phy.*, vol. 34, pp. 2581 – 2590, 1963.
[68] C. J. Chen, *Introduction to Scanning Tunneling Microscopy*, Oxford University Press, 1993.
[69] A. I. Oliva, E. Anguiano, N. Denisenko, M. Aguilar, "Analysis of scanning tunneling microscopy feedback system", *Rev. Sci. Instrum.,* vol. 66, pp. 3196 – 3203, 1995.
[70] J. P. Song, K. A. Morch, "Investigation of scanning tunneling microscopy tunneling barrier height in air and water", *J. Vac. Sci. Technol. B*, vol. 12, pp. 2237 – 2242, 1994.
[71] L. Boyer, S. Noel, F. Houze, "Apparent tunnel barrier heights of PtIr–Au interfaces in relation to the Au surface composition", *J. Vac. Sci. Technol. B*, vol. 16, pp. 2006 – 2011, 1998.
[72]Y. Tang, Y. Zhang, G. K. Fedder and L.R. Carley, "A dual probe STM imaging system and a low noise switched-capacitor transimpedance amplifier", *IEEE Sensors Journal*, vol. 13, pp. 2984 – 2991, 2013.
[73] C.L. Petersen, T.M. Hansen, P. Bøggild, A. Boisen, O. Hansen, T. Hassenkam, F. Grey, "Scanning microscopic four-point conductivity probes", *Sens. & Act. A*, vol. 96, pp. 53 – 58, 2002.
[74] X. Wang, L. Vincent, M. Yu, Y. Huang, C, Liu, "Architecture of a Three-Probe MEMS Nanomanipulator with nanoscale end-effectors", *Proc. IEEE/ASME AIM conference 2003*, pp. 891 – 896.
[75] J. Lee, X. Huang, P. B. Chu, "Nanoprecision MEMS capacitive sensor for linear and rotational positioning", *J. MEMS*, vol. 18, pp. 660 – 670, 2009.
[76] M. N. Horenstein, J. A. Perreault, T. G. Bifano, "Differential capacitive position sensor for planar MEMS structures with vertical motion", Sens*. Actuators, A*, vol. 80, pp. 53 – 61, 2000.
[77] M. A. Lantz, G. K. Binnig, M. Despont, U. Drechsler, "A micromechanical thermal displacement sensor with nanometre resolution", Nanotechnology, vol. 16, pp. 1089 – 1094, 2005.
[78] B. Krijnen, R. P. Hogervorst, J. W. van Dijk, J. Engelen, L. A. Woldering, D. M. Brouwer, L. Abelmann, H. Soemers, "A single-mask thermal displacement sensor in MEMS", *J. Micromech. Microeng.*, vol. 21, 035021, 2010.
[79] K.J. Kim, K. Park, J. Lee, Z.M. Zhang, W.P. King, "Nanotopographical imaging using a heated atomic force microscope cantilever probe", *Sens. & Act. A*, vol. 136, pp. 95 – 103, 2007.
[80] F. N. Hooge, "*1/f noise sources*", IEEE trans. Electron Devices, vol. 41, pp. 1926 – 1935, 1994.
[81] A. Sebastian, D. Wiesmann, "Modeling and experimental identification of silicon microheater dynamics: A systems approach", *J. MEMS*, vol. 17, pp. 911 – 920, 2008.
[82] J. Liu, L. Draghi, J. A. Bain, T.E. Schlesinger, G. K. Fedder, "Three-DOF CMOS-MEMS probes with embedded piezoresistive sensors", *Proc. IEEE MEMS'10 Conference*, pp. 284 – 287, 2010.

[83] J. R. Reinke, *CMOS-MEMS variable capacitors for reconfigurable RF circuits*, Ph.D. Thesis, Carnegie Mellon University, 2011.
[84] A. Sinha, T. Sheng, "The temperature dependence of stress in aluminum films on oxidized silicon substrates", *Thin Solid Films*, vol. 48, pp. 117 – 126, 1978.
[85]W. Hu, *Tip Based Nanofabrication using Multi-mode Scanning Probe Microscopy*, Ph.D. Thesis, Carnegie Mellon University, 2012.
[86] O. Ozcan, *Tip Based Automated Nanomanipulation using Scanning Probe Microscopy*, Ph.D. Thesis, Carnegie Mellon University, 2012.
[87] Y. Tang, Y. Zhang, G. K. Fedder, L. R. Carley, "An ultra-low noise switched capacitor transimpedance amplifier for parallel scanning tunneling microscopy", *Proc. Sensors'12*, 2012.
[88] A. A. Tseng, S. Jou, A. notargiacomo, T. P. Chen, "Recent developments in tip-based nanofabrication and its roadmap", *J. Nanosci. Nanoechnol*., vol. 8, pp. 1 – 20, 2008.